5-2018

Development of Anti-fouling Membranes for Water Treatment

Steven Weinman
Clemson University, stweinman@gmail.com

DEVELOPMENT OF ANTI-FOULING MEMBRANES FOR WATER TREATMENT

A Dissertation
Presented to
the Graduate School of
Clemson University

In Partial Fulfillment
of the Requirements for the Degree
Doctor of Philosophy
Chemical Engineering

---

by
Steven Thomas Weinman
May 2018

Accepted by:
Dr. Scott M. Husson, Committee Chair
Dr. Christopher L. Kitchens
Dr. David A. Bruce
Dr. David A. Ladner

ABSTRACT

The goal of my dissertation research was to devise new strategies to combat membrane fouling, which is a major hindrance in water treatment systems. Membrane fouling refers to the blocking of pores and the build-up of material on the membrane surface. There are many types of foulants, including but not limited to bacteria, biopolymers (such as alginate), natural organic matter, oils, proteins, particles, and salts (such as gypsum). Typical ways to combat fouling include expensive pretreatment procedures, physical membrane cleaning, and chemical treatments to the membranes. Chemical treatments tend to decrease the membrane lifetime, especially for nanofiltration and reverse osmosis membranes. One common strategy in the research community is to surface modify membranes to increase their fouling resistance. Chapter 1 reviews the surface modification methods used to reduce membrane fouling.

Chapter 2 presents my work on modifying ultrafiltration membranes with poly(2-((2-hydroxy-3-(methacryloyloxy)propyl)dimethylammonio)acetate) (poly(CBOH), a polymer that switches reversibly between a zwitterionic chemistry and a quaternary amine chemistry. Surface characterization showed successful membrane modification by UV-graft polymerization. Bacteria deposition studies showed that the poly(CBOH) chemistry performed better than other common anti-fouling chemistries. Biofilm studies showed that poly(CBOH) functionalized polyethersulfone membranes accumulated half the biovolume as unmodified membranes. Poly(CBOH) switches from an anti-fouling, zwitterion mode to an anti-microbial, quaternary amine mode by changing the environment pH. Studies were done to characterize the switching pH and time using

poly(CBOH) modified silicon wafers. Switching pH was determined to be 1.0, with 15 min being required to switch between the zwitterion and quaternary amine chemistries. Biofilm mortality was elevated on ultrafiltration membranes once the anti-fouling poly(CBOH) zwitterion was switched to the anti-microbial, poly(CB-Ring) quaternary amine, with dead-to-live cell ratio increasing from 0.33 to 1.04.

Chapter 3 describes my work to increase the fouling resistance of nanofiltration membranes by applying both a chemical coating and a nanometer sized pattern to the membrane surfaces. A line and groove nano-pattern was applied by thermal embossing directly onto a commercial polyamide thin-film composite nanofiltration membrane. Poly(ethylene glycol) diglycidyl ether (PEGDE) was reacted onto the patterned membrane surfaces by an epoxide ring opening reaction with unreacted carboxyl groups on the polyamide selective layer. Surface characterization showed successful nano-patterning and chemical modification of the membrane surfaces. Membrane performance (flux and salt rejection) was unaffected by patterning the polyamide membrane surface directly. The fouling results show that combining line and groove nano-patterning with PEGDE chemical modification yields a membrane that was more resistant to fouling than either method alone.

Chapter 4 presents my work to apply a nanometer sized pattern onto numerous commercial nanofiltration and reverse osmosis polyamide membranes. There have been differing views on the ability to pattern polyamide thin-film composite (TFC) membranes directly by nanoimprint lithography. The goal of this study was to understand what factors control patternability, working towards a set of heuristics for use by the

membrane community to pattern any polyamide TFC membrane. Initial results showed that each membrane patterned to a different degree. Despite completing a comprehensive set of experiments to investigate the roles played by membrane chemistry, surface properties, mechanical properties, and performance properties on pattern peak heights for thirteen commercial nanofiltration and reverse osmosis membranes, I found no correlation between the variables studied and patternability of *individual* membranes. I did discover significant differences in patternability between membranes grouped by polyamide class, with those prepared by interfacial polymerization of *m*-phenylenediame and trimesoyl chloride having the largest pattern peak heights. I further discovered that the humectant (pore filler) used for membrane preservation plays a role on the patternability of the membranes. Upon replacement of the original humectants used by the membrane manufacturers with a 15 wt% glycerol solution, the pattern peak heights approached a similar value for each class of membranes. Tests performed to elucidate the role of the glycerol on patternability were inconclusive. Thus, while the humectant clearly contributes to membrane patternability, the reason why remains unknown.

Overall, my research demonstrates the ability to reduce membrane biofouling by changing surface chemistry and surface features. Results of my work contribute to our understanding of membrane fouling and can be used to develop next-generation water treatment membranes with improved fouling resistance. Such membranes could be expected to lower the operations cost of using membranes to clean water.

DEDICATION

This dissertation is dedicated to my lovely wife Rose and to my wonderful parents Tom and Donna Weinman.

ACKNOWLEDGMENTS

I would like to express my sincerest thanks to my advisor Dr. Scott Husson for his support and guidance throughout my graduate studies. I could not have made a better choice for a Ph.D. advisor. His advice helped steer my ideas to something tangible I could do. His level of organization is something I strived for in my graduate studies. I could not have asked for a better mentor and role model for my career. If I can emulate Dr. Husson in my own career, I would consider myself successful. I have enjoyed learning from and with him about topics we both were uncertain where it would take us. I want to thank him for helping me see that an academic career is the way to go!

I would like to thank my parents Tom and Donna for their endless support. Without them, I would not have made it to Clemson. They helped instill a work ethic in me that helped make me a successful graduate student. I would also like to thank my wife, Rose. Without her love and support, graduate school would have been a lot harder. I thank her for always pushing me to be the best I can be. I would also like to thank my Lord and Savior Jesus Christ, without the skills He gave me, I would not be where I am today.

I thank my past and current group members Jinxiang, Heather, Juan, Nikki, Christine, Joe, Jaime, Anna, Mark, James, Abenazar, Valery, Shelby, Jake, and Cody for their friendship, help in the lab, and discussions whether pertaining to research or life. I want to thank an undergraduate student, Eric Fierce, who contributed to the success of the patterning project. I enjoyed getting to know and work with Eric.

I would like to thank my committee members Dr. Christopher L. Kitchens, Dr. David A. Bruce, and Dr. David A. Ladner for giving me helpful advice and suggestions for completing my work.

I would like to thank the many people (and their students) that have allowed me to use their equipment and/or have provided assistance in the safe operation of equipment: Dr. Terri Bruce, Rhonda Powell, Kim Ivey, Dr. Alex Kitaygorodskiy, Donald Mulwee, Dr. Christopher L. Kitchens, Dr. David A. Bruce, Dr. Amod Ogale, Dr. David A. Ladner, and Dr. Igor Luzinov.

Finally, I am thankful for financial support from a National Science Foundation Graduate Research Fellowship under award DGE-1246875. I am grateful for the support of the switchable chemistry project by the US-Israel Binational Agricultural Research and Development Fund for financial support under Research Grant Agreement No. US-4654-13. I am grateful for the support of the patterning project by the National Science Foundation under NSF award CBET-1534304 and Clemson University for funding through the Tiger Grant Award program under award 1401473. Any opinion, findings, and conclusions or recommendations expressed in this material are those of the authors(s) and do not necessarily reflect the views of the National Science Foundation.

TABLE OF CONTENTS

Page

TITLE PAGE i

ABSTRACT ii

DEDICATION v

ACKNOWLEDGMENTS vi

LIST OF TABLES x

LIST OF FIGURES xiii

CHAPTER

I. INTRODUCTION 1

1.1 Introduction 1
1.2 Anti-Fouling Strategies 3
1.3 Anti-Microbial Strategies 5
1.4 Combined Anti-Fouling and Anti-Microbial Strategies 6
1.5 Surface Patterning Strategies 7
1.6 Evaluating Effectiveness of Membrane Surface Modifications 10
1.7 Dissertation Structure 12

II. A SWITCHABLE ZWITTERIONIC MEMBRANE SURFACE CHEMISTRY FOR BIOFOULING CONTROL 13

2.1 Introduction 13
2.2 Material and Methods 15
2.3 Results and Discussion 32
2.4 Conclusions 58
2.5 Acknowledgements 58

III. INFLUENCE OF CHEMICAL COATING COMBINED WITH NANOPATTERNING ON ALGINATE FOULING DURING NANOFILTRATION 60

3.1 Introduction 60
3.2 Materials and Methods 62

Table of Contents (Continued)

Page

3.3 Results and Discussion 69
3.4 Conclusions 88
3.5 Acknowledgements 89

IV. NANOPATTERNING COMMERCIAL NANOFILTRATION AND REVERSE OSMOSIS MEMBRANES 90

4.1 Introduction 90
4.2 Materials and Methods 92
4.3 Theory 98
4.4 Results and Discussion 101
4.5 Conclusions 130
4.6 Acknowledgement 130

V. CONCLUSIONS AND RECOMMENDATIONS 131

5.1 Summary and Conclusions 131
5.2 Recommendations 134

APPENDICES 140

A: Statistical Analysis for A SWITCHABLE ZWITTERIONIC MEMBRANE SURFACE CHEMISTRY FOR BIOFOULING CONTROL 141
B: Statistical Analysis for NANOPATTERNING COMMERCIAL NANOFILTRATION AND REVERSE OSMOSIS MEMBRANES 148
C: Permissions to Reproduce Figures and Text 156

REFERENCES 170

LIST OF TABLES

Table Page

2.1 *Pseudomonas fluorescens* deposition (mass transfer) coefficients of unmodified GE Osmonics PES membranes and membranes modified with poly(CBOH), poly(SPE), and poly(PEGMA) by UV polymerization. Uncertainties represent one standard deviation among at least four different membrane samples 43

2.2 Water and diiodomethane contact angles for silicon wafers modified with poly(CBOH) and poly(CB-Ring). Contact angle data are included for common antifouling chemistries: PEG, PMAPS (sulfobetaine zwitterion), PDMAB (carboxybetaine zwitterion), and PMPC (phosphobetaine zwitterion) on silicon wafers. Surface energy calculations are based on the Owens-Wendt method. Uncertainties represent the data range from at least 3 measurements or the error values reported in the articles cited 52

2.3 Biofilm volumetric quantification (biovolume per Membrane area, biomass thickness, and biomass roughness coefficient) for each component of the biofilm formatted by *Sphingomonas wittichii* RW1 on unmodified, poly(CBOH) modified and poly(SPE) modified Microdyn-Nadir PM UP150 PES membranes. Uncertainties represent one standard deviation amongst at least five data points 55

2.4 Biofilm volumetric quantification (biovolume per membrane area, biomass thickness, and biomass roughness coefficient) for each component of the biofilm formatted by *Sphingomonas wittichii* RW1 on poly(CBOH) modified and poly(SPE) modified Microdyn-Nadir PM UP150 PES membranes after pH 1.0 acid treatment for 20 min. Uncertainties represent one standard deviation among at least eight data points 57

List of Tables (Continued)

Table Page

4.1 Membrane chemistry, support chemistry, and patterned peak heights (nm) of 13 commercial NF and RO membranes and 2 membrane supports. Error represents one standard deviation from at least 3 membrane pieces 102

4.2 Membrane chemistry, 45°C patterned peak heights (nm), and 75°C patterned peak heights (nm) of 13 commercial NF and RO membranes. Error represents one standard deviation from at least 3 membrane pieces 112

4.3 Water and diiodomethane contact angles for commercial nanofiltration and reverse osmosis membranes. Surface energy calculations are based on the Owens-Wendt method. Uncertainties represent one standard deviation from at least 12 data points from at least 3 membrane pieces 115

5.1 pK_a's of various organic acids 136

A-1 Statistical analysis results of the biofilm volumetric quantification between the unmodified, poly(CBOH) modified, and poly(SPE) modified Microdyn-Nadir PM UP150 PES membranes. Interpretation (what is statistically different) was done using a Tukey's t-test 143

A-2 Statistical analysis results of the biofilm volumetric quantification between the poly(CBOH) modified Microdyn-Nadir PM UP150 PES membranes with and without acid rinse 144

A-3 Statistical analysis results of the biofilm volumetric quantification between the poly(SPE) modified Microdyn-Nadir PM UP150 PES membranes with and without acid rinse 145

A-4 Statistical analysis results between the water contact angle data for the unmodified and polymer modified GE PES membranes 146

List of Tables (Continued)

Table Page

A-5 Statistical analysis results between the water contact angle data for the unmodified and polymer modified Microdyn-Nadir PM UP150 PES membranes 147

B-1 Statistical analysis results of the pristine, pressed, and patterned surface roughness of commercial nanofiltration and reverse osmosis membranes. Interpretation (what is statistically different) was done using a Tukey's t-test 149

B-2 Statistical analysis results of the pristine, pressed, and patterned permeance of commercial nanofiltration and reverse osmosis membranes. Interpretation (what is statistically different) was done using a Tukey's t-test 150

B-3 Statistical analysis results of the pristine, pressed, and patterned $MgSO_4$ rejection of commercial nanofiltration and reverse osmosis membranes. Interpretation (what is statistically different) was done using a Tukey's t-test 151

B-4 Statistical analysis results of the pattern peak heights of the as received and 15wt% glycerol filled membranes of commercial nanofiltration and reverse osmosis membranes 152

B-5 Statistical analysis results of the pattern peak heights of the 15wt% glycerol filled Dow NF270 and Synder NFG membranes using 5 min and 24.5 h soak times 153

B-6 Statistical analysis results of the Young's Modulus of the as received, rinsed, and 15wt% glycerol filled GE Duracid KH, GE DK, and TriSep X201 membranes using 5-minute soak time 154

B-7 Statistical analysis results of the water swelled and 15wt% glycerol swelled polyamide layer thickness of the Dow NF270, Synder NFG, TriSep X201, and GE Duracid KH membranes 155

LIST OF FIGURES

Figure Page

1.1 Conventional classification of pressure-driven water treatment membrane processes 2

1.2 Anti-fouling coating depiction 3

1.3 Bacteria inactivation using graphene oxide composite thin-film composite membranes 6

1.4 A surface capable of switching between anti-fouling zwitterion mode and anti-microbial quaternary amine mode 7

1.5 Depiction showing how patterns on a surface can alter the fluid flow and thus the membrane fouling propensity at both (a) 90° and (b) 0° 8

1.6 Plot used to determine threshold flux from constant-flux filtration measurements 12

2.1 Monomer synthesis schematic. CBtBu is the protected monomer and CBOH is the zwitterion monomer used in experiments 17

2.2 UV-photopolymerization schematic. BP is entrapped within PES to increase the reaction site density. CBOH is polymerized from both BP radicals and PES radicals 19

2.3 ATRP reaction schematic. BPA initiator is reacted with epoxide of PGMA and CBOH is polymerized from radical initiator by ATRP 22

2.4 Switching schematic between the anti-fouling, zwitterion chemistry (CBOH, left) and the anti-microbial, quaternary amine chemistry (CB-Ring, right). CBOH would switch to CB-Ring when exposed to a typical cleaning solution for membranes, and CB-Ring would switch to CBOH when exposed back to normal operating conditions 29

List of Figures (Continued)

Figure Page

2.5 (A) 1H-NMR spectrum and (B) 13C-NMR spectrum of protected monomer CBtBu. CBtBu was dissolved in chloroform-d at a concentration of 50 mg/mL. Lowercase letters were assigned to each proton and carbon type as specified in each spectrum 33

2.6 (A) 1H-NMR spectrum and (B) 13C-NMR spectrum of CBOH. CBOH was dissolved in deuterium oxide at a concentration of 50 mg/mL. Lowercase letters were assigned to each proton and carbon type as specified in each spectrum 35

2.7 ATR-FTIR spectra of (A) GE Osmonics PES membranes unmodified, BP entrapped, and modified by poly(CBOH), poly(SPE), and poly(PEGMA) and (B) Microdyn-Nadir PM UP150 PES membranes unmodified, BP entrapped, and modified by poly(SPE) and poly(CBOH). Scale bar represents (A) 0.02 absorbance units (a.u.) and (B) 0.05 absorbance units (a.u.) 37

2.8 Water contact angle of (A) unmodified and modified GE PES membranes and (B) unmodified and modified Microdyn-Nadir PM UP150 (MN) PES membranes. Error bars represent one standard deviation among at least three samples 38

2.9 SEM images of unmodified (A), BP entrapped (B), poly(SPE) modified (C), and poly(CBOH) modified (D) Microdyn-Nadir PM UP150 PES membranes. Images were taken at 30k resolution and the scale bar represents 1 μm 39

List of Figures (Continued)

Figure Page

2.10 Pure water permeability coefficient ($L/m^2/h/bar$) versus modified membrane type for (A) unmodified, BP entrapped, and modified by poly(CBOH), poly(SPE), and poly(PEGMA) GE PES and (B) unmodified, BP entrapped, poly(SPE) modified, and poly(CBOH) modified Microdyn-Nadir PM UP150 PES membranes. Membranes were tested in direct-flow configuration and the testable membrane area was 14.6 cm^2. Error bars represent one standard deviation among at least 4 samples 41

2.11 (A) 1H-NMR spectrum and (B) 13C-NMR spectrum of switched monomer CB-Ring. CBOH was dissolved in trifluoroacetic acid-d at a concentration of 50 mg/mL for 4 h before spectra was recorded. Lowercase letters were assigned to each proton and carbon type as specified in each spectrum 45

2.12 FTIR spectra of silicon wafers surface modified with initiator (BPA), poly(CBOH), poly(CB-Ring) (poly(CBOH) after immersion in TFA for 1 h), and poly(CBOH) after poly(CB-Ring) (poly(CB-Ring) after immersion in deionized water for 1 h). Poly(CBOH) layer thickness was approximately 60 nm. Scale bar represents 0.02 absorbance units (a.u.) 47

2.13 FTIR spectra of poly(CBOH) modified silicon wafers after being immersed in deionized water, TFA, and TFA/water solutions at pH values of 0.6, 1.0, and 1.5 for 1 h. The evolution of the peak at 1680 cm^{-1} and the increase in peak area at 1150 cm^{-1} indicates conversion from poly(CBOH) to poly(CB-Ring). Poly(CBOH) layer thickness is approximately 60 nm. Scale bar represents 0.02 absorbance units (a.u.) 49

List of Figures (Continued)

Figure Page

2.14 FTIR spectra of (A) poly(CBOH) modified silicon wafers conversion to poly(CB-Ring) by immersion in a TFA/water solution of pH 1.0 for 0 h, 0.25 h, and 0.5 h and (B) poly(CB-Ring) modified silicon wafers conversion to poly(CBOH) by immersion in deionized water for 0.1 h, 0.25 h, and 0.5 h. Poly(CBOH) layer thickness is approximately 60 nm. The scale bar in each figure represents 0.01 absorbance units (a.u.).....50

2.15 FTIR spectra of silicon wafers surface modified with poly(CBOH), poly(CB-Ring) (prepared by immersion of the poly(CBOH) sample in TFA for 0.33 h), and poly(CBOH) (prepared by immersion of the poly(CB-Ring) sample in deionized water for 0.33 h). The number of cycles of switching from poly(CBOH) to poly(CB-Ring) back to poly(CBOH) are shown in the legends of (A) 0-1, (B) 9-10, and (C) 49-50. Poly(CBOH) layer thickness is approximately 60 nm. Scale bar represents 0.01 absorbance units (a.u.) 51

2.16 CLSM images of the biofilm development by *Sphingomonas wittichii* RW1 on poly(CBOH) modified (top, A-B), poly(SPE) modified (middle, C-D) and pristine (bottom, E) Microdyn-Nadir PM UP150 PES membrane. Red, blue and green represent non-viable bacteria, EPS and viable bacteria. Figure 2.16A, 2.16C, and 2.16E represents biofilm on poly(CBOH) modified, poly(SPE) modified, and unmodified PES membrane respectively; while 2.16B and 2.16D indicates biofilm formation on the acid treated poly(CBOH) modified and poly(SPE) modified PES membrane, respectively. The deep orange color indicates overlapping zone of dead and live cells. Images are 635 μm × 635 μm and the scale bar represents 100 μm.....54

List of Figures (Continued)

Figure Page

3.1 Methodology of combining chemical coating and physical patterning on a membrane surface by deformation (i.e., embossing) of the membrane substrate. The chemical coating is a poly(ethylene glycol) diglycidyl ether aqueous solution 64

3.2 An AutoCAD drawing of the top (left) and bottom (right) of the acrylic membrane cross flow used to performance test the membranes. The cell dimensions are 7.62 cm (3.0 in) × 10.16 cm (4.0 in) × 2.54 cm (1.0 in) 67

3.3 Silicon stamp images produced by (A) AFM and (B) LEXT. The AFM image is 20 μm × 20 μm × 300 nm and gives an average groove depth of 231 ± 11 nm and a period of 625 nm. The LEXT image is an 84 μm × 87 μm image produced from stitching images together from the 100x objective with a 4x optical zoom. The scale bar in the LEXT image is 13.5 μm (y-direction) × 13 μm (x-direction) 71

3.4 A 5 μm × 5 μm × 400 nm AFM image of the silicon stamp 72

3.5 AFM images of the 3 types of membranes modified with varying concentrations of aqueous PEGDE solutions. Reaction with PEGDE only: 0 wt% (A, control), 5 wt% (B), 15 wt% (C); pressed with flat silicon wafer: 0 wt% (D), 5 wt% (E), 15 wt% (F); and patterned: 0 wt% (G), 5 wt% (H), 15 wt% (I). The common scale is 20 μm × 20 μm × 400 nm 74

3.6 A 5 μm × 5 μm × 300 nm AFM image of a 0 wt% patterned membrane 75

3.7 LEXT images of patterned membranes modified with varying concentrations of aqueous PEGDE solutions: 0 wt% (A), 5 wt% (B), 15 wt% (C). Common image scale is 65 μm × 65 μm. The images were produced from the 50x objective with a 4x optical zoom. The scale bar in each image is 10 μm (y-direction) × 10 μm (x-direction) 75

List of Figures (Continued)

Figure Page

3.8 A 65 μm × 65 μm image of an unmodified membrane surface produced by the LEXT from the 50x objective with a 4x optical zoom. The scale bar is 10 μm (y-direction) × 10 μm (x-direction)..... 76

3.9 ATR-FTIR spectra at a common scale for membranes modified by PEGDE only. Labels with percentages correspond to the varying concentrations of aqueous PEGDE reaction solutions used..... 77

3.10 Absorbance ratio of the 1072 cm^{-1} peak to the 1149 cm^{-1} peak from ATR-FTIR data for membranes modified by PEGDE only. The x-axis corresponds to the concentration of aqueous PEGDE reaction solutions used for chemical modification. The peak at 1072 cm^{-1} corresponds to the C-O stretching of the PEG ether group and the C-C aromatic stretching of the polyamide layer. The peak at 1149 cm^{-1} corresponds to the C-C aromatic stretching of the polyamide layer. The error bars represent one standard deviation from at least 3 different membrane samples..... 78

3.11 Water contact angle measurements of the reaction only membranes modified with 0 wt%, 5 wt%, and 15 wt% PEGDE solutions. The error bars represent one standard deviation among at least 9 data points..... 79

3.12 Solution flux [LMH] (A) and magnesium sulfate rejection [%] (B) versus weight percent of aqueous PEGDE solutions for the three types of membranes (reaction only, pressed with flat silicon wafers, and patterned). The feed was a 2000 ppm magnesium sulfate solution. The pressure applied to the feed side was 8.6 barg, the solution temperature was 22-23°C, the cross flow velocity was 3.0 ± 0.2 m/s, and the membrane area tested was 5.6 cm^2, with patterning on 62% of this area. The flow angle used between the solution flow and the membrane patterns was 0° (parallel). The error bars represent one standard deviation among 3 membrane samples..... 80

List of Figures (Continued)

Figure Page

3.13 Pure water flux data for GE HL membrane before and after patterning. The same exact membrane was used for these measurements. A 15 wt% glycerol solution was applied to the membrane in between the tests and before patterning occurred. 81

3.14 Sodium alginate fouling tests for membranes modified by PEGDE reaction only (A), membranes pressed with a flat silicon wafer (B), patterned membranes (C), and each membrane type with no chemical modification (D). A, B, and C includes data for membranes modified with the aqueous PEGDE solutions (0, 5, and 15 wt%). The feed solution comprised 30 mg/L sodium alginate, 10 mM NaCl, and 1 mM $CaCl_2$. The temperature was 22-23°C, the cross-flow velocity was 1.0 ± 0.1 m/s, and tested membrane area was 5.6 cm^2, with patterning on 68% of this area. The approximate initial starting flux was 120 LMH for all samples. The flow angle used between the solution flow and the membrane patterns was 90° (perpendicular). The error bars represent one standard deviation among 3 membrane samples 84

3.15 Average flux reduction for all membranes based on the integrated flux over a 2 h period 85

3.16 RMS height of the membrane surfaces. The results were obtained using the LEXT with the 50x objective at a 4x optical zoom. The membrane area studied per image was 0.004 mm^2. The error bars represent one standard deviation among at least 3 membrane samples 86

List of Figures (Continued)

Figure Page

3.17 Sodium alginate fouling tests for a patterned membrane modified with a 15 wt% aqueous PEGDE solution. The feed solution comprised 30 mg/L sodium alginate, 10 mM NaCl, and 1 mM $CaCl_2$. The temperature was 22-23°C, the cross-flow velocity was 1.0 ± 0.1 m/s, and tested membrane area was 5.6 cm^2. 68% of the membrane testable area was patterned. The approximate initial starting flux was 90 LMH. The flow angle used between the solution flow and the membrane patterns was 90° (perpendicular) 88

4.1 SEM images of the top surfaces of pristine (A) Dow BW30XFR, (B) Dow SW30HRLE, (C) Toray UTC-82V, (D) TriSep ACM4, (E) TriSep X201, (F) GE SG, (G) GE HL, (H) Dow NF270, (I) Synder NFG, (J) Nanostone NF4, (K) TriSep XN45, (L) GE DK, (M) GE Duracid KH. Images were taken at a 10k magnification and the common scale is 5 µm 103

4.2 SEM images of the cross-section of pristine (A) Dow BW30XFR, (B) Dow SW30HRLE, (C) Toray UTC-82V, (D) TriSep ACM4, (E) TriSep X201, (F) GE SG, (G) GE HL, (H) Dow NF270, (I) Synder NFG, (J) Nanostone NF4, (K) TriSep XN45, (L) GE DK, (M) GE Duracid KH. Images were taken at a 350 magnification and the common scale is 100 µm 104

4.3 AFM images of the top surfaces of pristine (A) Dow BW30XFR, (B) Dow SW30HRLE, (C) Toray UTC-82V, (D) TriSep ACM4, (E) TriSep X201, (F) GE SG, (G) GE HL, (H) Dow NF270, (I) Synder NFG, (J) Nanostone NF4, (K) TriSep XN45, (L) GE DK, (M) GE Duracid KH. The common scale is 20 µm × 20 µm × 1300 nm 105

4.4 SEM images of the top surfaces of patterned (A) Dow BW30XFR, (B) Dow SW30HRLE, (C) Toray UTC-82V, (D) TriSep ACM4, (E) TriSep X201, (F) GE SG, (G) GE HL, (H) Dow NF270, (I) Synder NFG, (J) Nanostone NF4, (K) TriSep XN45, (L) GE DK, (M) GE Duracid KH. Images were taken at a 10k magnification and the common scale bar is 5 µm 107

List of Figures (Continued)

Figure Page

4.5 SEM images of the cross-section of patterned (A) Dow BW30XFR, (B) Dow SW30HRLE, (C) Toray UTC-82V, (D) TriSep ACM4, (E) TriSep X201, (F) GE SG, (G) GE HL, (H) Dow NF270, (I) Synder NFG, (J) Nanostone NF4, (K) TriSep XN45, (L) GE DK, (M) GE Duracid KH. Images were taken at a 350 magnification and the common scale is 100 μm 108

4.6 AFM images of the top surfaces of patterned (A) Dow BW30XFR, (B) Dow SW30HRLE, (C) Toray UTC-82V, (D) TriSep ACM4, (E) TriSep X201, (F) GE SG, (G) GE HL, (H) Dow NF270, (I) Synder NFG, (J) Nanostone NF4, (K) TriSep XN45, (L) GE DK, (M) GE Duracid KH. The common scale is 20 μm × 20 μm × 600 nm 109

4.7 SEM images of the top surface of (A) pristine Dow BW30XFR, (B) patterned Dow BW30XFR, (C) pristine Dow NF270, and (D) patterned Dow NF270. Images were taken at a 150,000 magnification and the scale bar represents 300 nm 110

4.8 SEM images of the top surfaces of (A) pristine Nanostone PS20, (B) patterned Nanostone PS20, (C) pristine GE PW, and (D) patterned GE PW. Images were taken at a 10,000 magnification and the scale bar represents 5 μm 110

4.9 SEM images of the cross section of (A) pristine Nanostone PS20, (B) patterned Nanostone PS20, (C) pristine GE PW, and (D) patterned GE PW. Images were taken at a 400 magnification and the scale bar represents 100 μm 111

4.10 ATR-FTIR spectra of (A) *m*-phenylenediamine/trimesoyl chloride-based membranes and (B) piperazine/trimesoyl chloride-based membranes. Spectra are normalized to the peak at 1240 cm^{-1}. Note that the GE SG membrane selective layer is prepared from interfacial polymerization of *m*-phenylenediamine/piperazine/trimesoyl chloride, and the GE Duracid KH membrane selective layer is a polysulfonamide . 114

List of Figures (Continued)

Figure Page

4.11 ATR-FTIR spectra of a polysulfone (Nanostone PS20) and a polyethersulfone (GE PW) membrane. Spectra are normalized to the peak at 1240 cm^{-1} 116

4.12 ATR-FTIR spectra of the membrane support layers for (A) *m*-phenylenediamine/trimesoyl chloride based membranes and (B) piperazine/trimesoyl chloride based membranes. Note that the GE SG membrane selective layer is prepared from interfacial polymerization of *m*-phenylenediamine/piperazine/ trimesoyl chloride, and the GE Duracid KH membrane selective layer is a polysulfonamide. Spectra are normalized to the peak at 1240 cm^{-1} 116

4.13 RMS roughness of pristine, pressed, and patterned commercial polyamide membranes as determined by AFM. Error bars represent one standard deviation from at least 3 membrane pieces..... 118

4.14 (A) Dry and ethanol swollen thicknesses of polyamide layers measured by ellipsometry. (B) Number of monomer units between crosslinks of the polyamide layer as calculated by the Painter-Shenoy equation. Error bars represent one standard deviation from at least 3 membrane pieces..... 120

4.15 The number of ionized carboxylic acid groups per membrane volume at pHs 6.7 and 10.5 as determined by silver binding experiments. Error bars represent one standard deviation from at least 3 membrane pieces..... 121

4.16 (A) Permeance ($L/m^2/h/bar$) and (B) $MgSO_4$ rejection (%) of pristine, pressed, and patterned commercial polyamide membranes at 22-23°C. The feed was a 2000 ppm magnesium sulfate solution, the cross flow velocity was 3.0 ± 0.2 m/s, and the membrane area was 5.6 cm^2. Sixty-two percent of the membrane test area was pressed/patterned. The flow angle used between the solution flow and the membrane patterns was 0° (parallel). Error bars represent one standard deviation from at least 3 membrane pieces 122

List of Figures (Continued)

Figure Page

4.17 Membrane pattern peak heights (nm) for patterned commercial polyamide membranes as received and after replacing the original humectant with a 15 wt% glycerol solution. Error bars represent one standard deviation from at least 3 membrane pieces 124

4.18 Membrane pattern peak heights (nm) for Dow NF270 and Synder NFG membranes as received and after filling with a 15 wt% glycerol solution for 5 min and 24.5 h. Error bars represent one standard deviation from at least 50 measurements on at least 3 membrane pieces 125

4.19 Membrane pattern peak heights (nm) for the patterned Dow NF270, Dow BW30XFR, GE HL, Nanostone PS20, and GE Duracid KH membranes after replacing the original humectant with 0, 5, 15, 25, and 75 wt% glycerol solutions. Error bars represent one standard deviation from at least 3 membrane pieces 126

4.20 Young's Modulus (GPa) from AFM nano-indentation measurements of GE Duracid KH, GE DK, and TriSep X201 membranes as received, rinsed, and after filling with a 15 wt% glycerol solution. Error bars represent one standard deviation from at least 3 membrane pieces 128

4.21 Dry, water swollen, 15wt% (aq) glycerol swollen thicknesses of the isolated polyamide layer for the Dow NF270, Synder NFG, TriSep X201, and GE Duracid KH membranes measured by ellipsometry. Error bars represent one standard deviation from at least 3 membrane pieces 129

5.1 Switching pH characteristics of carboxybetaine polymers made from (A) γ-aminobutyric acid (yABa) and (B) 5-aminopentanoic acid (5AP) 136

CHAPTER ONE

INTRODUCTION

1.1 Introduction

Many people lack access to clean water, either for drinking or everyday use. Membranes are used commonly to purify water. In water treatment, there are 4 types of *pressure-driven* membrane processes: microfiltration, ultrafiltration, nanofiltration, and reverse osmosis [1, 2]. **Figure 1.1** shows the conventional classification of what each membrane process removes. Microfiltration (MF) membranes are the most open (have the largest pore size). MF operates through a sieving separation mechanism such that constituents of the process stream larger than the membrane pores are rejected. MF typically is used for solution clarifying, pretreatment processes, and bacteria removal [1, 3]. Ultrafiltration (UF) membranes have smaller pores than MF membranes, but they operate via the same sieving mechanism. UF also is used for pretreatment and to remove bacteria and virus particles [1]. Nanofiltration (NF) is the newest pressure-driven membrane process and operates using both a sieving effect and Donnan exclusion (charge effect) [1, 4]. NF typically is used to reject multivalent salts and to remove small organics that MF and UF cannot. Reverse osmosis (RO) is the most commonly used membrane process in the world for water desalination [3]. RO membranes are the tightest membrane (smallest pores) and operate through the solution-diffusion mechanism [1, 5].

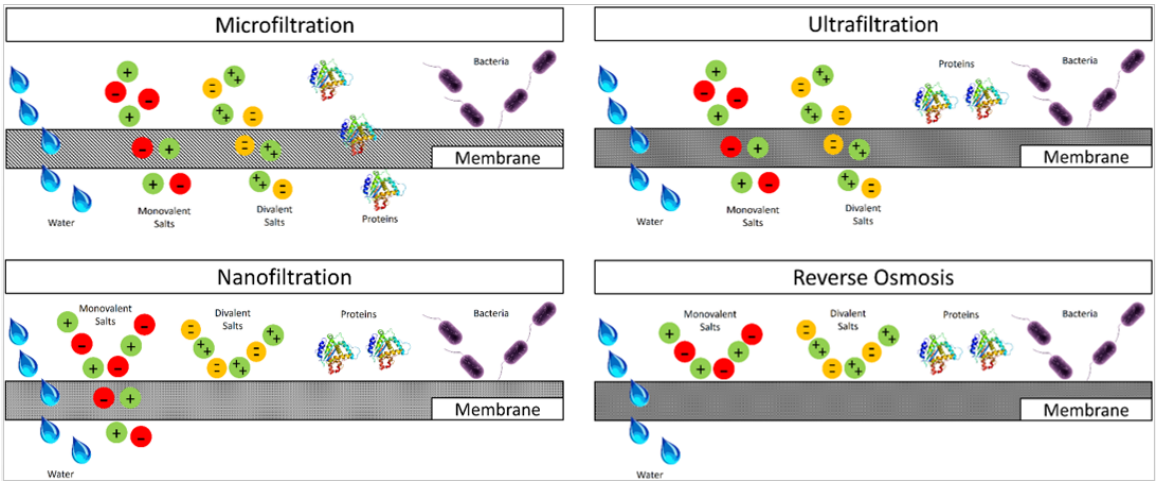

Figure 1.1 Conventional classification of pressure-driven water treatment membrane processes.

One drawback to these membrane processes is membrane fouling, which refers to the blocking of pores and the build-up of material on the membrane surface [6]. Membrane fouling can occur from a variety of foulant materials, such as: bacteria, biopolymers, natural organic matter, oils, proteins, particles, and salts. Membrane fouling causes a transient flux decline or pressure increase and a decrease in salt rejection [7].

One type of membrane fouling, known as biofouling, involves a multi-step process where bacteria, biopolymers, and proteins attach or adsorb onto the membrane surface or within the membrane pores. Biofouling is a major hindrance to membrane usage, because unlike other types of fouling, microorganisms can grow, multiply, and relocate on a membrane [7, 8]. The multi-step process of membrane biofouling involves the adsorption of biopolymers, such as glycoproteins and polysaccharides, to the membrane surface; attachment of microorganisms, such as bacteria and algae, to the biopolymer conditioning layer; and eventually growth of the microorganisms into a fully developed biofilm on the membrane surface [6].

Fouled membranes eventually require physical or chemical cleaning, which shortens the membrane life and greatly increases process operating costs [9]. As such, membrane (bio)fouling reduction/elimination has been a common topic in the literature, as summarized in excellent reviews [2, 10].

1.2 Anti-Fouling Strategies

One strategy to combat membrane fouling has been to coat the membrane with an anti-fouling chemistry [11-15], as depicted in **Figure 1.2** [16]. The purpose for these coatings is to increase the time between membrane cleanings and to increase the flux recovery after cleanings. Anti-fouling coatings make the membrane surface less favorable for foulant attachment by following the "Whitesides' rules": making the surface more hydrophilic (but not too hydrophilic), including hydrogen-bond acceptors, excluding hydrogen-bond donors, and having an overall neutral electrical charge [17, 18]. These coatings tend to be very effective by forming a strong hydration layer such that foulants have a hard coming into contact with the membrane surface [19]. Controlling hydrophilicity (e.g., targeting 35-45° water contact angle) is important to prevent high surface free energies that attract foulants.

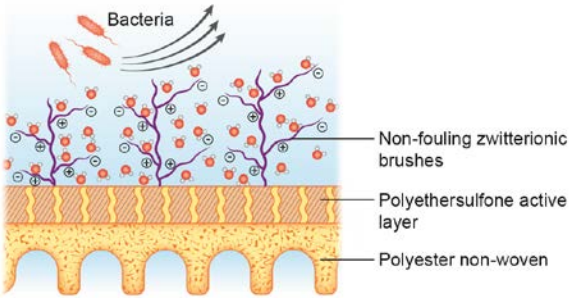

Figure 1.2. Anti-fouling coating depiction. *Reproduced with permission from Elsevier* [16].

Perhaps the most common anti-fouling chemistry is polyethylene glycol (PEG) based coatings [20]. There are numerous ways to coat membrane surfaces with PEG-based coatings. For example, PEG-based coatings can be grafted to or from a membrane by using UV-light [21] or controlled radical grafting strategies such as atom transfer radical polyermization (ATRP) [22-24]. Modified PEG can be coupled to unreacted carboxylic acid/acyl chloride groups on the membrane surface [25-28]. PEG can be applied by physical adsorption, including application by dip-coating [29, 30]. However, one common downside is that PEG tends to degrade under typical membrane cleaning conditions, such as treatment by hypochlorite solutions [31].

Bio-inspired chemistries represent another common class of anti-fouling coatings. Protein modification of membranes is a strategy that has been used [32]. Mussel-inspired polydopamine coatings [33-39] and chitosan-based coatings [40-42] have been used frequently to reduce fouling.

Zwitterionic chemistries are a more recent addition to the reportoire of coating strategies to reduce membrane fouling [19, 43, 44]. Zwitterions are overall charge neutral molecules that contain positively and negatively charged groups. There are three main types of zwitterions that have been used: (1) carboxybetaine, (2) sulfobetaine, and (3) phosphobetaine. Carboxybetaine zwitterions have carboxylic acid head groups (negatively charged group) and an inner quaternary amine (positively charged group) [45-48]. Sulfobetaine zwitterions have a sulfonate head group (negatively charged group) and an inner quaternary amine group [48-56]. Phosphobetaine zwitterions are most similar to the zwitterions in the body and have a quaternary amine head group and an

inner phosphate group [54, 55]. Sulfobetaine and phosphobetaine zwitterions also have been used to create self-assembled membranes [57-59].

1.3 Anti-Microbial Strategies

Another strategy to reduce biofouling is to kill or deactivate the bacteria upon contact with the membrane surface [60]. Methods include coating membranes with anti-microbial agents and embedding anti-microbial agents within the membrane structure. Quaternary amines are common anti-microbial coatings because they puncture the cell wall causing cell leakage and eventually cell death [61-65]. The length of the alky chain on the quaternary amine determines its effectiveness [66-68]. Alkyl chains with 6-8 carbons have been found to be the most effective [69, 70].

Composite membranes have been developed to reduce biofouling. In this approach an additive is used in the membrane fabrication process or attached to the membrane surface to impart anti-microbial properties. Silver nanoparticles have been incorporated into membrane surfaces to kill bacteria [71, 72]. Silver ions leach out from the nanoparticles and damage the cell membrane of the bacteria [73]. Gold nanoparticles are also capable of creating anti-microbial surfaces [74]. Carbon nanotubes have been attached to a membrane surface to make it anti-microbial by causing cell inactivation [75]. Graphene oxide also has been used to inactivate bacteria [76-78]. **Figure 1.3** shows the effect of using graphene oxide on a membrane to deactivate bacteria [76].

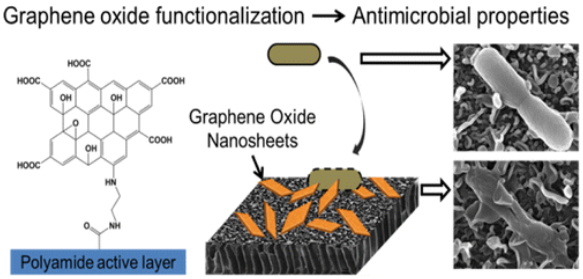

Figure 1.3. Bacteria inactivation using graphene oxide composite thin-film composite membranes. *Reproduced with permission from American Chemical Society* [76].

1.4 Combined Anti-Fouling and Anti-Microbial Strategies

Combining both anti-fouling functionality and anti-microbial functionality onto a single surface is another strategy to reduce membrane fouling. The anti-fouling mussel-inspired polydopamine coating has been used as a platform to also include anti-microbial functionality [79]. Combining two chemistries, one anti-fouling and one anti-microbial, is a common way to get achieve both functions on the same material surface [80-87]. Incorporating silver nanoparticles wthin an anti-fouling chemistry is another common approach to create a surface with the dual functionality [88-90].

A unique approach is to coat a surface with a chemistry that can switch reversibly from an anti-fouling mode to an anti-microbial mode. These coatings typically are zwitterionic in nature and expose the quaternary amine under certain conditions to impart the anti-microbial effect. Switchable zwitterion hydrogels have been studied [91, 92]. A zwitterionic coating capable of switching between anti-fouling mode and anti-microbial mode has been developed for multiple surfaces [16, 93, 94]. **Figure 1.4** shows an example of a surface that is able to resist bacteria attachment, switch to a new state and kill bacteria, and then switch back and release the dead bacteria [93].

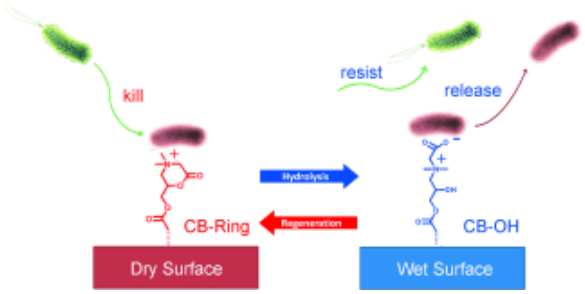

Figure 1.4. A surface capable of switching between anti-fouling zwitterion mode and anti-microbial quaternary amine mode. *Reproduced with permissions from John Wiley and Sons* [93].

1.5 Surface Patterning Strategies

A more recent strategy to reduce membrane fouling has been to change the surface structure of the membrane surface [95, 96]. There is a strong correlation between membrane (random) surface roughness and its propensity to foul [97, 98]. The rougher the membrane, the more likely it is to be fouled. Therefore, making smooth membrane surfaces has been a goal of many researchers [28, 99-101].

However imparting *ordered* roughness to a membrane surface may reduce its propensity to foul. By adding regular surface patterns, the fluid hydrodynamics right at and just above the membrane surface are altered [102]. **Figure 1.5** shows a depiction of patterns affecting the fluid flow at the membrane surface [102]. Depending on the flow angle used in a line and groove pattern, the anti-fouling properties of the membrane can change. A 0° flow angle (flow parallel to patterns) shows significant fouling, whereas a 45° or 90° flow angle (flow perpendicular to patterns) shows a significant reduction in fouling [103]. This reduction in fouling is caused by eddies that are formed at the membrane surface, inducing localized mixing such that foulant materials are less likely to

come in contact and adhere to the membrane. Patterns can range in size from nanometers to millimeters, with each showing promise towards fouling reduction. In fact, how bacteria attach onto a nanostructured surface has been studied [104]. They found post patterns could change the way that bacteria interact with the substrate surface, depending on the size and spacing of the posts [104]. The patterns can disrupt how the bacteria communicate, which increases the time for a biofilm to form [104].

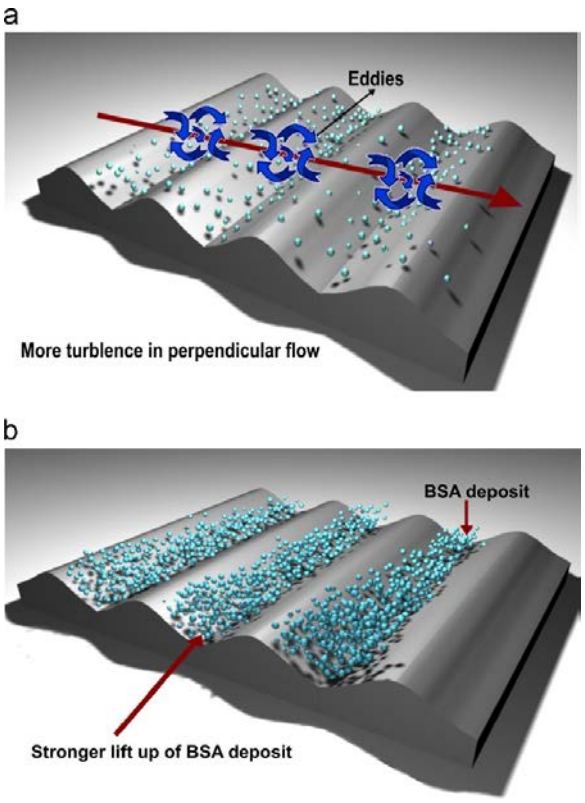

Figure 1.5. Depiction showing how patterns on a surface can alter the fluid flow and thus the membrane fouling propensity at both (a) 90° and (b) 0°. *Reproduced with permission from Elsevier* [102].

Nature has inspired many topographies to reduce fouling on surfaces [105, 106]. Sharklet™ is the most famous example, modeled after sharkskin [107-114]. These riblet type features were even used in swimsuits to reduce drag in the pool while swimming

[115-118]. Animals have inspired other surface features, such as those found on coral, butterfly wings, and hair [119-121]. Plants, such as lotus, clover, and rice leaves also have inspired other surface features to reduce fouling [120, 122, 123].

Strategies to impart regular patterns on membrane surfaces vary. Millimeter and micrometer sized line and groove patterns have been applied to a membrane via a patterned UV light procedure [124]. Millimeter sized squares were inkjet printed onto a reverse osmosis membrane [125]. Millimeter sized spacer imprints (diamond shapes) were imparted onto a polyvinylidene (PVDF) membrane surface to reduce fouling [126, 127]. Micrometer sized patterns have been studied most commonly in the membrane field and elsewhere. For example, micrometer sized pillars, wells, and crosses have been applied onto polydimethylsiloxane surfaces to reduce biological attachment [128-130]. Micrometer and nanometer sized patterns have been applied on membranes for fuel cell applications to increase power density [131-136]. Nanoimprint lithography (NIL) has been used to apply micrometer sized domes onto a membrane surface [137]. Micrometer sized prism and pyramid patterns have been applied to PVDF membranes through solution casting to mitigate fouling [138-143]. Solution casting also has been used to form patterns on polyethersulfone (PES) membranes [144-146]. Micrometer sized patterns have even been formed on hollow fibers on both the inner skin [147] and outer skin [148-151] to reduce fouling. Nanometer sized patterns have been used less frequently. Nanometer sized line and groove patterns have been imparted on membrane surfaces via NIL [28, 103, 152-154]. NIL also has been used to apply nanometer sized domes onto a membrane surface [137].

1.6 Evaluating Effectiveness of Membrane Surface Modifications

There are numerous ways to evaluate the effectiveness of anti-fouling and anti-microbial strategies. The most common way is to challenge membranes with a foulant solution and measure flux decline over time and compare results to a control membrane [28, 51]. The key with these studies is to ensure that the initial starting flux is the same for modified and control membranes, as modification oftentimes reduces membrane permeability. If the starting fluxes are unequal, then the amount of foulant material brought to the surface will be different, such that the rate of fouling will be different. There are many examples in the literature where claims are made about the effectiveness of a surface modification, in which the starting flux is lower for the modified membrane because a common pressure was used. If the starting fluxes are not the same, then the evaluation will be flawed [22]. Normalized or relative flux is another approach to view flux decline data. Instead of flux values, percentage flux drop is compared [25]. Here again, it is critical that the initial flux values are the same when comparing membranes. Another common approach is to look at transmembrane pressure (TMP) increase during constant-flux experiments [139, 155]. This approach is preferred since real world operation requires a constant flux. As foulants accumulate on the membrane surface, membrane permeability will decrease. Therefore, the TMP must be increased to maintain a constant flux. While evaluations done at one pressure (or one flux) are useful in an academic research lab for comparing different membrane modification strategies, they are not the most useful for translating findings to industrial settings.

Critical flux is perhaps the most commonly used concept to determine the effectiveness of a membrane coating that is readily translatable to industry [156]. The critical flux is defined as the point below which no fouling occurs and above which fouling occurs [152, 156-160]. Ideally, surface modification strategies would increase the critical flux. While useful in theory, critical flux is not strictly practical as there is no flux for which fouling is eliminated. Fouling will occur at all flux values, it is just a matter as to what extent.

Sustainable flux evaluates the economics of the membrane process. The sustainable flux is defined as the "net flux that can be maintained using mechanical and chemical enhancing means to meet an operation cost objective over the projected life of the membrane" [156]. The sustainable flux implies there is a balance between the fouling of the membrane and the operating and capital costs of the membrane process [156, 161-164]. Sustainable flux is a practical measure of the effectiveness of treatments, however it is difficult to evaluate in an academic research lab setting because operating and capital costs are difficult to determine.

Threshold flux is arguably the most practical measure of the effectiveness of treatments on fouling reductions for both academic and industrial purposes. The threshold flux is defined as the point below which a low and near constant rate of fouling occurs and above which the rate of fouling increases substantially [156]. **Figure 1.6** shows a common plot derived from constant-flux measurements and used to determine the threshold flux. Having a lower rate of fouling will give longer run times for the membranes between cleanings. The goal of threshold flux is to identify the highest flux

achievable (maximize productivity of the membrane) while keeping the fouling rates acceptably low to increase the time between cleanings [165-167].

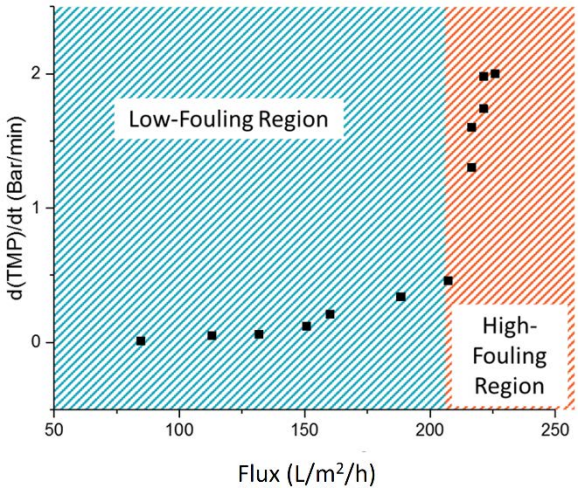

Figure 1.6. Plot used to determine threshold flux from constant-flux filtration measurements.

1.7 Dissertation Structure

The goal of my dissertation research was to devise new strategies to combat membrane fouling. Chapter 2 discusses a membrane surface chemistry capable of switching between anti-fouling and anti-microbial states depending on the solution pH. Chapter 3 discusses combining a PEG-based chemical coating with a nanometer sized line and groove pattern to create a superior anti-fouling membrane surface. Chapter 4 delves into the factors that influence membrane patterning by nanoimprint lithography to advance our understanding of how nanofiltration and reverse osmosis membranes pattern. Chapter 5 discusses the conclusions and recommendations for future work.

CHAPTER TWO

A SWITCHABLE ZWITTERIONIC MEMBRANE SURFACE CHEMISTRY FOR BIOFOULING CONTROL

[As published in the Journal of Membrane Science 548 (2018) 490-501 with minor revisions]

2.1 Introduction

Membrane biofouling is a process involving the adsorption of biopolymers, such as glycoproteins and polysaccharides, to the membrane surface; attachment of microorganisms, such as bacteria and algae, to the biopolymer conditioning layer; and eventually growth of the microorganisms into a fully developed biofilm on the membrane surface [6]. Biofouling is a major hindrance to membrane usage, because unlike other types of fouling, microorganisms can grow, multiply, and relocate on a membrane [7, 8]. Biofouling causes a transient flux decline in the case of constant-pressure filtration or a pressure increase in the case of constant flux filtration, either of which increases the process operational costs [168]. Chemical cleaning is required for fouled membranes, which leads to process downtime and shortens the membrane lifetime [9].

Biofouling prevention not surprisingly has been a trending topic in the literature. Modification of membrane surfaces has been the most common approach to reducing biofouling, and typically is done by chemical treatments or coatings [11-14]. Anti-fouling coatings make the membrane surface less favorable for biopolymer/bacteria attachment by following the “Whitesides’ rules”: making the surface more hydrophilic, including hydrogen-bond acceptors, excluding hydrogen-bond donors, and having an overall neutral electrical charge [17, 18]. Commonly studied anti-fouling coatings include

poly(ethylene glycol) (PEG) [21, 29] and zwitterions such as carboxybetaine [45, 46], sulfobetaine [52, 169], and phosphobetaine [54, 55], which are net charge neutral molecules that contain positive and negative charge groups. These coating types can form a strong hydration layer that decreases biofoulant adsorption or attachment [19, 29]. Recently, I showed that membrane biofouling resistance can be enhanced by combining chemical surface modification with physical surface modification using a nano-scale line and groove pattern [28], which I will discuss in more detail in Chapter 3.

Application of anti-microbial agents or biocides is another common strategy used to control membrane biofouling by killing bacteria that attach to the surface. Quaternary amine containing coatings are thought to disrupt the cell membrane, resulting in cell leakage and eventually cell death [61, 66]. Carbon nanotubes and graphene oxide have been shown to deactivate the bacteria upon contact with the membrane surface [75, 76]. Silver nanoparticles that severely damage the bacteria cell membrane also have been incorporated in membranes [71, 73].

There have been attempts to combine anti-fouling and anti-microbial approaches on one membrane [84]. One strategy has been to use an anti-fouling chemistry combined with silver nanoparticles [88-90]. A second strategy has been to add two chemistries to the membrane surface, one anti-fouling and the other anti-microbial [79, 83, 85-87, 170]. One such method is to pattern the two chemistries on the membrane in alternating rows of a stimuli-responsive polymer and a biocide, such that foulants will be brought in contact with the biocide, killed, and released by the stimuli responsive polymer [86].

This chapter of my dissertation contributes a method for applying one chemistry

to a membrane surface that is capable of switching between a unique anti-fouling, carboxybetaine zwitterion mode and an anti-microbial, quaternary amine mode [93, 94]. The novelty of this chemistry is that it can switch between the anti-fouling and the anti-microbial mode by changing the environment pH. Similar zwitterion chemistries with switching capabilities have been studied as hydrogels [91, 92]. This study is the first to apply a switchable zwitterion chemistry to control membrane biofouling, and the first to study its effectiveness under long-term exposure to water. Polyethersulfone ultrafiltration membranes were modified with this chemistry and other anti-fouling chemistries to provide direct comparisons of the resistance to bacteria attachment, cell viability, and biofilm growth on the membrane surfaces.

2.2 Materials and Methods

2.2.1 Materials

All chemicals were used as received, unless otherwise noted. The following chemicals were purchased from Sigma Aldrich: [2-(methacryloyloxy)ethyl]dimethyl-(3-sulfopropyl)ammonium hydroxide (SPE, 97%), 2,2'-bipyridyl (BPY, 99+%), 2-bromo-2-methylpropionic acid (BPA, 98%), Amberlite® IRA-400 chloride form, azobisisobutyronitrile (AIBN, 98%), benzophenone (BP, 99%), chloroform-d (99.8%), copper (I) bromide (99.999%), deuterium oxide (99.9%), glycidyl methacrylate (GMA, 97%), hydrogen peroxide (30% in water), iodomethane (99%), N,N-dimethylformamide (DMF, anhydrous, 99.8%), N,N'-methylenebis(acrylamide) (MBAA, 99%), poly(ethylene glycol) methacrylate (PEGMA, M_n = 360 g/mol), sarcosine *tert*-butyl ester hydrochloride (97%), sulfuric acid (95-98%), trifluoroacetic acid (TFA, 99+%),

trifluoroacetic acid-d (99.5%), and zinc tetrafluoroborate hydrate. The following chemicals were purchased from Acros Organics: chloroform (99%), dichloromethane (DCM, pure), diethyl ether (99.5%), and diiodomethane (99+%). Acetone (99.5+%), acetonitrile (anhydrous, 99.9%), ethanol (99.5% anhydrous), sodium bicarbonate (99+%), and tetrahydrofuran (THF, 99+%) were purchased from Fisher Scientific. Sodium hydroxide (97+%) was purchased from Alfa Aesar. Aqueous solutions were made with deionized water from a Milli-Q water purification system (Millipore-Sigma).

Prior to reaction, GMA was passed through a column of inhibitor remover (Sigma Aldrich) to remove monomethyl ether hydroquinone. Anhydrous DMF was opened and stored in a nitrogen atmosphere glovebox (MBraun USA). Poly(glycidyl methacrylate) (PGMA, MW = 290,000 g/mol, PDI = 1.7 (GPC)) [171] used for dip-coating silicon wafers was prepared by radical polymerization of GMA in methyl ethyl ketone at 60°C using AIBN as initiator. Amberlite® IRA-400 chloride form was converted to hydroxide form by reacting with a 1 M sodium hydroxide aqueous solution using a 1 meq resin:2 mmol sodium hydroxide stoichiometry for 35 min.

PES ultrafiltration membranes were kindly provided by Microdyn-Nadir GmbH (PM UP150, Microdyn-Nadir, 150 kDa MWCO) and GE Water & Process Technologies (GE Osmonics, unknown MWCO). The GE PES membrane was a gift from GE. Polished silicon wafers (1 cm × 3 cm) were purchased from Nova Electronic Materials.

2.2.2 Monomer Synthesis

The synthesis of the carboxybetaine zwitterion monomer (CBOH) is presented below in two parts: (1) synthesis of the protected monomer (CBtBu) and (2) deprotection

to yield the final product. **Figure 2.1** shows the process for the entire CBOH monomer synthesis. The steps are similar to those reported by Cao et al. [94], but with modifications.

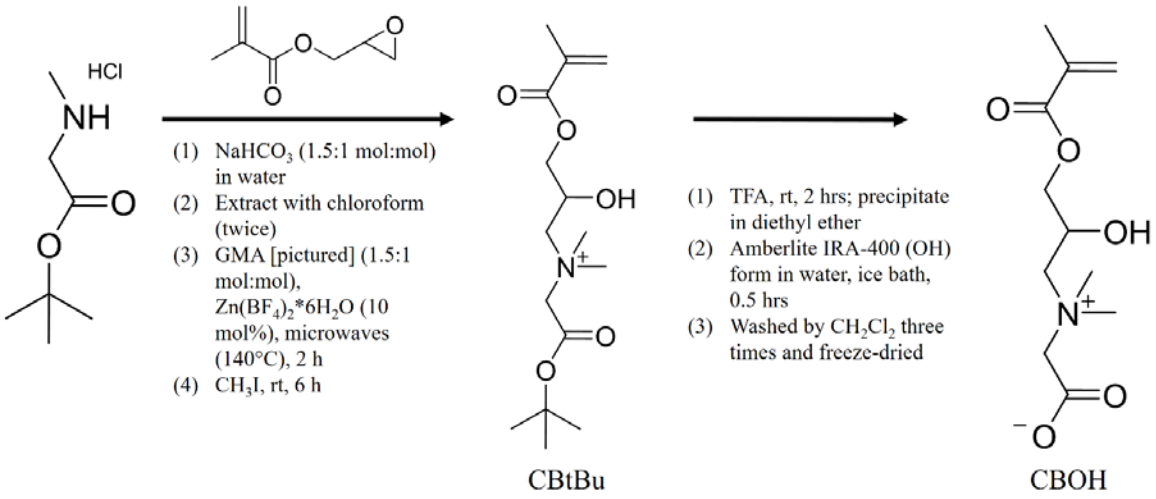

Figure 2.1. Monomer synthesis schematic. CBtBu is the protected monomer and CBOH is the zwitterion monomer used in experiments.

2.2.2.1 CBtBu Synthesis

Sarcosine *tert*-butyl ester hydrochloride was dissolved in water (6.5 mL water/g sarcosine *tert*-butyl ester hydrochloride) and neutralized with sodium bicarbonate (1.5 mol sodium bicarbonate:1 mol sarcosine *tert*-butyl ester hydrochloride) for 1 h under stirring. Sarcosine *tert*-butyl ester was extracted with chloroform (1:1 v/v, 2 times) and then reacted with dehibited GMA (1.5 mol GMA:1 mol sarcosine *tert*-butyl ester hydrochloride) in chloroform using zinc tetrafluoroborate hydrate (1 mol zinc tetrafluoroborate hydrate:10 mol sarcosine *tert*-butyl ester hydrochloride) as a catalyst. This reaction was done in a microwave reactor (MARS5, CEM) at 140 °C for 2 h. Undissolved catalyst and byproduct PGMA generated during the reaction were removed

by filtration (Whatman™ hardened low ash grade 50 filter paper, GE Healthcare Life Sciences). Iodomethane (20 mol iodomethane:1 mol sarcosine *tert*-butyl ester hydrochloride) was reacted with the monomer solution for 6 h under stirring to quaternize the nitrogen. The protected monomer (CBtBu) was precipitated in diethyl ether, filtered out (same filter paper as above), and dried under vacuum at 20-25 °C and -0.78 to -0.95 barg.

2.2.2.2 CBOH Synthesis

CBtBu was dissolved and reacted with TFA (2 mL TFA/g CBtBu) for 2 h under stirring. The reaction solution was precipitated in diethyl ether. The precipitate was dissolved in 100-150 mL water and reacted with Amberlite® IRA-400 hydroxide form (1 meq resin:1.01 mmol CBtBu) for 30 min in an ice bath under stirring. The resin was filtered out (same filter paper as above) and the undesired residual organics were extracted out with DCM (1:1 v/v, 3 times). The remaining aqueous solution was frozen and placed in a freeze-dryer (VirTis 6KBTEL-85) for 3-4 days to remove the water and precipitate CBOH.

2.2.3 Surface Modification

2.2.3.1 UV Polymerization

UV polymerization was performed to graft poly(CBOH), poly(PEGMA), and poly(SPE) from PES ultrafiltration membranes. **Figure 2.2** depicts the process for polymerizing poly(CBOH) from PES membranes. PES membranes were rinsed in deionized water to remove pore filler and pat dried. Photo-initiator, BP, was entrapped in PES membranes by immersing the PES membranes in a solution of 100 mM BP in

acetonitrile for 4 h with stirring. Acetonitrile was chosen because it swelled but did not dissolve the PES. The PES membranes were rinsed thoroughly with deionized water to collapse the swollen PES to entrap the BP and then pat dried. Next, UV polymerization was performed using a 365 nm UV light from an EL series UVLS-28 UV lamp (UVP, VWR International) (Husson lab) or a 315-600 nm range UV lamp (UVACUBE100 curing chamber equipped with Dr. Hönle lamp UV 150F and filter H1 (Hönle UV technology)) (Freger lab).

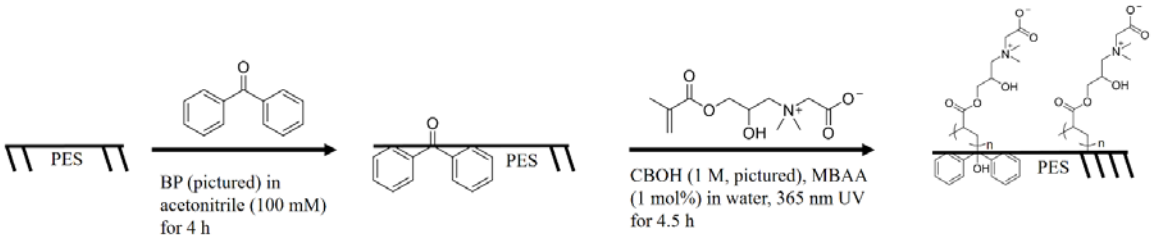

Figure 2.2. UV-photopolymerization schematic. BP is entrapped within PES to increase the reaction site density. CBOH is polymerized from both BP radicals and PES radicals.

Modification of Microdyn-Nadir PM UP150 PES membranes by poly(CBOH) and poly(SPE) was done in the Husson lab at Clemson University. The reaction solution comprised 1 M CBOH or SPE and 0.01 M MBAA in deionized water. A piece of BP-entrapped PES membrane was placed in a 50 mL glass beaker and 0.17 mL of reaction solution/cm^2 membrane area was placed on the membrane active side. A 30 mL glass beaker was placed on top of the membrane and the reaction solution such that no air bubbles were present between the membrane and the top glass beaker. To prepare larger membranes for flux experiments, membranes were placed in glass petri-dishes instead of beakers, with the membrane being placed in the top cover of petri-dish and the bottom part used to form the thin film of reaction solution. The membrane was exposed to 365

nm UV light with an intensity of at least 500 μW/cm^2 for 4.5 h (CBOH) or 25 min (SPE) from a source placed approximately 6.5 cm above the membrane. Modified membranes were rinsed thoroughly with deionized water, placed in deionized water in a shaker bath overnight (>15 h), and then pat dried. Samples for ATR-FTIR were vacuum dried at 20-25 °C and -0.78 to -0.95 barg. Samples for biofilm studies were immersed in a 15 wt% aqueous glycerol solution and dried in air for shipment to the Herzberg lab at Ben Gurion University.

Modification of GE Osmonics PES membranes was done in the Freger lab at Technion. The following protocol was used for poly(CBOH), poly(SPE), and poly(PEGMA) UV polymerizations. First, BP was entrapped in PES membrane samples as described earlier in this section. Then a piece of the membrane was placed in the cover of a glass Petri dish, 5 mL of a monomer/cross-linker solution in DI water (0.5M monomer, 0.005M MBAA) was put on top of the membrane, and the bottom part of the Petri dish turned upside down was placed on the membrane. This procedure produces a thin layer of the modification solution on top of the membrane between the two glass Petri dish components. The assembly was placed in the UV chamber (UVACUBE 100, Hönle UV technology) and UV-irradiated for 5 min (SPE and PEGMA monomers) or 10 min (CBOH monomer). The modified membranes were rinsed with DI water, washed with shaking in DI water overnight and stored in fresh DI water. A piece of each sample was dried at 30 °C for ATR-FTIR tests.

2.2.3.2 ATRP

Atom transfer radical polymerization (ATRP) was performed to graft

poly(CBOH) from silicon wafers substrates. **Figure 2.3** depicts the ATRP process for poly(CBOH). Silicon wafer substrate preparation was similar to that reported by Bhut et al. [172], with minor modifications. Substrates were cleaned in deionized water in test tubes by placing them in an ultrasonic bath for 20 min. The substrates were dried and placed in new test tubes for contact with a 1:3 (v/v) mixture of hydrogen peroxide and sulfuric acid at 80-90 °C for 1 h. [*Caution Piranha solution*: this mixture reacts violently with organic compounds. It should be used in small volumes with proper supervision and safety wear. Special precautions should be exercised in its disposal to avoid contact with organics.] Next, the substrates were rinsed thoroughly with de-ionized water and dried. PGMA was deposited onto the clean silicon wafer substrates from a 0.5 wt% PGMA solution in chloroform using a dip coater (QPI-128, Qualtech Products Industry Co. LTD) at an immersion and withdrawal rate of 60 mm/min. PGMA-coated silicon wafer substrates were annealed at 110 °C for 30 min under vacuum (-0.78 to -0.95 barg) to react some of the epoxy groups of PGMA to silanol groups on the silicon wafer substrate surface. BPA was reacted to the remaining epoxy groups of PGMA from the vapor phase at low pressure (-0.78 to -0.95 barg) and 100 °C for at least 18 h to form α-bromoester initiator groups on the silicon wafer substrate surface. After BPA reaction, the silicon wafer substrates were washed thoroughly with THF and deionized water and dried. Deionized water used for ATRP was de-oxygenated by three cycles of freeze–pump–thaw and transferred to the glove box.

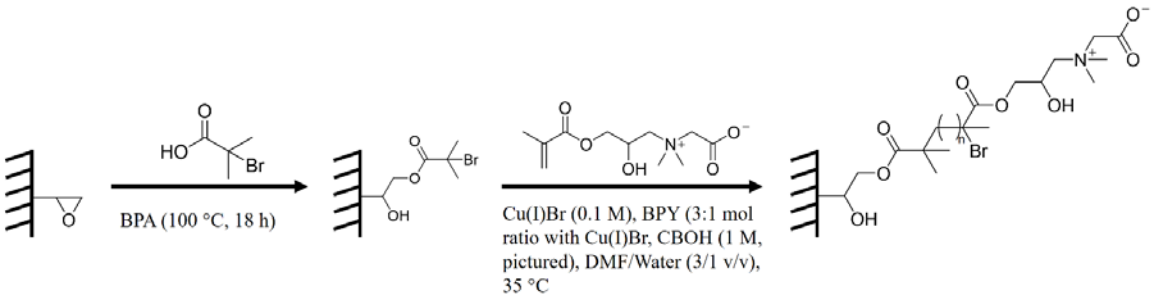

Figure 2.3. ATRP reaction schematic. BPA initiator is reacted with epoxide of PGMA and CBOH is polymerized from radical initiator by ATRP.

Poly(CBOH) was grown from initiator-functionalized silicon wafer substrates by surface-initiated ATRP similar to Cao et al. [94], but with minor modifications. Activator, copper (I) bromide (0.1 M), and amine ligand, BPY (0.3 M), were put in 3:1 (v/v) mixture of DMF and deionized water inside the glovebox. The mixture was sealed inside the glovebox and was placed in an ultrasonic bath for 2 h outside the glovebox to form the activator/ligand complex. CBOH monomer (0.1 M) was added to the solution inside the glovebox and was mixed until dissolved. Polymerization was carried out by placing an initiator-functionalized substrate into this reaction mixture. Polymerization was done at 35 °C for 3 h. Polymerization was terminated by removing the substrates from the reaction mixture and washing thoroughly with a 3:1 (v/v) DMF and deionized water mixture.

2.2.4 Characterization Techniques

2.2.4.1 NMR

^{1}H-NMR was performed with a 300 MHz NMR spectrometer (Bruker Avance) equipped with a 5 mm quadruple nucleus probe. The spectra were acquired from -4.1 to 16.5 ppm with a 30° pulse, an acquisition time of 2.65 s, and a total of 16 scans were

collected per sample. Samples were dissolved at a concentration of 50 mg/mL in chloroform-d (CBtBu), deuterium oxide (CBOH), or trifluoroacetic acid-d (CB-Ring) with tetramethylsilane as a reference peak. Integration and peak identification were performed with TopSpin 2.1 software (Bruker Corp.).

^{13}C-NMR was performed using the same 300 MHz NMR spectrometer. The spectra were acquired from -20 to 220 ppm and a total of at least 512 scans were collected per sample. Samples were dissolved at a concentration of 50 mg/mL in chloroform-d (CBtBu), deuterium oxide (CBOH), or trifluoroacetic acid-d (CB-Ring) with tetramethylsilane as a reference peak. Peak identification was performed with TopSpin 2.1 software (Bruker Corp.).

2.2.4.2 ATR-FTIR Spectroscopy

Attenuated total reflectance Fourier-transform infrared spectroscopy (ATR-FTIR) was used to characterize the surface chemistry of the unmodified and chemically modified PES membranes. Measurements at Clemson University were done using a Thermo Scientific Nicolet iS50R FT-IR with an ATR accessory (Specac Golden Gate) equipped with a diamond ATR crystal. Data were processed by OMNIC 9.3.32 software. Each spectrum was collected from 128 scans at a resolution of 4 cm^{-1} corrected with the ATR software, and manually baseline corrected. A background of the ATR crystal was taken before each set of samples was tested. Measurements at Technion were done using a Nicolet 8700 FT-IR spectrometer (Thermo Electron Corporation) with an ATR accessory (Smart MIRacle accessory, Pike). Each spectrum was collected from 64 scans at a resolution of 4 cm^{-1}, at least 5 different places were tested on each sample, and the

data were processed using OMNIC software.

2.2.4.3 FTIR Spectroscopy

Transmission Fourier-transform infrared spectroscopy (FTIR) was used to characterize the change in surface chemistry of the silicon wafers. Spectra were obtained using a Thermo Scientific Nicolet iS50R FT-IR. Data were processed by OMNIC 9.3.32 software (Thermo Scientific). Each spectrum was collected from 256 scans at a resolution of 4 cm^{-1}, and was manually baseline corrected. A background of an unmodified silicon wafer was taken before each set of samples was tested.

2.2.4.4 Ellipsometry

Multi-angle ellipsometry (Beaglehole Instruments, Picometer) was used to measure the dry thicknesses of PGMA, BPA, and poly(CBOH) layers on silicon wafers. The incident beam was produced by a 632.8 nm He–Ne laser source. Measurements were done at incidence angles from 56° to 80° with a step size of 4°. The reported thickness is the average of five random locations on each wafer. In this study, an air–poly(CBOH)–BPA–PGMA–silicon dioxide–silicon substrate multilayer model was applied to fit the data based on a Cauchy model. Layer thickness was allowed to vary and refractive index was fixed (air = 1.0, poly(CBOH) = 1.5, BPA = 1.451, PGMA = 1.525, silicon dioxide = 1.455, and silicon = 3.875). Layer thickness was calculated by IgorPro Software version 4.09A.

2.2.4.5 Static Contact Angle Goniometry

Water and diiodomethane contact angles were measured on silicon wafers to evaluate changes in hydrophilicity and surface free energy (SFE) associated with the

changes in surface chemistry. Water contact angle was performed on unmodified and modified GE PES membranes and unmodified and modified Microdyn-Nadir PM UP150 PES membranes. GE PES membranes water contact angle was measured using a Krüss DSA100 (Freger Lab). All other static contact angles were measured using a Krüss DSA 10-Mk2 contact angle goniometer. A liquid drop (~ 3.0 μL) was placed carefully on the sample surface. The sessile drop model was used in DSA version 1.80.0.2 Drop Shape Analysis software to determine contact angle. For consistency, measurements were taken 60 s after each droplet was placed on the surface. Measurements were done at a minimum of three locations on each sample to get an average contact angle value with standard deviation. SFE of the silicon wafers was calculated using the Owens-Wendt method [173, 174]. **Equation 2.1** was used to calculate the surface free energy (SFE) of silicon wafers:

$$\gamma_s = \gamma_s^d + \gamma_s^p \tag{2.1}$$

γ_s is the SFE of the silicon wafer, γ_s^d is the dispersion component of the SFE of the silicon wafer, and γ_s^p is the polar component of the SFE of the silicon wafer. Two liquids with different surface free energy components were used to determine the dispersion and polar components of the SFE. Using the SFE values (total, polar, and dispersion) for each fluid and the respective contact angles of each fluid on the silicon wafers, **Equations 2.2 and 2.3** were used to calculate the dispersion and polar components of the silicon wafer SFE [174].

$$\sqrt{\gamma_s^d} = \frac{\gamma_d(\cos\theta_d + 1) - \gamma_w(\cos\theta_w + 1)\sqrt{(\gamma_d^p/\gamma_w^p)}}{2\left(\sqrt{\gamma_d^d} - \sqrt{\gamma_d^p(\gamma_w^d/\gamma_w^p)}\right)} \tag{2.2}$$

$$\sqrt{\gamma_s^p} = \frac{\gamma_w(\cos\theta_w + 1) - 2\sqrt{\gamma_s^d \gamma_w^d}}{2\sqrt{\gamma_w^p}} \quad (2.3)$$

γ_d is the SFE of diiodomethane (50.8 mJ/m^2) [175], γ_d^d is the dispersive component of the diiodomethane SFE (49.5 mJ/m^2) [175], γ_d^p is the polar component of the diiodomethane SFE (1.3 mJ/m^2) [175], γ_w is the SFE of water (72.8 mJ/m^2) [175], γ_w^d is the dispersive component of the water SFE (21.8 mJ/m^2) [175], γ_w^p is the polar component of the water SFE (51 mJ/m^2) [175], θ_d is the diiodomethane contact angle, and θ_w is the water contact angle.

2.2.4.6 Scanning Electron Microscopy

Membrane surface morphology before and after modification was studied using a Hitachi S-4800 Scanning Electron Microscopy (SEM). Representative samples of the membranes were careful dried using hexamethyldisilazane (HMDS, Electron Microscopy Sciences) to prevent pore collapse [176]. The method involved soaking samples consecutively in ethanol-water solutions containing 25, 50, and 75% by volume for 5 min each. The samples were then soaked in 100% ethanol. Next the samples were soaked in a 50% ethanol/50% HMDS (v/v) solution and subsequently a 100% HMDS solution for 15 min each. Finally, the samples were then allowed to air dry. Membranes pieces were attached with carbon tape to aluminum stabs, and coated with gold-palladium prior to SEM measurements. The SEM measurements were performed at an accelerating voltage of 10 kV, a current voltage of 20 μA, and a magnification of 30,000x.

2.2.5 Substrate Performance Testing

2.2.5.1 Water Permeance Testing of Membranes

Water permeance was measured for the unmodified and surface modified PES membranes. Unmodified, BP entrapped, poly(CBOH) modified, poly(SPE) modified, and poly(PEGMA) modified GE PES membranes were tested at Technion in 165 mL cylindrical stainless steel direct-flow cell with an active membrane area of 11.3 cm^2 (diameter 38 mm) [177]. The cell was stirred magnetically and pressurized with nitrogen. The flux was determined at feed pressure of 3 bar by collecting and weighing the permeate.

Unmodified, BP entrapped, poly(CBOH), and poly(SPE) modified Microdyn-Nadir PES membranes were tested in direct-flow mode using a stainless steel Sterlitech HP4750 stirred cell with an active membrane area of 14.6 cm^2 at Clemson University. The cell was filled with approximately 280 mL of deionized water and pressurized to the desired pressure (up to 1.9 barg) with air (UN1002, Airgas). Each membrane was conditioned before making the flux measurement by passing at least 150 mL of water or running for 30 min, whichever came first. At least 8 g of permeate was collected while recording the time to measure permeance. At least 4 membranes were tested for each membrane type for statistical relevance.

2.2.5.2 Bacteria Deposition Studies on Membranes

Pseudomonas fluorescens bacteria tagged with green fluorescent protein (GFP) were pre-cultured by incubating at 30 °C in Luria-Bertani (LB) broth (Sigma-Aldrich) in the presence of 25 μg/mL Kanamycin (Sigma-Aldrich) for 24 h. Then a 0.5 mL aliquot was transferred to fresh LB broth solution that also contained 25 μg/mL Kanamycin, and cultured for another 5 h. The cultured bacteria in the stationary stage of growth were

centrifuged out, washed by suspending/centrifuging in 0.01 M NaCl (Sigma-Aldrich) solution three times, and finally suspended in a fresh 0.01 M NaCl solution and diluted to an optical density of 0.1 (bulk concentration $C_b = 2.99 \times 10^7 \pm 6 \times 10^6$ bacteria/cm^3). The experiments were carried out in a parallel plate flow cell setup (FC 81 flow cell, BioSurface Technologies) at room temperature. A glass slide with a 2.5 cm long piece of membrane glued on it was mounted inside the cell, forming the bottom of the channel. The bacterial suspension was fed to the cell at a flow rate of 2.0 mL/min, which corresponds to cross-flow velocity of 7.7 cm/min and shear rate of 230 min^{-1}. The bacteria deposited on the membrane surface were imaged and counted using a fluorescence microscope (Nikon LV100) equipped with a 20x objective lens and a digital camera. The imaged area was 0.148 mm^2 and was located in the middle of the cell. Images were taken every 5 min for 30-40 min. The mass transfer (deposition) coefficient k_d was calculated by **Equation 2.4** assuming first-order deposition kinetics [169]:

$$k_d = \frac{1}{C_b A}\frac{dN}{dt} \tag{2.4}$$

N is the number of bacteria in the image, A is the imaged area, and C_b is the bacteria concentration in the feed solution. The reported k_d values are averages of at least 3 tests performed for each sample type, each time using a fresh bacteria suspension.

2.2.5.3 Switching Between CBOH and CB-Ring

CBOH (monomer or polymer) has the ability to switch from the anti-fouling, zwitterion mode to the anti-microbial, quaternary amine mode (coined CB-Ring). **Figure 2.4** depicts the switching and Cao et al. [93] proposed the mechanism of reversible switching between CBOH and CB-Ring.

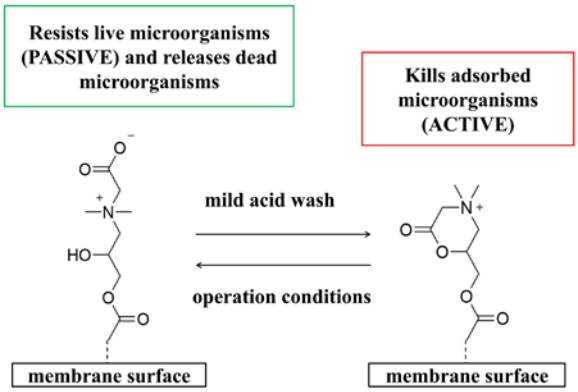

Figure 2.4. Switching schematic between the anti-fouling, zwitterion chemistry (CBOH, left) and the anti-microbial, quaternary amine chemistry (CB-Ring, right). CBOH would switch to CB-Ring when exposed to a typical cleaning solution for membranes, and CB-Ring would switch to CBOH when exposed back to normal operating conditions.

NMR was used to test switching of CBOH monomer to CB-Ring. CBOH monomer was dissolved in trifluoroacetic acid-d (50 mg/mL) and ^{1}H NMR and ^{13}C NMR spectra were collected after 4 h.

FTIR was used to study the switching of poly(CBOH) to poly(CB-Ring) and vice versa on silicon wafers. To switch from poly(CBOH) to poly(CB-Ring), the poly(CBOH) modified silicon wafers were placed in pure TFA for 1 h. To switch from poly(CB-Ring) to poly(CBOH), the poly(CB-Ring) modified silicon wafers were placed in deionized water for 1 h. To test the longevity of switching, a poly(CBOH) modified silicon wafer was placed in pure TFA for at least 0.33 h to switch to poly(CB-Ring), then the poly(CB-Ring) modified silicon wafer was placed in deionized water for at least 0.33 h to switch back to poly(CB-OH). This cyclical process was repeated 50 times, with FTIR spectra taken after 1, 10, and 50 cycles.

To test the pH at which the switching occurs, poly(CBOH) modified silicon

wafers were immersed in TFA/water solutions with pH values of 0.6, 1.0, and 1.5 for 1 h with pH measured using an accumet Basic AB15 pH meter (Fisher Scientific) equipped with an accumet 13-620-285 pH probe (Fisher Scientific). To test the time needed for complete switching to occur from poly(CBOH) to poly(CB-Ring), the poly(CBOH) modified silicon wafers were placed in a TFA/water solution at pH 1.0 for 0-30 min. To test the time needed for complete switching to occur from poly(CB-Ring) to poly(CBOH), poly(CBOH) modified silicon wafers were placed in a pure TFA solution for 1 h to ensure complete conversion to poly(CB-Ring). Next they were placed in deionized water for 0-30 min.

2.2.5.4 Biofilm Studies on Membranes

Biofilm studies on PES membranes were conducted with *Sphingomonas wittichii* RW1 (GenBank #NC 00951), which was obtained from the DSMZ (Deutsche Sammlung von Mikroorganismen and Zellkulturen GmbH) culture collection, Germany. The bacterium was grown on nutrient agar medium containing peptone (5 g/L) and meat extract (3 g/L) adjusted to pH 7 and supplemented with 150 μg/mL streptomycin (Sigma Aldrich, S6501). A single colony was inoculated overnight in 5 mL of the nutrient medium in a shaker–incubator at 150 rpm at 30 °C (ZHWY-1102C, ZHWY). Thereafter, the *S. wittichii* RW1 cells were diluted in the nutrient medium (1:100) and incubated for 24 h to achieve early stationary growth phase. Bacteria were harvested by centrifugation (4K15, Sigma) (4000g and 4 °C for 10 min) and the pellet was washed three times in fresh nutrient broth. After the washing steps, the optical density (OD_{600}) of the suspension was adjusted to 0.5 in wastewater effluents taken from MBR UF permeate,

treating municipal wastewater of Sede Boqer Ben Gurion University campus [178, 179] and supplemented with 12.5 mg/L peptone and 7.5 mg/L meat extract. Twenty-five milliliters of the bacterial suspension were injected into the biofilm growth chamber, which was previously loaded with 5 mm × 5 mm membranes fixed on glass cover slips, at flow rate of 2 mL/min, as previously reported by Bernstein et al. [56]. *S.wittichii* RW1 biofilm was grown on the membranes for 4 d before sampling of the membrane coupons. Note that the conditions used for biofilm growth were very aggressive to keep the time period for experiments to a reasonable length. The membrane pieces with biofilm were carefully removed and stained with concanavalinA (ConA) conjugated to Alexa Fluor 633 (Invitrogen, Israel), SYTO 9, and propidium iodide (PI) for probing EPS, live cells, and dead cells with a confocal laser scanning microscope (CLSM). Probing EPS, live cells, and dead cells of the biofilms was carried out before and after rinsing poly(CBOH) modified and poly(SPE) modified Microdyn-Nadir PES membranes with 0.1 M HCl (pH 1) for 20 min.

Microscopic observation and image acquisition were performed using Zeiss-Meta510, a CLSM equipped with Zeiss dry objective LCI Plan-Neofluar (20x magnification and numerical aperture of 0.5). The CLSM was equipped with detectors and filter sets for monitoring Alexa Fluor 633 bonded to ConA, SYTO 9, and PI stained cells (excitation wavelengths of 633, 568 and 488 nm, respectively). CLSM images were generated using the Zeiss LSM Image Browser. Images were analyzed, and the specific biovolume per membrane area ($\mu m^3/\mu m^2$), average thickness (μm) and roughness coefficient [180] of the biofilm layer were determined by COMSTAT [181], an image

processing software written as a script in MatLab 6.5 (The Math Works, Inc., Natick, MA) and equipped with an image-processing tool box. For every sample, five to six positions on the membrane were chosen and microscopically observed, acquired, and analyzed. Three-dimensional reconstruction of the CLSM image stacks was carried out using Imaris software (Imaris Bitplane, Zurich, Switzerland).

2.3 Results and Discussion

2.3.1 CBOH Monomer Synthesis

Protected monomer, CBtBu, was synthesized successfully. **Figure 2.5** depicts typical ^{1}H-NMR and ^{13}C-NMR spectra of CBtBu. Yield was approximately 85 mol% with approximately 85% purity as determined by NMR. Cao et al. [94] provided an interpretation for each NMR spectrum, however an interpretation is provided based on the results obtained from the experiments described. The following is the interpretation of the ^{1}H-NMR spectrum in **Figure 2.5A**, with lowercase letters assigned to identify each proton type as assigned in the image: 1.49 (a), 1.94 (i), 3.55-3.66 (c), 3.74-4.07 (d), 4.22-4.24 (b), 4.48-4.70 (f), 4.74-4.78 (e), 5.62-5.63 (h), 6.18 (g), 7.28 (residual chloroform). The following is the interpretation of the ^{13}C-NMR spectrum in **Figure 2.5B**, with lowercase letters assigned to identify each carbon type as assigned in the image: 18.30 (l), 27.94 (a), 53.8-54.5 (e), 62.57 (d), 63.51 (g), 65.19 (f), 65.81 (h),76.5-77.5 (residual chloroform), 85.41 (b), 126.90 (j), 135.37 (k), 163.34 (i), 166.99 (c).

Figure 2.5. (A) 1H-NMR spectrum and (B) 13C-NMR spectrum of protected monomer CBtBu. CBtBu was dissolved in chloroform-d at a concentration of 50 mg/mL. Lowercase letters were assigned to each proton and carbon type as specified in each spectrum.

The protected monomer, CBtBu, was deprotected successfully to become CBOH. **Figure 2.6** depicts typical ^{1}H-NMR and ^{13}C-NMR spectra of CBOH. Yield was approximately 80 mol% with approximately 85% purity as determined by NMR. Cao et al. [94] provided an interpretation for each NMR spectrum, however an interpretation is provided based on the results obtained from the experiments described. The following is the interpretation of the ^{1}H-NMR spectrum in **Figure 2.6A**, with lowercase letters assigned to identify each proton type as assigned in the image: 1.88-1.89 (h), 3.26-3.41 (b), 3.64-3.94 (c), 4.11-4.24 (a), 4.23-4.33 (e), 4.39-4.59 (d), 4.79 (residual water), 5.70-5.72 (g), 6.11-6.13 (f). The following is the interpretation of the ^{13}C-NMR spectrum in **Figure 2.6B**, with lowercase letters assigned to identify each carbon type as assigned in the image: 17.30 (j), 53.1-53.7 (c), 62.11 (e), 63.83 (d), 65.30 (f), 66.33 (b), 127.43 (h), 135.34 (i), 167.12 (g), 168.97 (a). The peaks for the tert-butyl protecting group are gone, indicating that the monomer was deprotected successfully.

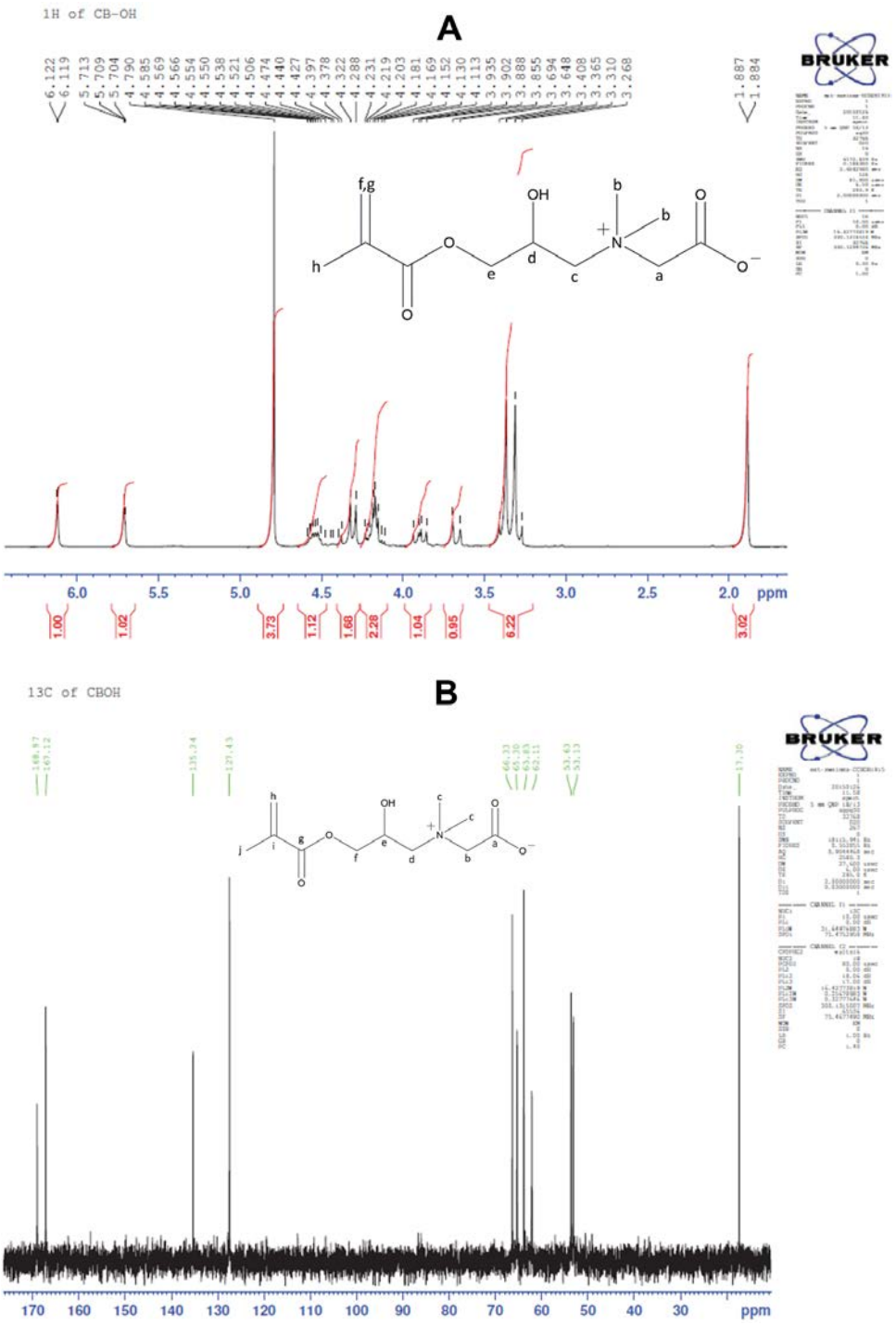

Figure 2.6. (A) 1H-NMR spectrum and (B) 13C-NMR spectrum of monomer CBOH. CBOH was dissolved in deuterium oxide at a concentration of 50 mg/mL. Lowercase letters were assigned to each proton and carbon type as specified in each spectrum.

2.3.2 PES Membrane Surface Modification

Polyethersulfone membranes were surface modified using UV-graft polymerization. Even though PES is UV active by itself [182], initial work found that the polymerization rate of CBOH from unmodified PES membranes was slow. Therefore, benzophenone (BP) photo-initiator was entrapped in the PES membranes to increase the polymerization rate and chain density by increasing the number of reaction sites on the PES membranes [183]. **Figure 2.7** shows the ATR-FTIR spectra of GE (A) and Microdyn-Nadir PM UP150 (B) PES membranes surface modified with various chemistries. The two unmodified membranes have different ATR-FTIR spectra due to the Microdyn-Nadir PM UP150 membrane being considered a hydrophilic PES membrane (see **Figure 2.8**). Most likely there is a coating or an additive on the Microdyn-Nadir PES membrane. PES membranes showed successful BP entrapping by the presence of its characteristic carbonyl stretching peak centered at about 1655 cm^{-1} (as indicated by the arrows on the right side in **Figure 2.7**). There is a slight evolution of a peak at about 1720 cm^{-1} in the polymer modified membrane spectrum (as indicated by arrows on the left side in **Figure 2.7**), which would correspond to carbonyl stretching of the grafted polymer layer. The small carbonyl stretching peak at about 1720 cm^{-1} indicates a very thin grafting layer of each polymer.

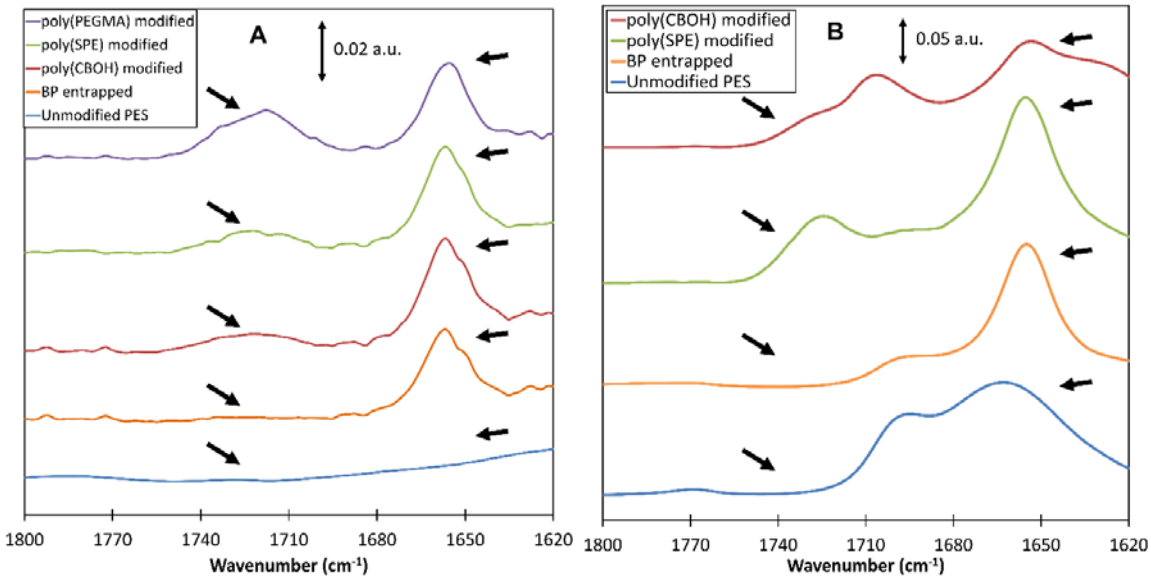

Figure 2.7. ATR-FTIR spectra of (A) GE Osmonics PES membranes unmodified, BP entrapped, and modified by poly(CBOH), poly(SPE), and poly(PEGMA) and (B) Microdyn-Nadir PM UP150 PES membranes unmodified, BP entrapped, and modified by poly(SPE) and poly(CBOH). Scale bar represents (A) 0.02 absorbance units (a.u.) and (B) 0.05 absorbance units (a.u.).

Figure 2.8A shows the water contact angle data for the GE PES membranes. The unmodified GE PES membranes had an average contact angle of 70°. The BP entrapped GE PES membranes showed a slight increase in water contact angle, while the polymer modified GE PES membranes showed a slight decrease in water contact angle. Statistically, using a t-test to compare the unmodified GE PES to the modified GE PES membranes, the BP entrapped and the poly(PEGMA) modified membranes are considered different from the unmodified membrane. **Figure 2.8B** shows the water contact angle data for the Microdyn-Nadir PES membranes. Microdyn-Nadir PM UP150 PES membranes are more hydrophilic than most common PES membranes with an average water contact angle of 51° [184-186]. Interestingly, unlike the GE PES

membranes, the BP entrapped Microdyn-Nadir PES membranes had a significantly reduced water contact angle of 22°. The poly(CBOH) modified PES membranes had a water contact angle of 39°, which is similar to that of the poly(CBOH) modified silicon wafers. All three Microdyn-Nadir PES membrane data points are statistically different from each other, therefore indicating the membrane surface was further hydrophilized upon surface modification.

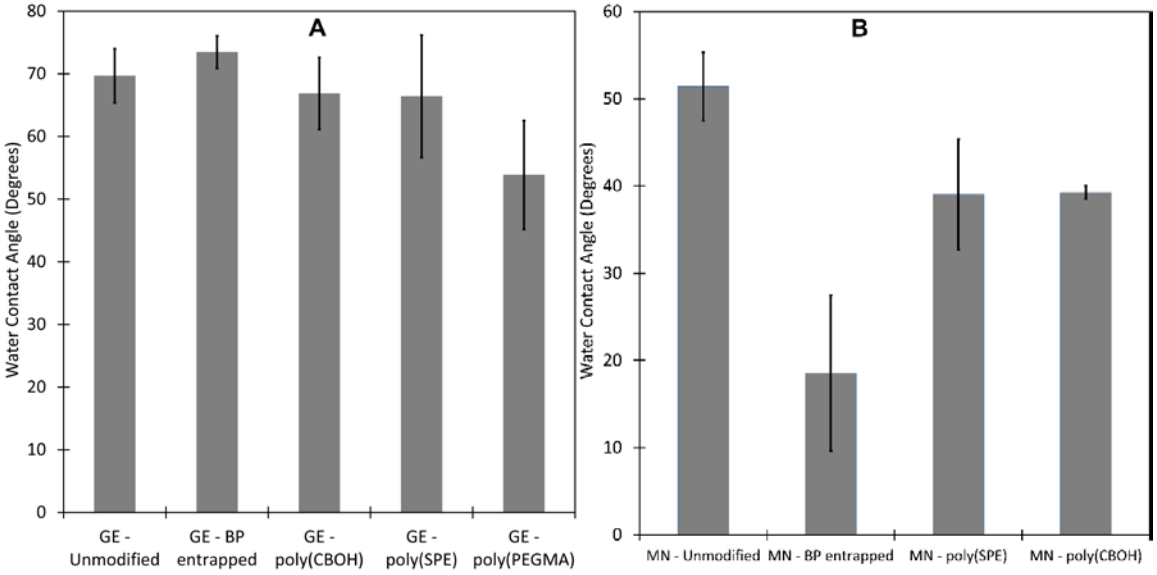

Figure 2.8. Water contact angle of (A) unmodified and modified GE PES membranes and (B) unmodified and modified Microdyn-Nadir PM UP150 (MN) PES membranes. Error bars represent one standard deviation among at least three samples.

Figure 2.9 shows representative SEM images of the unmodified and surface modified Microdyn-Nadir PES membranes. The BP entrapped membranes in **Figure 2.9B** shows a slightly different surface pore structure than the unmodified membranes in **Figure 2.9A**, most likely due to possible pore collapse from swelling in acetonitrile and subsequent collapse in water [187]. Poly(SPE) modified membranes showed a significant reduction in pore size as evidenced by the small pores seen in **Figure 2.9C**. Poly(CBOH)

modified membranes also showed a slight decrease in pore size in **Figure 2.9D**, however the pore size reduction is not as great as it was for the poly(SPE) modified membranes.

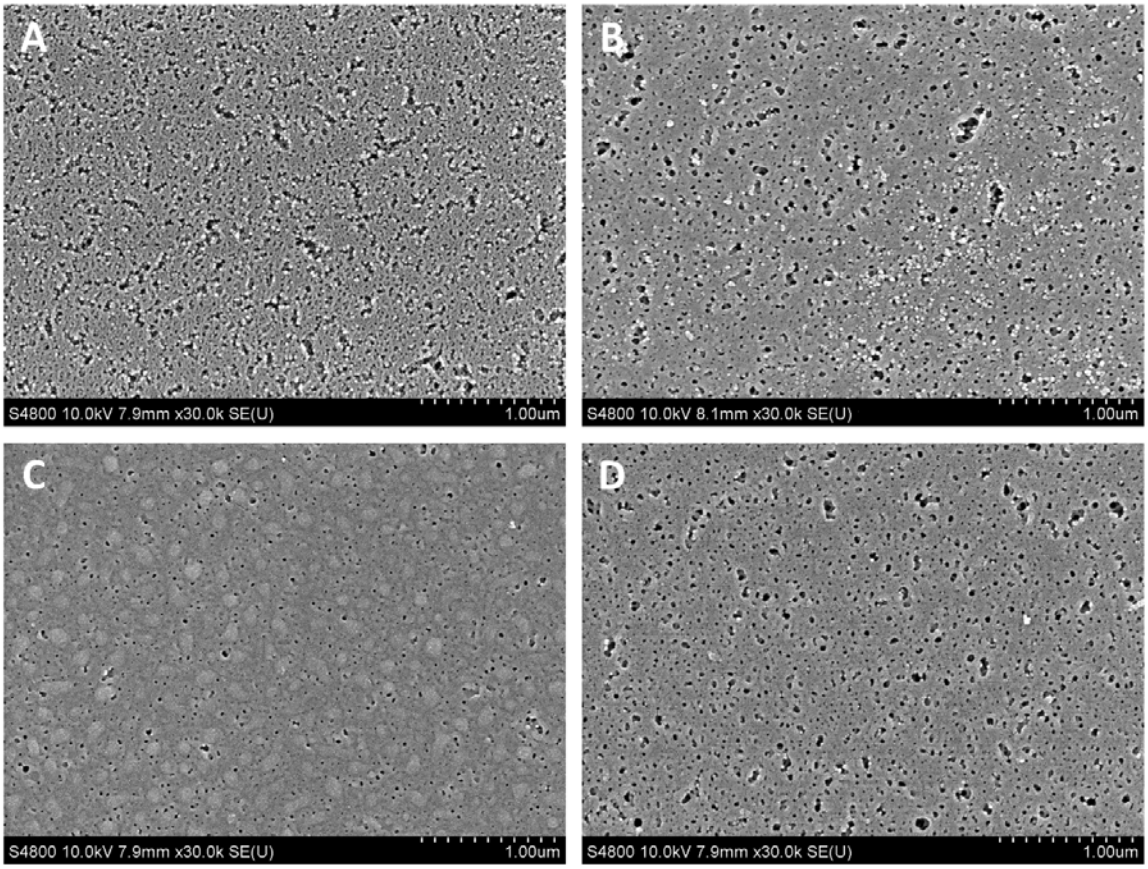

Figure 2.9. SEM images of unmodified (A), BP entrapped (B), poly(SPE) modified (C), and poly(CBOH) modified (D) Microdyn-Nadir PM UP150 PES membranes. Images were taken at 30k resolution and the scale bar represents 1 µm.

2.3.3 Water Permeance of Membranes

Water permeance of the modified PES membranes was measured to ensure the membrane was not plugged during surface modification. **Figure 2.10** shows the water permeability coefficient versus the modified PES membrane type. **Figure 2.10A** shows the results for the GE PES membranes. The unmodified GE PES had an average water permeance of 123 L/m^2/h/bar. The modified membranes had a statistically significant

lower water permeance than the unmodified GE PES. The BP entrapped GE PES had an average water permeance of 65 L/m^2/h/bar. This permeance reduction could be attributed to possible pore collapse due to the PES swelling in acetonitrile and subsequent collapse in water [187]. Poly(CBOH) modified, poly(SPE) modified, and poly(PEGMA) modified GE PES had average water permeances of 53, 31, and 26 L/m^2/h/bar respectively. The further decrease in water permeance could be from increased resistance due to the grafted polymer layer on the surfaces and pore size reduction (as described in **Section 2.3.2**).

Figure 2.10B shows the water permeance results for the Microdyn-Nadir PES membranes. The unmodified PES had an average water permeance of 915 L/m^2/h/bar, which is similar to what has been reported in the literature [48, 185]. The BP entrapped PES had an average water permeance of 503 L/m^2/h/bar, the poly(SPE) modified PES had an average water permeance of 22 L/m^2/h/bar, and the poly(CBOH) modified PES had an average water permeance of 770 L/m^2/h/bar. The error bars seem to indicate that the BP entrapped PES has a lower water permeance than the unmodified PES; however, a multiple mean hypothesis test shows that only the poly(SPE) modified Microdyn-Nadir PES was statistically different from the three other membrane types at 95% confidence. (All statistical analysis details are given in the **Appendix A**.) The decrease in water permeance in the poly(SPE) modified PES could be from increased resistance due to the grafted polymer layer on the surfaces and pore size reduction (as described in **Section 2.3.2**).

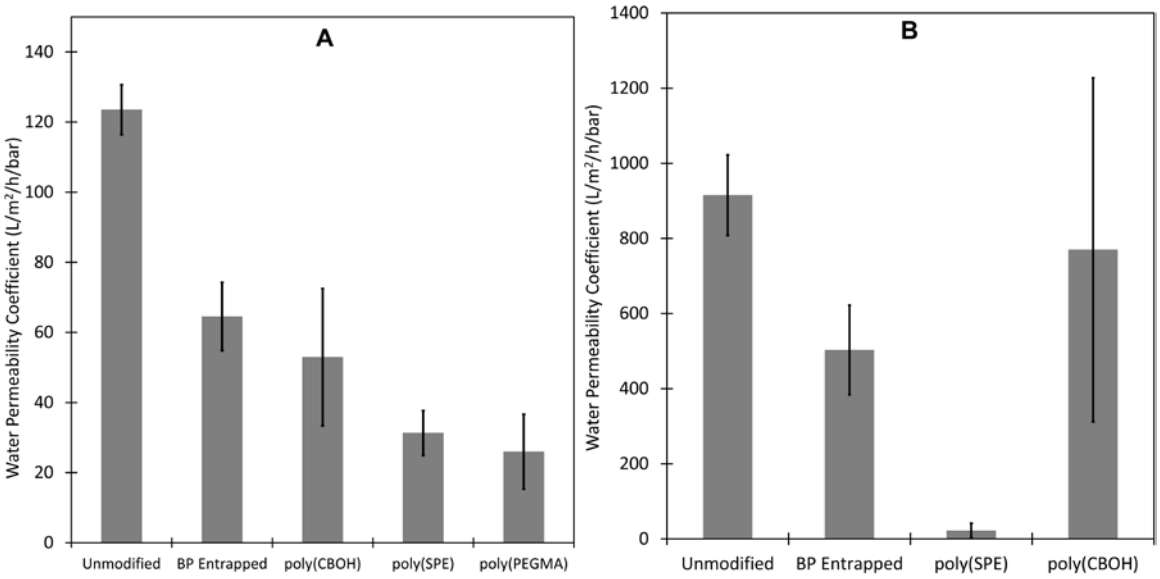

Figure 2.10. Pure water permeability coefficient (L/m^2/h/bar) versus modified membrane type for (A) unmodified, BP entrapped, and modified by poly(CBOH), poly(SPE), and poly(PEGMA) GE PES and (B) unmodified, BP entrapped, poly(SPE) modified, and poly(CBOH) modified Microdyn-Nadir PM UP150 PES membranes. Membranes were tested in direct-flow configuration and the testable membrane area was 14.6 cm^2. Error bars represent one standard deviation among at least 4 samples.

2.3.4 Bacteria Deposition on Membranes

Bacteria deposition studies were performed on the surface-modified GE Osmonics PES membranes. GFP-tagged *Pseudomonas fluorescens* bacteria were injected parallel to the surface-modified PES membranes under conditions of no permeate flow and the number of bacteria adsorbed onto each membrane was counted as a function of time. The purpose of this study was to see how different surface modifications affected the bacteria interactions (adsorption characteristics) with the PES membranes. **Table 2.1** shows the bacteria deposition coefficients that were calculated from **Equation 2.4** for each membrane type. As expected, unmodified PES had a higher bacteria deposition coefficient of 1.4 μm/min due to the hydrophobic nature of the unmodified GE PES

membranes (70° water contact angle [**Figure 2.8A**]). Even with a very thin surface modification layer on the PES (as described in **Section 2.3.2**), the bacteria deposition coefficient was reduced by approximately an order of magnitude with all modification types. Interestingly, the water contact angle of the dry polymer modified surfaces did not change much (only poly(PEGMA) modified PES had a statistically significant lower water contact angle [**Figure 2.8A**]), suggesting hydration of the grafted polymer layers upon immersion in water plays a more important role than hydrophilicity of the membrane surface, as indicated by water contact angle values. Poly(PEGMA) modified PES had the highest bacteria deposition coefficient of the modification layers with a value of 0.18 μm/min. Poly(SPE) modified PES had the next lowest bacteria deposition coefficient of 0.13 μm/min. Poly(CBOH) modified PES had the lowest bacteria deposition coefficient of 0.10 μm/min. The cause for the poly(CBOH) modified PES having the lowest bacteria deposition coefficient can be attributed to the increase in hydration upon immersion in water as well as the weaker hydrophobic interactions expected with bacteria as a result of a lower surface free energy as described in **Section 2.3.6**. However statistically, all three modification layers on PES can be considered the same using a multiple mean hypothesis test (95% confidence). By this same test, all three are statistically different from the unmodified PES. These data show that even a thin modification layer could reduce the frequency of membrane cleanings.

Table 2.1. *Pseudomonas fluorescens* deposition (mass transfer) coefficients of unmodified GE Osmonics PES membranes and membranes modified with poly(CBOH), poly(SPE), and poly(PEGMA) by UV polymerization. Uncertainties represent one standard deviation among at least four different membrane samples.

Sample	k_d (μm/min)
Unmodified PES	1.4 ± 0.33
poly(CBOH) modified	0.10 ± 0.07
poly(SPE) modified	0.13 ± 0.07
poly(PEGMA) modified	0.18 ± 0.07

2.3.5 Switching Characteristics of Poly(CBOH)

A unique feature of CBOH (monomer or polymer) is that it can switch reversibly between the anti-fouling, zwitterion mode (CBOH) and an anti-microbial, quaternary amine mode (CB-Ring). NMR was used to show that the CBOH monomer switches to the CB-Ring. Fundamental studies were done using silicon wafer substrates to assess the polymer switching characteristics. Silicon wafers were chosen for this phase of the work to enable characterization of layer thicknesses by ellipsometry and to determine the switching pH and switching time without the concern of membrane degradation in low pH environments. CBOH was polymerized from silicon wafers using the graft-from ATRP method. FTIR was used to track the changes in surface chemistry. Silicon dioxide thickness was 1.8 nm, PGMA thickness was 8-12 nm, BPA thickness was 3-5 nm, and poly(CBOH) thickness was 45-70 nm.

2.3.5.1 Demonstration of Monomer Switching

Figure 2.11 depicts the ^{1}H NMR and ^{13}C NMR spectra of CB-Ring. Cao et al. [94] provided an interpretation for each NMR spectrum, however an interpretation is provided based on the results obtained from the experiments described. The following is

the interpretation of the ^{1}H-NMR spectrum in **Figure 2.11A**, with lowercase letters assigned to identify each proton type as assigned in the image: 2.10 (h), 3.57 (sarcosine impurity of protons attached to terminal carbon(s) on the nitrogen), 3.69 (a), 4.05-4.38 (c), 4.49 (sarcosine impurity of protons attached to the carbon between the nitrogen and the carbonyl), 4.58-4.88 (b and e), 5.58-5.63 (d), 5.96 (g), 6.41 (f), 11.50 (residual trifluoroacetic acid). The following is the interpretation of the ^{13}C-NMR spectrum in **Figure 2.11B**, with lowercase letters assigned to identify each carbon type as assigned in the image: 18.79 (j), 54.46 (a), 56.68 (sarcosine impurity of terminal carbons attached to the nitrogen), 59.35 (d), 61.01 (f), 63.45 (e), 65.53 (sarcosine impurity of carbon between the nitrogen and the carbonyl), 75.50 (b), 111.4-122.7 (residual trifluoroacetic acid), 132.03 (h), 137.00 (i), 163.3-165.1 (residual trifluoroacetic acid), 165.52 (g), 170.23 (sarcosine impurity of the carbon in the carbonyl), 172.63 (c). The sarcosine impurities are seen only in this set of spectra because the switching was tested with a less pure sample as compared to the CBtBu and CBOH NMR spectra. Notice how each spectrum changed drastically from CBOH to CB-Ring, indicating a successful change in structure from CBOH to CB-Ring.

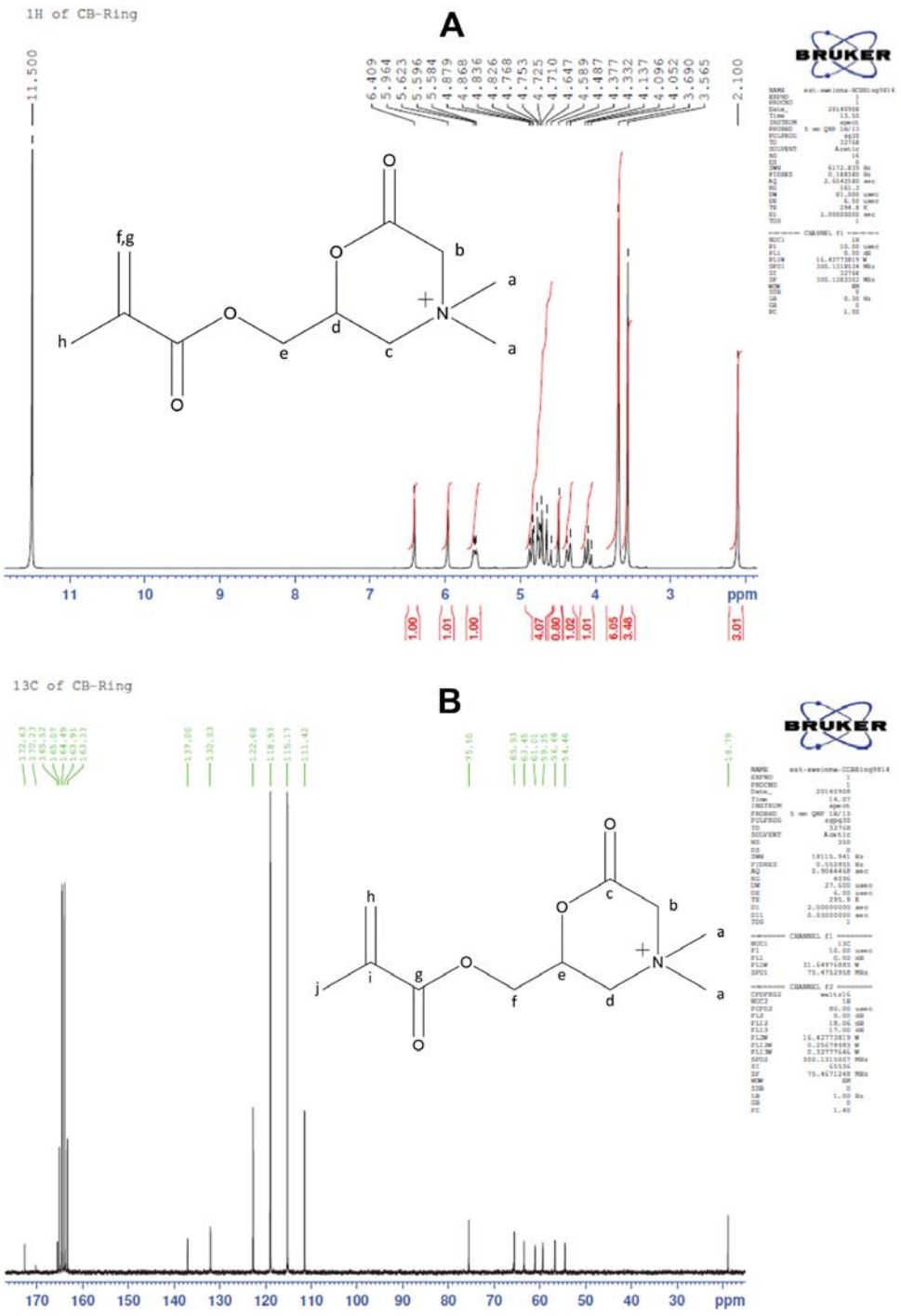

Figure 2.11. (A) 1H-NMR spectrum and (B) 13C-NMR spectrum of switched monomer CB-Ring. CBOH was dissolved in trifluoroacetic acid-d at a concentration of 50 mg/mL for 4 h before spectra was recorded. Lowercase letters were assigned to each proton and carbon type as specified in each spectrum.

2.3.5.2 Demonstration of Polymer Switching

Figure 2.12 shows the FTIR spectra demonstrating the successful grafting of poly(CBOH), successful switching to poly(CB-Ring), and successful switching back to poly(CBOH). The main peaks of interest to see the changes in surface chemistry are those from 1600 to 1800 cm^{-1} assigned to carbonyl stretching and those from 1150 to 1200 cm^{-1} assigned to C-O stretching. The peak at 1730 cm^{-1} in the BPA-modified spectrum is assigned to carbonyl stretching in PGMA and BPA. After poly(CBOH) grafting, the same peak at 1730 cm^{-1} increases in intensity, which corresponds to carbonyl stretching in the ester group next to the carbon backbone of the polymer. The new peak at 1640 cm^{-1} corresponds to the carboxylate anion of the poly(CBOH) zwitterion, indicating successful grafting of CBOH from the silicon wafers. Interestingly, the CBOH carboxylate anion peak shifted from 1705 cm^{-1} on PES membranes to 1640 cm^{-1} on silicon wafers. To test if the poly(CBOH) zwitterion switched to poly(CB-Ring), the poly(CBOH) modified silicon wafers were placed in pure TFA. The shift in the carbonyl stretching peak from 1640 cm^{-1} to 1680 cm^{-1} indicates a successful switch from poly(CBOH) to poly(CB-Ring). Also, the large increase in peak area at approximately 1150 cm^{-1} to 1200 cm^{-1} (assigned to C-O stretching) further supports successful switching from the carboxylate anion of poly(CBOH) (weak C-O stretching) to the acetate ester of poly(CB-Ring) (strong C-O stretching) [188]. The poly(CB-Ring) modified wafers were then placed in water to switch back to poly(CBOH). The spectrum for poly(CBOH) was fully recovered, indicating that switching was reversible.

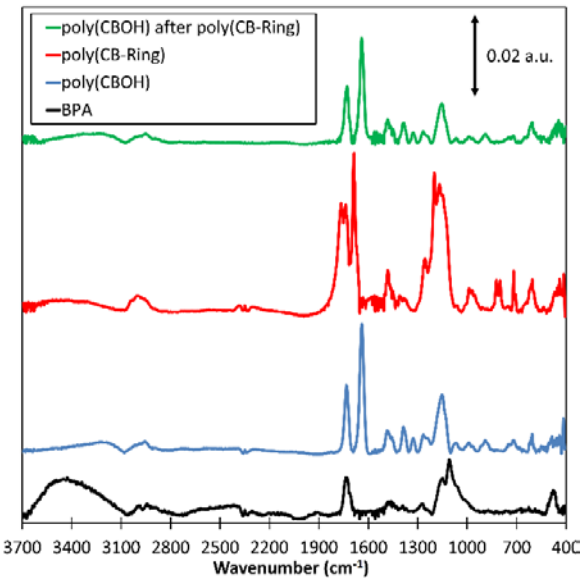

Figure 2.12. FTIR spectra of silicon wafers surface modified with initiator (BPA), poly(CBOH), poly(CB-Ring) (poly(CBOH) after immersion in TFA for 1 h), and poly(CBOH) after poly(CB-Ring) (poly(CB-Ring) after immersion in deionized water for 1 h). Poly(CBOH) layer thickness was approximately 60 nm. Scale bar represents 0.02 absorbance units (a.u.).

2.3.5.3 Determination of Switching pH

Poly(CBOH) modified silicon wafers were placed in solutions of various pH values for 1 h to study poly(CBOH) switching to poly(CB-Ring). As described by Cao et al. [93], the first step in the switching mechanism is protonation of the carboxylate anion, which requires a decrease in pH. Therefore, the solution pH was decreased from pH 7 in 0.5 increments until switching was observed by FTIR. **Figure 2.13** shows the FTIR spectra of the poly(CBOH) modified silicon wafers after immersion in deionized water, pure TFA, and TFA/water solutions at pH values of 0.6, 1, and 1.5 for 1 h. Switching started to occur at pH 1.5, however there was incomplete switching, as indicated by the presence of peaks at 1680 cm^{-1} and at 1640 cm^{-1} assigned to poly(CB-Ring) and

poly(CBOH). Also, the peak area change is noticeable at 1150 cm^{-1} (assigned to C-O stretching), but not as large as for poly(CB-Ring) from pure TFA, further indicating switching is incomplete. When the pH was reduced to 1, the area of the peak at 1640 cm^{-1} reduced significantly, and the area of the peak at 1150 cm^{-1} increased significantly, indicating almost complete switching to poly(CB-Ring). There was little difference between the spectra at pH 0.6 and pH 1. The poly(CBOH) carbonyl peak at 1640 cm^{-1} is barely seen in pH 0.6 and pH 1 spectra indicating almost complete switching. Interestingly, the pK_a value of the sarcosine acid group is 2.1 [189]. It appears that this pK_a value decreases (indicating an increase in acidity of the acid groups) by a full unit as a result of quaternization of the amine group on sarcosine during monomer synthesis [190], perhaps because the quaternary amine is a strong electron-withdrawing group near the carboxylic acid group. While using pH 1 cleaning solutions is not unprecedented, it may be desirable to carry out membrane cleaning under less aggressive conditions.

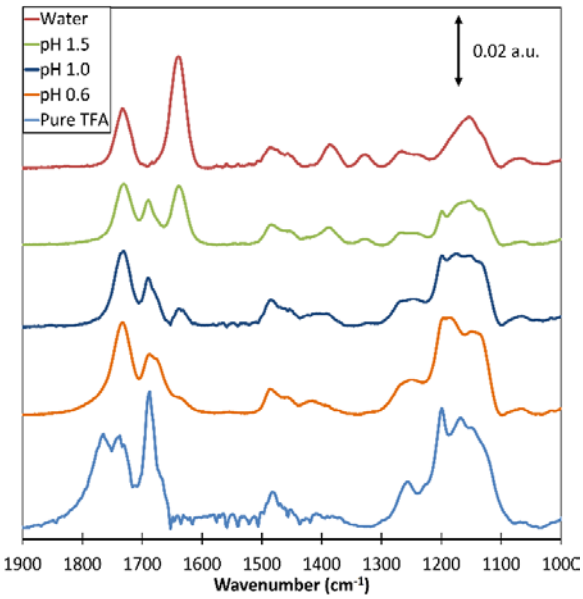

Figure 2.13. FTIR spectra of poly(CBOH) modified silicon wafers after being immersed in deionized water, TFA, and TFA/water solutions at pH values of 0.6, 1.0, and 1.5 for 1 h. The evolution of the peak at 1680 cm^{-1} and the increase in peak area at 1150 cm^{-1} indicates conversion from poly(CBOH) to poly(CB-Ring). Poly(CBOH) layer thickness is approximately 60 nm. Scale bar represents 0.02 absorbance units (a.u.).

2.3.5.4 Determination of Switching Times

Cao et al. [93, 94] report the switching kinetics for the monomer in solution, but not for the polymer modified gold surfaces used in their study. Poly(CBOH) modified silicon wafers were placed in a TFA/water solution of pH 1 for various times to determine the time required to switch from poly(CBOH) to poly(CB-Ring). **Figure 2.14A** shows the FTIR spectra of the poly(CBOH) modified silicon wafers in pH 1 solution for various times. Fifteen minutes (0.25 h) was sufficient to see complete switching, i.e., the peak at 1640 cm^{-1} assigned to carbonyl stretching in poly(CBOH) was absent and the peak area at 1150 cm^{-1} assigned to C-O stretching was greatly increased. A typical cleaning process for membranes lasts 30 min to 1 h [191, 192], so a switching

time of 15 min is practical. Poly(CB-Ring) modified silicon wafers were placed in deionized water for various times to determine the time required to switch from poly(CB-Ring) to poly(CBOH). **Figure 2.14B** shows the FTIR spectra of the poly(CB-Ring) modified silicon wafers in water for various times. Again, 0.25 h was sufficient to see complete switching, as evidenced by the lack of a peak at 1680 cm^{-1} assigned to carbonyl stretching in poly(CB-Ring) and the decrease in peak area at 1150 cm^{-1} assigned to C-O stretching.

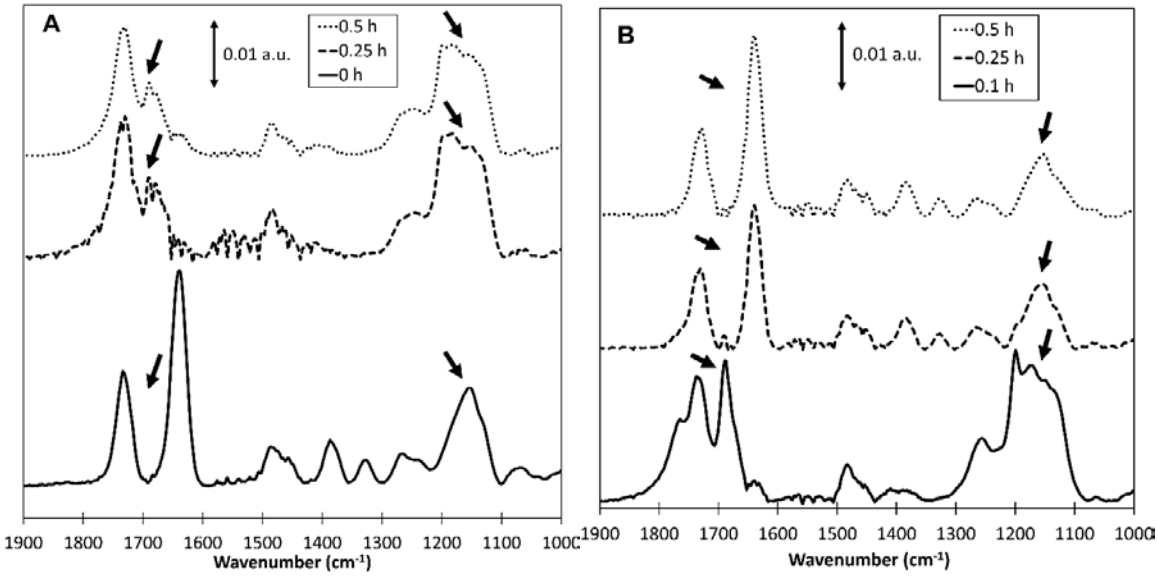

Figure 2.14. FTIR spectra of (A) poly(CBOH) modified silicon wafers conversion to poly(CB-Ring) by immersion in a TFA/water solution of pH 1.0 for 0 h, 0.25 h, and 0.5 h and (B) poly(CB-Ring) modified silicon wafers conversion to poly(CBOH) by immersion in deionized water for 0.1 h, 0.25 h, and 0.5 h. Poly(CBOH) layer thickness is approximately 60 nm. The scale bar in each figure represents 0.01 absorbance units (a.u.).

2.3.5.5 Demonstration of Polymer Layer Stability

To test if the switching mechanism would hold over numerous cycles, the surface of a polymer-modified silicon wafer was switched over 50 cycles. Each cycle comprised

placing the poly(CBOH) modified silicon wafer in pure TFA for at least 0.33 h to switch to poly(CB-ring) and then in deionized water for at least 0.33 h to switch back to poly(CBOH). **Figure 2.15** shows the FTIR spectra of the wafers after switching 1, 10, and 50 cycles. Switching was confirmed by the shift in the carbonyl stretching peak from 1640 cm^{-1} to 1680 cm^{-1} and the large increase in peak area from approximately 1150 cm^{-1} to 1200 cm^{-1} (assigned to C-O stretching). The switchability remained after 50 cycles, showing that this chemistry can withstand many cleaning cycles.

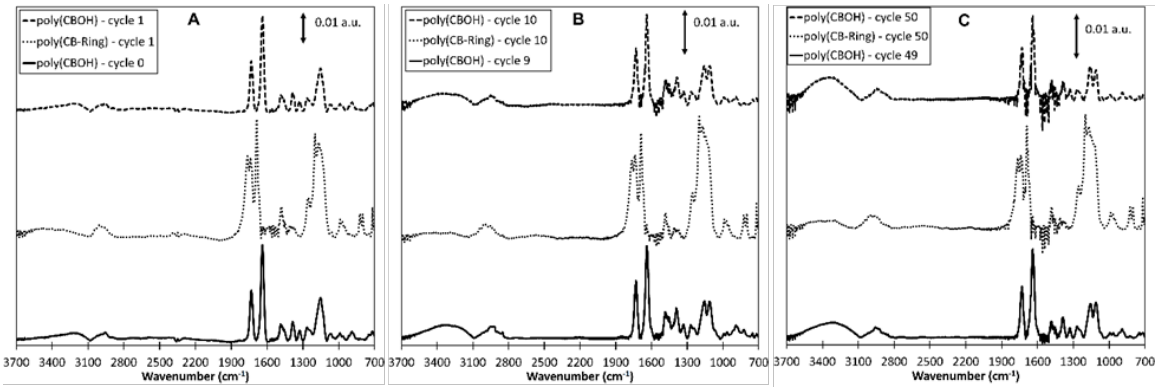

Figure 2.15. FTIR spectra of silicon wafers surface modified with poly(CBOH), poly(CB-Ring) (prepared by immersion of the poly(CBOH) sample in TFA for 0.33 h), and poly(CBOH) (prepared by immersion of the poly(CB-Ring) sample in deionized water for 0.33 h). The number of cycles of switching from poly(CBOH) to poly(CB-Ring) back to poly(CBOH) are shown in the legends of (A) 0-1, (B) 9-10, and (C) 49-50. Poly(CBOH) layer thickness is approximately 60 nm. Scale bar represents 0.01 absorbance units (a.u.).

2.3.6 Surface Free Energy Measurements

Surface free energies (SFEs) were calculated for poly(CBOH) modified silicon wafers and poly(CB-Ring) modified silicon wafers by measuring the contact angle of water and diiodomethane on each surface. **Table 2.2** presents the SFE data based on the Owens-Wendt method. Also included are the contact angle data for PEG and three other

common zwitterions on silicon wafers for comparison [175, 193]. SFE is a measure of the "stickiness" of a surface, and thus the lower the SFE, the lower the potential for foulants to adsorb to the surface. While the other zwitterions are more hydrophilic than CBOH as indicated by their lower water contact angles, CBOH has a lower affinity (higher contact angle) towards diiodomethane than all but PDMAB. This implies that CBOH could have weaker hydrophobic interactions with biopolymers/microorganisms than the other zwitterions, which would improve its effectiveness as an anti-fouling coating. Both the poly(CBOH) and the poly(CB-Ring) modified silicon wafers had lower SFEs than any of the common anti-fouling coatings. Thus, coating membranes with the poly(CBOH) chemistry was expected to improve biofouling resistance.

Table 2.2. Water and diiodomethane contact angles for silicon wafers modified with poly(CBOH) and poly(CB-Ring). Contact angle data are included for common antifouling chemistries: PEG, PMAPS (sulfobetaine zwitterion), PDMAB (carboxybetaine zwitterion), and PMPC (phosphobetaine zwitterion) on silicon wafers. Surface energy calculations are based on the Owens-Wendt method. Uncertainties represent the data range from at least 3 measurements or the error values reported in the articles cited.

	Contact Angle (degree)		**Surface energies (mJ/m^2)**		
	Water	**CH_2I_2**	**Dispersive**	**Polar**	**Total**
poly(CBOH)	41 ± 1	40 ± 1	30 ± 1	29 ± 1	59 ± 1
poly(CB-Ring)	42 ± 4	50 ± 1	25 ± 0	31 ± 3	57 ± 2
PEG [193]	39 ± 1	14 ± 3	40 ± 1	24 ± 1	64 ± 1
PMAPS [175]	11 ± 2	30 ± 2	32 ± 1	41 ± 1	73 ± 1
PDMAB [175]	16 ± 1.5	40 ± 2	28 ± 1	42 ± 2	71 ± 1
PMPC [175]	< 3	27 ± 2	34 ± 1	41 ± 1	75 ± 1

2.3.7 Biofilm Studies on Membranes

Biofilm studies were performed on unmodified, poly(CBOH) modified, and poly(SPE) modified Microdyn-Nadir PES membranes. Biofilm of a known biofouling

bacterium (*Sphingomonas wittichii* RW1) [194] was grown under conditions promoting rapid/strong biofilm growth by providing enrichment of nutrients for biofilm development on unmodified, poly(CBOH) modified, and poly(SPE) modified Microdyn-Nadir PES membranes, and the characteristics of each biofilm were determined. Anti-microbial effects of the grafted layer due to the switching of the poly(CBOH) zwitterion to poly(CB-Ring) quaternary amine were evaluated by conducting an analysis of the biofilm components (live cells, dead cells and EPS) with CLSM before and after 20 min exposure to 0.1 M HCl (pH 1). Data were compared to a control membrane that was modified by grafting a poly(SPE), "non-switchable" zwitterion layer. **Figure 2.16** shows representative biofilm images on unmodified, poly(CBOH) modified, and poly(SPE) modified PES membranes. **Table 2.3** shows the volumetric quantification of the biofilm components (live cells, dead cells, and EPS) for all three membrane types (no acid rinse). The biovolume per membrane area (live and dead cells) was reduced greatly upon surface modification of the PES membranes from 42 $\mu m^3/\mu m^2$ to 19 $\mu m^3/\mu m^2$ (poly(CBOH) modified) and 21 $\mu m^3/\mu m^2$ (poly(SPE) modified) (**Figure 2.16** and **Table 2.3**). These results can be seen in **Figure 2.16** where white spots indicate the membrane surface that is devoid of biomass. The corresponding average thickness of biomass was reduced from 70 µm to 36 µm (poly(CBOH) modified) and 39 µm (poly(SPE) modified).

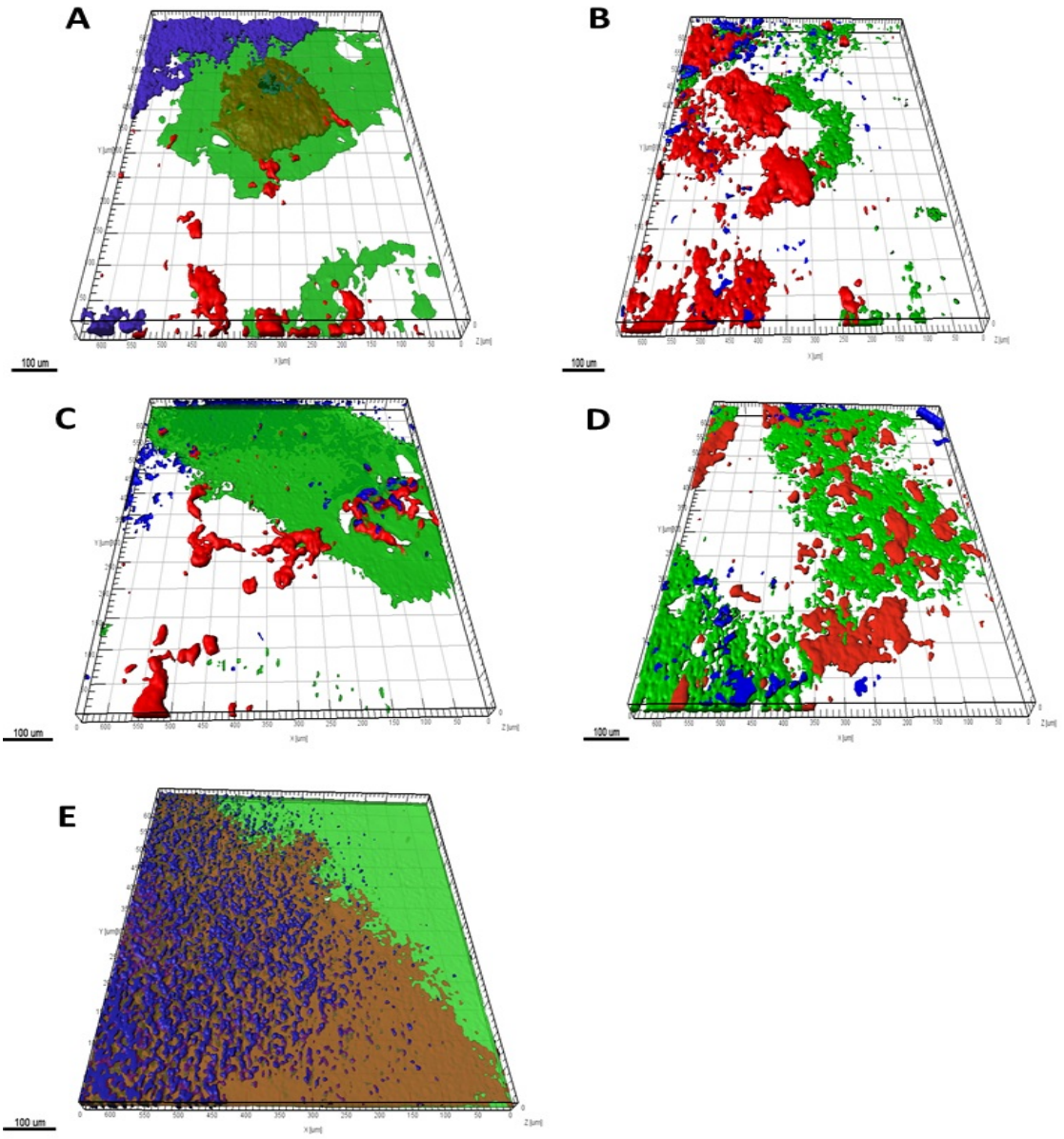

Figure 2.16. CLSM images of the biofilm development by *Sphingomonas wittichii* RW1 on poly(CBOH) modified (top, A-B), poly(SPE) modified (middle, C-D) and pristine (bottom, E) Microdyn-Nadir PM UP150 PES membrane. Red, blue and green represent non-viable bacteria, EPS and viable bacteria. Figure 2.16A, 2.16C, and 2.16E represents biofilm on poly(CBOH) modified, poly(SPE) modified, and unmodified PES membrane respectively; while 2.16B and 2.16D indicates biofilm formation on the acid treated poly(CBOH) modified and poly(SPE) modified PES membrane, respectively. The deep orange color indicates overlapping zone of dead and live cells. Images are 635 µm × 635 µm and the scale bar represents 100 µm.

Table 2.3. Biofilm volumetric quantification (biovolume per membrane area, biomass thickness, and biomass roughness coefficient) for each component of the biofilm formatted by *Sphingomonas wittichii* RW1 on unmodified, poly(CBOH) modified and poly(SPE) modified Microdyn-Nadir PM UP150 PES membranes. Uncertainties represent one standard deviation amongst at least five data points.

Membrane	**Unmodified PES**			**poly(CBOH)-PES**			**poly(SPE)-PES**		
	dead	**live**	**EPS**	**dead**	**live**	**EPS**	**dead**	**live**	**EPS**
Biovolume ($\mu m^3/\mu m^2$ membrane)	16.7 ± 2.5	25.2 ± 1.7	4.0 ± 0.8	4.7 ± 1.3	14.0 ± 2.6	2.2 ± 1.2	6.8 ± 1.6	14.7 ± 3.0	3.7 ± 0.4
Biomass Thickness (μm)	33.5 ± 4.4	36.5 ± 4.4	13.7 ± 2.6	9.6 ± 3.6	26.5 ± 5.1	3.1 ± 1.4	12.5 ± 2.8	26.7 ± 6.9	5.1 ± 2.3
Biomass Roughness Coefficient	0.1 ± 0.0	0.07 ± 0.0	1.2 ± 0.1	1.4 ± 0.7	0.1 ± 0.1	1.8 ± 1.5	1.0 ± 0.4	0.2 ± 0.2	1.4 ± 1.0

Table 2.4 shows the volumetric quantification of the biofilm components (live cells, dead cells, and EPS) for the poly(CBOH) modified and poly(SPE) modified PES membranes after exposing the biofilms to 0.1 M HCl for 20 min. After acid exposure, the biovolume of dead cells was elevated significantly only for the poly(CBOH) modified membrane (from 4.7 to 9.3 $\mu m^3/\mu m^2$), and the dead to live cells ratio increased from 0.33 to 1.04 (**Figure 2.16** and **Tables 2.3 and 2.4**). A larger number of dead cells and a smaller number of live cells were detected after rinsing with 0.1 M HCl only on the poly(CBOH) modified PES membrane (**Figure 2.16** and **Tables 2.3 and 2.4**). The EPS material was quantified with the fluorescently labeled ConA. EPS biovolume was determined to be statistically different only for the poly(CBOH) modified membrane, and EPS biomass thickness for poly(CBOH) and poly(SPE) modified membranes were

determined to be statistically different from the unmodified membrane. The reductions in dead and live biovolume and biomass thickness on the poly(CBOH) and poly(SPE) modified membranes (before exposure to 0.1 M HCl) relative to unmodified membrane were found to be statistically different at the 95% confidence level (**Table A-1**). The reduction in biomass on the poly(CBOH) and on the poly(SPE) modified PES membranes can be attributed to the increase in hydrophilicity and hydration of the grafted zwitterion layers (**Figure 2.8B**). Also, the elevation of dead cell biovolume and thickness and the reduction of live cell biomass thickness on the poly(CBOH) modified membranes before and after exposure to 0.1 M HCl were found to be statistically different at the 95% confidence level based on a two-tailed t-test (**Table A-2**). The dead and live cell biovolume and the live cell biomass thickness on the poly(SPE) modified membranes before and after exposure to 0.1 M HCl were found to be statistically the same at 95% confidence (**Table A-3**). While the overall number of cells and EPS on the poly(CBOH) modified and poly(SPE) modified PES membranes did not change after exposure to 0.1 M HCl (**Tables 2.3 and 2.4**), biofilm mortality was higher on the poly(CBOH) coated membrane. Acid washing with a pH 1.0 solution was expected to increase the biofilm mortality by itself. Therefore, the control of using another low-fouling zwitterion like poly(SPE) was necessary to determine if there was a significant enhancement in biofilm mortality after acid washing. This mortality, expressed as the dead to live cells ratio, was likely enhanced by the anti-microbial, quaternary amine group of the poly(CB-ring) layer (**Figure 2.4**) upon exposure to the pH 1.0 acid solution, since no enhancement was found for the non-switchable poly(SPE) coated membrane.

Table 2.4. Biofilm volumetric quantification (biovolume per membrane area, biomass thickness, and biomass roughness coefficient) for each component of the biofilm formatted by *Sphingomonas wittichii* RW1 on poly(CBOH) modified and poly(SPE) modified Microdyn-Nadir PM UP150 PES membranes after pH 1.0 acid treatment for 20 min. Uncertainties represent one standard deviation among at least eight data points.

Membrane after Acid treatment (pH 1)	**poly(CBOH)-PES**			**poly(SPE)-PES**		
	dead	**live**	**EPS**	**dead**	**live**	**EPS**
Biovolume ($\mu m^3/\mu m^2$ membrane)	9.4 ± 2.5	8.9 ± 7.8	1.9 ± 1.8	8.2 ± 2.5	13.9 ± 3.4	1.0 ± 0.9
Biomass Thickness (μm)	17.7 ± 4.4	14.7 ± 10.4	3.0 ± 2.9	17.0 ± 4.3	25.9 ± 6.1	0.2 ± 0.1
Biomass Roughness Coefficient	0.7 ± 0.4	0.8 ± 1.0	1.9 ± 0.7	0.8 ± 0.5	0.1 ± 0.09	2.0 ± 0.01

Interestingly, the total biomass roughness was much higher for poly(CBOH) modified and poly(SPE) modified PES membranes (both before and after exposure to 0.1 M HCl) than for unmodified PES membranes. A possible reason is because there is a more fully developed biofilm on the unmodified membranes, which would present a smoother surface than a patchy, less well developed biofilm on the poly(CBOH) modified and poly(SPE) modified membranes (as it appears in **Figure 2.16**) [195]. This patchiness of the biofilm on the poly(CBOH) modified and poly(SPE) modified membranes shows a slower rate of biofilm development on the modified membranes, further indicating the modification layers effectiveness towards biofouling control.

2.4 Conclusions

A method was developed for applying a new type of zwitterionic surface chemistry onto polyethersulfone ultrafiltration membranes to reduce membrane biofouling. Poly(CBOH) modified PES membranes reduced the bacteria deposition coefficient by an order of magnitude from unmodified PES, and less than half the amount of biofilm biomass was developed onto the modified membrane surface compared to the unmodified membrane. The enhanced fouling resistance of the poly(CBOH) modified PES membranes is attributed to the increase in surface hydrophilicity and hydration of the grafted polymer layer. A unique feature of this chemistry is its ability to switch from zwitterionic to cationic states. The short time required to switch from a low fouling zwitterion surface to an antimicrobial quaternary amine surface is practical for use. Biofilm mortality was elevated once the anti-fouling poly(CBOH) zwitterion was switched to the anti-microbial, poly(CB-Ring) quaternary amine.

2.5 Acknowledgements

I was supported by a National Science Foundation Graduate Research Fellowship under Award DGE-1246875. I thank the US-Israel Binational Agricultural Research and Development Fund for financial support under Research Grant Agreement No. US-4654-13. I thank Maria Bass and Viatcheslav Freger from Technion – Israel Institute of Technology, who performed the bacteria deposition studies. I thank Soumya Pandit and Moshe Herzberg, from Ben Gurion University of the Negev, who performed the biofilm studies. I thank Alex Kitaygorodskiy in the Clemson University Chemistry Department

for assistance with NMR measurements. I thank Donald Mulwee in the Clemson University Electron Microscopy Laboratory for assistance with SEM measurements.

CHAPTER THREE

INFLUENCE OF CHEMICAL COATING COMBINED WITH NANOPATTERNING ON ALGINATE FOULING DURING NANOFILTRATION

[As published in the Journal of Membrane Science 513 (2016) 146-154 with minor revisions]

3.1 Introduction

Membrane biofouling refers to the attachment or adsorption of biopolymers or organisms onto the membrane surface or within the membrane pores. It is a major hindrance to membrane usage [7, 168], causing a transient flux decline or pressure increase and a decrease in salt rejection. Fouled membranes require chemical cleaning, which shortens the membrane life and greatly increases membrane operating cost [9]. Biofouling is one of multiple steps in the process that leads to biofilm formation [6]. In this process, a conditioning film is adsorbed to the surface, typically comprising macromolecules from the solution or macromolecules secreted from bacteria. This conditioning of the surface provides favorable conditions for bacteria to adsorb or attach onto the surface, where they grow and form colonies, eventually leading to a biofilm.

Biofouling reduction/elimination on membranes has been a common topic in the literature. Specifically, surface modification of membranes is a common strategy [11], with numerous studies describing the use of chemical treatments and coatings. Anti-fouling coatings are designed to make the membrane surface less favorable for bacterial attachment; e.g., by making the surface more hydrophilic, by including hydrogen-bond acceptors, by excluding hydrogen-bond donors, and by having an overall neutral electrical charge [12, 17]. Examples of widely studied antifouling coatings include

poly(ethylene glycol) (PEG) due to its high degree of hydration [29, 196], and zwitterions, which are net charge neutral molecules that have positive and negative charge groups that can form a strong hydration layer that excludes biopolymers and bacteria [19]. Three zwitterions of interest are carboxybetaine [45], sulfobetaine [100], and phosphobetaine [55], with sulfobetaine being the most commonly used in the literature.

Another common strategy involves coating membranes with anti-microbial agents that are able to kill bacteria. Coatings with quaternary amine groups are common and are thought to disrupt the cell membrane allowing release of intracellular contents causing cell death [61, 66]. Graphene oxide and carbon nanotubes have shown promise by deactivating bacteria upon contact with these surfaces [75, 76]. Also, silver nanoparticles have been incorporated into membranes, making anti-microbial membranes that severely damage the bacteria cell membrane [71, 73].

A more recent area of interest has been physical modification of surfaces with a specific, ordered pattern to disrupt the hydrodynamic boundary layer at the surface, making foulants less likely to adhere. One of the first designs, coined Sharklet™ [107, 113, 130], used micron-scale patterns that mimic shark skin. Other groups have placed micro-patterned posts [144] and an imprinted spacer design [126] on membrane surfaces in an attempt to reduce biofouling. Micro-patterned hollow fibers also have been of interest with patterning on the outer skin of the hollow fiber to reduce fouling [150, 151, 197]. Other micro-patterns applied onto membranes to reduce fouling include line and groove patterns [145], pyramids [139], and prisms [142]. Nano-scale line and groove

patterns have been applied onto membranes to reduce protein fouling [153], colloidal particle fouling [103, 152], and gypsum scaling [198].

This chapter of my dissertation contributes a method for applying both a chemical coating and a nano-pattern to a membrane surface. First, a nano-scale line and groove pattern was applied to a polyamide thin-film composite membrane by thermal embossing. Next, poly(ethylene glycol) diglycidyl ether (PEGDE) was reacted onto the membrane as a PEG-based chemical coating. The membranes were tested for flux and salt rejection pre- and post-modification in a cross-flow system. Alginate was used as a model biopolymer foulant material [199]. To my knowledge, this study is the first to combine chemical and physical modification of a membrane surface to enhance biofouling resistance, but not the first time these two methods have been combined on a surface [200]. It also is the first to demonstrate the successful, direct thermal embossing of a nano-pattern onto a polyamide thin-film composite membrane.

3.2 Materials and Methods

3.2.1 Materials

Magnesium sulfate ($MgSO_4$, ≥ 99.5%), PEGDE (M_n = 500 Da), sodium alginate (from brown algae), and sodium chloride (NaCl, ≥ 99%) were used as received from Sigma Aldrich. Calcium chloride dihydrate ($CaCl_2 \cdot 2H_2O$) was used as received from Fisher Scientific. Aqueous solutions were made with deionized water from a Milli-Q water purification system (EMD Millipore).

Polyamide thin-film composite nanofiltration (NF) membranes (GE HL series) were purchased from Sterlitech Corporation. This membrane consists of a polyester

fabric backing, a polyethersulfone support layer, and a semi-aromatic (piperazine-trimesoyl chloride based) polyamide selective layer [201].

3.2.2 Membrane Surface Modification

3.2.2.1 Patterning the Membrane

Figure 3.1 illustrates the two-step process of patterning the membrane and applying a chemical coating to the membrane surface. The silicon line and groove stamps used to pattern the membranes were purchased from LightSmyth Technologies, Inc. The stamps were specified to have a 606 nm period between peaks, a 190 nm groove depth, and a 303 nm line width. A 29 mm × 12 mm stamp was used to prepare membranes for physiochemical characterization and salt rejection experiments. A 29 mm × 24 mm stamp was used to prepare membranes for the alginate fouling experiments. A Carver press (AutoFour/1512H model) was used to emboss the membranes with the stamp/wafer. First, the press plates were heated to 45 °C. A small aluminum plate was placed on the bottom press plate, the membrane was placed on top of the aluminum plate with polyamide surface facing up, and then the silicon stamp was placed on top of the polyamide surface with the stamp features facing the polyamide surface. A 30 cm × 30 cm Kimwipe was folded into $1/16^{th}$ its original size and placed on top of the stamp to act as a "cushion" to help prevent the stamp from breaking. Another small aluminum plate was placed on top of the Kimwipe. The press plates were closed at 25% pump speed until the force was 6670 N. A force was maintained at 6670 ± 1330 N, which was found to be sufficient for patterning without damaging the silicon stamps. After 20 min, the press was

released and the stamp was removed from the membrane, leaving a patterned membrane surface.

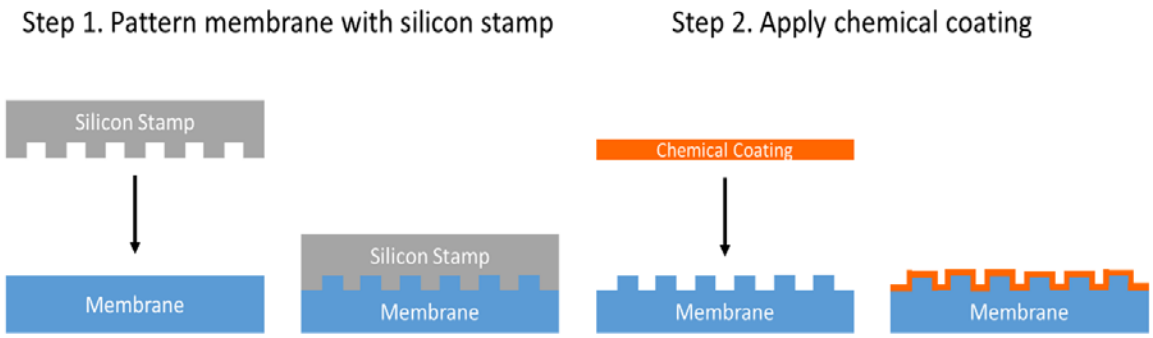

Figure 3.1. Methodology of combining chemical coating and physical patterning on a membrane surface by deformation (i.e., embossing) of the membrane substrate. The chemical coating is a poly(ethylene glycol) diglycidyl ether aqueous solution.

Control experiments were done to study the effect of the thermal compression alone. For the control process, a 29 mm × 10 mm flat silicon wafer from Nova Electronic Materials was used to prepare membranes for physiochemical characterization and salt rejection experiments. A 29 mm × 24 mm flat silicon wafer from UniversityWafer, Inc. was used to prepare membranes for the alginate fouling experiments.

3.2.2.2 Chemically Coating the Membrane

PEGDE was used to modify the membrane surface chemically. Aqueous solutions of 5 wt% and 15 wt% PEGDE were used. A control experiment was done using DI water. The reaction process followed that given by Van Wagner et al. [196] with minor modifications. Aluminum foil tape was placed on the membrane edges to create a solution boundary. Next, the reaction solution was heated to 42 ± 2°C by a hot plate and approximately 0.2 g/cm^2 membrane of solution was pipetted onto the membrane such that the whole membrane surface area was contacted by the solution. The solution was

allowed to react on the membrane for 10 min, and then the membrane was rinsed in DI water. The membranes used for the cross-flow filtration experiments were stored in DI water until use. The membranes used for physicochemical characterization were patted dry and then dried fully under vacuum at 20-25°C and -0.78 to -0.95 barg. In all cases, the entirety of the membrane testable area was modified with the desired reaction solution.

3.2.3 Membrane Characterization Techniques

3.2.3.1 Atomic Force Microscopy

Atomic force microscopy (AFM) was used to observe the surface morphology of the stamps and the membranes. Images were obtained using a Bioscope AFM (Bruker, Inc.) with NanoScope IIIa controller equipped with Nanoscope version 5.32R1 software. Silicon cantilevers (MikroMasch, Inc., HQ:NSC16/AL BS) were used as probes for the non-contact tapping mode measurements. AFM images were taken with a 256 × 256 pixel resolution over 20 μm × 20 μm or 5 μm × 5 μm areas at a scan rate of 0.5 Hz. The section analysis feature of the software was used to determine peak heights and peak periods (peak-to-peak distances).

3.2.3.2 Laser Measuring Microscopy

An Olympus LEXT OLS4000 3D laser measuring microscope (software version 2.2.3) was used to take images of the stamps and the patterned membrane surfaces on a larger scale than the AFM. Images were taken with 50x and 100x objective lenses at varying optical zooms (1x-8x). Surface roughness measurements were attained using the

50x objective with a 4x optical zoom (~0.004 mm^2 area). Surface roughness data were obtained as the root mean square (RMS) height of the surface.

3.2.3.3 ATR-FTIR

Attenuated total reflectance Fourier-transform infrared spectroscopy (ATR-FTIR) was used to characterize the surface chemistry of the pristine and chemically modified membranes. These measurements were done to detect that PEDGE had been grafted onto the membrane surface. Spectra were obtained using a Thermo Scientific Nicolet Nexus 870 FTIR ESP with a zinc selenide ATR crystal. Data were processed by OMNIC 8.3.103 software (Thermo Scientific). Each spectrum was collected at 128 scans at a resolution of 4 cm^{-1}, corrected with the ATR correction on software, and manually baseline corrected. A background of the crystal was taken before each set of samples was tested.

3.2.3.4 Static Water Contact Angle

The water contact angle of PEGDE modified membranes was measured using a Krüss Drop Shape Analysis System (product DSA 10-Mk2 equipped with software version DSA 1.80.0.2). Three microliters of DI water was placed onto the membrane surface and was allowed to equilibrate for 60 s. After the 60 s, the contact angle was measured using the software and recorded.

3.2.4 Membrane Performance Testing

A custom cross-flow cell was manufactured by Clemson Machining and Technical Services for all membrane performance testing. **Figure 3.2** shows an AutoCAD schematic of the cell. The drawing includes the two ports for the feed and the

concentrate, the single permeate port, the two o-rings for sealing purposes, and the four placements for screws to tighten the cell together. The testable membrane area, 5.6 cm^2, is set by the inner o-ring. The two small circles on the drawing are pin placements to help ensure proper alignment of the cell pieces. The test cell was made from acrylic and can withstand pressures up to 27.6 bar. The test solution was pumped from a feed tank to the test cell using a Giant Industries pump head (model 217A-5100 from Southern Municipal Equipment Co., Inc.) and a Marathon Electric pump motor (model E2001A from Motion Industries Inc.). The solution temperature was controlled by use of a Polyscience MM7 chiller (Grainger Industrial Supply) equipped with a homemade stainless-steel coil. The back pressure was controlled by a gate valve and measured by a stainless-steel pressure gauge (3702K44, McMaster-Carr Supply Company), and the concentrate flow rate was measured using an acrylic in-line flow meter (EW-32477-08, Cole Parmer). The permeate flow was collected on an Ohaus® Adventurer® AX precision balance (VWR International) and not recycled to the feed tank.

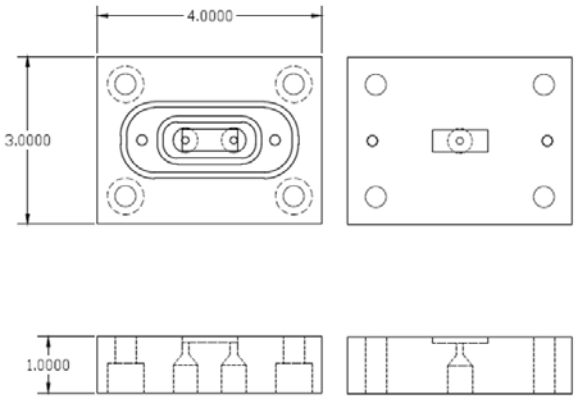

Figure 3.2. An AutoCAD drawing of the top (left) and bottom (right) of the acrylic membrane cross flow used to performance test the membranes. The cell dimensions are 7.62 cm (3.0 in) × 10.16 cm (4.0 in) × 2.54 cm (1.0 in).

3.2.4.1 Solution Flux and Salt Rejection

A 2000 ppm $MgSO_4$ test solution was used to evaluate the integrity of the membrane selective layer after patterning and/or chemical coating. The applied pressure was 8.6 barg and permeate was allowed to flow for 25 min before sample collection. The solution temperature was 22-23°C and the cross-flow velocity was 3.0 ± 0.2 m/s. A high cross-flow velocity was used to reduce concentration polarization. For patterned membranes, the flow angle was 0° relative to the line pattern, meaning that solution flow was parallel to the pattern lines. Sixty-two percent of the testable membrane area was patterned. The permeate flow was collected for 4 min and analyzed for flux and salt rejection measurements. A conductivity meter (Oakton CON 6+, Cole Parmer) was used to measure feed and permeate salt concentrations. The conductivity meter was calibrated by an ICP-OES (Optima 3100RL with autosampler, Perkin Elmer).

3.2.4.2 Solution Flux Measurements on a Single Membrane

To test the claim that the patterning process does not damage the membrane, the pure water flux of a pristine membrane was measured, a 15 wt% aqueous glycerol solution (used by manufacturers as a structure preserving agent) was applied onto the membrane, the membrane was pat dried, patterned, and then the pure water flux was tested again. Pressure was 8.6 bar, temperature was 22-23°C, cross flow rate was 1.0 m/s, and membrane area was 5.6 cm^2.

3.2.4.3 Sodium Alginate Fouling

Sodium alginate was used as a model biopolymer for fouling studies. A solution of 30 mg/L sodium alginate, 10 mM NaCl (585 ppm), and 1 mM $CaCl_2$ (111 ppm) was

used. Calcium ions were included in the feed solution because they cause alginate to gel, which can lead to an increase in the rate of fouling [202]. The solution temperature was 22-23°C and the cross-flow velocity was 1.0 ± 0.1 m/s. For patterned membranes, the flow angle was 90° relative to the line pattern. A 90° flow angle has been shown to reduce fouling due to vortices created at the membrane surface from the patterns [102, 103]. Sixty-eight percent of the testable membrane area was patterned. The approximate desired initial starting flux for each membrane tested was 120 L/m^2/h. Permeate was collected for approximately 1 min every 5 min for a total time of 2 h.

3.3 Results and Discussion

3.3.1 Membrane Surface Modification

3.3.1.1 Membrane Patterning

Polyamide nanofiltration membranes were patterned directly with silicon stamps. Thermal embossing was used to create the patterns on the membrane surface, which causes the polymer film to deform into the nanoscale grooves of the rigid silicon stamp [103]. Therefore, the pattern produced on the membrane is a negative replica of the pattern on the silicon stamp. **Figure 3.3** shows an AFM image and a LEXT image of the nano-patterned silicon stamp. A unique feature of the LEXT is the ability to stitch images together. For example, a 3 × 3 array of 30 μm × 30 μm images can be stitched together to give a 90 μm × 90 μm image with a higher resolution than taking one single 90 μm × 90 μm image. LEXT imaging also is much faster than AFM, producing an image in 1-2 min when AFM would take at least 30 min to produce an image of comparable size. The LEXT can resolve features 10 nm in size in the z-direction and 120 nm in the xy-plane.

AFM gave a peak-to-peak distance of 625 nm, which compares well to the 606 nm specification given by LightSmyth. The groove depth of the stamp from AFM was 231 ± 11 nm, which is reasonably close to the 190 nm specification given by LightSmyth. The LEXT image in **Figure 3.3B** shows the uniformity of the stamp across a larger area than readily accessible by AFM (84 μm × 87 μm). Although, the stamp features (peaks and valleys) appear to be curved on the AFM image in **Figure 3.3A**, **Figure 3.4** shows the stamp features appear flat in 5 μm × 5 μm images, as specified by LightSmyth. The "waviness" of the image is an artifact of the AFM.

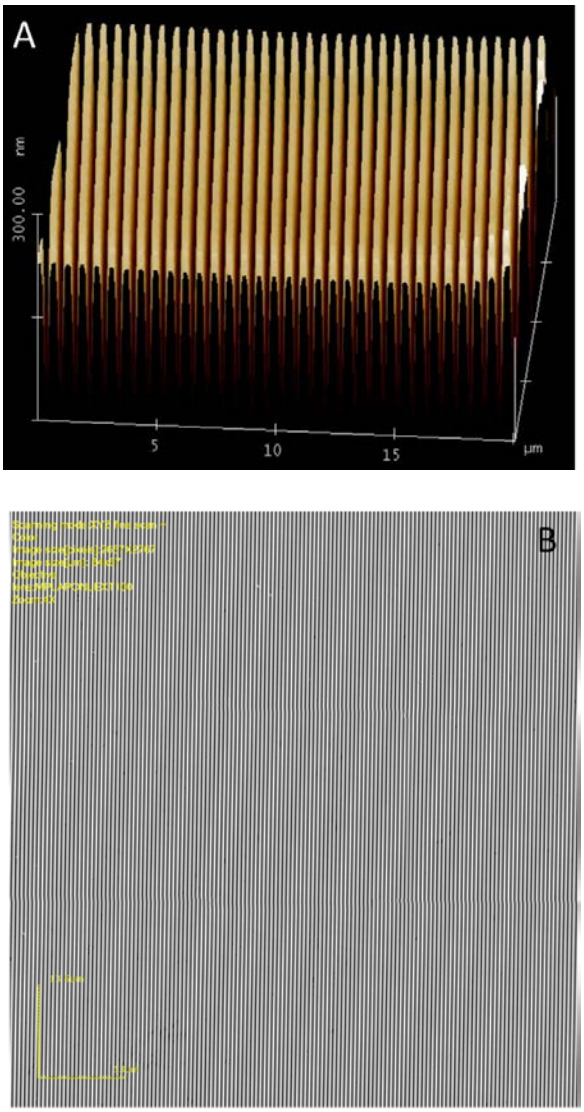

Figure 3.3. Silicon stamp images produced by (A) AFM and (B) LEXT. The AFM image is 20 µm × 20 µm × 300 nm and gives an average groove depth of 231 ± 11 nm and a period of 625 nm. The LEXT image is an 84 µm × 87 µm image produced from stitching images together from the 100x objective with a 4x optical zoom. The scale bar in the LEXT image is 13.5 µm (y-direction) × 13 µm (x-direction).

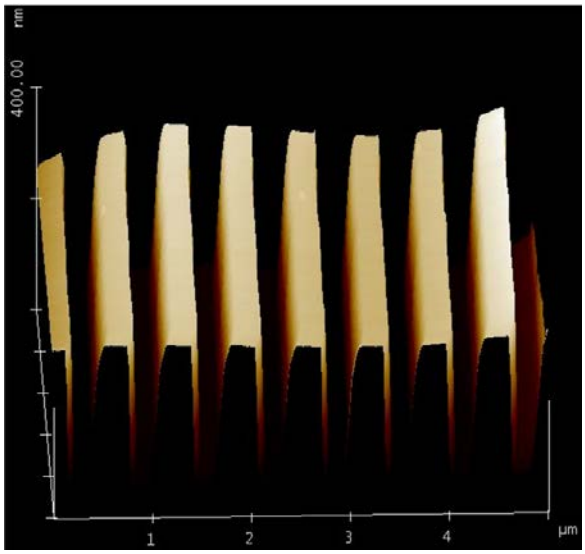

Figure 3.4. A 5 µm × 5 µm × 400 nm AFM image of the silicon stamp.

Membranes were patterned at 45 °C using a 20 min embossing time. Performing the thermal embossing at a lower temperature (30 °C) and 20 min resulted in incomplete and/or negligible patterning on the membrane. Embossing at a higher temperature (65 °C) for 10 min yielded similar groove depths as 45 °C for 20 min. These results imply that the ability of the membrane material to deform/flow is a key factor to pattern the membrane [103, 203]. Also, because embossing at the two higher temperatures yielded similar results for groove depths on the membrane (vide infra), the maximum obtainable groove depth may be limited.

Figure 3.5 presents representative AFM images of the three types of membranes (reaction with PEGDE only, pressed with flat wafer, and patterned). AFM and LEXT gave similar results for the groove depths of the patterned membranes. The average groove depth of the various PEGDE modified, patterned membranes from AFM was 64 ± 34 nm and from LEXT was 75 ± 24 nm. These groove depths are not the maximum

attainable values defined by the silicon stamp. The peak-to-peak distance was consistently 625 nm, exactly the same as the silicon stamp results from AFM. **Figure 3.6** shows the 5 μm × 5 μm image of a 0 wt%, patterned membrane. **Figures 3.5 and 3.6** show that the valleys and the peaks of the patterns were always curved. This low resolution in the pattern replication indicates that plastic deformation, rather than viscous flow, was the mechanism for membrane patterning [103]. **Figure 3.7** shows representative LEXT images of the patterned membranes. From the images, it is clear that the membrane surfaces had imperfections. Importantly, **Figure 3.8** shows that unmodified membrane surfaces also had similar imperfections. I did not observe any fracturing of the polyamide surface layer, nor is there evidence from flux and salt rejection studies (vide infra) to suggest that the selective layer is fractured. Stafford and colleagues [204] quantified the strain at the onset of cracking ε^* for nanoscale crosslinked polyamide thin films. They found ε^* to be $14.04 \pm 4.12\%$. In this case, the local strain defined by the height-to-pitch of the pattern is $10.6 \pm 5.6\%$. It therefore seems reasonable that that yield of the crosslinked polyamide film could occur to form the pattern without fracturing.

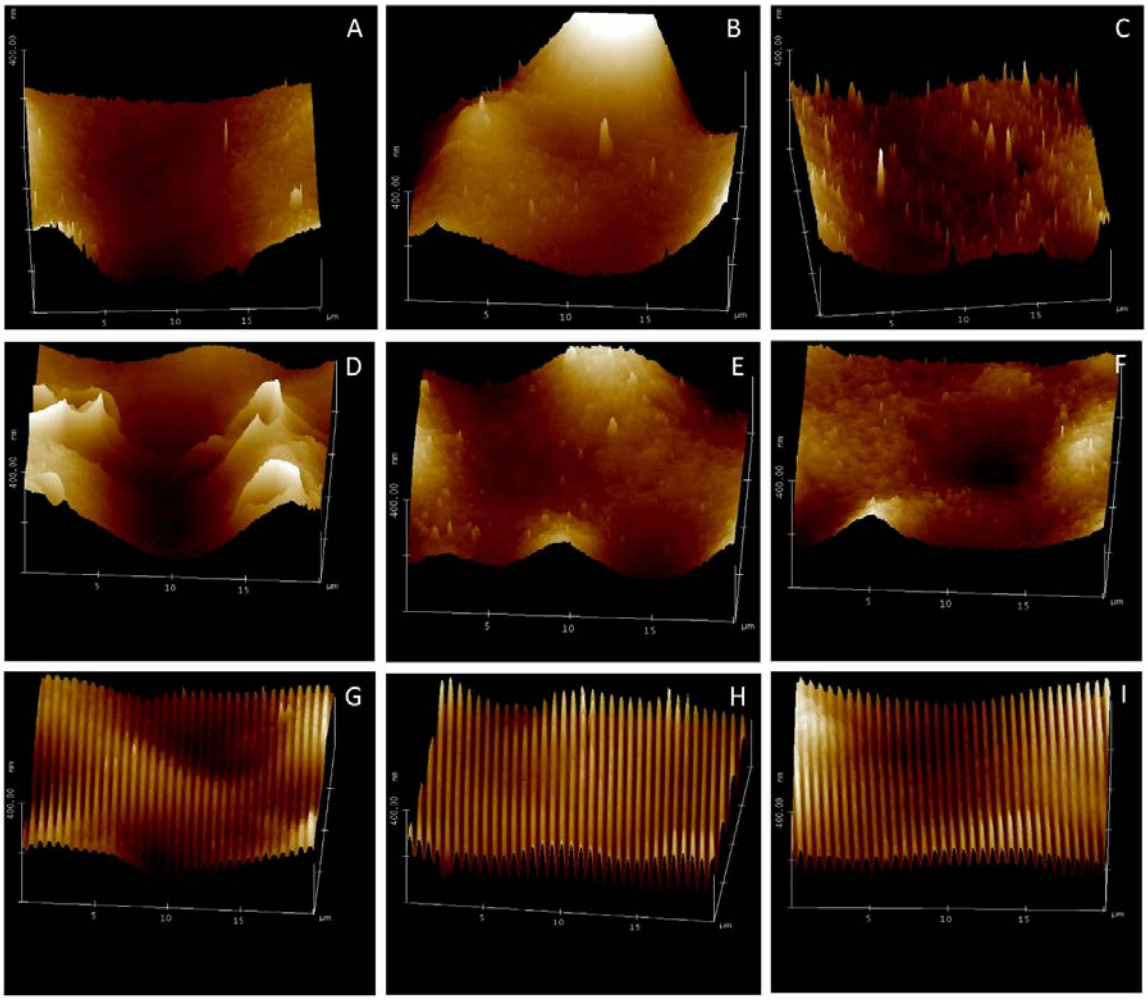

Figure 3.5. AFM images of the 3 types of membranes modified with varying concentrations of aqueous PEGDE solutions. Reaction with PEGDE only: 0 wt% (A, control), 5 wt% (B), 15 wt% (C); pressed with flat silicon wafer: 0 wt% (D), 5 wt% (E), 15 wt% (F); and patterned: 0 wt% (G), 5 wt% (H), 15 wt% (I). The common scale is 20 μm × 20 μm × 400 nm.

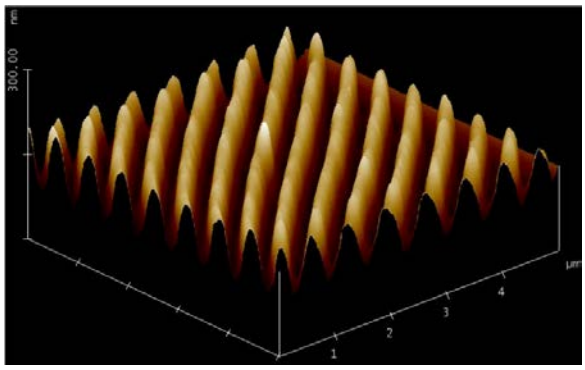

Figure 3.6. A 5 μm × 5 μm × 300 nm AFM image of a 0 wt% patterned membrane.

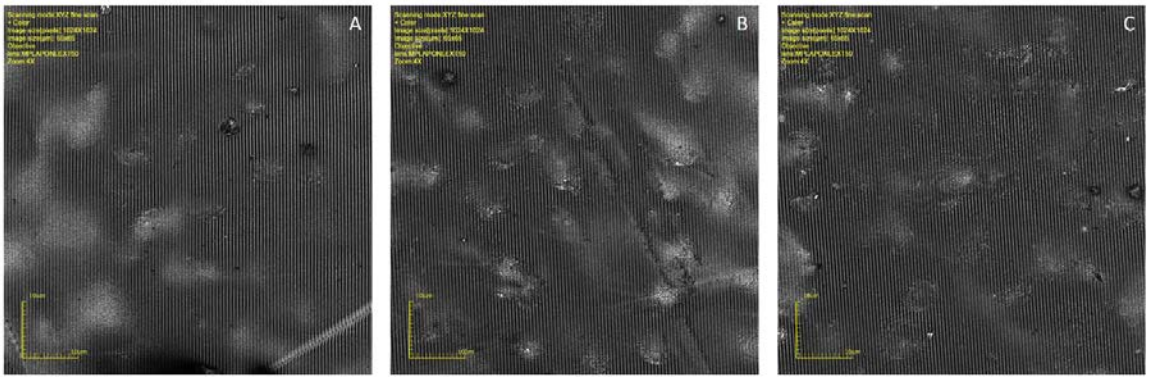

Figure 3.7. LEXT images of patterned membranes modified with varying concentrations of aqueous PEGDE solutions: 0 wt% (A), 5 wt% (B), 15 wt% (C). Common image scale is 65 μm × 65 μm. The images were produced from the 50x objective with a 4x optical zoom. The scale bar in each image is 10 μm (y-direction) × 10 μm (x-direction).

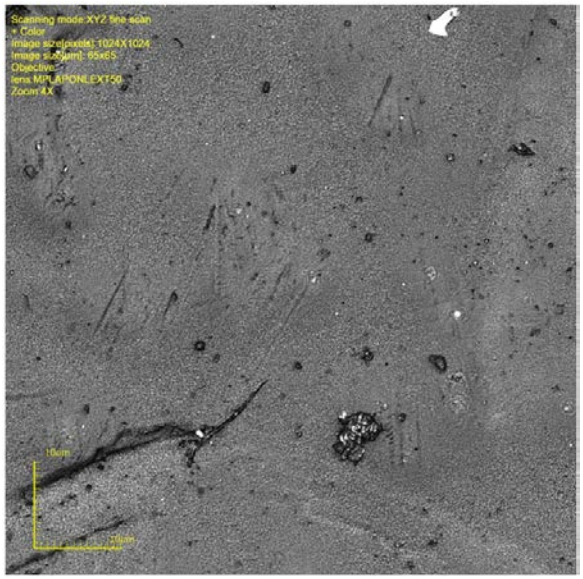

Figure 3.8. A 65 μm × 65 μm image of an unmodified membrane surface produced by the LEXT from the 50x objective with a 4x optical zoom. The scale bar is 10 μm (y-direction) × 10 μm (x-direction).

3.3.1.2 Chemical Modification

PEGDE was chosen to modify the surface chemistry of the membranes because it is available commercially, and its use for modification of polyamide surfaces has been shown to be relatively simple [27, 196]. The epoxide ring opening reaction is a standard reaction between an epoxide group of PEGDE and an unreacted carboxyl group on the polyamide selective layer surface. ATR-FTIR spectroscopy was done to characterize the membrane before and after reaction with PEGDE. The PEGDE reactant in this study has an average of 8-9 ethylene oxide repeat units per molecule; therefore, changes were expected in the absorbance peaks assigned to methylene stretching in the wavenumber region from 2800 to 2900 cm^{-1}. **Figure 3.9** shows the spectra of membranes modified by PEGDE in the wavenumber region of interest. The increase in peak heights at

approximately 2870 cm^{-1} and 2925 cm^{-1} indicate an increase in -CH_2- bonds, consistent with adding PEG onto the surface.

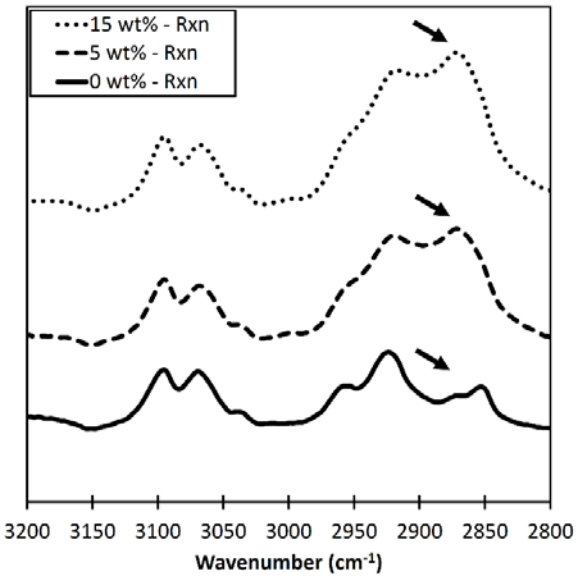

Figure 3.9. ATR-FTIR spectra at a common scale for membranes modified by PEGDE only. Labels with percentages correspond to the varying concentrations of aqueous PEGDE reaction solutions used.

Additional evidence that the reaction worked would be the appearance of an absorbance peak assigned to the PEG ether group (C-O-C) in the ATR-FTIR spectrum. However, the base polyamide membrane has an absorbance peak in the same region of the PEG ether group (~1070 cm^{-1}). This absorbance corresponds to the C-C aromatic stretching of the polyamide layer [27]. Therefore, to determine if chemical modification was successful, changes in the absorbance peak heights of the PEG ether peak/C-C aromatic stretching peak to the C-C aromatic stretching peak of the polyamide layer at ~1150 cm^{-1} [27], which does not change with the addition of PEG, were quantified. The expectation for a successful reaction is that this absorbance ratio will increase when PEGDE is added to the membrane surface because the peak at ~1070 cm^{-1} will increase

due to the incorporation of the ether groups [27]. **Figure 3.10** shows the dependence of the ratio of absorbance peak height at 1072 cm^{-1} to 1149 cm^{-1} on PEGDE weight percent for the reaction only membranes. As expected, the absorbance ratio increased with increasing PEGDE reaction concentration due to the presence of the PEG ether peaks on the membrane surface. This further validates a successful reaction of PEGDE onto the polyamide membrane surface.

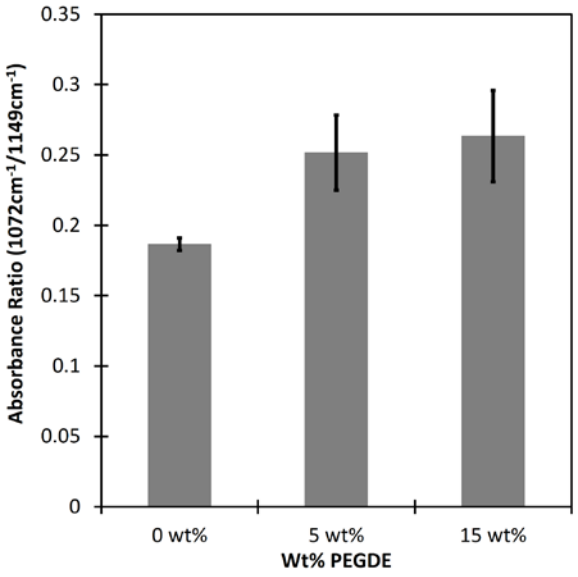

Figure 3.10. Absorbance ratio of the 1072 cm^{-1} peak to the 1149 cm^{-1} peak from ATR-FTIR data for membranes modified by PEGDE only. The x-axis corresponds to the concentration of aqueous PEGDE reaction solutions used for chemical modification. The peak at 1072 cm^{-1} corresponds to the C-O stretching of the PEG ether group and the C-C aromatic stretching of the polyamide layer. The peak at 1149 cm^{-1} corresponds to the C-C aromatic stretching of the polyamide layer. The error bars represent one standard deviation from at least 3 different membrane samples.

To further support the chemical reaction was successful, static water contact angle measurements were taken for membranes before and after modification with PEGDE. **Figure 3.11** shows the results for the reaction only membranes modified with PEGDE

solutions having different concentrations. The average water contact angle decreased from 42.3° ± 3.9° (0 wt%), to 33.1° ± 4.0° (15 wt%). While the average values for water contact angle are not very different, there does appear to be a slight increase in hydrophilicity when PEGDE is reacted onto the membrane surface based on the decrease in the average water contact angle values.

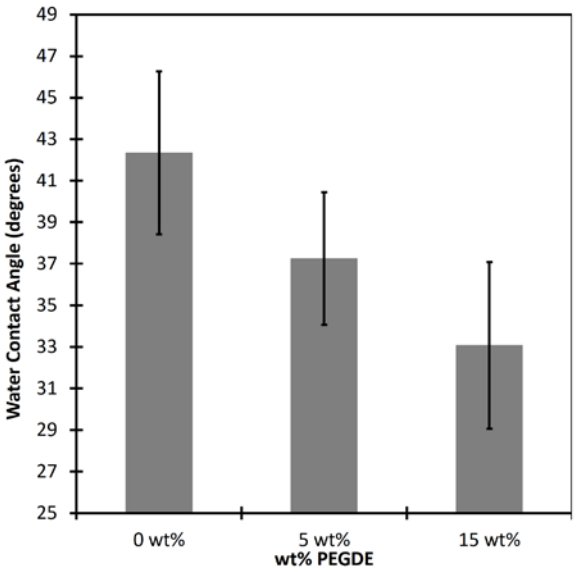

Figure 3.11. Water contact angle measurements of the reaction only membranes modified with 0 wt%, 5 wt%, and 15 wt% PEGDE solutions. The error bars represent one standard deviation among at least 9 data points.

3.3.2 Membrane Performance Testing

3.3.2.1 Solution Flux and Salt Rejection

An aqueous solution of magnesium sulfate was used to challenge the membranes to ensure there was no damage to the polyamide selective layer after patterning/pressing and/or chemical modification. The manufacturer (GE) specifies a minimum magnesium sulfate rejection of 95% for the HL membrane series. **Figure 3.12** shows the results for solution flux and salt rejection as a function of PEGDE reaction concentration for the

three types of membranes. The solution flux was not affected significantly by the thermal embossing process used to pattern the membranes. A multiple mean hypothesis test showed that only the 0 wt% reaction – 5 wt% patterned and 0 wt% reaction – 15 wt% reaction membranes are considered statistically different at 95% confidence. To further support this finding, the pure water flux of a pristine membrane was measured, a 15 wt% aqueous glycerol solution (used by manufacturers as a structure preserving agent) was applied to the membrane, the membrane was pat dried, patterned, and the pure water flux was tested again. **Figure 3.13** shows that the flux did not change. These results strongly support my claim that the patterning process does not damage the membrane.

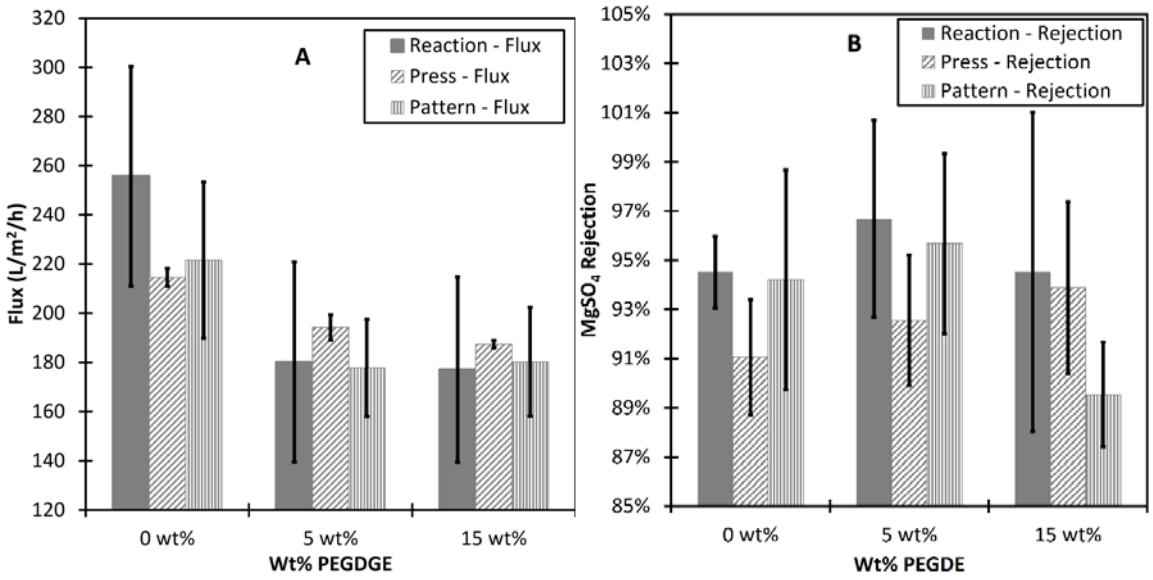

Figure 3.12. Solution flux [LMH] (A) and magnesium sulfate rejection [%] (B) versus weight percent of aqueous PEGDE solutions for the three types of membranes (reaction only, pressed with flat silicon wafers, and patterned). The feed was a 2000 ppm magnesium sulfate solution. The pressure applied to the feed side was 8.6 barg, the solution temperature was 22-23°C, the cross flow velocity was 3.0 ± 0.2 m/s, and the membrane area tested was 5.6 cm^2, with patterning on 62% of this area. The flow angle used between the solution flow and the membrane patterns was 0° (parallel). The error bars represent one standard deviation among 3 membrane samples.

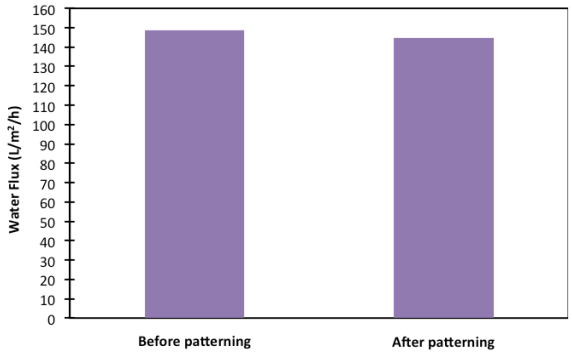

Figure 3.13. Pure water flux data for GE HL membrane before and after patterning. The same exact membrane was used for these measurements. A 15 wt% glycerol solution was applied to the membrane in between the tests and before patterning occurred.

However, the average flux values of each membrane type do decrease with increasing PEGDE concentration used to modify membranes chemically. This result is consistent with the added resistance to flow created by the addition of the PEGDE layer. One potential contributing factor to the measurement uncertainties is that samples were prepared from different membrane sheets. Membranes were purchased from a vendor (Sterlitech) in 30.5 cm × 30.5 cm flat sheets. No specifications were given from where on the commercial membrane roll these sheets were cut (e.g., middle versus edge sections).

The data shown in **Figure 3.12B** show no effect of thermal embossing on the salt rejection of the membrane. A multiple mean hypothesis test showed that all results were considered statistically the same at 95% confidence (p-value = 0.292). This result suggests that the polyamide selective layer is unimpaired by thermal embossing, consistent with the flux data. With the exception of the patterned, 15 wt% PEGDE sample, PEGDE modification does not appear to affect salt rejection. Since NF membranes rely on a combination of Donnan exclusion and size exclusion to reject salts

[205], it was expected that replacement of negatively charged carboxyl groups by neutral PEG groups would diminish the Donnan exclusion effect of the membrane leading to lower salt rejection. However, this does not appear to be the case. The GE HL membrane has a reported molecular weight cutoff of 150-300 Da. Given the higher molecular weight of PEGDE (500 Da), it may be restricted to react with carboxyl groups on the outer membrane surface only. Therefore, unreacted carboxyl groups in the subsurface region of the selective layer may remain and contribute to salt rejection through Donnan exclusion.

3.3.2.2 Sodium Alginate Fouling

Sodium alginate was used as a model biopolymer to foul the membranes during cross-flow filtration. Biopolymers can be a component of the conditioning film on a membrane surface prior to biofilm formation. Thus, if biopolymer adsorption/attachment to the membrane is reduced/eliminated, then bacteria attachment and subsequent growth into a biofilm can be reduced/eliminated. A 90° flow angle was used to see the full effect of fouling reduction caused by the patterning, as others have seen this orientation to be most effective [102, 103]. Also, a lower cross-flow velocity of 1.0 m/s was employed to better evaluate the effect of the patterning, since foulants are more likely to accumulate on the membrane surface at lower cross-flow velocities [206, 207]. It was hypothesized that combining the membrane patterning with the chemical modification would yield membranes with better fouling resistance than those prepared by either method alone.

Figure 3.14 shows the flux versus time graphs for each membrane type (reaction only, pressed with flat silicon wafers, and patterned) with each PEGDE reaction concentration. **Figure 3.14D** also shows a comparison between the three membrane types

(reaction only, pressed, and patterned) with no chemical modification (0 wt%). **Figure 3.15** summarizes the average flux reduction for all membranes based on the integrated flux over a 2 h period. Cumulative permeate volumes were used to calculate average flux values over the 2 h test period for all membrane types. These values were normalized by the initial flux values and converted to percentage average flux reduction. The approximate initial starting flux for each membrane tested was 120 $L/m^2/h$ to enable direct comparison of results. **Figures 3.14A and 3.15** show that the unmodified membrane (0 wt%) had the largest decrease in average flux values from 120 $L/m^2/h$ to 78 $L/m^2/h$. The effect of chemical modification alone had a positive impact on the resistance to fouling by reducing the flux decline. In both cases (5 and 15 wt%), the average flux declined from 121 $L/m^2/h$ to about 110 $L/m^2/h$. Statistically there was no difference in flux decline between membranes modified by the 5 and 15 wt% PEGDE solutions. The positive impact of the PEGDE chemical modification is attributed to the strong hydration layer that forms around PEG, as well as the increase in hydrophilicity of the membranes (**Figure 3.11**). The data show a decrease in the average water contact angle as the PEGDE reaction concentration increases, indicating an increase in membrane hydrophilicity with PEGDE addition. These results indicate that chemical modification alone is an effective method at reducing fouling, but there is still opportunity for improvement even with this simple model foulant solution.

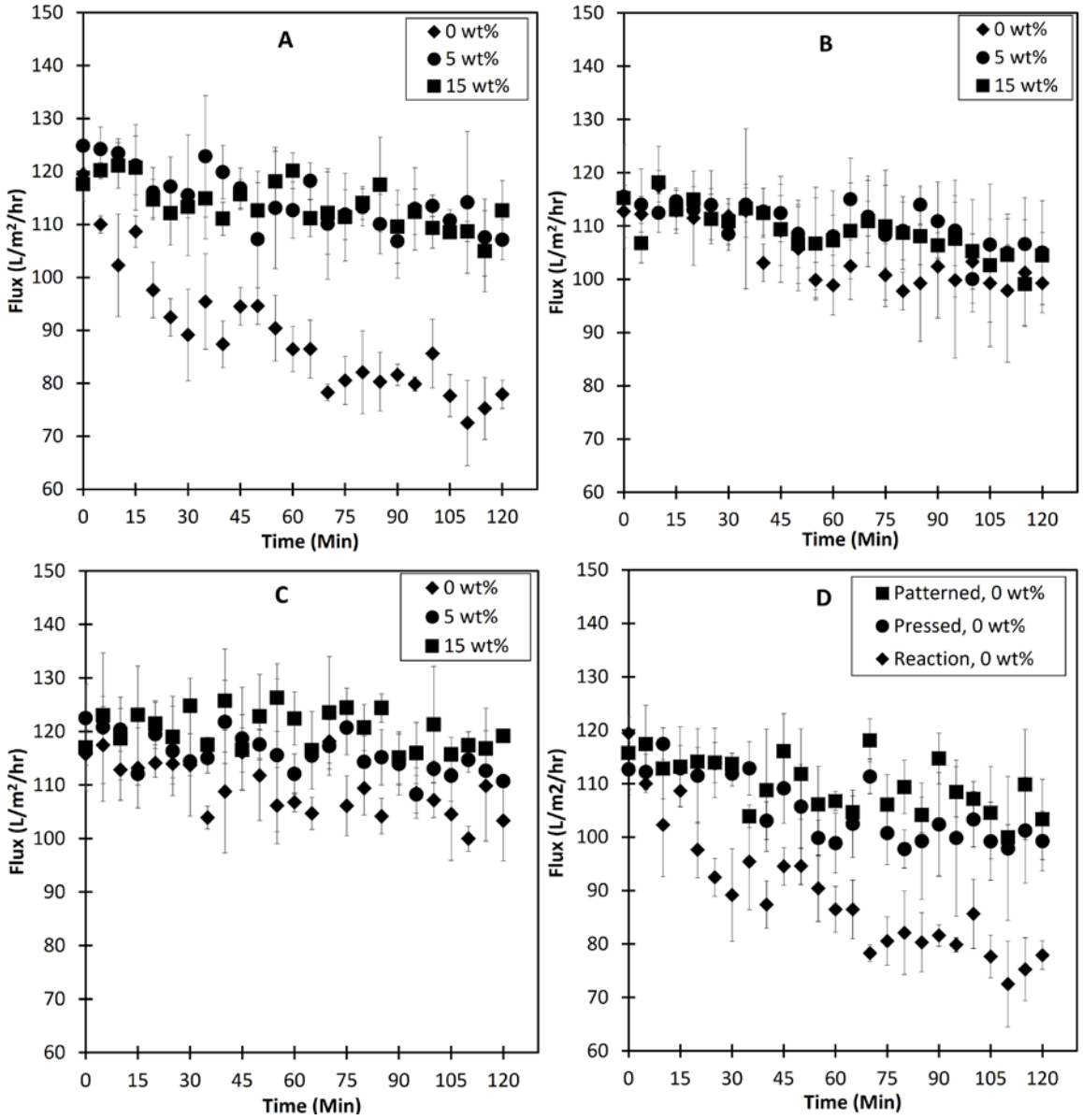

Figure 3.14. Sodium alginate fouling tests for membranes modified by PEGDE reaction only (A), membranes pressed with a flat silicon wafer (B), patterned membranes (C), and each membrane type with no chemical modification (D). A, B, and C includes data for membranes modified with the aqueous PEGDE solutions (0, 5, and 15 wt%). The feed solution comprised 30 mg/L sodium alginate, 10 mM NaCl, and 1 mM $CaCl_2$. The temperature was 22-23°C, the cross-flow velocity was 1.0 ± 0.1 m/s, and tested membrane area was 5.6 cm^2, with patterning on 68% of this area. The approximate initial starting flux was 120 LMH for all samples. The flow angle used between the solution flow and the membrane patterns was 90° (perpendicular). The error bars represent one standard deviation among 3 membrane samples.

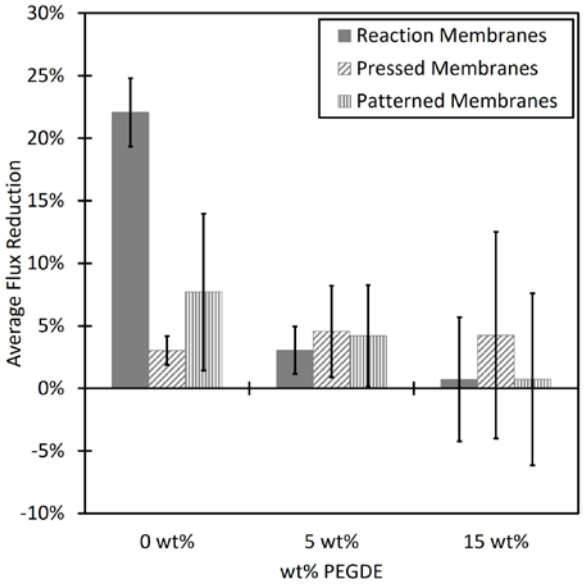

Figure 3.15. Average flux reduction for all membranes based on the integrated flux over a 2 h period.

Figures 3.14B and 15 show the results for the membranes pressed by flat silicon wafers and modified with PEGDE. The purpose of these experiments was to see if thermal compression of the membranes made a meaningful contribution to fouling reduction. As can be seen in **Figure 3.14D**, the unmodified, pressed membrane (0 wt%) had a significant reduction in fouling rate from 113 L/m^2/h to 100 L/m^2/h compared to the unmodified, non-pressed membrane. The cause for this result can be attributed to the reduction in membrane surface roughness as a result of pressing [100, 101, 202]. **Figure 3.16** shows the results obtained from the LEXT for surface roughness on a 0.004 mm^2 membrane area using a 50x objective with a numerical aperture of 0.95. The pressed membranes showed a significant decrease in the RMS height (which indicates roughness) of the surface compared to the reaction only membranes. The surface roughness data indicate that membranes were flattened by pressing, resulting in a membrane that has an

increased fouling resistance. Statistically, there was no difference among the pressed membranes (unmodified and PEGDE modified) in terms of membrane fouling (**Figure 3.15**). This result indicates that there may be a long-term benefit of reducing membrane surface roughness via compression on membrane fouling resistance.

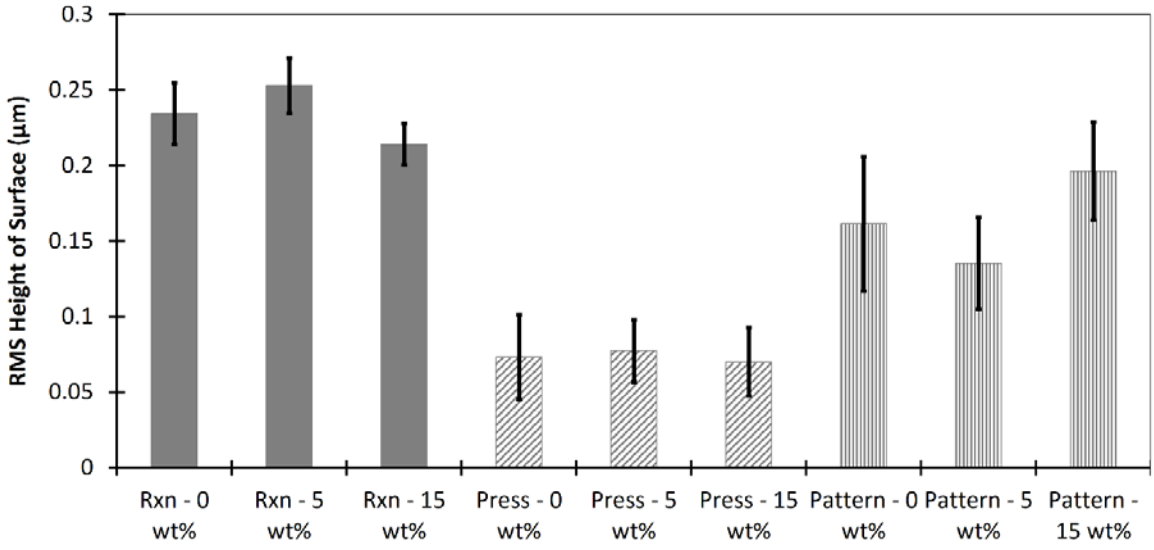

Figure 3.16. RMS height of the membrane surfaces. The results were obtained using the LEXT with the 50x objective at a 4x optical zoom. The membrane area studied per image was 0.004 mm^2. The error bars represent one standard deviation among at least 3 membrane samples.

Figure 3.14C shows the results of membrane fouling with alginate on the patterned membranes. The surface patterning alone had a similar effect to the pressing alone, having a flux decline from 117 $L/m^2/h$ to 103 $L/m^2/h$, as can be seen in **Figure 3.14D**. **Figure 3.16** shows that the membrane roughness for the patterned membranes was higher than the pressed membranes, which is not surprising since patterning introduces ordered “roughness” to the surface. Despite this higher roughness than pressed membranes, the patterned membranes performed as well or better during fouling

challenges. On average, the patterned membranes had slightly lower roughness than non-pressed membranes. While there may have been some benefit from reducing the membrane surface roughness, the introduction of ordered roughness on the membrane surface appears to have the added benefit of disrupting the hydrodynamic boundary layer during flow over the membrane.

Figure 3.14C also shows the added benefit of combining patterning with changes to the surface chemistry of the membrane. Statistically, there was no difference between patterned and pressed membranes in terms of membrane fouling; however, there does appear to be a slight difference in average membrane fluxes, with patterned membranes showing less average flux decline than pressed samples (**Figure 3.15**). Patterned membranes that were modified using 15 wt% PEGDE maintained a constant flux of approximately 120 LMH during the 2 h test. **Figure 3.17** shows a patterned membrane modified using 15 wt% PEGDE was also tested for 7 h with an initial flux of 90 LMH and saw essentially no flux decline as well. These results suggest that combining nanopatterning with chemical modification on a membrane surface can lead to a membrane with lower propensity to foul than by using either method alone.

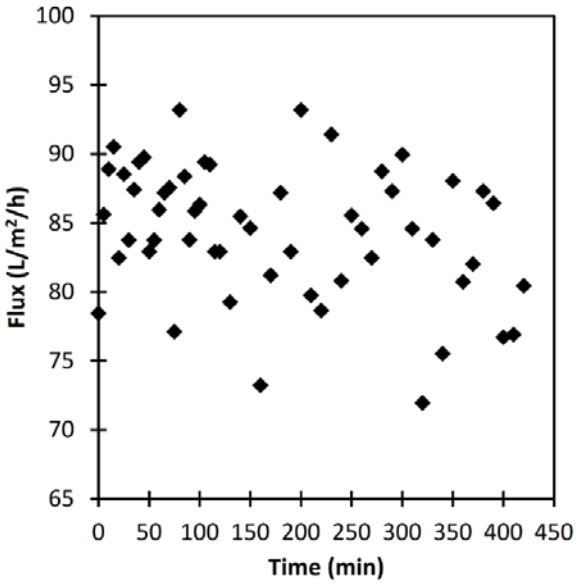

Figure 3.17. Sodium alginate fouling tests for a patterned membrane modified with a 15 wt% aqueous PEGDE solution. The feed solution comprised 30 mg/L sodium alginate, 10 mM NaCl, and 1 mM $CaCl_2$. The temperature was 22-23°C, the cross-flow velocity was 1.0 ± 0.1 m/s, and tested membrane area was 5.6 cm^2. 68% of the membrane testable area was patterned. The approximate initial starting flux was 90 LMH. The flow angle used between the solution flow and the membrane patterns was 90° (perpendicular).

3.4 Conclusions

A method was developed for combining physical nanopatterning and chemical modification of a polyamide thin-film composite nanofiltration membrane surface to reduce membrane fouling by alginate without hindering membrane flux or salt rejection. The patterned membrane surface consisted of a line and groove topography that was applied to the membrane by a thermal embossing process. Chemical modification was done using a PEG-based coating. Whereas the unmodified membranes had an average flux reduction of 22% based on the integrated flux over the 2 h test period, the chemically modified, patterned membranes had 0-8% flux reduction depending on the degree of chemical modification. The enhanced fouling resistance of the chemically modified,

patterned membranes was attributed to increases in surface hydrophilicity and water hydration, as well as the improved flow dynamics across the membrane surface caused by the patterns. Ongoing work is exploring a variety of nanopatterns and alternate chemical modification strategies, as PEG has a tendency to degrade when exposed to cleaning solutions.

3.5 Acknowledgements

I was supported by a National Science Foundation Graduate Research Fellowship under Award DGE-1246875. I thank the National Science Foundation for financial support under NSF award CBET-1534304. I thank Clemson University for funding through the Tiger Grant Award program. I thank Dr. Terri Bruce and Ms. Rhonda Powell of the Clemson Light Imaging Facility for help and discussions with LEXT measurements. I thank the Clemson Machining and Technical Services for fabrication of the custom cross-flow cell. I thank Na Li for her contribution to discussions on this work.

CHAPTER FOUR

NANOPATTERNING COMMERCIAL NANOFILTRATION AND REVERSE OSMOSIS MEMBRANES

[As submitted to Journal of Membrane Science for publication with minor revisions]

4.1 Introduction

Micrometer and sub-micrometer/nanometer sized features have been used to mitigate fouling on a variety of surfaces. Nature has inspired many biomimetic models with these antifouling surface features [105]. Sharklet™ was one of the first designs. Modeled after dermal scales on sharks, Sharklet™ was found to reduce cell attachment in marine biofouling applications and to reduce biofilm formation for biomedical applications [107-109, 113]. Coral and butterfly wings have inspired other animal-based models to mitigate fouling [119, 120]. Clover leaves, rice leaves, and lotus leaves are among the well-known plant-based models used to mitigate fouling [120-123].

Application of regular surface features to ultrafiltration and microfiltration water treatment membranes to control fouling has been studied recently [95, 96]. There are predominately two methods that have been used to pattern membranes: lithography and solution casting. Wardrip et al. used a maskless UV-lithographic patterning technique to generate striped patterns of polymer coatings on ultrafiltration membrane surfaces to mitigate bacteria fouling [124]. Maruf et al. imparted nanometer sized line and groove patterns through nanoimprint lithography (NIL) on polyethersulfone (PES) ultrafiltration membranes to mitigate colloidal and protein fouling [103, 152, 153]. NIL also has been used to apply micrometer and nanometer sized domes onto PES membranes to mitigate particle fouling [137] and to apply nanometer sized line and groove patterns on polytetrafluoroethylene membranes for membrane distillation

(MD) [154]. Lee, Park, and colleagues have applied micrometer sized prism and pyramid patterns through solution casting onto polyvinylidene fluoride (PVDF) membranes to mitigate particle fouling and wastewater fouling [138-140]. Millimeter sized spacer imprints were imparted onto a PVDF membrane to reduce fouling in wastewater treatment and MD seawater treatment [126, 127]. Micrometer sized patterns have been solution cast onto PES membranes to reduce yeast fouling [145]. Even hollow fibers have been patterned on both the inner skin [147] and outer skin [148-150] to reduce fouling. Most recently, a continuous roll-to-roll process was developed to apply a nanometer sized pattern onto PES ultrafiltration membranes [208].

Despite the upturn in membrane patterning research, nano-patterned thin-film composite (TFC) membranes have been studied only sparingly. TFC membranes used for water treatment typically have a polyamide selective layer formed by interfacial polymerization of *m*-phenylenediamine (mpd) or piperazine and 1,3,5-benzenetricarbonyl trichloride (a.k.a., trimesoyl chloride (tmc)). As pointed out by Ding et al., TFC membranes are a challenge to pattern due to the fragility of the polyamide layer [95]. To get around this issue, Maruf et al. and ElSherbiny et al. produced patterned TFC membranes by performing interfacial polymerization on top of PES ultrafiltration membranes that were pre-patterned using NIL [146, 198, 209, 210]. Contrary to claims that NIL cannot be applied directly to TFC membranes [209], I reported in Chapter 3 on the direct nano-patterning of a polyamide TFC nanofiltration membrane (GE HL series) combined with surface chemistry to reduce alginate fouling [28]. By limiting the local strain−defined by the height-to-pitch of the pattern−to values below the strain at the onset of cracking for crosslinked polyamide thin films [204, 211], I successfully patterned this TFC membrane. I did not observe any fracturing of the polyamide surface layer, nor was there evidence from flux and salt rejection studies to suggest that the selective layer was impaired.

Motivated by my initial success and the differing views on the utility of NIL for patterning polyamide TFC membranes, I carried out a study to better understand what factors control patternability. The goal of this study was to develop a set of heuristics that can be used in NIL to nano-pattern any TFC polyamide membrane. Towards this goal, I expanded upon my earlier study by applying a line and groove nanometer sized pattern onto thirteen commercial nanofiltration and reverse osmosis membranes. I studied numerous variables to investigate the roles played by membrane chemistry, surface properties, mechanical properties, performance properties, and pore filler on pattern peak heights for each of the nanofiltration and reverse osmosis membranes.

4.2 Materials and Methods

4.2.1 Materials

The following membranes were purchased from Sterlitech: GE DK, GE Duracid KH, GE HL, GE PW, GE SG, Nanostone NF4, Synder NFG, Toray UTC-82V, TriSep ACM4, TriSep X201, and TriSep XN45. The following membranes were kindly provided by Dow Water and Process Solutions: Dow BW30XFR, Dow NF270, and Dow SW30HRLE. Membranes were used as received except where stated.

The following chemicals were purchased from Sigma-Aldrich and used as received: 1-butanol (99+%), glycerol (99.5%), magnesium sulfate (anhydrous, ≥ 99.5%), nitric acid (aq) (70%), and silver nitrate (> 99%). The following chemicals were purchased from Acros Organics: dichloromethane (99.5%, stabilized with ethanol), diiodomethane (99+%), and ethanol (anhydrous, 99.5%). Sodium hydroxide (97+%) was purchased from Alfa Aesar. Aqueous solutions were prepared with deionized water from a Milli-Q water purification system (Millipore-Sigma).

4.2.2 Membrane Preparation

4.2.2.1 Patterning Membranes (As Received)

Silicon line and groove stamps (29 mm × 12 mm) used to pattern the membranes were purchased from LightSmyth Technologies, Inc. The stamps were specified to have a 606 nm period between peaks, a 190 nm groove depth, and a 303 nm line width. The stamping procedure is the same as reported in Chapter 3 [28]. A Carver press (AutoFour/1512H model) was used to emboss the membranes with the stamp/wafer at 45°C. The press plates were closed at 25% pump speed until the pressure (force/stamp area) was 69.5 bar. A pressure was maintained at 69.5 ± 13.9 bar for 20 min, which was found to be sufficient for patterning without damaging the stamp.

Control experiments were done to study the effect of compression alone. For the control process, a 1 cm × 3 cm flat, polished silicon wafer (Nova Electronic Materials) was used to prepare membranes for physiochemical characterization and salt rejection experiments.

4.2.2.2 Patterning Membranes (After Exchanging Humectant)

Membrane patterning also was done after replacement of the original humectants/pore fillers used by the membrane manufacturers with a known humectant. The membranes were rinsed in DI water, pat dried, immersed in a 5 to 75 wt% aqueous glycerol solution for 5 min, which was determined to be long enough for complete wetting to occur (**Figure 4.18**), pat dried, and stored in a plastic petri-dish overnight. The membranes were patterned as described in **Section 4.2.2.1**.

4.2.2.3 Polyamide Layer Isolation

The polyamide layer of each membrane studied was isolated using a technique similar to that of Coronell et al. [212]. The membranes were rinsed in DI water and pat dried prior to layer isolation. First, the polyester backing was peeled off. Next, the membrane (polyamide layer +

support) was placed on a silicon wafer with the polyamide layer face down and secured using c-clamps (MON 30841900, The Betty Mills Company, Inc., San Mateo, CA). Dichloromethane was used to rinse away the membrane support material. Approximately 4 mL of dichloromethane was pipetted onto each membrane piece and allowed to drain from the wafer during this rinse step. The clamp-silicon wafer assembly was placed into an oven at 75°C for at least 5 min. The assembly was removed from the oven, allowed to cool, and a razor blade was used to cut the polyamide layer near the clamp edges. The clamps were removed from the silicon wafer leaving an isolated polyamide layer.

4.2.3 Membrane Characterization Techniques

4.2.3.1 ATR-FTIR

Attenuated total reflectance Fourier-transform infrared spectroscopy (ATR-FTIR) was used to characterize the surface chemistry of the commercial membranes. Membranes were rinsed in DI water, pat dried, and dried under vacuum at -0.78 to -0.95 barg before analysis. The support material of each membrane was analyzed by ATR-FTIR after peeling off the membrane polyester backing. Spectra were obtained using a Thermo Scientific Nicolet iS50R FT-IR with an ATR accessory (Specac Golden Gate) equipped with a diamond ATR crystal at an approximate force of 356 N. Data were processed by OMNIC 9.3.32 software (Thermo Scientific). Each spectrum was collected at 128 scans at a resolution of 4 cm^{-1}, corrected with the ATR correction on software, and manually baseline corrected. A background of the ATR crystal was taken before each set of sample measurements. All spectra were normalized to the peak at 1240 cm^{-1}.

4.2.3.2 Scanning Electron Microscopy

Membrane top surface and cross-section morphology before and after patterning were studied using a Hitachi SU-6600 Variable Pressure Scanning Electron Microscope (SEM) or a

Hitachi S-4800 Field Emission SEM. Representative samples were rinsed in DI water and pat dried. Membranes used for cross-section imaging were cryo-cut as similarly reported [213]. The membrane and razor blade were held individually in hemostats, immersed in liquid nitrogen until the liquid nitrogen stopped boiling, removed from the liquid nitrogen, and the razor blade was used immediately to cut the membrane. Membrane pieces were attached with carbon tape to aluminum stabs and coated with gold-palladium prior to SEM measurements. The SEM measurements were performed at an accelerating voltage of 10.0 kV, a current voltage of 20.0 μA, and a magnification of 10,000x – 150,000x (top surface) or 350x - 400x (cross-section).

4.2.3.3 Atomic Force Microscopy

Atomic force microscopy (AFM) was used to observe the surface morphology of the membranes before and after patterning/pressing. Images were obtained using a Bioscope AFM (Bruker, Inc.) with NanoScope IIIa controller equipped with Nanoscope version 5.32R1 software. Silicon cantilevers (MikroMasch, Inc., HQ:NSC16/AL BS) were used as probes for the non-contact tapping mode measurements. AFM images were taken with a 256 × 256 pixel resolution over 20 μm × 20 μm at a scan rate of 0.5 Hz. The section analysis feature of the software was used to determine peak heights. The roughness analysis feature of the software was used to determine membrane surface roughness.

4.2.3.4 AFM Nano-Indentation

Young's Modulus of the membranes was determined using the AFM nano-indentation method with the same AFM and cantilever tips as **Section 4.2.3.3**. However, instead of using non-contact tapping mode, these tests required the use of contact mode. Each tip was calibrated to measure the tip sensitivity by bringing it in contact with a silicon wafer. The tip threshold was 100 nm, the scan size was 10.0 μm, and the scan rate was 1 Hz. The samples per line and the

force per line were either 16 or 32. Nanoscope Analysis v1.50 (Bruker, Inc.) software was used to analyze the data. The Sneddon (conical) model was used to calculate the Young's Modulus using the following constants: Spring Constant was 45 N/m, Tip Half Angle was 20°, Tip radius was 8 nm, and Poisson's ratio was assumed to be 0.39 for polyamide. The adhesion force was included, the minimum force fit boundary was 5%, and the maximum force fit boundary was 100%.

4.2.3.5 Ellipsometry

Multi-angle ellipsometry (Beaglehole Instruments, Picometer) was used to measure the thicknesses of dry, ethanol swollen, water swollen, and 15 wt% (aq) glycerol swollen polyamide layers isolated on silicon wafers. The incident beam was produced by a 632.8 nm He–Ne laser source. Measurements were done at incidence angles from 56° to 80° with a step size of 4°. Layer thickness was calculated by IgorPro Software version 4.09A. The reported thickness is the average of at least three membrane samples.

The dry polyamide layers were analyzed with an air–polyamide–silicon dioxide–silicon substrate multilayer model. This model was applied to fit the data based on a Cauchy model. Polyamide layer thickness and the polyamide refractive index were allowed to vary. The SiO_2 layer thickness was fixed at 1.8 nm, and the refractive indices of the other layers were fixed at air = 1.0, SiO_2 = 1.455, and silicon = 3.875.

Swelling measurements were done on the polyamide-silicon wafers placed inside a specially designed cylindrical flow cell (Beaglehole Instruments) and contacted with solvent (ethanol, water, or 15 wt% (aq) glycerol) for at least 30 min using a peristaltic pump. The swollen polyamide layers were analyzed with a solvent–polyamide– SiO_2–silicon substrate multilayer model. This model was applied to fit the data based on a Cauchy model. Polyamide

layer thickness and the polyamide refractive index were allowed to vary. The SiO_2 layer thickness was fixed at 1.8 nm, and the refractive indices of the other layers were fixed at ethanol = 1.36, 15 wt% (aq) glycerol = 1.35 [214], water = 1.33, SiO_2= 1.455, and silicon = 3.875.

4.2.3.6 Membrane Static Contact Angle Goniometry

Water and diiodomethane contact angle goniometry was performed on rinsed, pristine commercial membranes to evaluate differences in hydrophilicity and surface free energy (SFE). All static contact angles were measured using a Krüss DSA 10-Mk2 contact angle goniometer. A liquid drop (~ 3.0 µL) was placed carefully on the sample surface. The sessile drop model was used in DSA version 1.80.0.2 Drop Shape Analysis software to determine contact angle. For consistency, measurements were taken 60 s after each droplet was placed on the surface. Measurements were done at a minimum of three locations on each sample to get an average contact angle value with standard deviation.

4.2.3.7 Silver Binding Experiments

Silver ion binding was used to determine the carboxylic acid density of each membrane polyamide layer [215-217]. A 2.0 cm^2 membrane was rinsed with DI water and then the polyester backing was removed. Silver ion binding methods were adapted from Elimelech et al. [217]. Solutions of 40 µM and 1 µM $AgNO_3$ were used at both pH 6.7 and pH 10.5. Solution pH was adjusted with a 1.0 M NaOH solution and HNO_3 (70%). Each membrane was immersed in 10 mL of the 40 µM $AgNO_3$ solution for 10 min twice, using a fresh solution each time, to bind silver to the carboxylic acid groups at both solution pHs. Between each solution immersion the membrane was dried with a Kimwipe to prevent solution carryover. Each membrane was then immersed in 10 mL of the 1 µM $AgNO_3$ solution for 7 min four times, using a fresh solution each time, to rinse off unbound silver ions. Between each solution immersion the membrane was

dried with a Kimwipe to prevent solution carryover. The bound silver ions were eluted off the membrane by immersing each membrane in 5 mL of 1 wt% HNO_3 aqueous solution for 30 min. The membrane was removed and the solution was analyzed by Inductively Coupled Plasma (ICP). ICP was done by the Agricultural Service Laboratory at Clemson University. To convert the silver ion concentration in solution to carboxylic acid density in the membrane, it was assumed that the each silver ion exchanged with one sodium ion of an ionized carboxylic acid site (1:1 binding). It was assumed that the silver ions can access all free carboxylic acid groups in the polyamide films. The concentration of ionized carboxylic acid groups was determined via **Equation 4.1**:

$$[R-COO^-] = \frac{C_{Ag+} * V_{Ag+} * N_A}{A * l} \quad (4.1)$$

$[R\text{-}COO^-]$ is the ionized carboxyl acid density (number of groups per membrane volume), A is the projected surface area of the polyamide film, l is the average dry membrane polyamide layer thickness as shown in **Figure 4.14**, C_{Ag+} is the silver molar concentration measured via ICP, V_{Ag+} is the elution volume, and N_A is Avogadro's number.

4.2.4 Membrane Performance Testing

Membrane permeance and salt rejection were measured at 22-23°C using a custom cross-flow cell and testing procedures as reported in Chapter 3 [28]. A 2000 ppm $MgSO_4$ test solution was used to evaluate the integrity of the membrane selective layer after patterning/pressing. The applied pressure was 8.6 barg and permeate was allowed to flow for 50 min before sample collection. The cross-flow velocity was 3.0 ± 0.2 m/s, and the flow angle was 0° relative to the line pattern for patterned membranes.

4.3 Theory

4.3.1 Open Cell Foam Model

An open cell foam model (**Equation 4.2**) was used to calculate the effective Young's modulus (E^*) of the membrane support after filling with different glycerol solutions [203]:

$$E^* = E_0 C_1 \left(\frac{\rho^*}{\rho_0}\right)^2 \quad (4.2)$$

E_0 is the Young's Modulus of the bulk membrane material, C_1 is a constant, ρ^* is the effective density of the membrane support and ρ_0 is the density of the bulk membrane material (1.24 g/mL for polysulfone and 1.37 g/mL for PES). ρ^* was estimated by **Equation 4.3** to take into account air, glycerol, and the porous support material:

$$\rho^* = \rho_{support\ material} \times (1-\omega) + \rho_{air} \times \omega \times \frac{100-vol\%\ gly}{100} + \rho_{gly} \times \omega \times \frac{vol\%\ gly}{100} \quad (4.3)$$

ρ_{air} = 0.0012 g/mL, $\rho_{glycerol}$ = 1.26 g/mL, and ω is the membrane support porosity. Membrane support porosity was determined using **Equation 4.4** by peeling off the polyester backing layer of the membrane, rinsing out the manufacturer humectant, patting dry, measuring the dry mass (w_{dry}), filling with 1-butanol, patting dry, and measuring the wet mass (w_{wet}) [203]:

$$\omega = \frac{w_{wet} - w_{dry}}{A \times l \times \rho_{1-butanol}} \quad (4.4)$$

A is the projected membrane area, l is the membrane thickness measured by a micrometer (Digimatic Micrometer MDC-1"PX, Mitutoyo Corporation), and $\rho_{1\text{-butanol}}$ = 0.81 g/mL.

4.3.2 Painter-Shenoy Equation

For polyamide layers swollen with ethanol, the swelling ratio ($S_h = h_{wet}/h_{dry}$) was used in the Painter-Shenoy equation (**Equation 4.5**) to calculate the number of monomer units between cross-links (N) [218].

$$N = \frac{(P \times S_h)^2}{f_f \pm \sqrt{f_f^2 - f_x (P \times S_h)^3}} \quad (4.5)$$

$$f_f = \frac{1}{f} - \frac{1}{4}$$

$$f_x = \ln\left(1 - \frac{1}{P \times S_h}\right) + \frac{1}{P \times S_h} + \frac{\chi}{(P \times S_h)^2}$$

P = 1, f = 3, and χ is the Flory-Huggins parameter, as described in [218]. χ was calculated using solubility parameters (δ) for the various membrane types estimated using group contribution theory values from Painter and Coleman [219]: mpd-tmc based membranes (Dow BW30XFR, Dow SW30HRLE, Toray UTC-82V, TriSep ACM4, and TriSep X201) δ = 31.4 $MPa^{0.5}$, piperazine-tmc based membranes (GE HL, Dow NF270, Synder NFG, Nanostone NF4, TriSep XN45, and GE DK) δ = 29.5 $MPa^{0.5}$, polysulfonamide membrane (GE Duracid KH) δ = 23.4 $MPa^{0.5}$, and ethanol δ = 26.2 $MPa^{0.5}$. The following χ were used for different membrane types with ethanol as the solvent: mpd-tmc based membranes χ = 0.973, piperazine-tmc based χ = 0.602, mpd-piperazine-tmc based membrane (GE SG) χ = 0.788 (taken as the average of the mpd-tmc and piperazine-tmc values since composition is unknown), and polysulfonamide membrane χ = 0.519.

4.3.3 Owens-Wendt Method

Surface free energy (SFE) was calculated using the Owens-Wendt method [173, 174]. **Equation 4.6** was used to calculate the SFE of each membrane:

$$\gamma_s = \gamma_s^d + \gamma_s^p \tag{4.6}$$

γ_s is the SFE of the membrane, γ_s^d is the dispersion component of the SFE of the membrane, and γ_s^p is the polar component of the SFE of the membrane. Two liquids with different surface free energy components were used to determine the dispersion and polar components of the SFE. Using the SFE values (total, polar, and dispersion) for each fluid and the respective contact angles of each fluid on the membranes, **Equations 4.7 and 4.8** were used to calculate the dispersion and polar components of the membrane SFE [174].

$$\sqrt{\gamma_s^d} = \frac{\gamma_d(\cos\theta_d + 1) - \gamma_w(\cos\theta_w + 1)\sqrt{(\gamma_d^p/\gamma_w^p)}}{2\left(\sqrt{\gamma_d^d} - \sqrt{\gamma_d^p(\gamma_w^d/\gamma_w^p)}\right)} \quad (4.7)$$

$$\sqrt{\gamma_s^p} = \frac{\gamma_w(\cos\theta_w + 1) - 2\sqrt{\gamma_s^d\gamma_w^d}}{2\sqrt{\gamma_w^p}} \quad (4.8)$$

γ_d is the SFE of diiodomethane (50.8 mJ/m^2) [175], γ_d^d is the dispersive component of the diiodomethane SFE (49.5 mJ/m^2) [175], γ_d^p is the polar component of the diiodomethane SFE (1.3 mJ/m^2) [175], γ_w is the SFE of water (72.8 mJ/m^2) [175], γ_w^d is the dispersive component of the water SFE (21.8 mJ/m^2) [175], γ_w^p is the polar component of the water SFE (51 mJ/m^2) [175], θ_d is the diiodomethane contact angle, and θ_w is the water contact angle.

4.4 Results and Discussion

4.4.1 Patterning As Received Membranes

All thirteen commercial RO/NF membranes were patterned as received. In addition, two UF membranes used as representative membrane supports, GE PW and Nanostone PS20, were patterned as received. **Table 4.1** shows the patterned peak heights determined by AFM section analysis. Despite the many similarities among the polyamide TFC membranes, and somewhat to my surprise, not all membranes patterned the same. Some had peak heights similar to the representative membrane supports, some had peak heights much lower, and one showed no patterning at all. Based on the data, it appears that the polyamide layer offers some resistivity to patterning, especially in the piperazine-tmc based membranes.

To better understand what factor(s) may contribute to differences in pattern peaks, I first analyzed what happens to the membranes physically upon patterning. **Figures 4.1 and 4.2** show representative SEM images of pristine membrane top surfaces and cross-sections. The top surfaces of the mpd-tmc based membranes (images A-E) appear to be much rougher than those

of the piperazine-tmc based membranes (images G-L). AFM images in **Figure 4.3** and the data in **Figure 4.13** (discussed in **Section 4.4.2.2**) support this observation. The mpd-piperazine-tmc based membrane (image F) appears smoother than the mpd-tmc based membranes, indicating it may contains more piperazine than mpd in its polyamide layer. The sulfonamide-based membrane (image M) is also smoother than the mpd-tmc based membranes. All but one membrane (GE HL) appears to have a spongy cross-section. The GE HL cross-section is finger-like, most likely due to it having a PES based support (as described in **Section 4.4.2.1**). The cross-sections of the polysulfone (Psf) based membrane supports all appear spongy, but the void patterns vary widely. For example, the Dow SW30HRLE has long slanted voids in the support structure, whereas the TriSep ACM4 or XN45 membranes have a honeycomb-like support structure. Others like the Dow BW30XFR have voids in the middle of the support structure only.

Table 4.1. Membrane chemistry, support chemistry, and patterned peak heights (nm) of 13 commercial NF and RO membranes and 2 membrane supports. Error represents one standard deviation from at least 3 membrane pieces.

Membrane Chemistry	Membrane	Membrane Support Chemistry	Patterned Peak Height (nm)
MPD-TMC based	Dow BW30XFR	polysulfone	138.1 ± 33.8
	Dow SW30HRLE	polysulfone	143.2 ± 37.0
	Toray UTC-82V	polysulfone	196.2 ± 60.5
	TriSep ACM4	polysulfone	143.8 ± 31.7
	TriSep X201	polysulfone	220.3 ± 34.5
MPD-Piperazine-TMC based	GE SG	polysulfone	41.7 ± 14.7
Piperazine-TMC based	GE HL	polyethersulfone	104.8 ± 19.5
	Dow NF270	polysulfone	143.7 ± 15.3
	Synder NFG	polysulfone	43.7 ± 18.8
	Nanostone NF4	polysulfone	69.2 ± 5.9
	TriSep XN45	polysulfone	98.6 ± 32.6
	GE DK	polysulfone	17.3 ± 5.8
Sulfonamide based	GE Duracid KH	polysulfone	0.0 ± 0.0
polyethersulfone	GE PW	----------	150.1 ± 61.1
polysulfone	Nanostone PS20	----------	178.6 ± 50.1

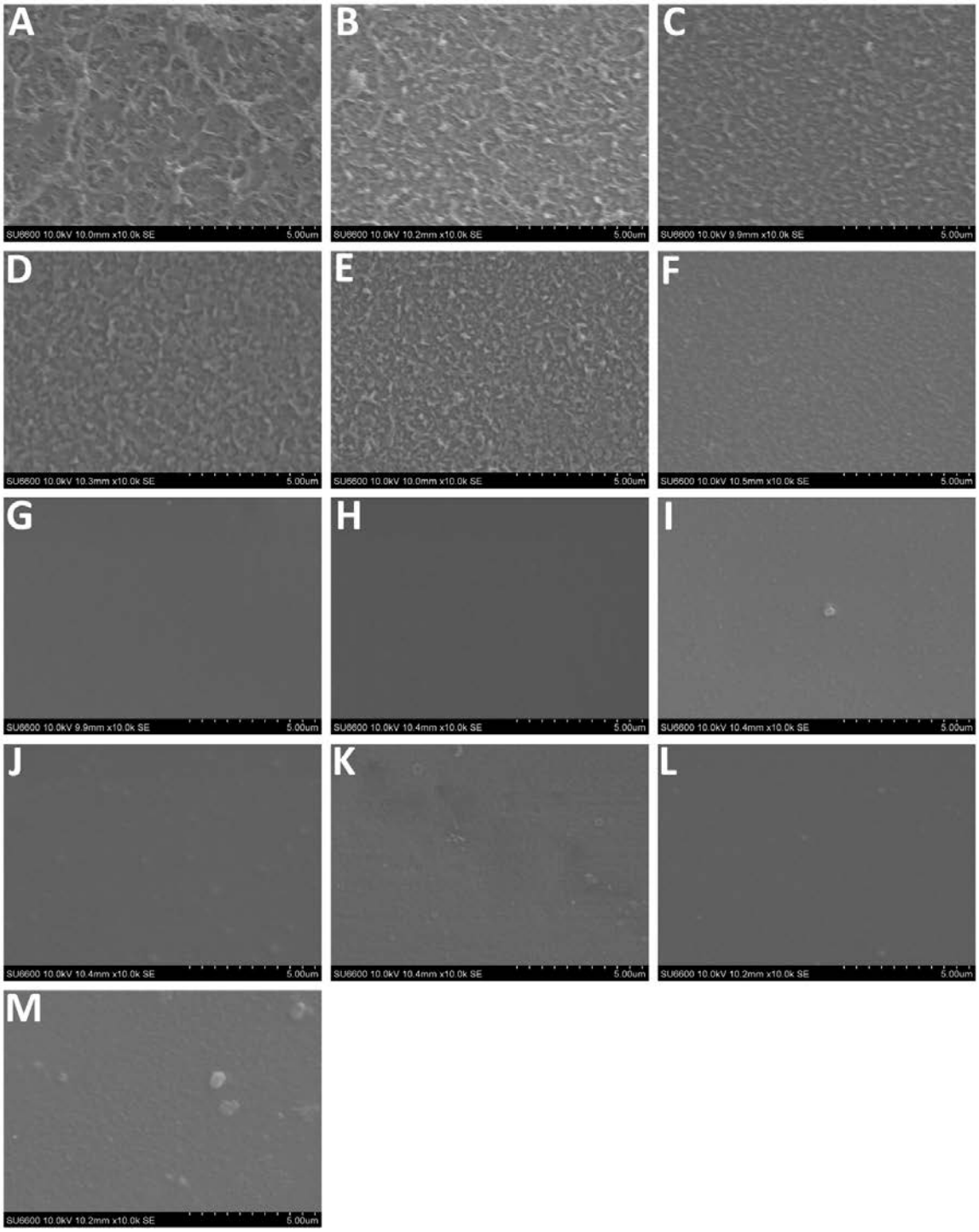

Figure 4.1. SEM images of the top surfaces of pristine (A) Dow BW30XFR, (B) Dow SW30HRLE, (C) Toray UTC-82V, (D) TriSep ACM4, (E) TriSep X201, (F) GE SG, (G) GE HL, (H) Dow NF270, (I) Synder NFG, (J) Nanostone NF4, (K) TriSep XN45, (L) GE DK, (M) GE Duracid KH. Images were taken at a 10k magnification and the common scale is 5 µm.

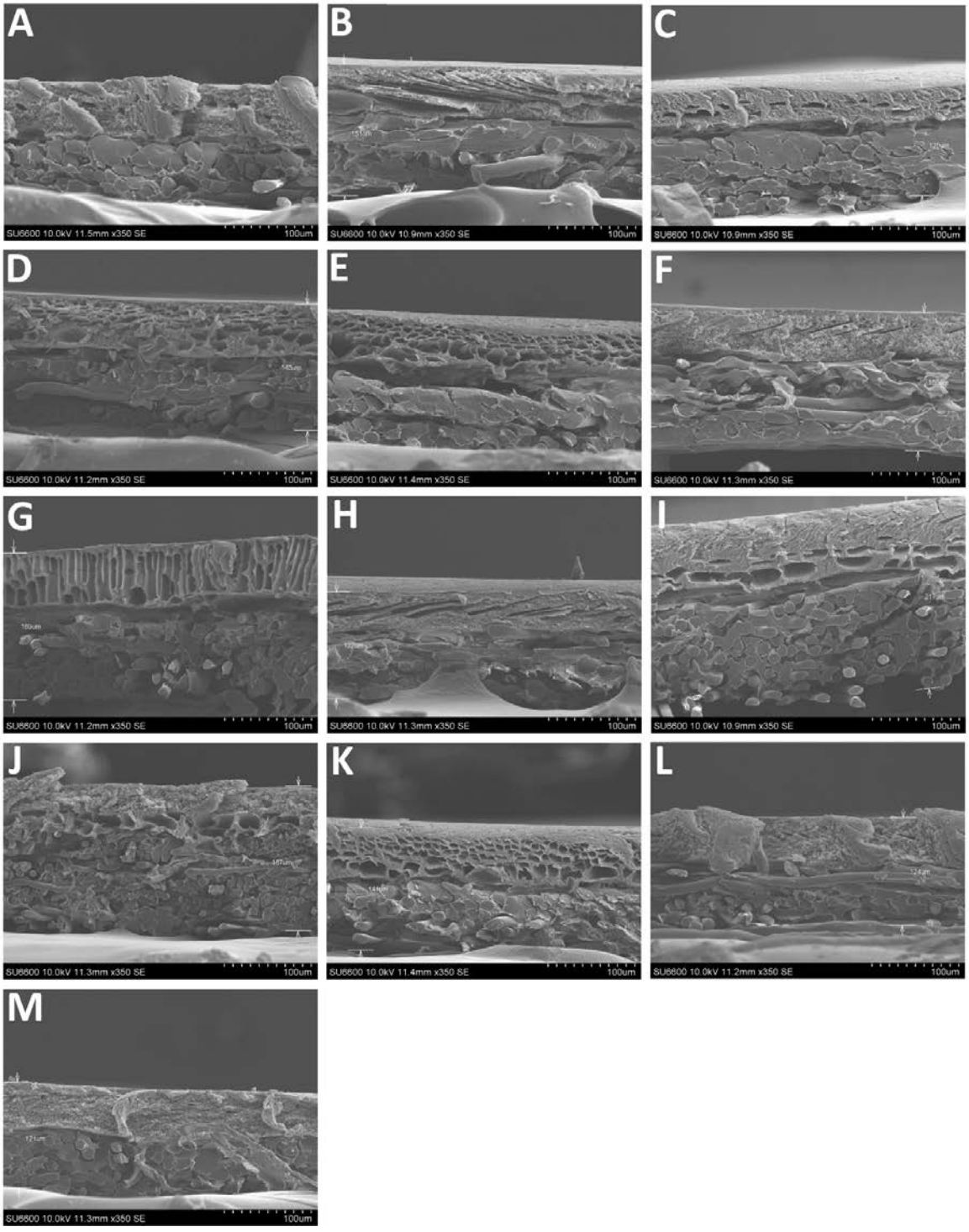

Figure 4.2. SEM images of the cross-section of pristine (A) Dow BW30XFR, (B) Dow SW30HRLE, (C) Toray UTC-82V, (D) TriSep ACM4, (E) TriSep X201, (F) GE SG, (G) GE HL, (H) Dow NF270, (I) Synder NFG, (J) Nanostone NF4, (K) TriSep XN45, (L) GE DK, (M) GE Duracid KH. Images were taken at a 350 magnification and the common scale is 100 µm.

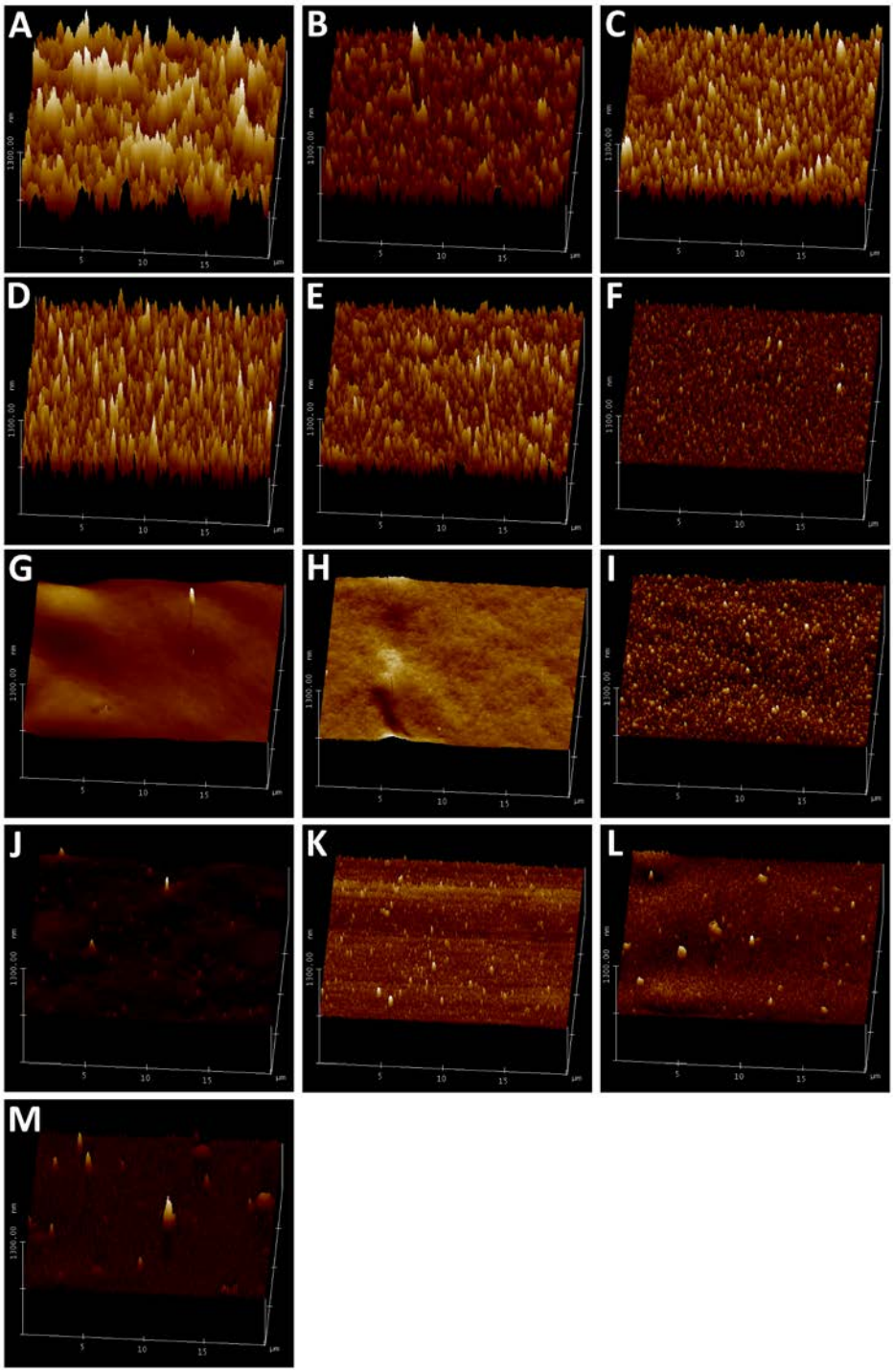

Figure 4.3. AFM images of the top surfaces of pristine (A) Dow BW30XFR, (B) Dow SW30HRLE, (C) Toray UTC-82V, (D) TriSep ACM4, (E) TriSep X201, (F) GE SG, (G) GE HL, (H) Dow NF270, (I) Synder NFG, (J) Nanostone NF4, (K) TriSep XN45, (L) GE DK, (M) GE Duracid KH. The common scale is 20 μm × 20 μm × 1300 nm.

Upon patterning, clear changes can be seen in the top surfaces of most membranes (**Figure 4.4**) and the cross-sections of all membranes (**Figure 4.5**). **Figure 4.6** shows representative AFM images that were used to calculate the peak height data in **Table 4.1**. While patterning was difficult to observe in some of the SEM images, the AFM images clearly show the extents of patterning. This discrepancy may be caused by the sample preparation required for SEM, which involved immersion in liquid nitrogen and metal sputter coating. **Figure 4.7** shows high magnification (150,000x) images of a pristine and patterned mpd-tmc based membrane (Dow BW30XFR) and a pristine and patterned piperazine-tmc based membrane (Dow NF270). The Dow NF270 membrane shows well-defined patterns after patterning. It is much more difficult to see the single period of the pattern display for the Dow BW30XFR membrane. This supports my claim that the leaf-like surface features of the mpd-tmc polyamide membranes are "molded" into the peaks of the patterned area. The membrane cross-sections all show a similar compression upon patterning. The thickness decreases and the voids in the Psf membrane supports collapsed, as would be expected with thermal embossing by NIL. The finger-like structures in the GE HL PES support appear to buckle and in some cases break. This deformation makes sense as membrane supports have been shown to undergo plastic deformation when the NIL process is below T_g [95, 203]. Interestingly, this buckling and breaking of the fingers in the support layer showed no effect on flux or rejection in the GE HL membrane in Chapter 3 [28]. Top surface and cross-section SEM images of pristine and patterned support membranes (GE PW and Nanostone PS20) are presented in **Figures 4.8 and 4.9**. These images show similar outcomes to the TFC membranes.

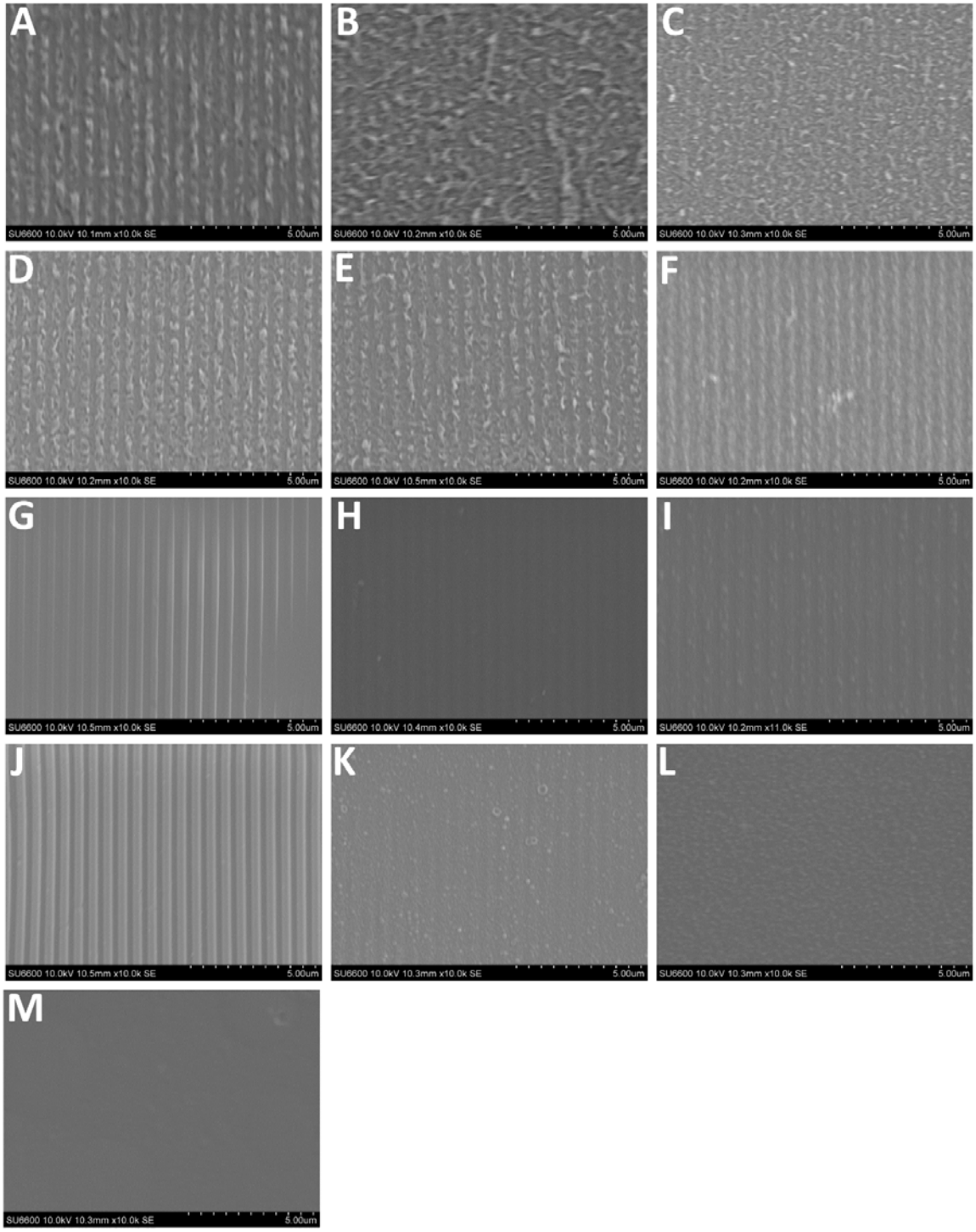

Figure 4.4. SEM images of the top surfaces of patterned (A) Dow BW30XFR, (B) Dow SW30HRLE, (C) Toray UTC-82V, (D) TriSep ACM4, (E) TriSep X201, (F) GE SG, (G) GE HL, (H) Dow NF270, (I) Synder NFG, (J) Nanostone NF4, (K) TriSep XN45, (L) GE DK, (M) GE Duracid KH. Images were taken at a 10k magnification and the common scale bar is 5 μm.

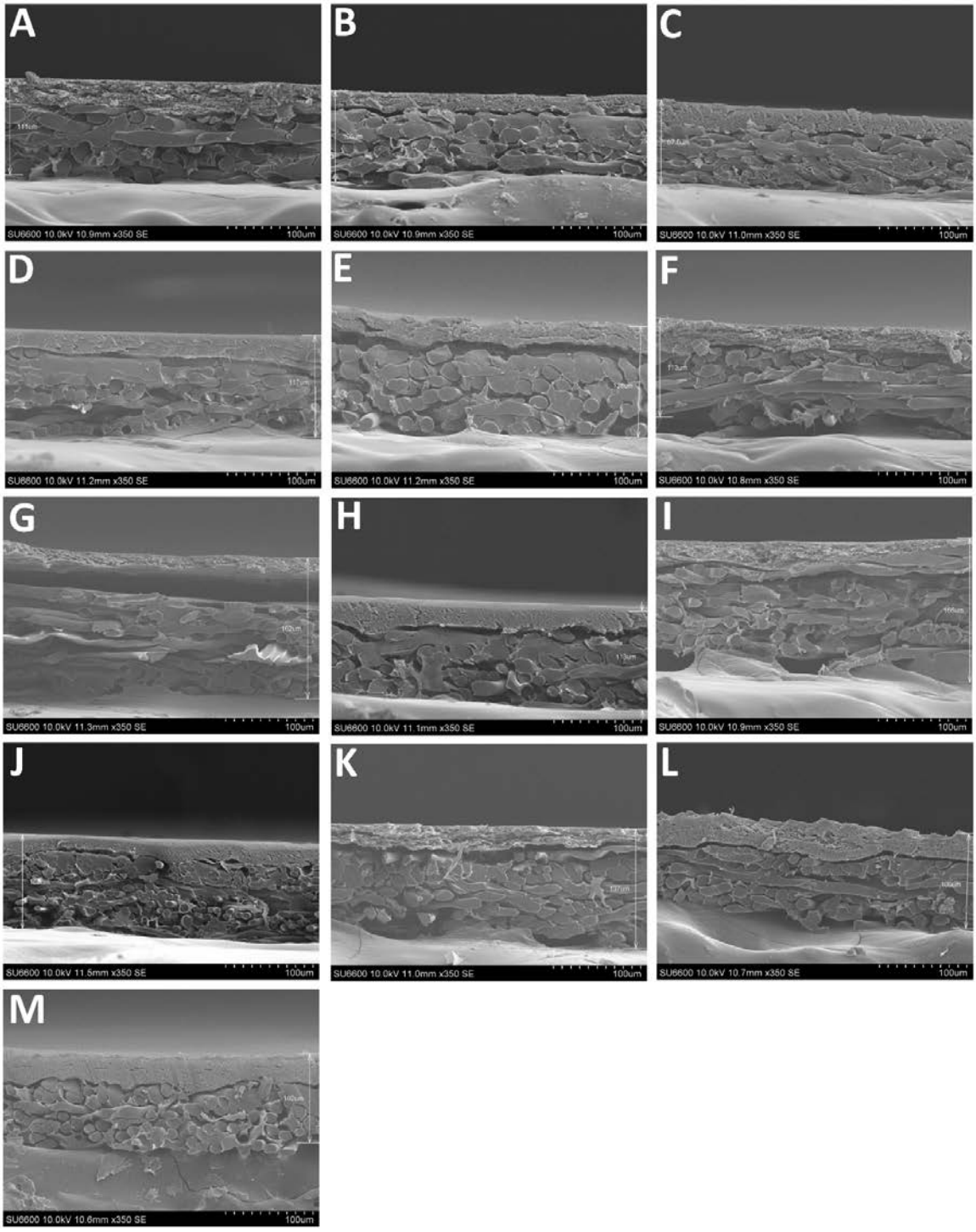

Figure 4.5. SEM images of the cross-section of patterned (A) Dow BW30XFR, (B) Dow SW30HRLE, (C) Toray UTC-82V, (D) TriSep ACM4, (E) TriSep X201, (F) GE SG, (G) GE HL, (H) Dow NF270, (I) Synder NFG, (J) Nanostone NF4, (K) TriSep XN45, (L) GE DK, (M) GE Duracid KH. Images were taken at a 350 magnification and the common scale is 100 µm.

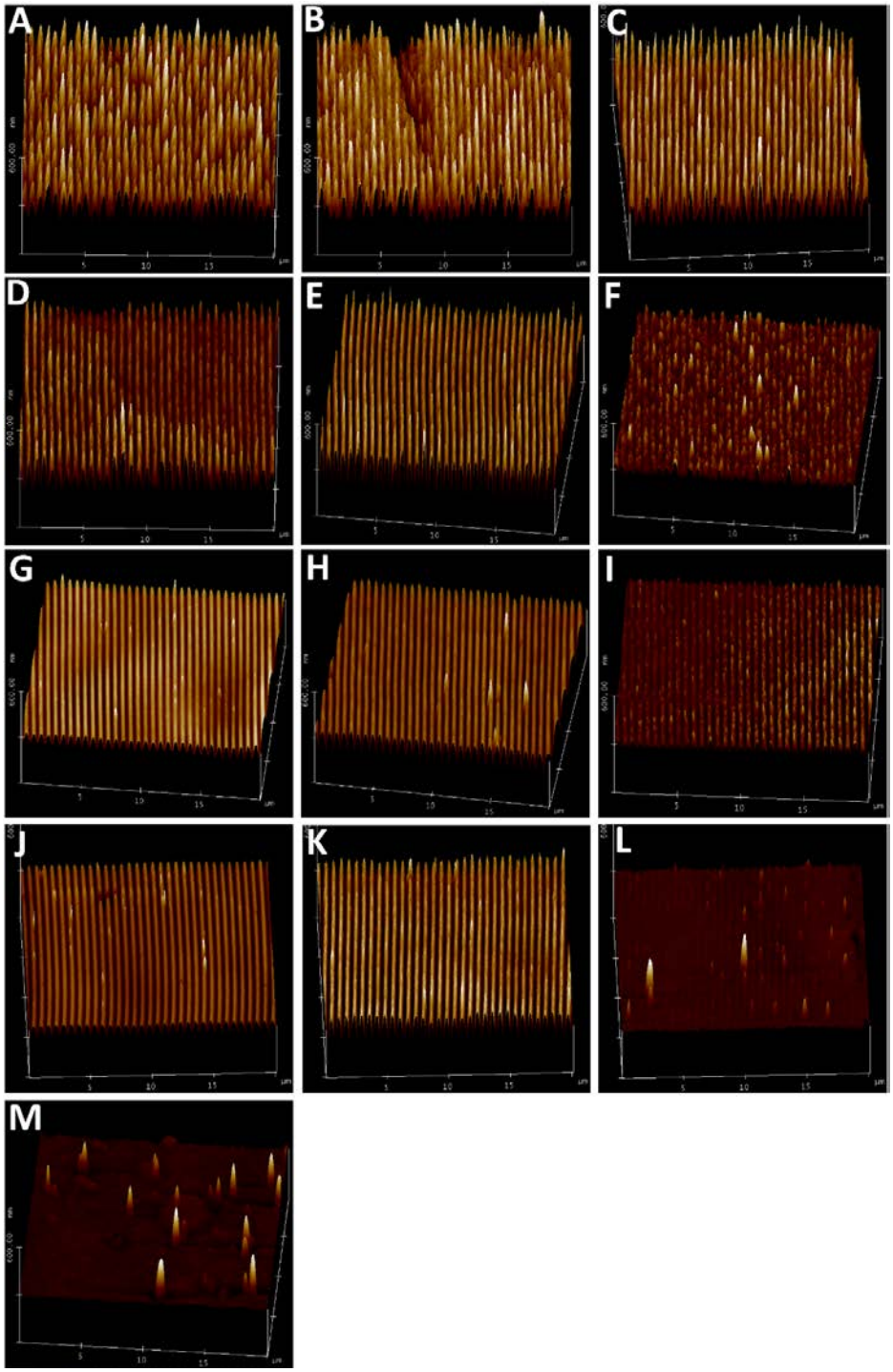

Figure 4.6. AFM images of the top surfaces of patterned (A) Dow BW30XFR, (B) Dow SW30HRLE, (C) Toray UTC-82V, (D) TriSep ACM4, (E) TriSep X201, (F) GE SG, (G) GE HL, (H) Dow NF270, (I) Synder NFG, (J) Nanostone NF4, (K) TriSep XN45, (L) GE DK, (M) GE Duracid KH. The common scale is 20 μm × 20 μm × 600 nm.

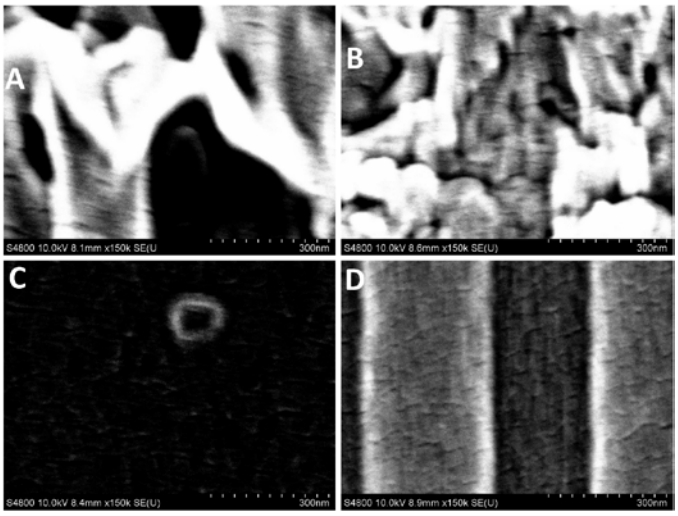

Figure 4.7. SEM images of the top surface of (A) pristine Dow BW30XFR (B) patterned Dow BW30XFR (C) pristine Dow NF270, and (D) patterned Dow NF270. Images were taken at a 150,000 magnification and the scale bar represents 300 nm.

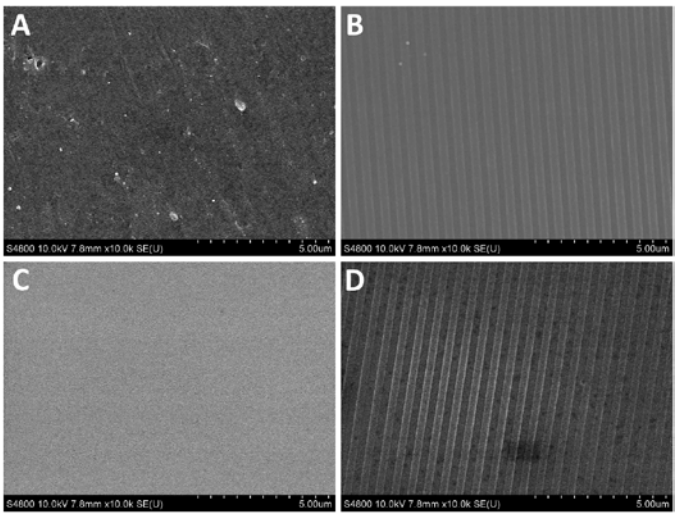

Figure 4.8. SEM images of the top surfaces of (A) pristine Nanostone PS20, (B) patterned Nanostone PS20, (C) pristine GE PW, and (D) patterned GE PW. Images were taken at a 10,000 magnification and the scale bar represents 5 µm.

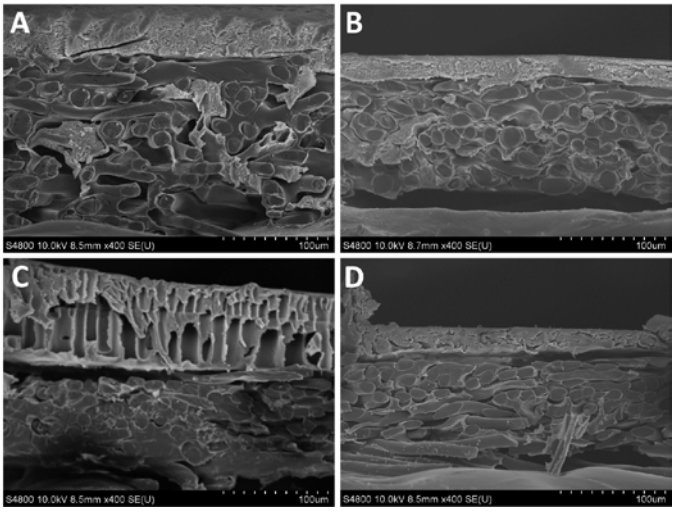

Figure 4.9. SEM images of the cross section of (A) pristine Nanostone PS20, (B) patterned Nanostone PS20, (C) pristine GE PW, and (D) patterned GE PW. Images were taken at a 400 magnification and the scale bar represents 100 µm.

4.4.1.1 Membrane Patterning Temperature

The temperature used for patterning was investigated. Because the membranes pattern via a plastic deformation mechanism [95, 203], it was thought that increasing the patterning temperature would increase the membrane pattern peak heights and decrease their variance. The membranes were patterned as previously described, except the press plates were heated to 75°C instead of 45°C. This temperature remains much below the T_g of the polyamide or support layers to avoid potential pore sealing [95, 220]. Interestingly, increasing the patterning temperature did not consistently increase the pattern peak heights nor did it consistently decrease the peak height variance as shown in **Table 4.2**. In some cases, such as Dow BW30XFR and Nanostone NF4, the pattern peak heights increased; whereas in other cases, such as TriSep X201 and GE HL, the pattern peak heights decreased. The same outcome applies to the variance in pattern peak heights– some increased while others decreased. Most interestingly is that the GE Duracid KH

membrane showed patterning at 75°C but not at 45°C.

Table 4.2. Membrane chemistry, 45°C patterned peak heights (nm), and 75°C patterned peak heights (nm) of 13 commercial NF and RO membranes. Error represents one standard deviation from at least 3 membrane pieces.

Membrane Chemistry	Membrane	45°C Peak Heights (nm)	75°C Peak Heights (nm)
MPD - TMC based	Dow BW30XFR	138 ± 34	174 ± 32
	Dow SW30HR	143 ± 37	129 ± 51
	Toray UTC-82V	196 ± 61	141 ± 59
	TriSep ACM4	144 ± 32	168 ± 38
	TriSep X201	220 ± 35	142 ± 51
MPD - Piperazine - TMC based	GE SG	42 ± 15	90 ± 12
Piperazine - TMC based	GE HL	73 ± 30	23 ± 8
	Dow NF270	144 ± 15	106 ± 47
	Synder NFG	44 ± 19	53 ± 22
	Nanostone NF4	69 ± 6	187 ± 24
	TriSep XN45	99 ± 33	79 ± 15
	GE DK	17 ± 6	36 ± 11
Sulfonamide based	GE Duracid KH	0 ± 0	32 ± 11

4.4.2 Membrane Chemistry and Surface Properties

4.4.2.1 Membrane Polyamide and Support Layer Chemistry

After collecting the imaging data, I began my search for a correlation(s) between membrane properties and patternability. The first variables I studied were membrane chemistry and surface properties. **Figure 4.10** shows the ATR-FTIR spectra of all thirteen commercial membranes. Based on the ATR-FTIR spectra and the manufacturer specification sheets, the membranes were grouped into classes. **Figure 4.10A** shows the membranes with a polyamide layer that appears to be mpd-tmc based. **Figure 4.10B**

shows the membranes with a polyamide layer that appears to be piperazine-tmc based. Mpd-tmc based membranes show both amide I and amide II bands, while piperazine-tmc based membranes show only an amide I band [201]. The GE SG membrane polyamide layer appears to contain a mixture of mpd and piperazine with tmc [201, 221], and the GE Duracid KH membrane separation layer appears to be a polysulfonamide chemistry [222]. Some membranes, such as GE SG and GE DK, appear to have a hydrophilic coating based on the broad peak in the 3100-3700 cm^{-1} range. **Table 4.3** shows the water and diiodomethane contact angles and surface free energies of each membrane, none of which correlate with membrane patternability (pattern peak heights). As described below, all membranes had a Psf support except for the GE HL membrane which had a PES support. Polyamide chemistry appears to play at least some role in patternability of the membranes, as mpd-tmc based membranes had an average peak height statistically higher (95% confidence, p-value = 0.0045) than piperazine-tmc based membranes.

Membrane support chemistry was determined by ATR-FTIR. To determine if there is a difference in the ATR-FTIR spectra between polysulfone (Psf) and polyethersulfone (PES), a Psf membrane (Nanostone PS20) and a PES membrane (GE PW) were analyzed by ATR-FTIR. **Figure 4.11** shows the ATR-FTIR spectrum of each membrane. The main difference between the Psf and PES membranes is that the Psf membrane has a doublet peak and the PES membrane has a singlet peak around 1500 cm^{-1}. This difference in the spectra is caused by differences in the aromatic ring stretching of the two polymers. Skeletal vibrations involving carbon-carbon stretching within the aromatic ring absorb in the 1500-1400 cm^{-1} range [188]. The skeletal bands can appear as

doublets, depending on the nature of the ring substituents [188]. Most likely the doublet in the Psf spectrum is caused by the –C(CH_3)$_2$– group attached to two aromatic rings in Psf. This group is not present in PES.

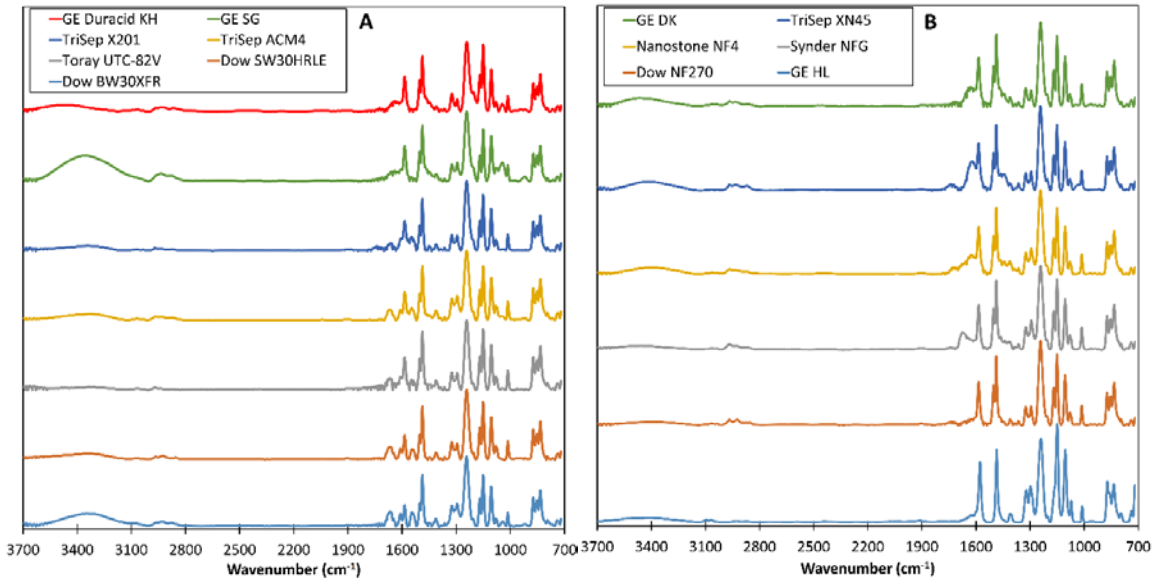

Figure 4.10. ATR-FTIR spectra of (A) *m*-phenylenediamine/trimesoyl chloride-based membranes and (B) piperazine/trimesoyl chloride-based membranes. Spectra are normalized to the peak at 1240 cm^{-1}. Note that the GE SG membrane selective layer is prepared from interfacial polymerization of *m*-phenylenediamine/piperazine/trimesoyl chloride, and the GE Duracid KH membrane selective layer is a polysulfonamide.

Table 4.3. Water and diiodomethane contact angles for pristine commercial nanofiltration and reverse osmosis membranes. Surface energy calculations are based on the Owens-Wendt method. Uncertainties represent one standard deviation from at least 12 data points from at least 3 membrane pieces.

	Contact Angle (degree)		Surface Energies (mJ/m^2)		
Membrane	**Water**	**CH_2I_2**	**Dispersive**	**Polar**	**Total**
Dow BW30XFR	102.3 ± 5.8	70.6 ± 2.1	21.5 ± 1.2	1.2 ± 1.1	22.8 ± 1.3
Dow SW30HRLE	66.5 ± 6.3	41.1 ± 3.2	33.5 ± 2.1	11.7 ± 3.8	45.1 ± 2.7
Toray UTC-82V	58.1 ± 8.3	33.4 ± 4.2	35.9 ± 2.7	15.6 ± 5.3	51.5 ± 3.4
TriSep ACM4	33.0 ± 3.9	39.1 ± 6.1	29.9 ± 3.0	33.7 ± 3.8	63.5 ± 1.8
TriSep X201	49.1 ± 5.1	48.2 ± 5.3	27.0 ± 3.0	25.5 ± 4.7	52.5 ± 3.2
GE SG	73.6 ± 2.9	45.1 ± 2.8	32.5 ± 1.7	7.9 ± 1.7	40.5 ± 1.5
GE HL	41.5 ± 2.6	47.2 ± 3.0	26.7 ± 1.8	30.5 ± 2.8	57.2 ± 1.4
Dow NF270	21.4 ± 2.3	52.7 ± 2.5	22.1 ± 1.3	45.8 ± 1.1	67.9 ± 1.0
Synder NFG	62.5 ± 2.9	52.0 ± 1.1	26.9 ± 0.8	16.2 ± 2.1	43.1 ± 1.6
Nanostone NF4	36.2 ± 6.4	44.7 ± 5.0	27.4 ± 2.6	33.4 ± 4.7	60.8 ± 3.6
TriSep XN45	39.8 ± 3.1	47.5 ± 1.7	26.4 ± 1.1	32.0 ± 2.6	58.3 ± 1.8
GE DK	44.6 ± 1.7	47.2 ± 1.9	27.0 ± 1.1	28.4 ± 1.7	55.4 ± 0.9
GE Duracid KH	62.2 ± 4.2	51.3 ± 2.7	27.1 ± 1.8	16.7 ± 3.4	43.8 ± 2.4

To analyze the membrane support layer for all thirteen TFC membranes, the polyamide-support layers were peeled off the membrane polyester backing, and the support layer was analyzed by ATR-FTIR. Each membrane support was compared to the Psf and PES spectra in **Figure 4.11** to determine whether it was Psf or PES. **Figure 4.12** shows the ATR-FTIR spectrum of each membrane support. The only membrane that had a PES support was the GE HL membrane. All other membranes (Dow BW30XFR, Dow SW30HRLE, Toray UTC-82V, TriSep ACM4, TriSep X201, GE SG, GE Duracid KH, Dow NF270, Synder NFG, Nanostone NF4, TriSep XN45, and GE DK) had a Psf support.

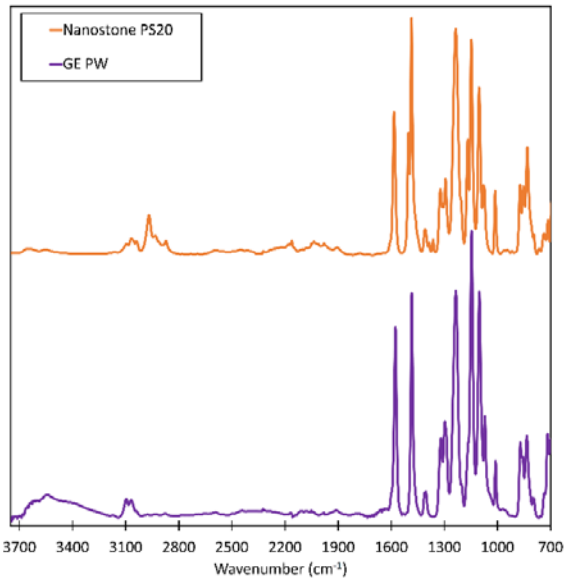

Figure 4.11. ATR-FTIR spectra of a polysulfone (Nanostone PS20) and a polyethersulfone (GE PW) membrane. Spectra are normalized to the peak at 1240 cm^{-1}.

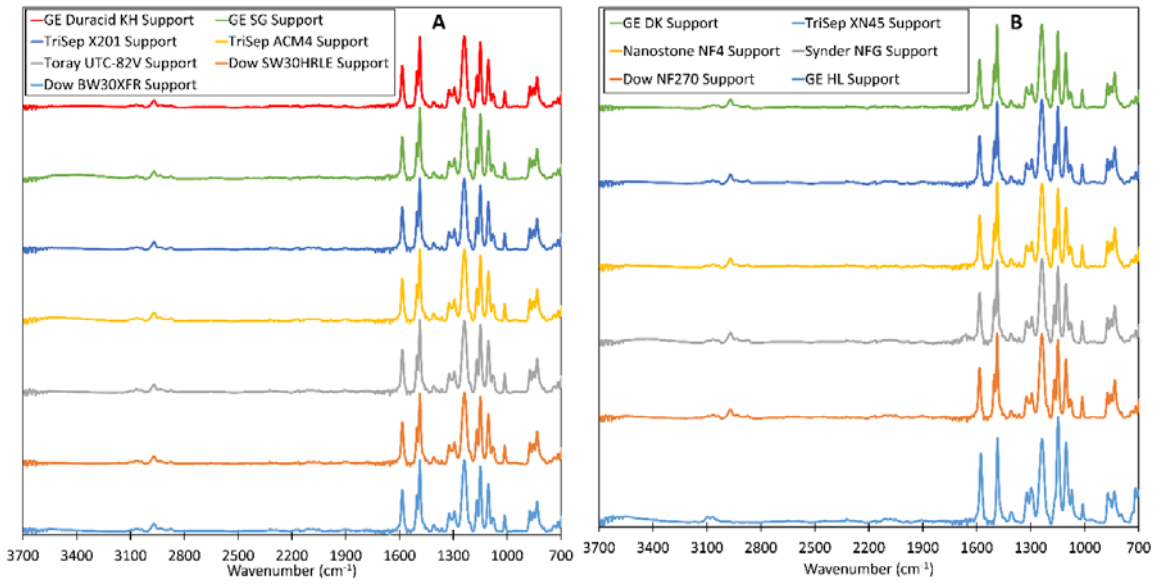

Figure 4.12. ATR-FTIR spectra of the membrane support layers for (A) *m*-phenylenediamine/trimesoyl chloride based membranes and (B) piperazine/trimesoyl chloride based membranes. Note that the GE SG membrane selective layer is prepared from interfacial polymerization of *m*-phenylenediamine/piperazine/trimesoyl chloride, and the GE Duracid KH membrane selective layer is a polysulfonamide. Spectra are normalized to the peak at 1240 cm^{-1}.

4.4.2.2 Membrane Surface Roughness

In **Figure 4.4**, I observed that the original leaf-like surface features on mpd-tmc based membranes (images A-E) appeared to be "molded" into the peaks of the patterned area. **Figure 4.7** further confirmed the "molded" leaf-like features in the patterned membranes. Based on this observation and the observation that mpd-tmc membranes on average had statistically higher peak heights, I decided to test whether membrane surface roughness correlates to pattern peak height for individual membranes. **Figure 4.13** shows surface roughness values for pristine, pressed, and patterned membranes determined by AFM. Consistent with my initial study in Chapter 3 [28], membrane roughness decreased universally upon pressing, caused by the flattening of the surface upon compression with a flat silicon wafer. With the exception of Dow SW30HRLE, the patterned membrane roughness was higher than the pressed membrane roughness. I expected this finding, as patterning introduces an ordered roughness to the membrane surface. As expected, the mpd-tmc based membranes had rougher pristine membrane surfaces than the piperazine-tmc based membranes [212, 223]. It does appear, therefore, that surface roughness plays some role in patternability of the membranes. However, the pristine membrane surface roughness did not provide any new information. That is, while the rougher mpd-tmc membranes on average have statistically higher pattern peak heights, no correlation was found between pristine membrane roughness and membrane patternability for individual membranes within a membrane class.

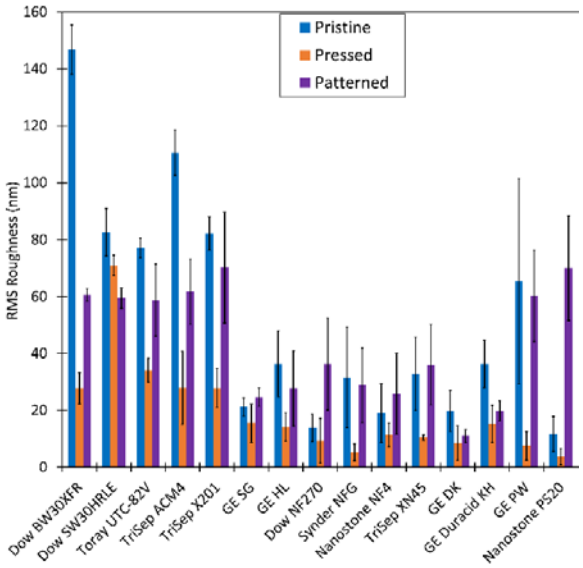

Figure 4.13. RMS roughness of pristine, pressed, and patterned commercial polyamide membranes as determined by AFM. Error bars represent one standard deviation from at least 3 membrane pieces.

4.4.2.3 Polyamide Cross-Linking Density

Based on the earlier observation that the polyamide layer appears to offer some resistivity to patterning, I decided to test whether polyamide crosslinking density correlates to pattern peak height for individual membranes. The hypothesis was that polyamide layers with higher cross-linking density would be more resistant to patterning. The Painter-Shenoy equation (**Equation 4.5**) was used to determine the number of monomer units between cross-link sites [218]. The larger the number of monomer units between cross-links, the lower the cross-linking density. This equation requires thickness data for dry and solvent-swollen films. The polyamide layers were isolated on silicon wafers and ellipsometry was used to determine their thicknesses in air and swollen in ethanol.

Figure 4.14A shows the dry and ethanol swollen polyamide layer thickness of

each membrane, and **Figure 4.14B** shows the number of monomer units between cross-links calculated from the Painter-Shenoy equation. Some of the piperazine-tmc layers, such as GE HL, Dow NF270, and Synder NFG, were extremely thin (< 25 nm), consistent with what is seen in the literature [212]. Surprisingly, the ethanol swollen polyamide layer thicknesses were similar for each membrane, all falling between 130 and 150 nm. Neither the dry polyamide layer thickness nor the swelling ratio (S_h) correlates with membrane patternability. However, it does appear that the ability to swell significantly (i.e., relatively lower crosslinking density) is important to enable pattern peak heights larger than the polyamide layer thickness without disrupting salt rejection (vide infra). In other words, some polyamide layers are stretched to reach their pattern peak heights because the peak heights are larger than the dry thicknesses measured. The swelling ratios were used to calculate the number of monomer units between cross-links by the Painter-Shenoy equation. Unfortunately, this equation does have limitations, and the results depend strongly on the value of the Flory-Huggins parameter used. Some swelling ratios, such as those for GE HL, Dow NF270, and Synder NFG, were too high for the equation to work. Also, it is unlikely that the Nanostone NF4 and GE Duracid KH membranes have 15+ monomer units between cross-links, as all of these polyamide layers are highly cross-linked.

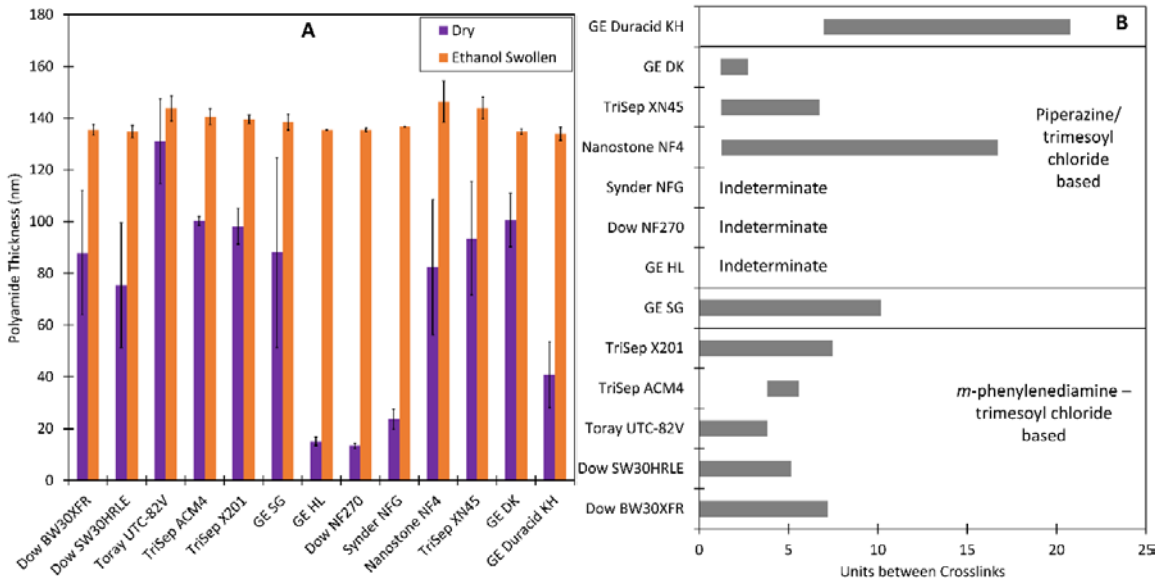

Figure 4.14. (A) Dry and ethanol swollen thicknesses of polyamide layers measured by ellipsometry. (B) Number of monomer units between crosslinks of the polyamide layer as calculated by the Painter-Shenoy equation. Error bars represent one standard deviation from at least 3 membrane pieces.

Further attempts were made to correlate pattern peak height to the number of free carboxylic acid groups in the polyamide layers, as described in **Figure 4.15**. It was theorized that the density of ionized carboxylic acid groups could indicate the degree of cross-linking of each polyamide layer. The higher the density, the less cross-linked and vice versa. The data were analyzed to see if the swelling ratio (S_h) of the polyamide layer reported in the manuscript would correlate with the silver binding data. However, the correlations were poor. Therefore, polyamide crosslinking density does not appear to correlate to pattern peak height for individual membranes.

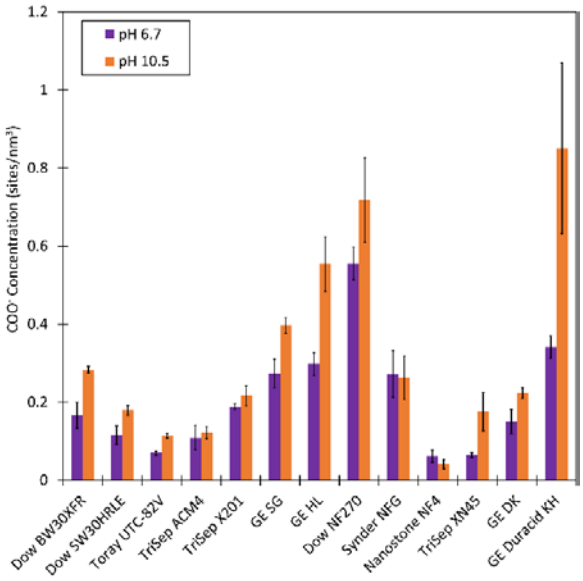

Figure 4.15. The number of ionized carboxylic acid groups per membrane volume at pHs 6.7 and 10.5 as determined by silver binding experiments. Error bars represent one standard deviation from at least 3 membrane pieces.

4.4.4.3 Membrane Performance Properties

Attempts also were made to correlate the membrane permeance and rejection properties to the membrane pattern peak height for individual membranes. The pristine, pressed, and patterned membranes were challenged with a 2000 ppm magnesium sulfate solution. **Figure 4.16A** shows the permeance of each membrane. As expected, the piperazine-tmc based membranes (nanofiltration membranes) had a higher permeance than the mpd-tmc based membranes (reverse osmosis membranes). Eight of the 13 membranes had statistically the same permeance values after pressing or patterning at 95% confidence. (Statistical information is given in **Appendix B**.) The remaining five membranes showed a decrease in permeance upon both pressing and patterning, indicating that the compression of the membrane support/polyamide layer increased transport resistance.

Figure 4.16B shows the $MgSO_4$ rejection of each membrane. Pristine membranes were tested to ensure a proper control with my testing system for comparisons to the pressed and patterned membranes. Ten of the 13 membranes had statistically the same rejection values after pressing or patterning at 95% confidence. (Statistical information is given in the **Appendix B**.) For the membranes that had a decrease in rejection upon patterning, it is possible that the fracturing strain was exceeded, resulting in an increase in salt passage through the polyamide layer [204, 211]. Despite these efforts, I found that neither membrane permeance nor membrane rejection correlated with individual membrane patternability.

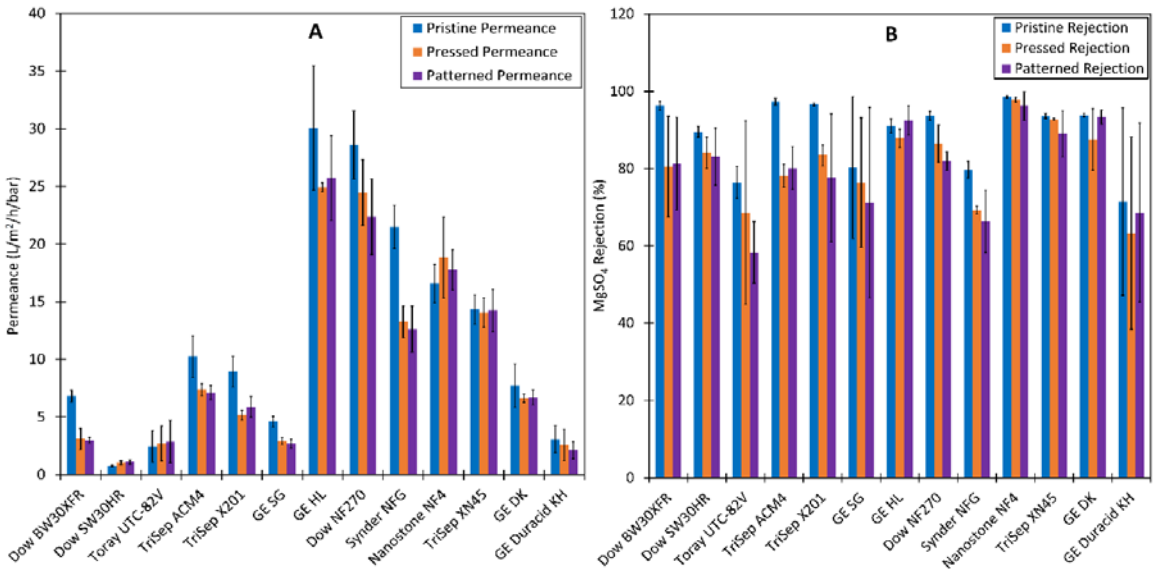

Figure 4.16. (A) Permeance ($L/m^2/h/bar$) and (B) $MgSO_4$ rejection (%) of pristine, pressed, and patterned commercial polyamide membranes at 22-23°C. The feed was a 2000 ppm magnesium sulfate solution, the cross flow velocity was 3.0 ± 0.2 m/s, and the membrane area was 5.6 cm^2. Sixty-two percent of the membrane test area was pressed/patterned. The flow angle used between the solution flow and the membrane patterns was 0° (parallel). Error bars represent one standard deviation from at least 3 membrane pieces.

4.4.4 Membrane Humectant

In Chapter 3 [28], I discovered that a humectant is needed within the membrane to preserve the permeance properties of the membrane following patterning. However, neither the humectant nor the concentration of humectant used by manufacturers is known. I hypothesized that differences in individual membrane patternability could be caused by differences in these variables. To test this hypothesis, the membranes were rinsed thoroughly with water to remove the humectant, filled with a specific glycerol solution, dried, and patterned to investigate if the pattern peak heights changed.

Figure 4.17 shows the patterned peak heights of the as received and 15 wt% glycerol filled membranes. All of the patterned peak heights were determined to be statistically different at 95% confidence upon patterning with a 15 wt% glycerol humectant, compared to the original humectant. The pattern peak heights appear to move closer to the same value for all membranes of a given chemistry class (mpd-tmc membranes ~160 nm and piperazine-tmc membranes ~70 nm). However, the membrane supports (GE PW and Nanostone PS20) had statistically the same membrane pattern peak heights upon patterning with a 15 wt% glycerol filled membrane instead of patterning as received. This data set further supports the observation that the polyamide layer offers some resistivity to patterning as first discussed in **Section 4.4.1**.

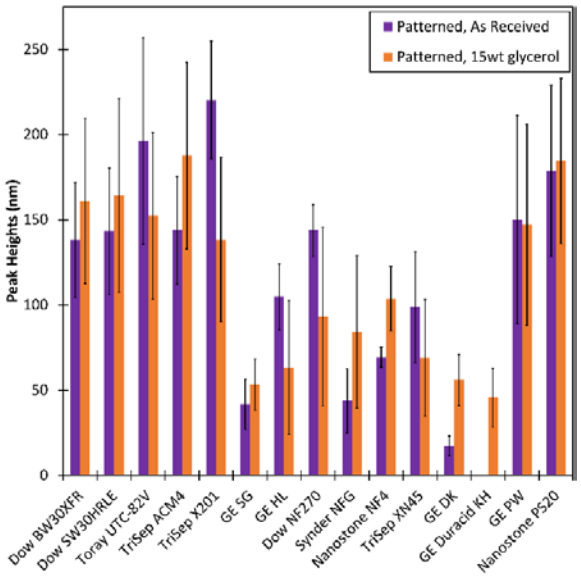

Figure 4.17. Membrane pattern peak heights (nm) as determined by AFM for patterned commercial polyamide membranes as received and after replacing the original humectant with a 15 wt% glycerol solution. Error bars represent one standard deviation from at least 3 membrane pieces.

Glycerol soaking time was studied to ensure the membranes were soaked long enough in the glycerol solution. The Dow NF270 and Synder NFG membranes were rinsed in DI water, pat dried, immersed in a 15 wt% glycerol solution for either 5 min or 24.5 h, pat dried, and allowed to air dry overnight in a plastic petri-dish. The membranes were patterned and AFM was used to measure the peak heights. **Figure 4.18** shows the membrane pattern peak heights for each membrane as received, immersed in a 15wt% (aq) glycerol for 5 min, and immersed in a 15wt% (aq) glycerol for 24.5 h. The as received patterned membrane peak heights were statistically different from the patterned membrane peak heights after immersion in 15wt% (aq) glycerol solution for 5 min. Statistically, there was no difference between the 5 min and 24.5 h immersion time. Therefore it was determined that 5 min was an acceptable immersion time.

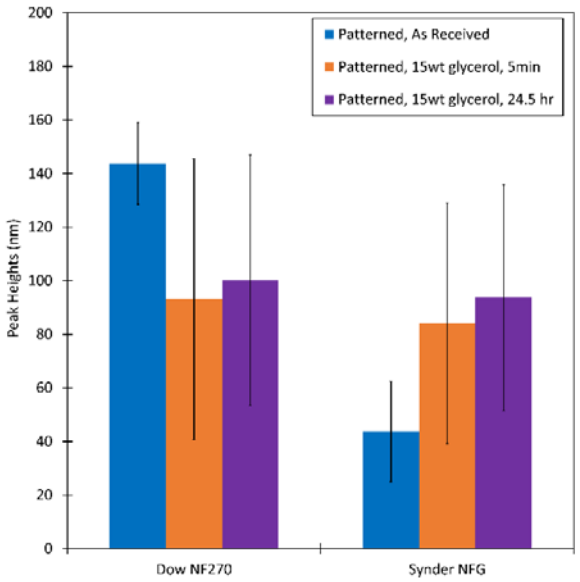

Figure 4.18. Membrane pattern peak heights (nm) for Dow NF270 and Synder NFG membranes as received and after filling with a 15 wt% glycerol solution for 5 min and 24.5 h. Error bars represent one standard deviation from at least 50 measurements on at least 3 membrane pieces.

Knowing that the humectant matters, I wondered if the concentration of humectant in the membrane matters, and if so, can I use it to control the peak heights of each membrane for a constant applied pressure. I hypothesized that as the amount of glycerol in the pores increased, pattern peak height would decrease because the Young's Modulus of the membrane supports would be higher by replacing air with glycerol. Building on work by Ding et al. [203], the open cell foam model was adopted to estimate the Young's Modulus of the membrane support with different amounts of glycerol in the membrane support pores. I attempted to correlate peak height to E^{*-1} (ρ^{*-2}) by changing the glycerol content in the membrane, and thus changing the effective density of the membrane. **Figure 4.19** shows the membrane pattern peak heights for Dow NF270, Dow BW30XFR, GE HL, Nanostone PS20, and GE Duracid KH using glycerol pore filling

solutions from 0 to 75 wt% glycerol. I did not observe the expected trend of declining pattern peak height with increasing glycerol content, and therefore no correlation to bulk Young's Modulus was found. Interestingly, the GE Duracid KH membrane showed no patterning when filled with 0 wt% glycerol (only air in the pores after drying) but showed similar patternability for all the glycerol filled membranes. This membrane also could not be patterned as received, which may indicate that the manufacturer does not apply humectant to this product.

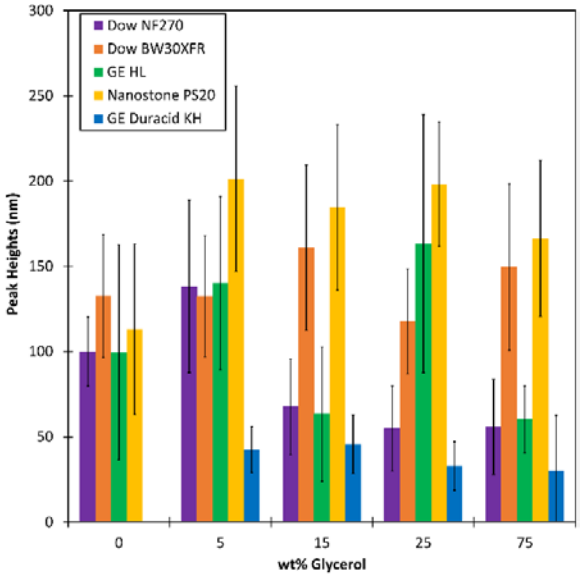

Figure 4.19. Membrane pattern peak heights (nm) for the patterned Dow NF270, Dow BW30XFR, GE HL, Nanostone PS20, and GE Duracid KH membranes after replacing the original humectant with 0, 5, 15, 25, and 75 wt% glycerol solutions. Error bars represent one standard deviation from at least 3 membrane pieces.

Although the amount of glycerol used as a humectant does not correlate with membrane patternability, it does appear that its presence makes a difference. AFM nano-indentation was used to determine if glycerol affected the Young's Modulus of the polyamide layers. **Figure 4.20** shows the Young's Modulus of as received, rinsed, and

15wt% (aq) glycerol filled GE Duracid KH, GE DK, and TriSep X201 membranes using a 5 min glycerol soak time. I theorized that if glycerol was plasticizing the polyamide layer, the changes in patterning upon filling with 15wt% glycerol could be determined based on the change in the polyamide layer stiffness or Young's Modulus. It was expected that if the Young's Modulus decreased upon filling with 15wt% glycerol, then pattern peak heights would increase and vice versa. The number of data points received from these tests was so large (> 700 per membrane type) that a multiple mean hypothesis test could not be performed as the variances were not considered equal (p-value < 0.0001). A t-test was used to compare the data. However, because the data set is so large, all but 2 data points were considered statistically different. The TriSep X201 membrane rinsed and immersed in 15wt% (aq) glycerol solution for 5 min were the only data points considered statistically the same. The GE Duracid KH membrane had a constant Young's Modulus around 8.7 GPa and the TriSep X201 membrane had a constant Young's Modulus around 2.7 GPa. The GE DK membrane was the only membrane that appeared to have any change in Young's Modulus. The as received and rinsed Young's Modulus for GE DK was around 4.2 GPa, whereas that for the membrane immersed in 15wt% (aq) glycerol solution for 5 min was around 2.7 GPa. The best case to study was the GE Duracid KH membrane because it did not pattern as received, but did once filled with 15wt% glycerol. However, because no change in the Young's Modulus data was seen, it was determined that this test was not applicable to determine why there are differences in patterning the as received membranes.

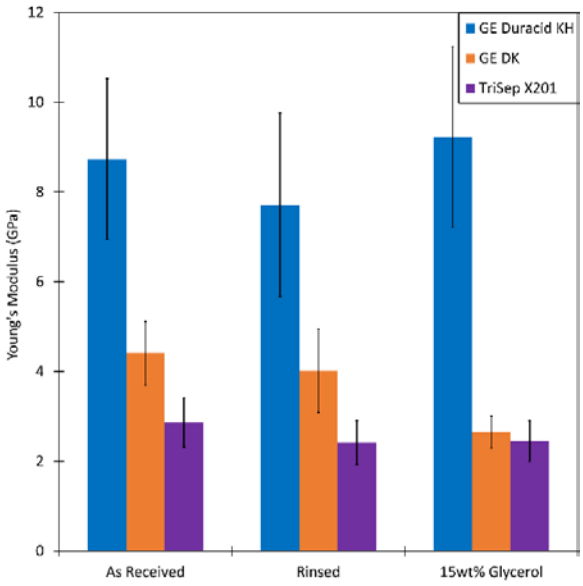

Figure 4.20. Young's Modulus (GPa) from AFM nano-indentation measurements of GE Duracid KH, GE DK, and TriSep X201 membranes as received, rinsed, and after filling with a 15 wt% glycerol solution. Error bars represent one standard deviation from at least 3 membrane pieces.

Swelling studies using pure DI water and a 15 wt% (aq) glycerol solution were done on isolated polyamide layers of select membranes in an attempt to understand why glycerol changed the patternability of the membranes. I theorized that if the glycerol is acting as a plasticizer of the polyamide layer, then there should be a change in polyamide thickness. **Figure 4.21** shows the data for the polyamide layers of Dow NF270, Synder NFG, TriSep X201, and GE Duracid KH. Dow NF270 and Synder NFG were chosen because they are both piperazine-tmc based membranes but have opposite trends in pattern peak height when filled with a 15wt% glycerol solution (Dow NF270 decreased and Synder NFG increased). TriSep X201 was chosen to compare to the Dow NF270 data because it is an mpd-tmc membrane but had a similar decrease in pattern peak height when filled with a 15wt% glycerol solution. GE Duracid KH was chosen because of the

appearance of patterning when filling with a 15wt% glycerol solution. However, the swelling tests showed no conclusive trend. Dow NF270 thickness was statistically the same at approximately 110 nm, Synder NFG was statistically the same at approximately 64 nm, and GE Duracid KH was statistically the same at approximately 307 nm. TriSep X201 was statistically different showing an increase from 129 nm to 219 nm when soaked in the 15wt% glycerol solution. However, that trend is opposite from expected and it is the only membrane to show any statistically significant changes. Therefore, it was determined that this test was not appropriate to determine why there are differences in patterning the as received membranes. The prevailing thought is that glycerol is acting as a plasticizer or lubricant; however, no tests performed so far have led to conclusive results.

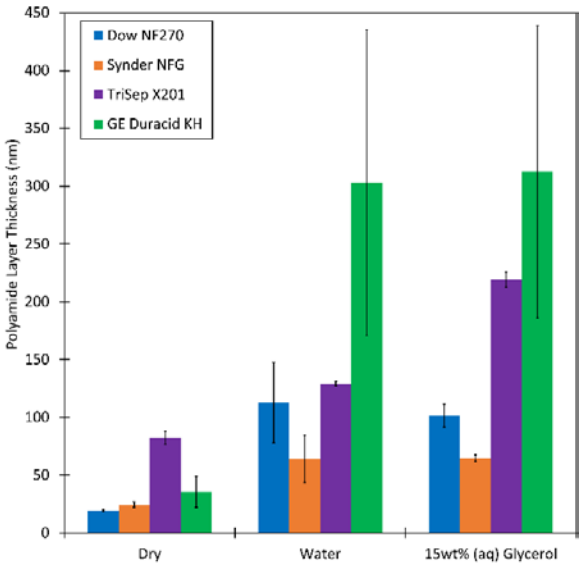

Figure 4.21. Dry, water swollen, 15wt% (aq) glycerol swollen thicknesses of the isolated polyamide layer for the Dow NF270, Synder NFG, TriSep X201, and GE Duracid KH membranes measured by ellipsometry. Error bars represent one standard deviation from at least 3 membrane pieces.

4.5. Conclusions

Nanoimprint lithography was used to pattern many commercial thin-film composite nanofiltration and reverse osmosis membranes of varying chemistries. Membrane chemistry, membrane surface properties, membrane mechanical properties, and membrane performance properties were studied to understand why membranes pattern differently. A significant difference was found in the patternability among classes of membranes. The mpd-tmc based membranes had an average peak height statistically higher than the piperazine-tmc based membranes, which may be related to surface roughness. However, no correlations were found between the study variables and pattern peak heights for individual membranes within the membrane classes. One interesting result is that the humectant appears to play some role. When a common humectant (glycerol) was used for all membranes, the membrane pattern peak heights changed and became more uniform within each polyamide class. While it is clear that the humectant facilitates patterning, attempts to understand the mechanism showed no conclusive results.

4.6 Acknowledgements

I was supported by a National Science Foundation Graduate Research Fellowship under Award DGE-1246875. I wish to acknowledge the National Science Foundation for financial support under NSF award CBET-1534304. I thank Clemson University for funding through the Tiger Grant Award program. I thank Dr. Caleb Funk for providing the Dow membranes. I thank the Clemson Machining and Technical Services for fabrication of the custom cross-flow cell.

CHAPTER FIVE

CONCLUSIONS AND RECOMMENDATIONS

5.1 Summary and Conclusions

This dissertation describes two techniques that were used to reduce the fouling propensity of water treatment membranes. Chapter 1 introduced membrane fouling and more specifically membrane biofouling. It highlights the various methods used to combat membrane fouling, including anti-fouling surfaces that are used to make the membrane "less sticky" to foulant attachment and anti-microbial surfaces are used to kill or deactivate bacteria upon contact with the membrane surface. It describes anti-fouling, anti-microbial surfaces that take a combined approach to resist foulant attachment and kill bacteria upon attachment to the membrane surface. It describes surface patterning as a tool to alter the fluid flow at the membrane surface such that the foulants are less likely to come in contact with the membrane surface. Chapter 1 also highlights the various methods used to measure success in fouling reduction. Flux reduction over time is the most common method in academia. Threshold flux is argued to be the most appropriate method to translate from bench scale to industrial scale.

Chapter 2 focused on developing a membrane surface with a switchable chemistry that can act as either anti-fouling or anti-microbial depending on the environment pH. Poly(CBOH) was found to be a great anti-fouling surface at neutral pH and capable of enhancing the biofilm mortality by switching to the anti-microbial mode at pH 1.0. A thin layer of poly(CBOH) on the membrane surface was found to reduce the bacteria deposition coefficient by over an order of magnitude over the pristine membrane.

Poly(CBOH) modified membranes accumulated half the biomass compared to the pristine membrane. A practical time of 15 minutes was found to switch from anti-fouling mode to anti-microbial mode and vice versa. A less than desirable low switching pH of 1.0 was needed to cause the switching from anti-fouling mode to anti-microbial mode. Even still, the poly(CBOH) modified membranes enhanced biofilm mortality at pH 1.0 compared to another zwitterion modified membrane. Future chemistry designs should aim to increase the switching pH to make it more practical and closer to a typical cleaning solution pH, and I propose some in **Section 5.2.1**.

Chapters 3 and 4 described a method for applying a nanometer-sized line and groove surface pattern onto thin-film composite membranes. In Chapter 3, the line and groove pattern was combined with an anti-fouling coating to make a superior anti-alginate fouling membrane surface. A piperazine-tmc based nanofiltration membrane was chosen for this study. This was the first study known to show direct patterning of a TFC membrane. The nanometer-sized line and groove pattern was applied onto the membrane using a silicon stamp by a thermal embossing nanoimprint lithography method. Control experiments were done by using the same thermal embossing method but with a flat silicon wafer. Poly(ethylene glycol) diglycidyl ether was used as an anti-fouling coating by reacting the epoxide groups of PEGDE with the unreacted carboxylic acid groups of the polyamide membrane. The pattern was successfully applied onto the membrane through visualization methods such as AFM and LEXT. The chemical reaction was deemed successful by ATR-FTIR and contact angle characterization. Magnesium sulfate rejection experiments showed that membrane performance (flux and rejection) was not

altered by either physical patterning or chemical coating. Flux decline over time experiments were performed using a model biopolymer, alginate, as a foulant. Chemical coating alone showed a significant improvement on the membrane's fouling resistance. The flat silicon wafer compression experiments showed that simply flattening the membrane surface (thus decreasing the surface roughness) is similar to using the chemical coating in terms of reducing the amount of alginate fouling on the membrane. Membrane compression and patterning showed similar fouling reduction. However, by combining the patterning with the chemical coating, little to no fouling was observed over the course of testing. Future designs should alter the surface coating chemistry because PEG degrades under typical cleaning solutions.

In Chapter 4, the same line and groove pattern used in Chapter 3 was applied onto thirteen different commercial nanofiltration and reverse osmosis polyamide membranes. The pattern was applied onto the membrane surface using the same thermal embossing NIL process as in Chapter 3. Membrane chemistry, membrane surface properties, membrane mechanical properties, and membrane performance properties were studied to understand why membranes pattern differently. A significant difference was found in the patternability among classes of membranes. The mpd-tmc based membranes had an average peak height statistically higher than the piperazine-tmc based membranes, which may be related to surface roughness. However, no correlations were found between the study variables and pattern peak heights for individual membranes within the membrane classes. One interesting result is that the humectant appears to play some role. When a common humectant (glycerol) was used for all membranes, the membrane pattern peak

heights changed and became more uniform within each polyamide class. While it is clear that the humectant facilitates patterning, attempts to understand the mechanism showed no conclusive results. Future work should explore if patternability depends on humectant type and seek to uncover what humectant/concentration of humectant is used by membrane manufacturers.

5.2 Recommendations

5.2.1 Switchable Chemistry

The switching studies in Chapter 2 show that a pH of 1.0 is required to switch the poly(CBOH) chemistry from anti-fouling mode to anti-microbial mode. However, a switching pH of 1.0 is not desirable for a membrane chemical cleaning. I suggest that future work be done to explore ways to increase the switching pH. Cao, et al. proposed the switching mechanism of this chemistry [93]. The first step in the switching process is protonation of the carboxylic acid head group of the CBOH zwitterion. Interestingly, the switching pH does not appear to match the pK_a of sarcosine or to increase upon polymerization as has been seen in some previous studies [224, 225]. While sarcosine has a pK_a much greater than 1.0, it is believed that the presence of the quaternary amine close to the carboxylic acid within the zwitterion decreases its pK_a [190]. To assess the role of proximate groups on the acid pK_a and guide selection of precursor molecules that ultimately may lead to an increased switching pH, I selected a set of potential precursor molecules with pK_a values that are similar but different to the base sarcosine unit in the CBOH monomer. **Table 5.1** shows some organic acids and their pK_a values. The addition of methyl groups on sarcosine and N,N-dimethylglycine compared to glycine decreased

the pK_a of the carboxylic acid group. The quaternary amine of betaine reduced the pK_a by 0.6 units from glycine. The prevailing thought is that upon polymerization, one of two things occurs: (1) the pK_a of the carboxylic acid is further reduced by the presence of additional monomer units or (2) charge shielding occurs and the surface groups switch while buried groups do not. However, when increasing the alkyl chain length between the quaternary amine and the carboxylic acid the pK_a of the carboxylic acid increases. For example, γ-aminobutyric acid has a pK_a of 4.1 and 5-aminopentanoic acid has a pK_a of 4.3, almost 2.0 units higher than glycine. Therefore, if a carboxybetaine monomer can be made that contains γ-aminobutyric acid or 5-aminopentanoic acid instead of sarcosine, then perhaps the switching pH could be increased. I have done some preliminary work in this area and have found that the two new monomers are difficult to synthesize because the protected intermediate does not precipitate. To get around this hurdle, I dip-coated silicon wafers with PGMA and reacted the new organic acids with the unreacted epoxide groups of PGMA. **Figure 5.1** shows the switching characteristics of the wafers synthesized by (A) γ-aminobutyric acid and (B) 5-aminopentanoic acid. As can be seen in the peaks between 1150 cm^{-1} and 1200 cm^{-1}, the switching pH increased moderately to 2.5. Although this result is promising, more work needs to be done to increase the switching pH to a more optimal value of approximately 4.0. One recommendation is to add a methyl group to the alpha-carbon of the carboxylic acid because it decreases the acidity of the carboxylic acid [226].

Table 5.1. pK_a values of various organic acids

Organic Acid	pKa
Betaine 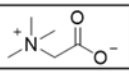	1.8
N,N-Dimethylglycine 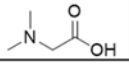	2.0
Sarcosine 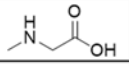	2.2
Glycine 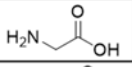	2.4
γ-Aminobutyric Acid 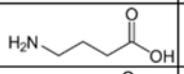	4.1
5-Aminopentanoic Acid 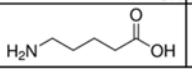	4.3

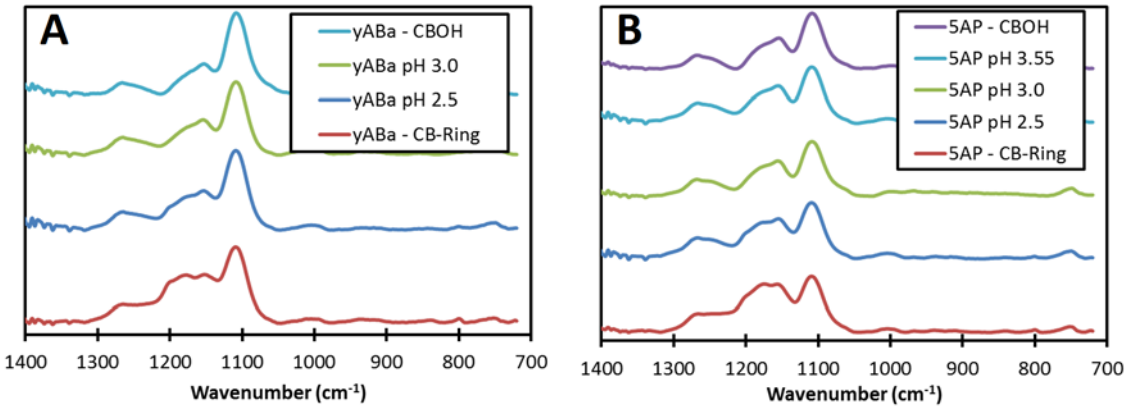

Figure 5.1. Switching pH characteristics of carboxybetaine polymers made from (A) γ-aminobutyric acid (yABa) and (B) 5-aminopentanoic acid (5AP).

As mentioned in Chapter 1, the length of the alkyl chain can affect the potency of the quaternary amine towards cell death [69, 70]. In addition to increasing the switching pH, I recommend exploring ways to increase the alkyl chain length on the quaternary amine to either 6 or 8 units long. I have done some preliminary work in this area with the sarcosine based CBOH. However, the intermediate protected version of this monomer would also not precipitate. It is unknown if increasing the alkyl chain length will affect the ability of the monomer to ring close (switch) or if it will alter the switching pH in

some way. While these chemistries seem reasonably straightforward to synthesize on silicon wafers, the challenge will be to synthesize them on membranes directly. If the monomers can be synthesized and purified with reasonable yields, then that would help solve this issue by enabling the use of standard polymer grafting methods.

5.2.2 Combining Anti-Fouling Chemistry with Surface Patterning

As stated in Chapters 1 and 3, PEG-based coatings tend to degrade under typical membrane cleaning solutions [31]. Therefore, I recommend changing the anti-fouling chemistry used to something that will be more stable under chemical cleanings. For example, the zwitterionic chemistry studied in Chapter 2 would be useful to combine with these nano-patterns [16]. The challenge will be to synthesize the zwitterion polymer or oligomer and cap it with an epoxide group that will readily react with the unreacted carboxylic acid groups of the polyamide membrane surface. This can be done through ATRP, which will allow for control over the molecular weight of the polymer [227, 228]. The molecular weight of the polymer can then be a variable studied in conjunction with the addition of surface patterns to determine the most effective coating.

To really understand the effectiveness of the combined coating, patterning approach, I recommend longer run times with a more challenging solution. Multiday experiments would provide the data that are needed to understand how these surfaces might perform under continuous operation. Increasing the alginate and calcium concentrations would give a more challenging solution for the membrane to resist fouling. Decreasing the cross-flow velocity also would help determine the surfaces' effectiveness. In Chapter 3, a cross-flow velocity of 1.0 m/s was used. If the cross-flow

velocity was reduced to <0.5 m/s, that would provide the data that are needed to understand how hydrodynamic effects caused by the patterns affect the fouling resistance. Another approach to evaluate the surface modification's effectiveness would be to investigate the threshold flux change after different modifications. These studies could be done using an automated system like the one in our lab that keeps the flux constant by changing the applied pressure on the feed side of the membrane. The pressure increase over a defined time is recorded and slope analysis is used to determine the threshold flux.

5.2.3 Nano-Patterning Commercial Polyamide Membranes

In Chapter 4, 13 different commercial polyamide thin-film composite membranes were patterned with a line and groove nano-pattern. Numerous variables were studied to determine what caused differences in the patterned peak heights of the as received membranes. One variable that was not studied was the type of humectant. Unknown factors are the type and concentration of the humectants in the as received membranes. I recommend performing a water soak of each membrane in with 15 mL of water under gentle agitation for a time sufficiently long to allow humectant to diffuse from the membrane pores. Chromatography followed by Mass Spectrometry (GC-MS or LC-MS) can be used to determine what humectant is used by manufacturers. The challenge will be determining the humectant concentration. One method could be to use the same chromatography method with a calibration standard once the humectant is known. A second method would be to do total organic carbon (TOC) analysis on each humectant solution. Once the humectant is known, then the concentration can be determined through the TOC analysis.

Interestingly, when filled with a 15 wt% glycerol solution of my making, the pattern peak heights of the membranes changed. When changing the concentration of glycerol, the peak heights did not vary according to the expected trend. Based on this unexpected finding, perhaps the membrane pores do not fill uniformly with the humectant. Therefore, I recommend to image using SEM the cross section and top surfaces of the membranes as received (no rinsing) and after filling with a 15 wt% glycerol solution (rinsed membranes have already been imaged and presented in Chapter 4). This would allow visual inspection of the membranes to determine if the filling procedure leads to visual differences in how the glycerol pore fills the membranes. Differences in filling procedure seems unlikely to be the cause of the different peak heights as the industrial way of pore filling the membranes is through a roll-to-roll dip-coating procedure, which is not very different from my immersion procedure.

A final recommendation would be to change the humectant used for membrane preservation to study the role of humectant type on patternability of individual membranes within a polyamide membrane class. This study would be especially important if differences are found in the humectant types used among the commercial membranes. For example, a viscous poly(ethylene glycol) solution could be used to fill the membrane pores prior to patterning, and the pattern peak heights would be measured and compared to results using glycerol.

APPENDICES

Appendix A

Statistical Analysis for A SWITCHABLE ZWITTERIONIC MEMBRANE SURFACE CHEMISTRY FOR BIOFOULING CONTROL

[As published in the Journal of Membrane Science 548 (2018) 490-501 with minor revisions]

Hypothesis testing (multiple mean or t-test) was done to determine statistical relevance of the data sets. SAS® Studio (v. 3.5 enterprise edition) was used online at http://support.sas.com/software/products/ondemand-academics/#s1=2 for all statistical analyses. The Brown and Forsythe's test for homogeneity was done to test for equal variance in the multiple mean hypothesis tests. Equal variance is required to perform the multiple mean hypothesis test. All tests were done using 95% confidence ($\alpha = 0.05$); therefore, if the p-value is greater than α then the variances or means are considered to be equal and if the p-value is less than α then the variances or means are considered to be unequal.

Water permeability coefficient statistical analysis was done using a multiple mean hypothesis test for the data in **Figure 2.10**. GE PES membrane (**Figure 2.10A**) variances were considered equal with a p-value of 0.6338. The p-value for the multiple mean test was < 0.0001, concluding at least one set of data was significantly different from the rest. Using a Tukey's t-test on the data, it was concluded that the unmodified GE PES was statistically different from the modified GE PES. The BP entrapped PES was statistically different from poly(SPE) modified PES and poly(PEGMA) modified PES. The poly(CBOH) modified PES was statistically different from poly(PEGMA) modified PES. To perform the multiple mean hypothesis test on the Microdyn-Nadir PES membranes

(**Figure 2.10B**), it was necessary to take the square root of all data to obtain equal variances (p-value = 0.0079 before taking the square root and p-value = 0.0875 after). The p-value was 0.001 for the multiple mean test, concluding at least one set of data was significantly different from the rest. Using a Tukey's t-test on the data, it was concluded that the poly(SPE) modified Microdyn-Nadir PES was statistically different from the unmodified Microdyn-Nadir PES, BP entrapped Microdyn-Nadir PES, and the poly(CBOH) modified Microdyn-Nadir PES.

Bacteria deposition statistical analysis was done using a multiple mean hypothesis test for the data in **Table 2.1**. The variances were considered equal with a p-value of 0.149. The p-value for the multiple mean test was < 0.0001, concluding at least one set of data was significantly different from the rest. Using a Tukey's t-test on the data, it was concluded that unmodified PES was statistically different from the surface modified PES membranes. All the surface modified PES membranes were considered statistically the same at 95% confidence.

The biofilm volumetric quantification (no acid rinse) statistical analysis was done using a multiple mean hypothesis test for the data in **Table 2.3**. **Table A-1** presents the results of the statistical analysis for all nine variables. Using a Tukey's t-test on the data, it was concluded that all biovolumes, all biomass thicknesses, and no biomass roughness values between the unmodified membrane and the poly(CBOH) modified or poly(SPE) modified membranes were considered statistically different.

Table A-1. Statistical analysis results of the biofilm volumetric quantification between the unmodified, poly(CBOH) modified, and poly(SPE) modified Microdyn-Nadir PM UP150 PES membranes. Interpretation (what is statistically different) was done using a Tukey's t-test.

Test Variable	Equal Variance p-value	Equal Means p-value	Statistically Different (95% Confidence)
Dead Biovolume	0.351	< 0.0001	All
Live Biovolume	0.250	< 0.0001	Unmodified – poly(CBOH) Unmodified – poly(SPE)
EPS Biovolume	0.190	0.0012	Unmodified – poly(CBOH) poly(CBOH) – poly(SPE)
Dead Biomass Thickness	0.654	< 0.0001	Unmodified – poly(CBOH) Unmodified – poly(SPE)
Live Biomass Thickness	0.225	0.0093	Unmodified – poly(CBOH) Unmodified – poly(SPE)
EPS Biomass Thickness	0.390	< 0.0001	Unmodified – poly(CBOH) Unmodified – poly(SPE)
Dead Biomass Roughness	0.0004	N/A	N/A
Live Biomass Roughness	0.304	0.594	All Statistically the Same
EPS Biomass Roughness	0.195	0.558	All Statistically the Same

The biofilm volumetric quantification for poly(CBOH) modified membranes without and with acid rinse were done on the data from **Table 2.3** and **Table 2.4** using a pooled (equal variance) or Satterthwaite (unequal variance) two-tailed t-test. **Table A-2** presents the results of the statistical analysis for all nine variables. If the equal variance p-value was less than 0.05, then the Satterthwaite t-test was used, otherwise the pooled t-test was used. Dead biovolume, dead biomass thickness, live biomass thickness, and dead biomass roughness coefficient are all considered to be statistically different. Live

biovolume, EPS biovolume, EPS biomass thickness, live biomass roughness coefficient, and EPS biomass coefficient are all considered to be statistically the same.

Table A-2. Statistical analysis results of the biofilm volumetric quantification between the poly(CBOH) modified Microdyn-Nadir PM UP150 PES membranes with and without acid rinse.

Test Variable	Equal Variance p-value	t-test used	Equal Means p-value	Interpretation (95% Confidence)
Dead Biovolume	0.0792	pooled	< 0.0001	Statistically Different
Live Biovolume	0.0036	Satterthwaite	0.075	Statistically the Same
EPS Biovolume	0.185	pooled	0.693	Statistically the Same
Dead Biomass Thickness	0.573	pooled	0.0003	Statistically Different
Live Biomass Thickness	0.044	Satterthwaite	0.007	Statistically Different
EPS Biomass Thickness	0.038	Satterthwaite	0.894	Statistically the Same
Dead Biomass Roughness	0.143	pooled	0.022	Statistically Different
Live Biomass Roughness	< 0.0001	Satterthwaite	0.082	Statistically the Same
EPS Biomass Roughness	0.024	Satterthwaite	0.930	Statistically the Same

The biofilm volumetric quantification for poly(SPE) modified membranes with and without acid rinse were done on the data from **Table 2.3** and **Table 2.4** using a pooled (equal variance) or Satterthwaite (unequal variance) two-tailed t-test. **Table A-3** presents the results of the statistical analysis for all nine variables. If the equal variance p-

value was less than 0.05, then the Satterthwaite t-test was used, otherwise the pooled t-test was used. EPS biovolume, dead biomass thickness, and EPS biomass thickness are all considered to be statistically different. Dead biovolume, live biovolume, live biomass thickness, dead biomass roughness coefficient, live biomass roughness coefficient, and EPS biomass coefficient are all considered to be statistically the same.

Table A-3. Statistical analysis results of the biofilm volumetric quantification between the poly(SPE) modified Microdyn-Nadir PM UP150 PES membranes with and without acid rinse.

Test Variable	**Equal Variance p-value**	**t-test used**	**Equal Means p-value**	**Interpretation (95% Confidence)**
Dead Biovolume	0.222	pooled	0.140	Statistically the Same
Live Biovolume	0.692	pooled	0.583	Statistically the Same
EPS Biovolume	0.092	pooled	< 0.0001	Statistically Different
Dead Biomass Thickness	0.222	pooled	0.130	Statistically Different
Live Biomass Thickness	0.718	pooled	0.775	Statistically the Same
EPS Biomass Thickness	< 0.0001	Satterthwaite	0.0002	Statistically Different
Dead Biomass Roughness	0.332	pooled	0.382	Statistically the Same
Live Biomass Roughness	0.024	Satterthwaite	0.820	Statistically the Same
EPS Biomass Roughness	< 0.0001	Satterthwaite	0.113	Statistically the Same

GE PES water contact angle statistical analysis was done using a pooled (equal variance) or Satterthwaite (unequal variance) two-tailed t-test between the data for the unmodified PES and modified PES in **Figure 2.8A**. **Table A-4** presents the results of the statistical analysis for all tests. If the equal variance p-value was less than 0.05, then the Satterthwaite t-test was used, otherwise the pooled t-test was used. A multiple mean hypothesis test could not be done because the variances were not considered equal. Unmodified compared with BP entrapped and poly(PEGMA) are considered statistically different, while unmodified compared with poly(CBOH) and poly(SPE) are considered statistically the same.

Table A-4. Statistical analysis results between the water contact angle data for the unmodified and polymer modified GE PES membranes.

Test Variable	Equal Variance p-value	t-test used	Equal Means p-value	Interpretation (95% Confidence)
BP entrapped	0.103	pooled	0.019	Statistically Different
poly(CBOH)	0.705	pooled	0.349	Statistically the Same
poly(SPE)	0.186	pooled	0.488	Statistically the Same
poly(PEGMA)	0.216	pooled	0.002	Statistically Different

Microdyn-Nadir PM UP150 water contact angle statistical analysis was done using a pooled (equal variance) or Satterthwaite (unequal variance) two-tailed t-test between the data for the unmodified PES and modified PES in **Figure 2.8B**. **Table A-5** presents the results of the statistical analysis for all tests. If the equal variance p-value was less than 0.05, then the Satterthwaite t-test was used, otherwise the pooled t-test was used. A multiple mean hypothesis test could not be done because the variances were not

considered equal. All modified Microdyn-Nadir membranes were considered statistically different from the unmodified Microdyn-Nadir membranes.

Table A-5. Statistical analysis results between the water contact angle data for the unmodified and polymer modified Microdyn-Nadir PM UP150 PES membranes.

Test Variable	**Equal Variance p-value**	**t-test used**	**Equal Means p-value**	**Interpretation (95% Confidence)**
BP entrapped	0.0003	Satterthwaite	< 0.0001	Statistically Different
poly(CBOH)	0.1395	Pooled	< 0.0001	Statistically Different
poly(SPE)	0.0029	Satterthwaite	< 0.0001	Statistically Different

Appendix B

Statistical Analysis for NANOPATTERNING COMMERCIAL NANOFILTRATION AND REVERSE OSMOSIS MEMBRANES

[As submitted to Journal of Membrane Science for publication with minor revisions]

Hypothesis testing (multiple mean or t-test) was done to determine statistical relevance of the data sets. SAS® Studio (v. 3.5 enterprise edition) was used online at http://support.sas.com/software/products/ondemand-academics/#s1=2 for all statistical analyses. The Brown and Forsythe's test for homogeneity was done to test for equal variance in the multiple mean hypothesis tests. Equal variance is required to perform the multiple mean hypothesis test. Interpretation (what is statistically different) of a multiple mean hypothesis test was done using a Tukey's t-test. A pooled (equal variance) or Satterthwaite (unequal variance) two-tailed t-test was used where multiple mean hypothesis tests were not acceptable. All tests were done using 95% confidence ($\alpha = 0.05$); therefore, if the p-value is greater than α then the variances or means are considered to be equal and if the p-value is less than α then the variances or means are considered to be unequal.

Surface roughness statistical analysis was done using a multiple mean hypothesis test for the data in **Figure 4.13**. **Table B-1** shows results for the statistical analysis for each membrane. The pristine, pressed, and patterned roughness were considered statistically the same for GE SG, GE HL, Synder NFG, Nanostone NF4, TriSep XN45, and GE DK membranes. The following pristine, pressed, and patterned roughness were all considered statistically different for Dow BW30XFR, Dow SW30HRLE, Toray UTC-

82V, and TriSep ACM4 membranes. Pressed and pristine roughness were considered statistically different for TriSep X201, GE Duracid KH, GE PW, and Nanostone PS20 membranes. Patterned and pressed roughness were considered statistically different for TriSep X201, Dow NF270, GE PW, and Nanostone PS20 membranes. Patterned and pristine roughness were considered statistically different for GE Duracid KH and Nanostone PS20 membranes.

Table B-1. Statistical analysis results of the pristine, pressed, and patterned surface roughness of commercial nanofiltration and reverse osmosis membranes. Interpretation (what is statistically different) was done using a Tukey's t-test.

Test Variable	**Equal Variance p-value**	**Equal Means p-value**	**Statistically Different (95% Confidence)**
Dow BW30XFR	0.4946	< 0.0001	All are Statistically Different
Dow SW30HRLE	0.5611	0.0020	All are Statistically Different
Toray UTC-82V	0.3425	0.0001	All are Statistically Different
TriSep ACM4	0.8354	< 0.0001	All are Statistically Different
TriSep X201	0.6525	0.0003	Pressed – Pristine Patterned - Pressed
GE SG	0.8978	0.1097	All are Statistically Same
GE HL	0.4347	0.1101	All are Statistically Same
Dow NF270	0.1880	0.0218	Patterned - Pressed
Synder NFG	0.1286	0.0720	All are Statistically Same
Nanostone NF4	0.4192	0.2996	All are Statistically Same
TriSep XN45	0.4324	0.0574	All are Statistically Same
GE DK	0.6801	0.0719	All are Statistically Same
GE Duracid KH	0.7048	0.0163	Pressed – Pristine Patterned - Pristine
GE PW	0.1591	0.0115	Pressed – Pristine Patterned - Pressed
Nanostone PS20	0.0702	0.0001	Patterned – Pristine Patterned - Pressed

Membrane permeance statistical analysis was done using a multiple mean hypothesis test for the data in **Figure 4.16A**. **Table B-2** shows results for the statistical analysis for each membrane. The following membrane permeances were considered statistically the same: Dow SW30HRLE, Toray UTC-82V, GE HL, Dow NF270, Nanostone NF4, TriSep XN45, GE DK, and GE Duracid KH. The following membrane permeances were considered statistically different for the pressed-pristine and patterned-pristine membranes: Dow BW30XFR, TriSep ACM4, TriSep X201, GE SG, and Synder NFG.

Table B-2. Statistical analysis results of the pristine, pressed, and patterned permeance of commercial nanofiltration and reverse osmosis membranes. Interpretation (what is statistically different) was done using a Tukey's t-test.

Test Variable	**Equal Variance p-value**	**Equal Means p-value**	**Statistically Different (95% Confidence)**
Dow BW30XFR	0.5132	0.0004	Pressed – Pristine Patterned – Pristine
Dow SW30HRLE	0.7461	0.0539	All Statistically the Same
Toray UTC-82V	0.9705	0.9534	All Statistically the Same
TriSep ACM4	0.6366	0.0270	Pressed – Pristine Patterned – Pristine
TriSep X201	0.5808	0.0064	Pressed – Pristine Patterned – Pristine
GE SG	0.9589	0.0014	Pressed – Pristine Patterned – Pristine
GE HL	0.3735	0.2756	All Statistically the Same
Dow NF270	0.9866	0.1096	All Statistically the Same
Synder NFG	0.8724	0.0015	Pressed – Pristine Patterned – Pristine
Nanostone NF4	0.5951	0.5606	All Statistically the Same
TriSep XN45	0.8740	0.9758	All Statistically the Same
GE DK	0.3193	0.4754	All Statistically the Same
GE Duracid KH	0.8916	0.6142	All Statistically the Same

Membrane $MgSO_4$ rejection statistical analysis was done using a multiple mean hypothesis test for the data in **Figure 4.16B**. **Table B-3** shows results for the statistical analysis for each membrane. All rejections were considered statistically the same except for the TriSep ACM4 pressed-pristine and patterned-pristine membranes, the Dow NF270 patterned-pristine membranes, and the Synder NFG patterned-pristine membranes.

Table B-3. Statistical analysis results of the pristine, pressed, and patterned $MgSO_4$ rejection of commercial nanofiltration and reverse osmosis membranes. Interpretation (what is statistically different) was done using a Tukey's t-test.

Test Variable	Equal Variance p-value	Equal Means p-value	Statistically Different (95% Confidence)
Dow BW30XFR	0.4890	0.1883	All Statistically the Same
Dow SW30HRLE	0.4336	0.2982	All Statistically the Same
Toray UTC-82V	0.3081	0.3761	All Statistically the Same
TriSep ACM4	0.4348	0.0013	Pressed – Pristine Patterned – Pristine
TriSep X201	0.3280	0.1227	All Statistically the Same
GE SG	0.9491	0.8625	All Statistically the Same
GE HL	0.7101	0.1759	All Statistically the Same
Dow NF270	0.4407	0.0112	Patterned – Pristine
Synder NFG	0.3852	0.0327	Patterned – Pristine
Nanostone NF4	0.4923	0.4549	All Statistically the Same
TriSep XN45	0.3308	0.2947	All Statistically the Same
GE DK	0.1485	0.2673	All Statistically the Same
GE Duracid KH	0.9994	0.9156	All Statistically the Same

Statistical analyses of pattern peak heights of the as received and 15wt% glycerol filled membranes were done using a pooled (equal variance) or Satterthwaite (unequal

variance) two-tailed t-test for the data in **Figure 4.17**. **Table B-4** shows results for the statistical analysis for each membrane. All peak heights were statistically different except for the membrane supports (Nanostone PS20 and GE PW). This indicates that the humectant used could play a role in how the membrane patterns. It also indicates that there is possible plasticization of the polyamide layer with glycerol.

Table B-4. Statistical analysis results of the pattern peak heights of the as received and 15wt% glycerol filled membranes of commercial nanofiltration and reverse osmosis membranes.

Test Variable	**Equal Variance p-value**	**t-test used**	**Equal Means p-value**	**Interpretation (95% Confidence)**
Dow BW30XFR	0.0068	Satterthwaite	0.0013	Statistically Different
Dow SW30HRLE	0.0014	Satterthwaite	0.0089	Statistically Different
Toray UTC-82V	0.0837	pooled	< 0.0001	Statistically Different
TriSep ACM4	< 0.0001	Satterthwaite	< 0.0001	Statistically Different
TriSep X201	0.0107	Satterthwaite	< 0.0001	Statistically Different
GE SG	0.9030	pooled	< 0.0001	Statistically Different
GE HL	< 0.0001	Satterthwaite	< 0.0001	Statistically Different
Dow NF270	< 0.0001	Satterthwaite	< 0.0001	Statistically Different
Synder NFG	< 0.0001	Satterthwaite	< 0.0001	Statistically Different
Nanostone NF4	< 0.0001	Satterthwaite	< 0.0001	Statistically Different
TriSep XN45	0.7364	pooled	< 0.0001	Statistically Different
GE DK	< 0.0001	Satterthwaite	< 0.0001	Statistically Different
GE Duracid KH	< 0.0001	Satterthwaite	< 0.0001	Statistically Different
GE PW	0.7527	pooled	0.7309	Statistically the Same
Nanostone PS20	0.7465	pooled	0.4239	Statistically the Same

Statistical analyses of pattern peak heights of the 15wt% glycerol filled for 5 min and 24.5 h membranes were done using a pooled (equal variance) or Satterthwaite

(unequal variance) two-tailed t-test for the data in **Figure 4.18**. **Table B-5** shows results for the statistical analysis for each membrane. Both membrane peaks heights were considered statistically the same at both 5 min and 24.5 h immersion, indicating that 5 min immersion time is long enough.

Table B-5. Statistical analysis results of the pattern peak heights of the 15wt% glycerol filled Dow NF270 and Synder NFG membranes using 5 min and 24.5 h soak times.

Test Variable	**Equal Variance p-value**	**t-test used**	**Equal Means p-value**	**Interpretation (95% Confidence)**
Dow NF270	0.2216	pooled	0.2843	Statistically the Same
Synder NFG	0.5713	pooled	0.1497	Statistically the Same

Statistical analysis on the Young's Modulus of the as received, rinsed, and 15wt% glycerol filled membranes using a 5 min soak time was done using a pooled (equal variance) or Satterthwaite (unequal variance) two-tailed t-test for the data in **Figure 4.20**. **Table B-6** shows results for the statistical analysis for each membrane. Everything was considered statistically different except for the TriSep X201 rinsed and 15 wt% glycerol filled membranes.

Table B-6. Statistical analysis results of the Young's Modulus of the as received, rinsed, and 15wt% glycerol filled GE Duracid KH, GE DK, and TriSep X201 membranes using 5-minute soak time.

Test Variable	Equal Variance p-value	t-test used	Equal Means p-value	Interpretation (95% Confidence)
GE Duracid KH As Received – Rinsed	0.0002	Satterthwaite	< 0.0001	Statistically Different
GE Duracid KH As Received – 15wt% Glycerol	0.0013	Satterthwaite	< 0.0001	Statistically Different
GE Duracid KH Rinsed – 15wt% Glycerol	0.6175	pooled	< 0.0001	Statistically Different
GE DK As Received - Rinsed	< 0.0001	Satterthwaite	< 0.0001	Statistically Different
GE DK As Received – 15wt% Glycerol	< 0.0001	Satterthwaite	< 0.0001	Statistically Different
GE DK Rinsed – 15wt% Glycerol	< 0.0001	Satterthwaite	< 0.0001	Statistically Different
TriSep X201 As Received - Rinsed	0.0029	Satterthwaite	< 0.0001	Statistically Different
TriSep X201 As Received – 15wt% Glycerol	< 0.0001	Satterthwaite	< 0.0001	Statistically Different
TriSep X201 Rinsed – 15wt% Glycerol	0.0154	Satterthwaite	0.2213	Statistically the Same

Water swelled and 15wt% glycerol swelled polyamide layer thickness statistical analysis was done using a pooled (equal variance) or Satterthwaite (unequal variance) two-tailed t-test for the data in **Figure 4.21**. **Table B-7** shows results for the statistical analysis for each membrane. Dow NF270, Synder NFG, and GE Duracid KH were considered statistically the same, while the TriSep X201 was considered statistically different.

Table B-7. Statistical analysis results of the water swelled and 15wt% glycerol swelled polyamide layer thickness of the Dow NF270, Synder NFG, TriSep X201, and GE Duracid KH membranes.

Test Variable	**Equal Variance p-value**	**t-test used**	**Equal Means p-value**	**Interpretation (95% Confidence)**
Dow NF270	0.1542	pooled	0.6171	Statistically the Same
Synder NFG	0.0390	Satterthwaite	0.9644	Statistically the Same
TriSep X201	0.1473	pooled	< 0.0001	Statistically Different
GE Duracid KH	0.9533	pooled	0.9329	Statistically the Same

Appendix C

Permissions to reproduce figures and text

Permission was received to reproduce selected figures in Chapter 1 as well as to reproduce the full content presented in Chapters 2 and 3 through the Copyright Clearance Center (www.copyright.com). All documentation of the approvals is listed in the following pages.

Chapter 2

Chapter 3


Copyright Clearance Center
RightsLink®
Home
Create Account
Help
journal of MEMBRANE SCIENCE
Title: Influence of chemical coating combined with nanopatterning on alginate fouling during nanofiltration
Author: Steven T. Weinman,Scott M. Husson
Publication: Journal of Membrane Science
Publisher: Elsevier
Date: 1 September 2016
© 2016 Elsevier B.V. All rights reserved.
LOGIN
If you're a copyright.com user, you can login to RightsLink using your copyright.com credentials.
Already a RightsLink user or want to learn more?
Please note that, as the author of this Elsevier article, you retain the right to include it in a thesis or dissertation, provided it is not published commercially. Permission is not required, but please ensure that you reference the journal as the original source. For more information on this and on your other retained rights, please visit: https://www.elsevier.com/about/our-business/policies/copyright#Author-rights
BACK
CLOSE WINDOW
Copyright © 2018 Copyright Clearance Center, Inc. All Rights Reserved. Privacy statement. Terms and Conditions.
Comments? We would like to hear from you. E-mail us at customercare@copyright.com

Figure 1.3

Copyright Clearance Center RightsLink®

Home | Create Account | Help

ACS Publications
Most Trusted. Most Cited. Most Read.

Title: Thin-Film Composite Polyamide Membranes Functionalized with Biocidal Graphene Oxide Nanosheets

Author: François Perreault, Marissa E. Tousley, Menachem Elimelech

Publication: Environmental Science & Technology Letters

Publisher: American Chemical Society

Date: Jan 1, 2014

Copyright © 2014, American Chemical Society

LOGIN

If you're a copyright.com user, you can login to RightsLink using your copyright.com credentials.

Already a RightsLink user o want to learn more?

PERMISSION/LICENSE IS GRANTED FOR YOUR ORDER AT NO CHARGE

This type of permission/license, instead of the standard Terms & Conditions, is sent to you because no fee is being charged for your order. Please note the following:

- Permission is granted for your request in both print and electronic formats, and translations.
- If figures and/or tables were requested, they may be adapted or used in part.
- Please print this page for your records and send a copy of it to your publisher/graduate school.
- Appropriate credit for the requested material should be given as follows: "Reprinted (adapted) with permission from (COMPLETE REFERENCE CITATION). Copyright (YEAR) American Chemical Society." Insert appropriate information in place of the capitalized words.
- One-time permission is granted only for the use specified in your request. No additional uses are granted (such as derivative works or other editions). For any other uses, please submit a new request.

If credit is given to another source for the material you requested, permission must be obtained

Figure 1.4

JOHN WILEY AND SONS LICENSE TERMS AND CONDITIONS

Feb 26, 2018

This Agreement between Steven Weinman ("You") and John Wiley and Sons ("John Wiley and Sons") consists of your license details and the terms and conditions provided by John Wiley and Sons and Copyright Clearance Center.

License Number	4296691186671
License date	Feb 26, 2018
Licensed Content Publisher	John Wiley and Sons
Licensed Content Publication	Angewandte Chemie International Edition
Licensed Content Title	Reversibly Switching the Function of a Surface between Attacking and Defending against Bacteria
Licensed Content Author	Zhiqiang Cao,Luo Mi,Jose Mendiola,Jean-Rene Ella-Menye,Lei Zhang,Hong Xue,Shaoyi Jiang
Licensed Content Date	Dec 30, 2011
Licensed Content Pages	4
Type of use	Dissertation/Thesis
Requestor type	University/Academic
Format	Print and electronic
Portion	Figure/table
Number of figures/tables	1
Original Wiley figure/table number(s)	Figure 1
Will you be translating?	No
Title of your thesis / dissertation	DEVELOPMENT OF ANTI-FOULING MEMBRANES FOR WATER TREATMENT
Expected completion date	Mar 2018
Expected size (number of pages)	200
Requestor Location	Steven Weinman 201 Tillwa Court Apt. 224 CENTRAL, SC 29630 United States Attn: Steven Weinman
Publisher Tax ID	EU826007151
Total	0.00 USD
Terms and Conditions	

TERMS AND CONDITIONS

This copyrighted material is owned by or exclusively licensed to John Wiley & Sons, Inc. or one of its group companies (each a"Wiley Company") or handled on behalf of a society with which a Wiley Company has exclusive publishing rights in relation to a particular work (collectively "WILEY"). By clicking "accept" in connection with completing this licensing

transaction, you agree that the following terms and conditions apply to this transaction (along with the billing and payment terms and conditions established by the Copyright Clearance Center Inc., ("CCC's Billing and Payment terms and conditions"), at the time that you opened your RightsLink account (these are available at any time at http://myaccount.copyright.com).

Terms and Conditions

- The materials you have requested permission to reproduce or reuse (the "Wiley Materials") are protected by copyright.
- You are hereby granted a personal, non-exclusive, non-sublicensable (on a stand-alone basis), non-transferable, worldwide, limited license to reproduce the Wiley Materials for the purpose specified in the licensing process. This license, **and any CONTENT (PDF or image file) purchased as part of your order,** is for a one-time use only and limited to any maximum distribution number specified in the license. The first instance of republication or reuse granted by this license must be completed within two years of the date of the grant of this license (although copies prepared before the end date may be distributed thereafter). The Wiley Materials shall not be used in any other manner or for any other purpose, beyond what is granted in the license. Permission is granted subject to an appropriate acknowledgement given to the author, title of the material/book/journal and the publisher. You shall also duplicate the copyright notice that appears in the Wiley publication in your use of the Wiley Material. Permission is also granted on the understanding that nowhere in the text is a previously published source acknowledged for all or part of this Wiley Material. Any third party content is expressly excluded from this permission.
- With respect to the Wiley Materials, all rights are reserved. Except as expressly granted by the terms of the license, no part of the Wiley Materials may be copied, modified, adapted (except for minor reformatting required by the new Publication), translated, reproduced, transferred or distributed, in any form or by any means, and no derivative works may be made based on the Wiley Materials without the prior permission of the respective copyright owner. **For STM Signatory Publishers clearing permission under the terms of the STM Permissions Guidelines only, the terms of the license are extended to include subsequent editions and for editions in other languages, provided such editions are for the work as a whole in situ and does not involve the separate exploitation of the permitted figures or extracts,** You may not alter, remove or suppress in any manner any copyright, trademark or other notices displayed by the Wiley Materials. You may not license, rent, sell, loan, lease, pledge, offer as security, transfer or assign the Wiley Materials on a stand-alone basis, or any of the rights granted to you hereunder to any other person.
- The Wiley Materials and all of the intellectual property rights therein shall at all times remain the exclusive property of John Wiley & Sons Inc, the Wiley Companies, or their respective licensors, and your interest therein is only that of having possession of and the right to reproduce the Wiley Materials pursuant to Section 2 herein during the continuance of this Agreement. You agree that you own no right, title or interest in or to the Wiley Materials or any of the intellectual property rights therein. You shall have no rights hereunder other than the license as provided for above in Section 2. No right, license or interest to any trademark, trade name, service mark or other branding ("Marks") of WILEY or its licensors is granted hereunder, and you agree that you shall not assert any such right, license or interest with respect thereto

- NEITHER WILEY NOR ITS LICENSORS MAKES ANY WARRANTY OR REPRESENTATION OF ANY KIND TO YOU OR ANY THIRD PARTY, EXPRESS, IMPLIED OR STATUTORY, WITH RESPECT TO THE MATERIALS OR THE ACCURACY OF ANY INFORMATION CONTAINED IN THE MATERIALS, INCLUDING, WITHOUT LIMITATION, ANY IMPLIED WARRANTY OF MERCHANTABILITY, ACCURACY, SATISFACTORY QUALITY, FITNESS FOR A PARTICULAR PURPOSE, USABILITY, INTEGRATION OR NON-INFRINGEMENT AND ALL SUCH WARRANTIES ARE HEREBY EXCLUDED BY WILEY AND ITS LICENSORS AND WAIVED BY YOU.

- WILEY shall have the right to terminate this Agreement immediately upon breach of this Agreement by you.

- You shall indemnify, defend and hold harmless WILEY, its Licensors and their respective directors, officers, agents and employees, from and against any actual or threatened claims, demands, causes of action or proceedings arising from any breach of this Agreement by you.

- IN NO EVENT SHALL WILEY OR ITS LICENSORS BE LIABLE TO YOU OR ANY OTHER PARTY OR ANY OTHER PERSON OR ENTITY FOR ANY SPECIAL, CONSEQUENTIAL, INCIDENTAL, INDIRECT, EXEMPLARY OR PUNITIVE DAMAGES, HOWEVER CAUSED, ARISING OUT OF OR IN CONNECTION WITH THE DOWNLOADING, PROVISIONING, VIEWING OR USE OF THE MATERIALS REGARDLESS OF THE FORM OF ACTION, WHETHER FOR BREACH OF CONTRACT, BREACH OF WARRANTY, TORT, NEGLIGENCE, INFRINGEMENT OR OTHERWISE (INCLUDING, WITHOUT LIMITATION, DAMAGES BASED ON LOSS OF PROFITS, DATA, FILES, USE, BUSINESS OPPORTUNITY OR CLAIMS OF THIRD PARTIES), AND WHETHER OR NOT THE PARTY HAS BEEN ADVISED OF THE POSSIBILITY OF SUCH DAMAGES. THIS LIMITATION SHALL APPLY NOTWITHSTANDING ANY FAILURE OF ESSENTIAL PURPOSE OF ANY LIMITED REMEDY PROVIDED HEREIN.

- Should any provision of this Agreement be held by a court of competent jurisdiction to be illegal, invalid, or unenforceable, that provision shall be deemed amended to achieve as nearly as possible the same economic effect as the original provision, and the legality, validity and enforceability of the remaining provisions of this Agreement shall not be affected or impaired thereby.

- The failure of either party to enforce any term or condition of this Agreement shall not constitute a waiver of either party's right to enforce each and every term and condition of this Agreement. No breach under this agreement shall be deemed waived or excused by either party unless such waiver or consent is in writing signed by the party granting such waiver or consent. The waiver by or consent of a party to a breach of any provision of this Agreement shall not operate or be construed as a waiver of or consent to any other or subsequent breach by such other party.

- This Agreement may not be assigned (including by operation of law or otherwise) by you without WILEY's prior written consent.

- Any fee required for this permission shall be non-refundable after thirty (30) days from receipt by the CCC.

- These terms and conditions together with CCC's Billing and Payment terms and conditions (which are incorporated herein) form the entire agreement between you and WILEY concerning this licensing transaction and (in the absence of fraud) supersedes all prior agreements and representations of the parties, oral or written. This Agreement may not be amended except in writing signed by both parties. This Agreement shall be binding upon and inure to the benefit of the parties' successors, legal representatives, and authorized assigns.

- In the event of any conflict between your obligations established by these terms and conditions and those established by CCC's Billing and Payment terms and conditions, these terms and conditions shall prevail.

- WILEY expressly reserves all rights not specifically granted in the combination of (i) the license details provided by you and accepted in the course of this licensing transaction, (ii) these terms and conditions and (iii) CCC's Billing and Payment terms and conditions.

- This Agreement will be void if the Type of Use, Format, Circulation, or Requestor Type was misrepresented during the licensing process.

- This Agreement shall be governed by and construed in accordance with the laws of the State of New York, USA, without regards to such state's conflict of law rules. Any legal action, suit or proceeding arising out of or relating to these Terms and Conditions or the breach thereof shall be instituted in a court of competent jurisdiction in New York County in the State of New York in the United States of America and each party hereby consents and submits to the personal jurisdiction of such court, waives any objection to venue in such court and consents to service of process by registered or certified mail, return receipt requested, at the last known address of such party.

WILEY OPEN ACCESS TERMS AND CONDITIONS

Wiley Publishes Open Access Articles in fully Open Access Journals and in Subscription journals offering Online Open. Although most of the fully Open Access journals publish open access articles under the terms of the Creative Commons Attribution (CC BY) License only, the subscription journals and a few of the Open Access Journals offer a choice of Creative Commons Licenses. The license type is clearly identified on the article.

The Creative Commons Attribution License

The Creative Commons Attribution License (CC-BY) allows users to copy, distribute and transmit an article, adapt the article and make commercial use of the article. The CC-BY license permits commercial and non-

Creative Commons Attribution Non-Commercial License

The Creative Commons Attribution Non-Commercial (CC-BY-NC)License permits use, distribution and reproduction in any medium, provided the original work is properly cited and is not used for commercial purposes.(see below)

Creative Commons Attribution-Non-Commercial-NoDerivs License

The Creative Commons Attribution Non-Commercial-NoDerivs License (CC-BY-NC-ND) permits use, distribution and reproduction in any medium, provided the original work is properly cited, is not used for commercial purposes and no modifications or adaptations are made. (see below)

Use by commercial "for-profit" organizations

Use of Wiley Open Access articles for commercial, promotional, or marketing purposes requires further explicit permission from Wiley and will be subject to a fee.

Further details can be found on Wiley Online Library
http://olabout.wiley.com/WileyCDA/Section/id-410895.html

Other Terms and Conditions:

v1.10 Last updated September 2015

Questions? customercare@copyright.com or +1-855-239-3415 (toll free in the US) or +1-978-646-2777.

Figure 1.5

ELSEVIER LICENSE
TERMS AND CONDITIONS

Feb 26, 2018

This Agreement between Steven Weinman ("You") and Elsevier ("Elsevier") consists of your license details and the terms and conditions provided by Elsevier and Copyright Clearance Center.

License Number	4296770412569
License date	Feb 26, 2018
Licensed Content Publisher	Elsevier
Licensed Content Publication	Journal of Membrane Science
Licensed Content Title	Effect of surface pattern formation on membrane fouling and its control in phase inversion process
Licensed Content Author	R. Jamshidi Gohari,W.J. Lau,T. Matsuura,A.F. Ismail
Licensed Content Date	Nov 1, 2013
Licensed Content Volume	446
Licensed Content Issue	n/a
Licensed Content Pages	6
Start Page	326
End Page	331
Type of Use	reuse in a thesis/dissertation
Portion	figures/tables/illustrations
Number of figures/tables/illustrations	1
Format	both print and electronic
Are you the author of this Elsevier article?	No
Will you be translating?	No
Original figure numbers	Figure 5
Title of your thesis/dissertation	DEVELOPMENT OF ANTI-FOULING MEMBRANES FOR WATER TREATMENT
Expected completion date	Mar 2018
Estimated size (number of pages)	200
Requestor Location	Steven Weinman 201 Tillwa Court Apt. 224 CENTRAL, SC 29630 United States Attn: Steven Weinman
Publisher Tax ID	98-0397604
Total	0.00 USD
Terms and Conditions	

INTRODUCTION

1. The publisher for this copyrighted material is Elsevier. By clicking "accept" in connection with completing this licensing transaction, you agree that the following terms and conditions apply to this transaction (along with the Billing and Payment terms and conditions established by Copyright Clearance Center, Inc. ("CCC"), at the time that you opened your Rightslink account and that are available at any time at http://myaccount.copyright.com).

GENERAL TERMS

2. Elsevier hereby grants you permission to reproduce the aforementioned material subject to the terms and conditions indicated.

3. Acknowledgement: If any part of the material to be used (for example, figures) has appeared in our publication with credit or acknowledgement to another source, permission must also be sought from that source. If such permission is not obtained then that material may not be included in your publication/copies. Suitable acknowledgement to the source must be made, either as a footnote or in a reference list at the end of your publication, as follows:

"Reprinted from Publication title, Vol /edition number, Author(s), Title of article / title of chapter, Pages No., Copyright (Year), with permission from Elsevier [OR APPLICABLE SOCIETY COPYRIGHT OWNER]." Also Lancet special credit - "Reprinted from The Lancet, Vol. number, Author(s), Title of article, Pages No., Copyright (Year), with permission from Elsevier."

4. Reproduction of this material is confined to the purpose and/or media for which permission is hereby given.

5. Altering/Modifying Material: Not Permitted. However figures and illustrations may be altered/adapted minimally to serve your work. Any other abbreviations, additions, deletions and/or any other alterations shall be made only with prior written authorization of Elsevier Ltd. (Please contact Elsevier at permissions@elsevier.com). No modifications can be made to any Lancet figures/tables and they must be reproduced in full.

6. If the permission fee for the requested use of our material is waived in this instance, please be advised that your future requests for Elsevier materials may attract a fee.

7. Reservation of Rights: Publisher reserves all rights not specifically granted in the combination of (i) the license details provided by you and accepted in the course of this licensing transaction, (ii) these terms and conditions and (iii) CCC's Billing and Payment terms and conditions.

8. License Contingent Upon Payment: While you may exercise the rights licensed immediately upon issuance of the license at the end of the licensing process for the transaction, provided that you have disclosed complete and accurate details of your proposed use, no license is finally effective unless and until full payment is received from you (either by publisher or by CCC) as provided in CCC's Billing and Payment terms and conditions. If full payment is not received on a timely basis, then any license preliminarily granted shall be deemed automatically revoked and shall be void as if never granted. Further, in the event that you breach any of these terms and conditions or any of CCC's Billing and Payment terms and conditions, the license is automatically revoked and shall be void as if never granted. Use of materials as described in a revoked license, as well as any use of the materials beyond the scope of an unrevoked license, may constitute copyright infringement and publisher reserves the right to take any and all action to protect its copyright in the materials.

9. Warranties: Publisher makes no representations or warranties with respect to the licensed material.

10. Indemnity: You hereby indemnify and agree to hold harmless publisher and CCC, and their respective officers, directors, employees and agents, from and against any and all claims arising out of your use of the licensed material other than as specifically authorized pursuant to this license.

11. No Transfer of License: This license is personal to you and may not be sublicensed, assigned, or transferred by you to any other person without publisher's written permission.

12. No Amendment Except in Writing: This license may not be amended except in a writing signed by both parties (or, in the case of publisher, by CCC on publisher's behalf).
13. Objection to Contrary Terms: Publisher hereby objects to any terms contained in any purchase order, acknowledgment, check endorsement or other writing prepared by you, which terms are inconsistent with these terms and conditions or CCC's Billing and Payment terms and conditions. These terms and conditions, together with CCC's Billing and Payment terms and conditions (which are incorporated herein), comprise the entire agreement between you and publisher (and CCC) concerning this licensing transaction. In the event of any conflict between your obligations established by these terms and conditions and those established by CCC's Billing and Payment terms and conditions, these terms and conditions shall control.
14. Revocation: Elsevier or Copyright Clearance Center may deny the permissions described in this License at their sole discretion, for any reason or no reason, with a full refund payable to you. Notice of such denial will be made using the contact information provided by you. Failure to receive such notice will not alter or invalidate the denial. In no event will Elsevier or Copyright Clearance Center be responsible or liable for any costs, expenses or damage incurred by you as a result of a denial of your permission request, other than a refund of the amount(s) paid by you to Elsevier and/or Copyright Clearance Center for denied permissions.

LIMITED LICENSE

The following terms and conditions apply only to specific license types:
15. **Translation**: This permission is granted for non-exclusive world **English** rights only unless your license was granted for translation rights. If you licensed translation rights you may only translate this content into the languages you requested. A professional translator must perform all translations and reproduce the content word for word preserving the integrity of the article.
16. **Posting licensed content on any Website**: The following terms and conditions apply as follows: Licensing material from an Elsevier journal: All content posted to the web site must maintain the copyright information line on the bottom of each image; A hyper-text must be included to the Homepage of the journal from which you are licensing at http://www.sciencedirect.com/science/journal/xxxxx or the Elsevier homepage for books at http://www.elsevier.com; Central Storage: This license does not include permission for a scanned version of the material to be stored in a central repository such as that provided by Heron/XanEdu.
Licensing material from an Elsevier book: A hyper-text link must be included to the Elsevier homepage at http://www.elsevier.com . All content posted to the web site must maintain the copyright information line on the bottom of each image.

Posting licensed content on Electronic reserve: In addition to the above the following clauses are applicable: The web site must be password-protected and made available only to bona fide students registered on a relevant course. This permission is granted for 1 year only. You may obtain a new license for future website posting.
17. **For journal authors:** the following clauses are applicable in addition to the above:
Preprints:
A preprint is an author's own write-up of research results and analysis, it has not been peer-reviewed, nor has it had any other value added to it by a publisher (such as formatting, copyright, technical enhancement etc.).
Authors can share their preprints anywhere at any time. Preprints should not be added to or enhanced in any way in order to appear more like, or to substitute for, the final versions of articles however authors can update their preprints on arXiv or RePEc with their Accepted Author Manuscript (see below).
If accepted for publication, we encourage authors to link from the preprint to their formal publication via its DOI. Millions of researchers have access to the formal publications on ScienceDirect, and so links will help users to find, access, cite and use the best available

version. Please note that Cell Press, The Lancet and some society-owned have different preprint policies. Information on these policies is available on the journal homepage.
Accepted Author Manuscripts: An accepted author manuscript is the manuscript of an article that has been accepted for publication and which typically includes author-incorporated changes suggested during submission, peer review and editor-author communications.
Authors can share their accepted author manuscript:

- immediately
  - via their non-commercial person homepage or blog
  - by updating a preprint in arXiv or RePEc with the accepted manuscript
  - via their research institute or institutional repository for internal institutional uses or as part of an invitation-only research collaboration work-group
  - directly by providing copies to their students or to research collaborators for their personal use
  - for private scholarly sharing as part of an invitation-only work group on commercial sites with which Elsevier has an agreement
- After the embargo period
  - via non-commercial hosting platforms such as their institutional repository
  - via commercial sites with which Elsevier has an agreement

In all cases accepted manuscripts should:

- link to the formal publication via its DOI
- bear a CC-BY-NC-ND license - this is easy to do
- if aggregated with other manuscripts, for example in a repository or other site, be shared in alignment with our hosting policy not be added to or enhanced in any way to appear more like, or to substitute for, the published journal article.

Published journal article (JPA): A published journal article (PJA) is the definitive final record of published research that appears or will appear in the journal and embodies all value-adding publishing activities including peer review co-ordination, copy-editing, formatting, (if relevant) pagination and online enrichment.
Policies for sharing publishing journal articles differ for subscription and gold open access articles:
Subscription Articles: If you are an author, please share a link to your article rather than the full-text. Millions of researchers have access to the formal publications on ScienceDirect, and so links will help your users to find, access, cite, and use the best available version.
Theses and dissertations which contain embedded PJAs as part of the formal submission can be posted publicly by the awarding institution with DOI links back to the formal publications on ScienceDirect.
If you are affiliated with a library that subscribes to ScienceDirect you have additional private sharing rights for others' research accessed under that agreement. This includes use for classroom teaching and internal training at the institution (including use in course packs and courseware programs), and inclusion of the article for grant funding purposes.
Gold Open Access Articles: May be shared according to the author-selected end-user license and should contain a CrossMark logo, the end user license, and a DOI link to the formal publication on ScienceDirect.
Please refer to Elsevier's posting policy for further information.
18. **For book authors** the following clauses are applicable in addition to the above:
Authors are permitted to place a brief summary of their work online only. You are not allowed to download and post the published electronic version of your chapter, nor may you scan the printed edition to create an electronic version. **Posting to a repository:** Authors are permitted to post a summary of their chapter only in their institution's repository.

19. **Thesis/Dissertation**: If your license is for use in a thesis/dissertation your thesis may be submitted to your institution in either print or electronic form. Should your thesis be published commercially, please reapply for permission. These requirements include permission for the Library and Archives of Canada to supply single copies, on demand, of the complete thesis and include permission for Proquest/UMI to supply single copies, on demand, of the complete thesis. Should your thesis be published commercially, please reapply for permission. Theses and dissertations which contain embedded PJAs as part of the formal submission can be posted publicly by the awarding institution with DOI links back to the formal publications on ScienceDirect.

Elsevier Open Access Terms and Conditions

You can publish open access with Elsevier in hundreds of open access journals or in nearly 2000 established subscription journals that support open access publishing. Permitted third party re-use of these open access articles is defined by the author's choice of Creative Commons user license. See our open access license policy for more information.

Terms & Conditions applicable to all Open Access articles published with Elsevier:

Any reuse of the article must not represent the author as endorsing the adaptation of the article nor should the article be modified in such a way as to damage the author's honour or reputation. If any changes have been made, such changes must be clearly indicated.

The author(s) must be appropriately credited and we ask that you include the end user license and a DOI link to the formal publication on ScienceDirect.

If any part of the material to be used (for example, figures) has appeared in our publication with credit or acknowledgement to another source it is the responsibility of the user to ensure their reuse complies with the terms and conditions determined by the rights holder.

Additional Terms & Conditions applicable to each Creative Commons user license:

CC BY: The CC-BY license allows users to copy, to create extracts, abstracts and new works from the Article, to alter and revise the Article and to make commercial use of the Article (including reuse and/or resale of the Article by commercial entities), provided the user gives appropriate credit (with a link to the formal publication through the relevant DOI), provides a link to the license, indicates if changes were made and the licensor is not represented as endorsing the use made of the work. The full details of the license are available at http://creativecommons.org/licenses/by/4.0.

CC BY NC SA: The CC BY-NC-SA license allows users to copy, to create extracts, abstracts and new works from the Article, to alter and revise the Article, provided this is not done for commercial purposes, and that the user gives appropriate credit (with a link to the formal publication through the relevant DOI), provides a link to the license, indicates if changes were made and the licensor is not represented as endorsing the use made of the work. Further, any new works must be made available on the same conditions. The full details of the license are available at http://creativecommons.org/licenses/by-nc-sa/4.0.

CC BY NC ND: The CC BY-NC-ND license allows users to copy and distribute the Article, provided this is not done for commercial purposes and further does not permit distribution of the Article if it is changed or edited in any way, and provided the user gives appropriate credit (with a link to the formal publication through the relevant DOI), provides a link to the license, and that the licensor is not represented as endorsing the use made of the work. The full details of the license are available at http://creativecommons.org/licenses/by-nc-nd/4.0.

Any commercial reuse of Open Access articles published with a CC BY NC SA or CC BY NC ND license requires permission from Elsevier and will be subject to a fee.

Commercial reuse includes:

- Associating advertising with the full text of the Article
- Charging fees for document delivery or access
- Article aggregation
- Systematic distribution via e-mail lists or share buttons

Posting or linking by commercial companies for use by customers of those companies.

20. **Other Conditions**:

v1.9

REFERENCES

[1] B. Van der Bruggen, C. Vandecasteele, T. Van Gestel, W. Doyen, R. Leysen, A review of pressure-driven membrane processes in wastewater treatment and drinking water production, Environmental Progress & Sustainable Energy, 22 (2003) 46-56.
[2] M.M. Pendergast, E.M. Hoek, A review of water treatment membrane nanotechnologies, Energy & Environmental Science, 4 (2011) 1946-1971.
[3] W. Ho, K. Sirkar, Membrane handbook, Springer Science & Business Media, 2012.
[4] A. Mohammad, Y. Teow, W. Ang, Y. Chung, D. Oatley-Radcliffe, N. Hilal, Nanofiltration membranes review: Recent advances and future prospects, Desalination, 356 (2015) 226-254.
[5] D.R. Paul, Reformulation of the solution-diffusion theory of reverse osmosis, Journal of Membrane Science, 241 (2004) 371-386.
[6] W. Guo, H.-H. Ngo, J. Li, A mini-review on membrane fouling, Bioresource Technology, 122 (2012) 27-34.
[7] T. Nguyen, F.A. Roddick, L. Fan, Biofouling of water treatment membranes: a review of the underlying causes, monitoring techniques and control measures, Membranes, 2 (2012) 804-840.
[8] H.-C. Flemming, G. Schaule, T. Griebe, J. Schmitt, A. Tamachkiarowa, Biofouling—the Achilles heel of membrane processes, Desalination, 113 (1997) 215-225.
[9] M. Herzberg, M. Elimelech, Biofouling of reverse osmosis membranes: role of biofilm-enhanced osmotic pressure, Journal of Membrane Science, 295 (2007) 11-20.
[10] M. Rezakazemi, A. Dashti, H. Riasat Harami, N. Hajilari, Inamuddin, Fouling-resistant membranes for water reuse, Environmental Chemistry Letters, (2018).
[11] D. Rana, T. Matsuura, Surface modifications for antifouling membranes, Chemical Reviews, 110 (2010) 2448-2471.
[12] G.-d. Kang, Y.-m. Cao, Development of antifouling reverse osmosis membranes for water treatment: a review, Water Research, 46 (2012) 584-600.
[13] V. Kochkodan, N. Hilal, A comprehensive review on surface modified polymer membranes for biofouling mitigation, Desalination, 356 (2015) 187-207.
[14] V. Kochkodan, D.J. Johnson, N. Hilal, Polymeric membranes: Surface modification for minimizing (bio) colloidal fouling, Advances in Colloid and Interface Science, 206 (2014) 116-140.
[15] M. Zhou, H. Liu, J.E. Kilduff, R. Langer, D.G. Anderson, G. Belfort, High throughput synthesis and screening of new protein resistant surfaces for membrane filtration, AIChE Journal, 56 (2010) 1932-1945.
[16] S.T. Weinman, M. Bass, S. Pandit, M. Herzberg, V. Freger, S.M. Husson, A switchable zwitterionic membrane surface chemistry for biofouling control, Journal of Membrane Science, 548 (2018) 490-501.
[17] E. Ostuni, R.G. Chapman, R.E. Holmlin, S. Takayama, G.M. Whitesides, A survey of structure-property relationships of surfaces that resist the adsorption of protein, Langmuir, 17 (2001) 5605-5620.

[18] Q. Wei, T. Becherer, S. Angioletti-Uberti, J. Dzubiella, C. Wischke, A.T. Neffe, A. Lendlein, M. Ballauff, R. Haag, Protein interactions with polymer coatings and biomaterials, Angewandte Chemie International Edition, 53 (2014) 8004-8031.
[19] M. Hadidi, A.L. Zydney, Fouling behavior of zwitterionic membranes: Impact of electrostatic and hydrophobic interactions, Journal of Membrane Science, 452 (2014) 97-103.
[20] I. Banerjee, R.C. Pangule, R.S. Kane, Antifouling coatings: recent developments in the design of surfaces that prevent fouling by proteins, bacteria, and marine organisms, Advanced Materials, 23 (2011) 690-718.
[21] B.T. McVerry, M.C. Wong, K.L. Marsh, J.A. Temple, C. Marambio-Jones, E. Hoek, R.B. Kaner, Scalable Antifouling Reverse Osmosis Membranes Utilizing Perfluorophenyl Azide Photochemistry, Macromolecular Rapid Communications, 35 (2014) 1528-1533.
[22] D. Wandera, H.H. Himstedt, M. Marroquin, S.R. Wickramasinghe, S.M. Husson, Modification of ultrafiltration membranes with block copolymer nanolayers for produced water treatment: The roles of polymer chain density and polymerization time on performance, Journal of membrane Science, 403 (2012) 250-260.
[23] N. Tomer, S. Mondal, D. Wandera, S.R. Wickramasinghe, S.M. Husson, Modification of nanofiltration membranes by surface-initiated atom transfer radical polymerization for produced water filtration, Separation Science and Technology, 44 (2009) 3346-3368.
[24] D. Wandera, S.R. Wickramasinghe, S.M. Husson, Modification and characterization of ultrafiltration membranes for treatment of produced water, Journal of Membrane Science, 373 (2011) 178-188.
[25] G. Kang, M. Liu, B. Lin, Y. Cao, Q. Yuan, A novel method of surface modification on thin-film composite reverse osmosis membrane by grafting poly (ethylene glycol), Polymer, 48 (2007) 1165-1170.
[26] X. Lu, S. Romero-Vargas Castrillón, D.L. Shaffer, J. Ma, M. Elimelech, In situ surface chemical modification of thin-film composite forward osmosis membranes for enhanced organic fouling resistance, Environmental Science & Technology, 47 (2013) 12219-12228.
[27] S.R.-V. Castrillón, X. Lu, D.L. Shaffer, M. Elimelech, Amine enrichment and poly (ethylene glycol)(PEG) surface modification of thin-film composite forward osmosis membranes for organic fouling control, Journal of Membrane Science, 450 (2014) 331-339.
[28] S.T. Weinman, S.M. Husson, Influence of chemical coating combined with nanopatterning on alginate fouling during nanofiltration, Journal of Membrane Science, 513 (2016) 146-154.
[29] G.-d. Kang, Z.-n. Liu, H.-j. Yu, Y.-m. Cao, Enhancing antifouling property of commercial polyamide reverse osmosis membrane by surface coating using a brush-like polymer containing poly (ethylene glycol) chains, Desalination and Water Treatment, 37 (2012) 139-145.
[30] M. Chapman Wilbert, J. Pellegrino, A. Zydney, Bench-scale testing of surfactant-modified reverse osmosis/nanofiltration membranes, Desalination, 115 (1998) 15-32.

[31] E. Gaudichet-Maurin, F. Thominette, Ageing of polysulfone ultrafiltration membranes in contact with bleach solutions, Journal of Membrane Science, 282 (2006) 198-204.
[32] S. Yu, G. Yao, B. Dong, H. Zhu, X. Peng, J. Liu, M. Liu, C. Gao, Improving fouling resistance of thin-film composite polyamide reverse osmosis membrane by coating natural hydrophilic polymer sericin, Separation and Purification Technology, 118 (2013) 285-293.
[33] Z.-X. Wang, C.-H. Lau, N.-Q. Zhang, Y.-P. Bai, L. Shao, Mussel-inspired tailoring of membrane wettability for harsh water treatment, Journal of Materials Chemistry A, 3 (2015) 2650-2657.
[34] Z. Wang, X. Jiang, X. Cheng, C.H. Lau, L. Shao, Mussel-inspired hybrid coatings that transform membrane hydrophobicity into high hydrophilicity and underwater superoleophobicity for oil-in-water emulsion separation, ACS Applied Materials & Interfaces, 7 (2015) 9534-9545.
[35] Y.-S. Choi, H. Kang, D.-G. Kim, S.-H. Cha, J.-C. Lee, Mussel-Inspired Dopamine- and Plant-Based Cardanol-Containing Polymer Coatings for Multifunctional Filtration Membranes, ACS Applied Materials & Interfaces, 6 (2014) 21297-21307.
[36] S. Kasemset, A. Lee, D.J. Miller, B.D. Freeman, M.M. Sharma, Effect of polydopamine deposition conditions on fouling resistance, physical properties, and permeation properties of reverse osmosis membranes in oil/water separation, Journal of Membrane Science, 425 (2013) 208-216.
[37] B.D. McCloskey, H.B. Park, H. Ju, B.W. Rowe, D.J. Miller, B.D. Freeman, A bioinspired fouling-resistant surface modification for water purification membranes, Journal of Membrane Science, 413 (2012) 82-90.
[38] G.P. Maier, M.V. Rapp, J.H. Waite, J.N. Israelachvili, A. Butler, Adaptive synergy between catechol and lysine promotes wet adhesion by surface salt displacement, Science, 349 (2015) 628-632.
[39] H.-C. Yang, J. Luo, Y. Lv, P. Shen, Z.-K. Xu, Surface engineering of polymer membranes via mussel-inspired chemistry, Journal of Membrane Science, 483 (2015) 42-59.
[40] S. Zhang, F. Lu, L. Tao, N. Liu, C. Gao, L. Feng, Y. Wei, Bio-Inspired Anti-Oil-Fouling Chitosan-Coated Mesh for Oil/Water Separation Suitable for Broad pH Range and Hyper-Saline Environments, ACS Applied Materials & Interfaces, 5 (2013) 11971-11976.
[41] S. Boributh, A. Chanachai, R. Jiraratananon, Modification of PVDF membrane by chitosan solution for reducing protein fouling, Journal of Membrane Science, 342 (2009) 97-104.
[42] C. Wang, F. Yang, F. Meng, H. Zhang, Y. Xue, G. Fu, High flux and antifouling filtration membrane based on non-woven fabric with chitosan coating for membrane bioreactors, Bioresource Technology, 101 (2010) 5469-5474.
[43] Q. Li, J. Imbrogno, G. Belfort, X.L. Wang, Making polymeric membranes antifouling via “grafting from” polymerization of zwitterions, Journal of Applied Polymer Science, 132 (2015).

[44] S. Jiang, Z. Cao, Ultralow-fouling, functionalizable, and hydrolyzable zwitterionic materials and their derivatives for biological applications, Advanced Materials, 22 (2010) 920-932.
[45] Y.-C. Chiang, Y. Chang, C.-J. Chuang, R.-C. Ruaan, A facile zwitterionization in the interfacial modification of low bio-fouling nanofiltration membranes, Journal of Membrane Science, 389 (2012) 76-82.
[46] S. Tada, C. Inaba, K. Mizukami, S. Fujishita, M. Gemmei-Ide, H. Kitano, A. Mochizuki, M. Tanaka, T. Matsunaga, Anti-Biofouling Properties of Polymers with a Carboxybetaine Moiety, Macromolecular Bioscience, 9 (2009) 63-70.
[47] H. Choi, Y. Jung, S. Han, T. Tak, Y.-N. Kwon, Surface modification of SWRO membranes using hydroxyl poly (oxyethylene) methacrylate and zwitterionic carboxylated polyethyleneimine, Journal of Membrane Science, 486 (2015) 97-105.
[48] M. Birkner, M. Ulbricht, Ultrafiltration membranes with markedly different pH-and ion-responsivity by photografted zwitterionic polysulfobetain or polycarbobetain, Journal of Membrane Science, 494 (2015) 57-67.
[49] M. Ginic-Markovic, T.G. Barclay, K.T. Constantopoulos, E. Markovic, S.R. Clarke, J.G. Matisons, Biofouling resistance of polysulfobetaine coated reverse osmosis membranes, Desalination, 369 (2015) 37-45.
[50] Y.-L. Ji, Q.-F. An, Q. Zhao, W.-D. Sun, K.-R. Lee, H.-L. Chen, C.-J. Gao, Novel composite nanofiltration membranes containing zwitterions with high permeate flux and improved anti-fouling performance, Journal of Membrane Science, 390 (2012) 243-253.
[51] Y.-H. Zhao, K.-H. Wee, R. Bai, Highly hydrophilic and low-protein-fouling polypropylene membrane prepared by surface modification with sulfobetaine-based zwitterionic polymer through a combined surface polymerization method, Journal of Membrane Science, 362 (2010) 326-333.
[52] Y. Zhang, Z. Wang, W. Lin, H. Sun, L. Wu, S. Chen, A facile method for polyamide membrane modification by poly (sulfobetaine methacrylate) to improve fouling resistance, Journal of Membrane Science, 446 (2013) 164-170.
[53] Z. Zhang, S. Chen, Y. Chang, S. Jiang, Surface grafted sulfobetaine polymers via atom transfer radical polymerization as superlow fouling coatings, The Journal of Physical Chemistry B, 110 (2006) 10799-10804.
[54] P.-S. Liu, Q. Chen, S.-S. Wu, J. Shen, S.-C. Lin, Surface modification of cellulose membranes with zwitterionic polymers for resistance to protein adsorption and platelet adhesion, Journal of Membrane Science, 350 (2010) 387-394.
[55] F. Razi, I. Sawada, Y. Ohmukai, T. Maruyama, H. Matsuyama, The improvement of antibiofouling efficiency of polyethersulfone membrane by functionalization with zwitterionic monomers, Journal of Membrane Science, 401 (2012) 292-299.
[56] R. Bernstein, V. Freger, J.-H. Lee, Y.-G. Kim, J. Lee, M. Herzberg, ‘Should I stay or should I go?’Bacterial attachment vs biofilm formation on surface-modified membranes, Biofouling, 30 (2014) 367-376.
[57] P. Bengani, Y. Kou, A. Asatekin, Zwitterionic copolymer self-assembly for fouling resistant, high flux membranes with size-based small molecule selectivity, Journal of Membrane Science, 493 (2015) 755-765.

[58] P. Bengani-Lutz, E. Converse, P. Cebe, A. Asatekin, Self-Assembling Zwitterionic Copolymers as Membrane Selective Layers with Excellent Fouling Resistance: Effect of Zwitterion Chemistry, ACS Applied Materials & Interfaces, 9 (2017) 20859-20872.
[59] P. Bengani-Lutz, R.D. Zaf, P.Z. Culfaz-Emecen, A. Asatekin, Extremely fouling resistant zwitterionic copolymer membranes with ~ 1nm pore size for treating municipal, oily and textile wastewater streams, Journal of Membrane Science, 543 (2017) 184-194.
[60] K. Glinel, P. Thebault, V. Humblot, C.M. Pradier, T. Jouenne, Antibacterial surfaces developed from bio-inspired approaches, Acta Biomaterialia, 8 (2012) 1670-1684.
[61] Y.-F. Yang, H.-Q. Hu, Y. Li, L.-S. Wan, Z.-K. Xu, Membrane surface with antibacterial property by grafting polycation, Journal of Membrane Science, 376 (2011) 132-141.
[62] V.P. Dhende, S. Samanta, D.M. Jones, I.R. Hardin, J. Locklin, One-step photochemical synthesis of permanent, nonleaching, ultrathin antimicrobial coatings for textiles and plastics, ACS Applied Materials & Interfaces, 3 (2011) 2830-2837.
[63] E.-R. Kenawy, S.D. Worley, R. Broughton, The Chemistry and Applications of Antimicrobial Polymers: A State-of-the-Art Review, Biomacromolecules, 8 (2007) 1359-1384.
[64] S.B. Lee, R.R. Koepsel, S.W. Morley, K. Matyjaszewski, Y. Sun, A.J. Russell, Permanent, Nonleaching Antibacterial Surfaces. 1. Synthesis by Atom Transfer Radical Polymerization, Biomacromolecules, 5 (2004) 877-882.
[65] T. Abel, J.I. Cohen, R. Engel, M. Filshtinskaya, A. Melkonian, K. Melkonian, Preparation and investigation of antibacterial carbohydrate-based surfaces, Carbohydrate Research, 337 (2002) 2495-2499.
[66] J.C. Tiller, C.-J. Liao, K. Lewis, A.M. Klibanov, Designing surfaces that kill bacteria on contact, Proceedings of the National Academy of Sciences, 98 (2001) 5981-5985.
[67] J.C. Tiller, S.B. Lee, K. Lewis, A.M. Klibanov, Polymer surfaces derivatized with poly(vinyl-N-hexylpyridinium) kill airborne and waterborne bacteria, Biotechnology and Bioengineering, 79 (2002) 465-471.
[68] T. Thorsteinsson, M. Másson, K.G. Kristinsson, M.A. Hjálmarsdóttir, H. Hilmarsson, T. Loftsson, Soft Antimicrobial Agents: Synthesis and Activity of Labile Environmentally Friendly Long Chain Quaternary Ammonium Compounds, Journal of Medicinal Chemistry, 46 (2003) 4173-4181.
[69] A.C. Engler, A. Shukla, S. Puranam, H.G. Buss, N. Jreige, P.T. Hammond, Effects of Side Group Functionality and Molecular Weight on the Activity of Synthetic Antimicrobial Polypeptides, Biomacromolecules, 12 (2011) 1666-1674.
[70] I. Yudovin-Farber, N. Beyth, E. Weiss, A. Domb, Antibacterial effect of composite resins containing quaternary ammonium polyethyleneimine nanoparticles, J Nanopart Res, 12 (2010) 591-603.
[71] J. Yin, Y. Yang, Z. Hu, B. Deng, Attachment of silver nanoparticles (AgNPs) onto thin-film composite (TFC) membranes through covalent bonding to reduce membrane biofouling, Journal of Membrane Science, 441 (2013) 73-82.

[72] X. Cao, M. Tang, F. Liu, Y. Nie, C. Zhao, Immobilization of silver nanoparticles onto sulfonated polyethersulfone membranes as antibacterial materials, Colloids and Surfaces B: Biointerfaces, 81 (2010) 555-562.
[73] W.-R. Li, X.-B. Xie, Q.-S. Shi, H.-Y. Zeng, O.-Y. You-Sheng, Y.-B. Chen, Antibacterial activity and mechanism of silver nanoparticles on Escherichia coli, Applied Microbiology and Biotechnology, 85 (2010) 1115-1122.
[74] K. Wybrańska, J. Paczesny, K. Serejko, K. Sura, K. Włodyga, I. Dzięcielewski, S.T. Jones, A. Śliwa, I. Wybrańska, R. Hołyst, O.A. Sherman, M. Fiałkowski, Gold–Oxoborate Nanocomposites and Their Biomedical Applications, ACS Applied Materials & Interfaces, 7 (2015) 3931-3939.
[75] A. Tiraferri, C.D. Vecitis, M. Elimelech, Covalent binding of single-walled carbon nanotubes to polyamide membranes for antimicrobial surface properties, ACS Applied Materials & Interfaces, 3 (2011) 2869-2877.
[76] F.o. Perreault, M.E. Tousley, M. Elimelech, Thin-film composite polyamide membranes functionalized with biocidal graphene oxide nanosheets, Environmental Science & Technology Letters, 1 (2013) 71-76.
[77] B. Mi, Graphene oxide membranes for ionic and molecular sieving, Science, 343 (2014) 740-742.
[78] Z.-B. Zhang, J.-J. Wu, Y. Su, J. Zhou, Y. Gao, H.-Y. Yu, J.-S. Gu, Layer-by-layer assembly of graphene oxide on polypropylene macroporous membranes via click chemistry to improve antibacterial and antifouling performance, Applied Surface Science, 332 (2015) 300-307.
[79] J. Jiang, L. Zhu, L. Zhu, H. Zhang, B. Zhu, Y. Xu, Antifouling and antimicrobial polymer membranes based on bioinspired polydopamine and strong hydrogen-bonded poly (N-vinyl pyrrolidone), ACS Applied Materials & Interfaces, 5 (2013) 12895-12904.
[80] B.P. Tripathi, N.C. Dubey, S. Choudhury, F. Simon, M. Stamm, Antifouling and antibiofouling pH responsive block copolymer based membranes by selective surface modification, Journal of Materials Chemistry B, 1 (2013) 3397-3409.
[81] T. Cai, W.J. Yang, K.-G. Neoh, E.-T. Kang, Poly (vinylidene fluoride) membranes with hyperbranched antifouling and antibacterial polymer brushes, Industrial & Engineering Chemistry Research, 51 (2012) 15962-15973.
[82] M. Herzberg, A. Sweity, M. Brami, Y. Kaufman, V. Freger, G. Oron, S. Belfer, R. Kasher, Surface properties and reduced biofouling of graft-copolymers that possess oppositely charged groups, Biomacromolecules, 12 (2011) 1169-1177.
[83] G. Ye, J. Lee, F. Perreault, M. Elimelech, Controlled Architecture of Dual-Functional Block Copolymer Brushes on Thin-Film Composite Membranes for Integrated “Defending” and “Attacking” Strategies against Biofouling, ACS Applied Materials & Interfaces, 7 (2015) 23069-23079.
[84] L. Mi, S. Jiang, Integrated antimicrobial and nonfouling zwitterionic polymers, Angewandte Chemie International Edition, 53 (2014) 1746-1754.
[85] P. Zou, W. Hartleb, K. Lienkamp, It takes walls and knights to defend a castle–synthesis of surface coatings from antimicrobial and antibiofouling polymers, Journal of Materials Chemistry, 22 (2012) 19579-19589.

[86] Q. Yu, J. Cho, P. Shivapooja, L.K. Ista, G.P. López, Nanopatterned Smart Polymer Surfaces for Controlled Attachment, Killing, and Release of Bacteria, ACS Applied Materials & Interfaces, 5 (2013) 9295-9304.
[87] Y. Mei, C. Yao, X. Li, A simple approach to constructing antibacterial and anti-biofouling nanofibrous membranes, Biofouling, 30 (2014) 313-322.
[88] M.S. Rahaman, H. Thérien-Aubin, M. Ben-Sasson, C.K. Ober, M. Nielsen, M. Elimelech, Control of biofouling on reverse osmosis polyamide membranes modified with biocidal nanoparticles and antifouling polymer brushes, Journal of Materials Chemistry B, 2 (2014) 1724-1732.
[89] I. Sawada, R. Fachrul, T. Ito, Y. Ohmukai, T. Maruyama, H. Matsuyama, Development of a hydrophilic polymer membrane containing silver nanoparticles with both organic antifouling and antibacterial properties, Journal of Membrane Science, 387 (2012) 1-6.
[90] G.M. Nisola, J.S. Park, A.B. Beltran, W.-J. Chung, Silver nanoparticles in a polyether-block-polyamide copolymer towards antimicrobial and antifouling membranes, RSC Advances, 2 (2012) 2439-2448.
[91] B. Cao, Q. Tang, L. Li, J. Humble, H. Wu, L. Liu, G. Cheng, Switchable antimicrobial and antifouling hydrogels with enhanced mechanical properties, Advanced Healthcare Materials, 2 (2013) 1096-1102.
[92] B. Cao, L. Li, Q. Tang, G. Cheng, The impact of structure on elasticity, switchability, stability and functionality of an all-in-one carboxybetaine elastomer, Biomaterials, 34 (2013) 7592-7600.
[93] Z. Cao, L. Mi, J. Mendiola, J.R. Ella-Menye, L. Zhang, H. Xue, S. Jiang, Reversibly switching the function of a surface between attacking and defending against bacteria, Angewandte Chemie International Edition, 51 (2012) 2602-2605.
[94] Z. Cao, N. Brault, H. Xue, A. Keefe, S. Jiang, Manipulating Sticky and Non-Sticky Properties in a Single Material, Angewandte Chemie International Edition, 50 (2011) 6102-6104.
[95] Y. Ding, S. Maruf, M. Aghajani, A.R. Greenberg, Surface patterning of polymeric membranes and its effect on antifouling characteristics, Separation Science and Technology, 52 (2017) 240-257.
[96] O. Heinz, M. Aghajani, A.R. Greenberg, Y. Ding, Surface-patterning of polymeric membranes: fabrication and performance, Current Opinion in Chemical Engineering, 20 (2018) 1-12.
[97] E.M. Vrijenhoek, S. Hong, M. Elimelech, Influence of membrane surface properties on initial rate of colloidal fouling of reverse osmosis and nanofiltration membranes, Journal of Membrane Science, 188 (2001) 115-128.
[98] L. Chen, Y. Tian, C.-q. Cao, J. Zhang, Z.-n. Li, Interaction energy evaluation of soluble microbial products (SMP) on different membrane surfaces: Role of the reconstructed membrane topology, Water Research, 46 (2012) 2693-2704.
[99] J.S. Louie, I. Pinnau, I. Ciobanu, K.P. Ishida, A. Ng, M. Reinhard, Effects of polyether–polyamide block copolymer coating on performance and fouling of reverse osmosis membranes, Journal of Membrane Science, 280 (2006) 762-770.

[100] R. Yang, J. Xu, G. Ozaydin-Ince, S.Y. Wong, K.K. Gleason, Surface-tethered zwitterionic ultrathin antifouling coatings on reverse osmosis membranes by initiated chemical vapor deposition, Chemistry of Materials, 23 (2011) 1263-1272.
[101] J. Wei, C. Qiu, Y.-N. Wang, R. Wang, C.Y. Tang, Comparison of NF-like and RO-like thin film composite osmotically-driven membranes—implications for membrane selection and process optimization, Journal of Membrane Science, 427 (2013) 460-471.
[102] R.J. Gohari, W.J. Lau, T. Matsuura, A.F. Ismail, Effect of surface pattern formation on membrane fouling and its control in phase inversion process, Journal of Membrane Science, 446 (2013) 326-331.
[103] S.H. Maruf, L. Wang, A.R. Greenberg, J. Pellegrino, Y. Ding, Use of nanoimprinted surface patterns to mitigate colloidal deposition on ultrafiltration membranes, Journal of Membrane Science, 428 (2013) 598-607.
[104] A.I. Hochbaum, J. Aizenberg, Bacteria pattern spontaneously on periodic nanostructure arrays, Nano Letters, 10 (2010) 3717-3721.
[105] A.J. Scardino, R. de Nys, Mini review: Biomimetic models and bioinspired surfaces for fouling control, Biofouling, 27 (2011) 73-86.
[106] W.G. Bae, H.N. Kim, D. Kim, S.H. Park, H.E. Jeong, K.Y. Suh, 25th anniversary article: scalable multiscale patterned structures inspired by nature: the role of hierarchy, Advanced Materials, 26 (2014) 675-700.
[107] R.M. May, M.G. Hoffman, M.J. Sogo, A.E. Parker, G.A. O'Toole, A.B. Brennan, S.T. Reddy, Micro-patterned surfaces reduce bacterial colonization and biofilm formation in vitro: Potential for enhancing endotracheal tube designs, Clinical and Translational Medicine, 3 (2014) 1-9.
[108] J.T. Decker, C.M. Kirschner, C.J. Long, J.A. Finlay, M.E. Callow, J.A. Callow, A.B. Brennan, Engineered antifouling microtopographies: an energetic model that predicts cell attachment, Langmuir, 29 (2013) 13023-13030.
[109] C.M. Kirschner, A.B. Brennan, Bio-inspired antifouling strategies, Annual Review of Materials Research, 42 (2012) 211-229.
[110] S.T. Reddy, K.K. Chung, C.J. McDaniel, R.O. Darouiche, J. Landman, A.B. Brennan, Micropatterned surfaces for reducing the risk of catheter-associated urinary tract infection: an in vitro study on the effect of sharklet micropatterned surfaces to inhibit bacterial colonization and migration of uropathogenic Escherichia coli, Journal of Endourology, 25 (2011) 1547-1552.
[111] J.F. Schumacher, C.J. Long, M.E. Callow, J.A. Finlay, J.A. Callow, A.B. Brennan, Engineered nanoforce gradients for inhibition of settlement (attachment) of swimming algal spores, Langmuir, 24 (2008) 4931-4937.
[112] K.K. Chung, J.F. Schumacher, E.M. Sampson, R.A. Burne, P.J. Antonelli, A.B. Brennan, Impact of engineered surface microtopography on biofilm formation of Staphylococcus aureus, Biointerphases, 2 (2007) 89-94.
[113] M.L. Carman, T.G. Estes, A.W. Feinberg, J.F. Schumacher, W. Wilkerson, L.H. Wilson, M.E. Callow, J.A. Callow, A.B. Brennan, Engineered antifouling microtopographies–correlating wettability with cell attachment, Biofouling, 22 (2006) 11-21.

[114] D. Zhao, Q. Tian, M. Wang, Y. Jin, Study on the hydrophobic property of shark-skin-inspired micro-riblets, Journal of Bionic Engineering, 11 (2014) 296-302.
[115] L. Wen, J.C. Weaver, G.V. Lauder, Biomimetic shark skin: design, fabrication and hydrodynamic function, Journal of Experimental Biology, 217 (2014) 1656-1666.
[116] B. Dean, B. Bhushan, Shark-skin surfaces for fluid-drag reduction in turbulent flow: a review, Philosophical Transactions of the Royal Society of London A: Mathematical, Physical and Engineering Sciences, 368 (2010) 4775-4806.
[117] Y. Luo, Y. Liu, J. Anderson, X. Li, Y. Li, Improvement of water-repellent and hydrodynamic drag reduction properties on bio-inspired surface and exploring sharkskin effect mechanism, Applied Physics A, 120 (2015) 369-377.
[118] J. Oeffner, G.V. Lauder, The hydrodynamic function of shark skin and two biomimetic applications, Journal of Experimental Biology, 215 (2012) 785-795.
[119] N.H. Vrolijk, N.M. Targett, R.E. Baier, A.E. Meyer, Surface characterisation of two gorgonian coral species: Implications for a natural antifouling defence, Biofouling, 2 (1990) 39-54.
[120] G.D. Bixler, A. Theiss, B. Bhushan, S.C. Lee, Anti-fouling properties of microstructured surfaces bio-inspired by rice leaves and butterfly wings, Journal of Colloid and Interface Science, 419 (2014) 114-133.
[121] F. Wan, Q. Ye, B. Yu, X. Pei, F. Zhou, Multiscale hairy surfaces for nearly perfect marine antibiofouling, Journal of Materials Chemisty B, 1 (2013) 3599-3606.
[122] Y.T. Cheng, D.E. Rodak, C.A. Wong, C.A. Hayden, Effects of micro- and nano-structures on the self-cleaning behaviour of lotus leaves, Nanotechnology, 17 (2006) 1359.
[123] B. Bharat, J. Yong Chae, Micro- and nanoscale characterization of hydrophobic and hydrophilic leaf surfaces, Nanotechnology, 17 (2006) 2758.
[124] N.C. Wardrip, M. Dsouza, M. Urgun-Demirtas, S.W. Snyder, J.A. Gilbert, C.J. Arnusch, Printing-assisted surface modifications of patterned ultrafiltration membranes, ACS Applied Materials & Interfaces, 8 (2016) 30271-30280.
[125] S. Badalov, Y. Oren, C.J. Arnusch, Ink-jet printing assisted fabrication of patterned thin film composite membranes, Journal of Membrane Science, 493 (2015) 508-514.
[126] J.A. Kharraz, M. Bilad, H.A. Arafat, Simple and effective corrugation of PVDF membranes for enhanced MBR performance, Journal of Membrane Science, 475 (2015) 91-100.
[127] J.A. Kharraz, M. Bilad, H.A. Arafat, Flux stabilization in membrane distillation desalination of seawater and brine using corrugated PVDF membranes, Journal of Membrane Science, 495 (2015) 404-414.
[128] L. Hoipkemeier-Wilson, J.F. Schumacher, M.L. Carman, A.L. Gibson, A.W. Feinberg, M.E. Callow, J.A. Finlay, J.A. Callow, A.B. Brennan, Antifouling potential of lubricious, micro-engineered, PDMS elastomers against zoospores of the green fouling alga Ulva (Enteromorpha), Biofouling, 20 (2004) 53-63.
[129] M. Vucko, A. Poole, C. Carl, B. Sexton, F. Glenn, S. Whalan, R. de Nys, Using textured PDMS to prevent settlement and enhance release of marine fouling organisms, Biofouling, 30 (2014) 1-16.

[130] R. Vasudevan, A.J. Kennedy, M. Merritt, F.H. Crocker, R.H. Baney, Microscale patterned surfaces reduce bacterial fouling-microscopic and theoretical analysis, Colloids and Surfaces B: Biointerfaces, 117 (2014) 225-232.
[131] M.H. Yildirim, J. te Braake, H.C. Aran, D.F. Stamatialis, M. Wessling, Micro-patterned Nafion membranes for direct methanol fuel cell applications, Journal of Membrane Science, 349 (2010) 231-236.
[132] J.W. Bae, Y.-H. Cho, Y.-E. Sung, K. Shin, J.Y. Jho, Performance enhancement of polymer electrolyte membrane fuel cell by employing line-patterned Nafion membrane, Journal of Industrial and Engineering Chemistry, 18 (2012) 876-879.
[133] A. Omosebi, R.S. Besser, Electron beam patterned Nafion membranes for DMFC applications, Journal of Power Sources, 228 (2013) 151-158.
[134] Y.-H. Cho, J.W. Bae, O.-H. Kim, J.Y. Jho, N. Jung, K. Shin, H. Choi, H. Choe, Y.-H. Cho, Y.-E. Sung, High performance direct methanol fuel cells with micro/nano-patterned polymer electrolyte membrane, Journal of Membrane Science, 467 (2014) 36-40.
[135] S.M. Kim, Y.S. Kang, C. Ahn, S. Jang, M. Kim, Y.-E. Sung, S.J. Yoo, M. Choi, Prism-patterned Nafion membrane for enhanced water transport in polymer electrolyte membrane fuel cell, Journal of Power Sources, 317 (2016) 19-24.
[136] S. Cuynet, A. Caillard, J. Bigarré, P. Buvat, Impact of the patterned membrane morphology on PEMFC performances of ultra-low platinum loaded MEAs, International Journal of Hydrogen Energy, 42 (2017) 7974-7985.
[137] J.H. Jang, J. Lee, S.-Y. Jung, D.-C. Choi, Y.-J. Won, K.H. Ahn, P.-K. Park, C.-H. Lee, Correlation between particle deposition and the size ratio of particles to patterns in nano-and micro-patterned membrane filtration systems, Separation and Purification Technology, 156 (2015) 608-616.
[138] Y.-J. Won, S.-Y. Jung, J.-H. Jang, J.-W. Lee, H.-R. Chae, D.-C. Choi, K.H. Ahn, C.-H. Lee, P.-K. Park, Correlation of membrane fouling with topography of patterned membranes for water treatment, Journal of Membrane Science, 498 (2016) 14-19.
[139] Y.-J. Won, J. Lee, D.-C. Choi, H.R. Chae, I. Kim, C.-H. Lee, I.-C. Kim, Preparation and application of patterned membranes for wastewater treatment, Environmental Science & Technology, 46 (2012) 11021-11027.
[140] D.-C. Choi, S.-Y. Jung, Y.-J. Won, J.H. Jang, J.-W. Lee, H.-R. Chae, J. Lim, K.H. Ahn, S. Lee, J.-H. Kim, P.-K. Park, C.-H. Lee, Effect of Pattern Shape on the Initial Deposition of Particles in the Aqueous Phase on Patterned Membranes during Crossflow Filtration, Environmental Science & Technology Letters, 4 (2017) 66-70.
[141] Y.K. Lee, Y.-J. Won, J.H. Yoo, K.H. Ahn, C.-H. Lee, Flow analysis and fouling on the patterned membrane surface, Journal of Membrane Science, 427 (2013) 320-325.
[142] Y.-J. Won, D.-C. Choi, J.H. Jang, J.-W. Lee, H.R. Chae, I. Kim, K.H. Ahn, C.-H. Lee, I.-C. Kim, Factors affecting pattern fidelity and performance of a patterned membrane, Journal of Membrane Science, 462 (2014) 1-8.
[143] S.Y. Jung, Y.-J. Won, J.H. Jang, J.H. Yoo, K.H. Ahn, C.-H. Lee, Particle deposition on the patterned membrane surface: Simulation and experiments, Desalination, 370 (2015) 17-24.

[144] I.S. Ngene, R.G. Lammertink, M. Wessling, W.G. Van der Meer, Particle deposition and biofilm formation on microstructured membranes, Journal of Membrane Science, 364 (2010) 43-51.
[145] Y. Gençal, E. Durmaz, P. Çulfaz-Emecen, Preparation of patterned microfiltration membranes and their performance in crossflow yeast filtration, Journal of Membrane Science, 476 (2015) 224-233.
[146] I.M.A. ElSherbiny, A.S.G. Khalil, M. Ulbricht, Surface micro-patterning as a promising platform towards novel polyamide thin-film composite membranes of superior performance, Journal of Membrane Science, 529 (2017) 11-22.
[147] P. Culfaz, M. Wessling, R. Lammertink, Hollow fiber ultrafiltration membranes with microstructured inner skin, Journal of Membrane Science, 369 (2011) 221-227.
[148] P.Z. Çulfaz, E. Rolevink, C. van Rijn, R.G. Lammertink, M. Wessling, Microstructured hollow fibers for ultrafiltration, Journal of Membrane Science, 347 (2010) 32-41.
[149] P. Culfaz, M. Wessling, R. Lammertink, Fouling behavior of microstructured hollow fiber membranes in submerged and aerated filtrations, Water Research, 45 (2011) 1865-1871.
[150] M. Hashino, T. Katagiri, N. Kubota, Y. Ohmukai, T. Maruyama, H. Matsuyama, Effect of surface roughness of hollow fiber membranes with gear-shaped structure on membrane fouling by sodium alginate, Journal of Membrane Science, 366 (2011) 389-397.
[151] I. Kim, D.-C. Choi, J. Lee, H.-R. Chae, J.H. Jang, C.-H. Lee, P.-K. Park, Y.-J. Won, Preparation and application of patterned hollow-fiber membranes to membrane bioreactor for wastewater treatment, Journal of Membrane Science, 490 (2015) 190-196.
[152] S.H. Maruf, A.R. Greenberg, J. Pellegrino, Y. Ding, Critical flux of surface-patterned ultrafiltration membranes during cross-flow filtration of colloidal particles, Journal of Membrane Science, 471 (2014) 65-71.
[153] S.H. Maruf, M. Rickman, L. Wang, J. Mersch IV, A.R. Greenberg, J. Pellegrino, Y. Ding, Influence of sub-micron surface patterns on the deposition of model proteins during active filtration, Journal of Membrane Science, 444 (2013) 420-428.
[154] M. Xie, W. Luo, S.R. Gray, Surface pattern by nanoimprint for membrane fouling mitigation: Design, performance and mechanisms, Water Research, (2017).
[155] D.J. Miller, S. Kasemset, D.R. Paul, B.D. Freeman, Comparison of membrane fouling at constant flux and constant transmembrane pressure conditions, Journal of Membrane Science, 454 (2014) 505-515.
[156] R.W. Field, G.K. Pearce, Critical, sustainable and threshold fluxes for membrane filtration with water industry applications, Advances in Colloid and Interface Science, 164 (2011) 38-44.
[157] R.W. Field, D. Wu, J.A. Howell, B.B. Gupta, Critical flux concept for microfiltration fouling, Journal of Membrane Science, 100 (1995) 259-272.
[158] P. Le Clech, B. Jefferson, I.S. Chang, S.J. Judd, Critical flux determination by the flux-step method in a submerged membrane bioreactor, Journal of Membrane Science, 227 (2003) 81-93.

[159] B. Espinasse, P. Bacchin, P. Aimar, On an experimental method to measure critical flux in ultrafiltration, Desalination, 146 (2002) 91-96.
[160] F. Fan, H. Zhou, H. Husain, Identification of wastewater sludge characteristics to predict critical flux for membrane bioreactor processes, Water Research, 40 (2006) 205-212.
[161] A. Brookes, B. Jefferson, G. Guglielmi, S. Judd, Sustainable flux fouling in a membrane bioreactor: impact of flux and MLSS, Separation Science and Technology, 41 (2006) 1279-1291.
[162] P. Bacchin, P. Aimar, R.W. Field, Critical and sustainable fluxes: theory, experiments and applications, Journal of Membrane Science, 281 (2006) 42-69.
[163] G. Guglielmi, D. Chiarani, D. Saroj, G. Andreottola, Impact of chemical cleaning and air-sparging on the critical and sustainable flux in a flat sheet membrane bioreactor for municipal wastewater treatment, Water Science and Technology, 57 (2008) 1873-1879.
[164] Z. Wu, X. Wang, Z. Wang, X. Du, Identification of sustainable flux in the process of using flat-sheet membrane for simultaneous thickening and digestion of waste activated sludge, Journal of Hazardous Materials, 162 (2009) 1397-1403.
[165] M. Stoller, M. Bravi, A. Chianese, Threshold flux measurements of a nanofiltration membrane module by critical flux data conversion, Desalination, 315 (2013) 142-148.
[166] J. Luo, Z. Zhu, L. Ding, O. Bals, Y. Wan, M.Y. Jaffrin, E. Vorobiev, Flux behavior in clarification of chicory juice by high-shear membrane filtration: evidence for threshold flux, Journal of Membrane Science, 435 (2013) 120-129.
[167] J. Luo, S.T. Morthensen, A.S. Meyer, M. Pinelo, Filtration behavior of casein glycomacropeptide (CGMP) in an enzymatic membrane reactor: fouling control by membrane selection and threshold flux operation, Journal of Membrane Science, 469 (2014) 127-139.
[168] O. Habimana, A. Semião, E. Casey, The role of cell-surface interactions in bacterial initial adhesion and consequent biofilm formation on nanofiltration/reverse osmosis membranes, Journal of Membrane Science, 454 (2014) 82-96.
[169] M.L.M. Tirado, M. Bass, M. Piatkovsky, M. Ulbricht, M. Herzberg, V. Freger, Assessing biofouling resistance of a polyamide reverse osmosis membrane surface-modified with a zwitterionic polymer, Journal of Membrane Science, 520 (2016) 490-498.
[170] Y. Sui, X. Gao, Z. Wang, C. Gao, Antifouling and antibacterial improvement of surface-functionalized poly (vinylidene fluoride) membrane prepared via dihydroxyphenylalanine-initiated atom transfer radical graft polymerizations, Journal of Membrane Science, 394 (2012) 107-119.
[171] H.C. Chenette, J.M. Welsh, S.M. Husson, Affinity membrane adsorbers for binding arginine-rich proteins, Separation Science and Technology, 52 (2017) 276-286.
[172] B.V. Bhut, S.R. Wickramasinghe, S.M. Husson, Preparation of high-capacity, weak anion-exchange membranes for protein separations using surface-initiated atom transfer radical polymerization, Journal of Membrane Science, 325 (2008) 176-183.
[173] D.K. Owens, R. Wendt, Estimation of the surface free energy of polymers, Journal of Applied Polymer Science, 13 (1969) 1741-1747.

[174] A. Rudawska, E. Jacniacka, Analysis for determining surface free energy uncertainty by the Owen–Wendt method, International Journal of Adhesion and Adhesives, 29 (2009) 451-457.
[175] M. Kobayashi, Y. Terayama, H. Yamaguchi, M. Terada, D. Murakami, K. Ishihara, A. Takahara, Wettability and antifouling behavior on the surfaces of superhydrophilic polymer brushes, Langmuir, 28 (2012) 7212-7222.
[176] S. Nakasone, Characterization of Polyethersulfone (PES) and Polyvinylidene Difluoride (PVDF) Resistive Membranes under In Vitro Staphylococcus aureus Challenge, in, 2014.
[177] K. Baransi-Karkaby, M. Bass, S. Levchenko, S. Eitan, V. Freger, Facile Modification of Reverse Osmosis Membranes by Surfactant-Assisted Acrylate Grafting for Enhanced Selectivity, Environmental Science & Technology, 51 (2017) 2347-2354.
[178] W. Ying, R. Kumar, M. Herzberg, R. Kasher, Diminished swelling of cross-linked aromatic oligoamide surfaces revealing a new fouling mechanism of reverse-osmosis membranes, Environmental Science & Technology, 49 (2015) 6815-6822.
[179] W. Ying, N. Siebdrath, W. Uhl, V. Gitis, M. Herzberg, New insights on early stages of RO membranes fouling during tertiary wastewater desalination, Journal of Membrane Science, 466 (2014) 26-35.
[180] R. Murga, P.S. Stewart, D. Daly, Quantitative analysis of biofilm thickness variability, Biotechnology and Bioengineering, 45 (1995) 503-510.
[181] A. Heydorn, A.T. Nielsen, M. Hentzer, C. Sternberg, M. Givskov, B.K. Ersbøll, S. Molin, Quantification of biofilm structures by the novel computer program COMSTAT, Microbiology, 146 (2000) 2395-2407.
[182] M. Bass, V. Freger, Facile evaluation of coating thickness on membranes using ATR-FTIR, Journal of Membrane Science, 492 (2015) 348-354.
[183] D. He, H. Susanto, M. Ulbricht, Photo-irradiation for preparation, modification and stimulation of polymeric membranes, Progress in Polymer Science, 34 (2009) 62-98.
[184] J. Haberkamp, M. Ernst, G. Makdissy, P.M. Huck, M. Jekel, Protein fouling of ultrafiltration membranes-investigation of several factors relevant for tertiary wastewater treatment, Journal of Environmental Engineering and Science, 7 (2008) 651-660.
[185] P. Kaner, D.J. Johnson, E. Seker, N. Hilal, S.A. Altinkaya, Layer-by-layer surface modification of polyethersulfone membranes using polyelectrolytes and AgCl/TiO 2 xerogels, Journal of Membrane Science, 493 (2015) 807-819.
[186] L. De Bartolo, S. Morelli, M. Rende, A. Gordano, E. Drioli, New modified polyetheretherketone membrane for liver cell culture in biohybrid systems: adhesion and specific functions of isolated hepatocytes, Biomaterials, 25 (2004) 3621-3629.
[187] M. Ulbricht, H. Yang, Porous polypropylene membranes with different carboxyl polymer brush layers for reversible protein binding via surface-initiated graft copolymerization, Chemistry of Materials, 17 (2005) 2622-2631.
[188] R.M. Silverstein, F.X. Webster, D.J. Kiemle, Spectrometric Identification of Organic Compounds, 7th ed., John Wiley & Sons, Inc., 2011.
[189] R.M.C. Dawson, D.C. Elliot, W.H. Elliot, K.M. Jones, Data for biochemical research, 3rd ed., Oxford University Press, 1986.

[190] D.B. Thomas, Y.A. Vasilieva, R.S. Armentrout, C.L. McCormick, Synthesis, characterization, and aqueous solution behavior of electrolyte-and pH-responsive carboxybetaine-containing cyclocopolymers, Macromolecules, 36 (2003) 9710-9715.
[191] W.S. Ang, S. Lee, M. Elimelech, Chemical and physical aspects of cleaning of organic-fouled reverse osmosis membranes, Journal of Membrane Science, 272 (2006) 198-210.
[192] A. Subramani, E.M. Hoek, Biofilm formation, cleaning, re-formation on polyamide composite membranes, Desalination, 257 (2010) 73-79.
[193] O. Moreau, C. Portella, F. Massicot, J. Herry, A. Riquet, Adhesion on polyethylene glycol and quaternary ammonium salt-grafted silicon surfaces: Influence of physicochemical properties, Surface and Coatings Technology, 201 (2007) 5994-6004.
[194] L. Bereschenko, A. Stams, G. Euverink, M. Van Loosdrecht, Biofilm formation on reverse osmosis membranes is initiated and dominated by Sphingomonas spp, Applied and Environmental Microbiology, 76 (2010) 2623-2632.
[195] D. Janjaroen, F. Ling, G. Monroy, N. Derlon, E. Mogenroth, S.A. Boppart, W.-T. Liu, T.H. Nguyen, Roles of ionic strength and biofilm roughness on adhesion kinetics of Escherichia coli onto groundwater biofilm grown on PVC surfaces, Water Research, 47 (2013) 2531-2542.
[196] E.M. Van Wagner, A.C. Sagle, M.M. Sharma, Y.-H. La, B.D. Freeman, Surface modification of commercial polyamide desalination membranes using poly (ethylene glycol) diglycidyl ether to enhance membrane fouling resistance, Journal of Membrane Science, 367 (2011) 273-287.
[197] P. Culfaz, M. Haddad, M. Wessling, R. Lammertink, Fouling behavior of microstructured hollow fibers in cross-flow filtrations: Critical flux determination and direct visual observation of particle deposition, Journal of Membrane Science, 372 (2011) 210-218.
[198] S.H. Maruf, A.R. Greenberg, J. Pellegrino, Y. Ding, Fabrication and characterization of a surface-patterned thin film composite membrane, Journal of Membrane Science, 452 (2014) 11-19.
[199] M. Hashino, T. Katagiri, N. Kubota, Y. Ohmukai, T. Maruyama, H. Matsuyama, Effect of membrane surface morphology on membrane fouling with sodium alginate, Journal of Membrane Science, 366 (2011) 258-265.
[200] F. Wan, X. Pei, B. Yu, Q. Ye, F. Zhou, Q. Xue, Grafting polymer brushes on biomimetic structural surfaces for anti-algae fouling and foul release, ACS Applied Materials & Interfaces, 4 (2012) 4557-4565.
[201] C.Y. Tang, Y.-N. Kwon, J.O. Leckie, Effect of membrane chemistry and coating layer on physiochemical properties of thin film composite polyamide RO and NF membranes: I. FTIR and XPS characterization of polyamide and coating layer chemistry, Desalination, 242 (2009) 149-167.
[202] Q. Li, Z. Xu, I. Pinnau, Fouling of reverse osmosis membranes by biopolymers in wastewater secondary effluent: Role of membrane surface properties and initial permeate flux, Journal of Membrane Science, 290 (2007) 173-181.

[203] S.H. Maruf, Z. Li, J.A. Yoshimura, J. Xiao, A.R. Greenberg, Y. Ding, Influence of nanoimprint lithography on membrane structure and performance, Polymer, 69 (2015) 129-137.
[204] J.Y. Chung, J.-H. Lee, K.L. Beers, C.M. Stafford, Stiffness, Strength, and Ductility of Nanoscale Thin Films and Membranes: A Combined Wrinkling–Cracking Methodology, Nano Letters, 11 (2011) 3361-3365.
[205] A. Szymczyk, Y. Lanteri, P. Fievet, Modelling the transport of asymmetric electrolytes through nanofiltration membranes, Desalination, 245 (2009) 396-407.
[206] H. Choi, K. Zhang, D.D. Dionysiou, D.B. Oerther, G.A. Sorial, Influence of cross-flow velocity on membrane performance during filtration of biological suspension, Journal of Membrane Science, 248 (2005) 189-199.
[207] S. Suwarno, X. Chen, T. Chong, D. McDougald, Y. Cohen, S. Rice, A. Fane, Biofouling in reverse osmosis processes: The roles of flux, crossflow velocity and concentration polarization in biofilm development, Journal of Membrane Science, 467 (2014) 116-125.
[208] J. Hutfles, W. Chapman, J. Pellegrino, Roll-to-roll nanoimprint lithography of ultrafiltration membrane, Journal of Applied Polymer Science, 135 (2018).
[209] S.H. Maruf, A.R. Greenberg, Y. Ding, Influence of substrate processing and interfacial polymerization conditions on the surface topography and permselective properties of surface-patterned thin-film composite membranes, Journal of Membrane Science, 512 (2016) 50-60.
[210] M. Rickman, S. Maruf, E. Kujundzic, R.H. Davis, A. Greenberg, Y. Ding, J. Pellegrino, Fractionation and flux decline studies of surface-patterned nanofiltration membranes using NaCl-glycerol-BSA solutions, Journal of Membrane Science, 527 (2017) 102-110.
[211] J.-H. Lee, J.Y. Chung, E.P. Chan, C.M. Stafford, Correlating chlorine-induced changes in mechanical properties to performance in polyamide-based thin film composite membranes, Journal of Membrane Science, 433 (2013) 72-79.
[212] L. Lin, C. Feng, R. Lopez, O. Coronell, Identifying facile and accurate methods to measure the thickness of the active layers of thin-film composite membranes – A comparison of seven characterization techniques, Journal of Membrane Science, 498 (2016) 167-179.
[213] L. Huang, N.-N. Bui, M.T. Meyering, T.J. Hamlin, J.R. McCutcheon, Novel hydrophilic nylon 6,6 microfiltration membrane supported thin film composite membranes for engineered osmosis, Journal of Membrane Science, 437 (2013) 141-149.
[214] L.F. Hoyt, New Table of the Refractive Index of Pure Glycerol at 20°C, Industrial & Engineering Chemistry, 26 (1934) 329-332.
[215] O. Coronell, B.J. Mariñas, D.G. Cahill, Depth Heterogeneity of Fully Aromatic Polyamide Active Layers in Reverse Osmosis and Nanofiltration Membranes, Environmental Science & Technology, 45 (2011) 4513-4520.
[216] O. Coronell, B.J. Mariñas, X. Zhang, D.G. Cahill, Quantification of Functional Groups and Modeling of Their Ionization Behavior in the Active Layer of FT30 Reverse Osmosis Membrane, Environmental Science & Technology, 42 (2008) 5260-5266.

[217] D. Chen, J.R. Werber, X. Zhao, M. Elimelech, A facile method to quantify the carboxyl group areal density in the active layer of polyamide thin-film composite membranes, Journal of Membrane Science, 534 (2017) 100-108.
[218] E.P. Chan, A.P. Young, J.-H. Lee, C.M. Stafford, Swelling of Ultrathin Molecular Layer-by-Layer Polyamide Water Desalination Membranes, Journal of Polymer Science Part B: Polymer Physics, 51 (2013) 1647-1655.
[219] P.C. Painter, M.M. Coleman, Fundamentals of polymer science: an introductory text, 2 ed., CRC Press LLC, 1997.
[220] S.H. Maruf, D.U. Ahn, A.R. Greenberg, Y. Ding, Glass transition behaviors of interfacially polymerized polyamide barrier layers on thin film composite membranes via nano-thermal analysis, Polymer, 52 (2011) 2643-2649.
[221] O. Akin, F. Temelli, Probing the hydrophobicity of commercial reverse osmosis membranes produced by interfacial polymerization using contact angle, XPS, FTIR, FE-SEM and AFM, Desalination, 278 (2011) 387-396.
[222] Y.-S. Zimmermann, C. Niewersch, M. Lenz, Z.h.Z. Kül, P.F.-X. Corvini, A. Schäffer, T. Wintgens, Recycling of indium from CIGS photovoltaic cells: Potential of combining acid-resistant nanofiltration with liquid–liquid extraction, Environmental Science & Technology, 48 (2014) 13412-13418.
[223] C.Y. Tang, Y.-N. Kwon, J.O. Leckie, Effect of membrane chemistry and coating layer on physiochemical properties of thin film composite polyamide RO and NF membranes: II. Membrane physiochemical properties and their dependence on polyamide and coating layers, Desalination, 242 (2009) 168-182.
[224] H. Dong, H. Du, X. Qian, Prediction of p K a Values for Oligo-methacrylic Acids Using Combined Classical and Quantum Approaches, The Journal of Physical Chemistry B, 113 (2009) 12857-12859.
[225] H. Dong, H. Du, S.R. Wickramasinghe, X. Qian, The Effects of Chemical Substitution and Polymerization on the pK_a Values of Sulfonic Acids, The Journal of Physical Chemistry B, 113 (2009) 14094-14101.
[226] J.G. Smith, Organic Chemistry, 3rd ed., McGraw-Hill, 2010.
[227] K. Matyjaszewski, Atom Transfer Radical Polymerization (ATRP): Current Status and Future Perspectives, Macromolecules, 45 (2012) 4015-4039.
[228] K. Matyjaszewski, J. Xia, Atom Transfer Radical Polymerization, Chemical Reviews, 101 (2001) 2921-2990.